



HAL
open science

Nonlinear Transport in Topological Materials and Heterostructures

Diego García Ovalle

► **To cite this version:**

Diego García Ovalle. Nonlinear Transport in Topological Materials and Heterostructures. Condensed Matter [cond-mat]. Aix Marseille Université (AMU), 2023. English. NNT : 2023AIXM0353 . tel-04479691

HAL Id: tel-04479691

<https://hal.science/tel-04479691>

Submitted on 27 Feb 2024

HAL is a multi-disciplinary open access archive for the deposit and dissemination of scientific research documents, whether they are published or not. The documents may come from teaching and research institutions in France or abroad, or from public or private research centers.

L'archive ouverte pluridisciplinaire **HAL**, est destinée au dépôt et à la diffusion de documents scientifiques de niveau recherche, publiés ou non, émanant des établissements d'enseignement et de recherche français ou étrangers, des laboratoires publics ou privés.



Distributed under a Creative Commons Attribution - NonCommercial - NoDerivatives 4.0 International License

.....

THÈSE DE DOCTORAT

Soutenue a Aix-Marseille Université

le 23 octobre, 2023 par

Diego García Ovalle

Titre de la thèse :
Nonlinear Transport in Topological Materials and
Heterostructures

Discipline

Physique et Sciences de la Matière

Spécialité

Matière Condensée et Nanosciences

École doctorale

ED 352 Physique et Sciences de la Matière

Laboratoire

Centre Interdisciplinaire de Nanoscience de Mar-
seille (CINaM)

Composition du jury

• Aurélien Manchon

Directeur de thèse

• Aix-Marseille Université

• Inti Sodemann

Rapporteur

• University of Leipzig

• Adolfo Grushin

Rapporteur

• CNRS, Institute Néel, Gre-
noble

• Fabienne Michelini

Présidente du jury

• Aix-Marseille Université

• Adeline Crépieux

Examinatrice

• Aix-Marseille Université

• Luis Hueso

Examineur

• NanoGune, San Sebastián

• Laurent Vila

Examineur

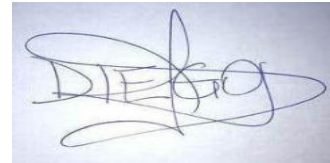
• CEA, Spintec, Grenoble

Affidavit

I, undersigned, Diego García Ovalle, hereby declare that the work presented in this manuscript is my own work, carried out under the scientific direction of Aurélien Manchon, in accordance with the principles of honesty, integrity and responsibility inherent to the research mission. The research work and the writing of this manuscript have been carried out in compliance with both the french national charter for Research Integrity and the Aix-Marseille University charter on the fight against plagiarism.

This work has not been submitted previously either in this country or in another country in the same or in a similar version to any other examination body.

Marseille, July 13th, 2023.

A handwritten signature in blue ink, appearing to read 'DIEGO', with a stylized flourish underneath.

Cette œuvre est mise à disposition selon les termes de la [Licence Creative Commons Attribution - Pas d'Utilisation Commerciale - Pas de Modification 4.0 International](https://creativecommons.org/licenses/by-nc-nd/4.0/).

Acknowledgements

Firstly, I want to express my sincere gratitude to my PhD director Aurélien Manchon for his support, guidance and confidence. Thank you very much for picking me from so far away from France and from a context completely different from you. Besides, I am very grateful for pushing my boundaries to the limit where I did not explore before, for believe in me and for giving me the opportunity to share my work and experience with amazing co-workers across the globe. Moreover, I really appreciate your kindness with me and the team, and your effort to accompany us in the road to become world leaders in Spintronics and Condensed Matter Physics. I strongly hope that this would be the first of many multiple collaborations between us. The time that I have been here working with you has confirmed me that my hard and passionate work will inevitably give me the recognition and relevancy in the physics community that I have always deserved.

Secondly, I acknowledge the help and support of Andrés Saul, Lisa Michez and Christophe Bichara for being always available for hearing me, even about my craziest ideas about the research. These discussions have inspired me profoundly in my ongoing efforts to challenge the boundaries of quantum transport and spintronics. Several avenues for future projects are already gather in a binding that has been motivated by these fruitful conversations. Then, I must thank the company of all PhD students working at CINaM. I feel that there is a part of the work that would not be successful if the small coffee breaks or a beer after the lab would not have happened.

Last but not least, I dedicate this paragraph and my research to the love and dedication of my mother, María Luz Ovalle, for encourage me on the road to pursue my dreams. She has been the perfect light that nature chose for me, showing me a remarkable strength to face life as it is, with the good and the bad. My present and my plans for the future as a theoretical physicist would not be possible without her fighting spirit. One day you are going to see me win the Nobel Prize in Physics.

List of Publications and Participation in Conferences

List of Publications in the Context of the Thesis Project :

1. D García Ovalle, A Pezo and A Manchon (2023). "Magneto-optical probe of none-equilibrium orbital magnetism via the second-order Hall effect". *In preparation*.
2. D García Ovalle, A Pezo and A Manchon (2023). "Spin-orbit torque for field-free switching in C_{3v} crystals". <https://link.aps.org/doi/10.1103/PhysRevB.107.094422>
3. D García Ovalle, A Pezo and A Manchon (2022). "Influence of the surface states on the nonlinear Hall effect in Weyl semimetals". <https://link.aps.org/doi/10.1103/PhysRevB.106.214435>
4. L Liu, A Pezo, C Zhou et al. (2022). "Crystal symmetry dependent in-plane Hall effect". *Submitted for publication*.

Collaborations During the Thesis Project :

1. A Pezo, D García Ovalle and A Manchon (2023). "Orbital Hall physics in two-dimensional Dirac materials". <https://link.aps.org/doi/10.1103/PhysRevB.108.075427>
2. A Pezo, D García Ovalle and A Manchon (2022). "Orbital Hall effect in crystals : Interatomic vs intra-atomic contributions". <https://journals.aps.org/prb/abstract/10.1103/PhysRevB.106.104414>

Awards

1. Third Best Poster Award. Topological Matter School 2023. August 21 - August 25, 2023. San Sebastián, Spain.
2. Best Presentation Student Award. 13th Meeting on Nanoscience Advances. September 26 - September 29, 2022. Porquerolles, France.

Participation in Conferences and Summer Schools During the Thesis :

1. Joint European Magnetic Symposia 2023. August 27 - September 1, 2023. Madrid, Spain.
2. Topological Matter School 2023. August 21 - August 25, 2023. San Sebastián, Spain.
3. APS March Meeting 2023. March 5 - March 10, 2023. Las Vegas, United States.
4. MMM 2022. October 31 - November 4, 2022. Minneapolis, United States.
5. 13th Meeting on Nanoscience Advances. September 26 - September 29, 2022. Porquerolles, France.
6. ETSF Young Research Meeting. September 5 - September 9, 2022. Marseille, France.
7. Orbitronics : from Topological Matter to Next Level Electronics. July 19 - July 22, 2022. Ingelheim, Germany.
8. APS March Meeting 2022. March 14 - March 18, 2022. Chicago, United States.

Résumé

Dans cette Thèse de doctorat, nous étudions théoriquement la réponse électronique non linéaire des systèmes non centrosymétriques, telle que la réponse de Hall d'ordre supérieur dans les matériaux non magnétiques et les propriétés magnétoélectriques hors équilibre dans les aimants de basse symétrie. Nous avons appliqué des analyses de symétrie basées sur la théorie des invariants et effectué des simulations de transport quantique basées sur le formalisme cinétique quantique perturbatif pour explorer la nature de différents effets non conventionnels d'intérêt primordial en spintronique théorique et expérimentale et en matière condensée. Plus précisément, nous démontrons que l'effet Hall du second ordre dans les semi-métaux de Weyl est plus sensible à la géométrie des états quantiques qu'à leur topologie. De plus, le comportement du courant de Hall correspondant est lié à l'inclinaison des cônes de Weyl appartenant au système et au niveau de Fermi par rapport à l'énergie de Weyl. En outre, nous montrons l'émergence d'un effet Kerr magnéto-optique induit par un courant non nul dans des matériaux non magnétiques, preuve supplémentaire du lien entre l'aimantation orbitale hors équilibre et l'effet Hall du second ordre entraîné par le dipôle de la courbure de Berry. Nous sommes ensuite intéressés à la réponse magnétoélectrique des matériaux magnétiques de basse symétrie. En étudiant la réponse linéaire en champ électrique, mais d'ordre supérieur dans les composants de l'aimantation, nous concluons que de nouveaux termes encore non identifiés sont autorisés par les symétries réduites du cristal magnétique. Dans le cas des cristaux trigonaux, on découvre une pléthore d'effets Hall et de couples spin-orbite atypiques, mettant l'accent sur leur origine microscopique. Dans ce contexte, nous montrons que leur émergence et leur ampleur sont liées à l'interaction entre le remplissage de la bande et la distorsion trigonale de la surface de Fermi. Les réponses non linéaires des matériaux quantiques ouvrent des perspectives inédites en physique de la matière condensée, puisqu'elles nous invitent à explorer de nouveaux mécanismes pour sonder, entre autres, la structure de bande des matériaux non conventionnels.

Mots clés : Courbure de Berry, effet Hall non linéaire, matériaux quantiques, Spin-Orbit Torque, symétries

Abstract

In this doctoral Thesis, we investigate theoretically the nonlinear electronic response of non-centrosymmetric systems, such as the higher order Hall response in non-magnetic materials and the non-equilibrium magnetoelectric properties in low symmetry magnets. We have applied symmetry analyses based on the Invariant theory and performed quantum transport simulations based on the perturbative quantum kinetic formalism, exploring the nature of different unconventional effects of prime interest in theoretical and experimental spintronics and condensed matter. Specifically, we demonstrate that the second order Hall effect in Weyl semimetals is more sensitive to the geometry of the quantum states than their topology. Moreover, the behavior of the corresponding Hall current is connected to the inclination of the Weyl cones pertaining the system and the Fermi level with respect to the Weyl energy. Besides, we show the emergence of a non-vanishing current-induced magneto-optical Kerr effect in non-magnetic materials, as an additional evidence of the connection between non-equilibrium orbital magnetization and the second order Hall effect driven by the Berry curvature dipole. We then moved to the magnetoelectric response of low symmetry magnetic materials. Investigating the linear response in electric field, but higher order in magnetization components, we conclude that yet unidentified new terms are allowed by the reduced symmetries of the magnetic crystal. In the case of trigonal crystals, we discover a plethora of atypical Hall effects and spin-orbit torques, putting an emphasis on their microscopic origin. In this context, we show that their emergence and magnitude are related with the interplay between the band filling and the trigonal warping of the Fermi surface. The nonlinear responses of quantum materials open unprecedented perspectives in condensed matter physics, as they invite us to explore new mechanisms for probing, among others, the band structure of unconventional materials.

Keywords: Berry curvature, nonlinear Hall effect, quantum materials, spin-orbit torque, symmetries

Résumé Étendu

a. Vue Générale de la Thèse

Dans ce projet de thèse, nous nous concentrons sur l'obtention de réponses non conventionnelles d'ordre élevé en perturbation (électrique ou magnétique), et dérivées de contraintes de symétrie telles que l'inversion temporelle, l'inversion spatiale et les symétries cristallines de l'échantillon. Nous considérons également la réciprocité de Onsager dans les cas où elle est obligatoire. C'est pourquoi, afin d'identifier l'origine de la réponse, nous utilisons une analyse microscopique, qui permet également de trouver un moyen de la maximiser. Nous avons réalisé ces études à travers une analyse détaillée de modèles de liaisons fortes en développant des simulations numériques.

Compte tenu de l'intérêt croissant pour les matériaux topologiques, qui sont capables de présenter de forts effets Hall dus aux divergences dans la courbure de Berry, nous nous concentrons dans le Chapitre 3 sur l'influence des états de surface des métaux de Weyl sur l'effet Hall non linéaire du second ordre en le champ électrique. Ici, on peut en déduire que la réponse dans le régime de type II peut être stimulée par des états de surface qui ne sont pas topologiques, entraînant une dépendance non triviale de l'effet Hall en fonction de l'épaisseur du système.

Ensuite, au Chapitre 4, nous montrons nos résultats sur l'effet Kerr magnéto-optique (MOKE) dans les systèmes non magnétiques sans symétrie d'inversion. Ce travail montre que, contrairement au régime linéaire, la rotation de Kerr est générée à l'aide d'un champ électrique continu, qui à son tour produit une aimantation orbitale hors équilibre. Nous illustrons ce processus dans le cas où la configuration de mesure est polaire, mais il peut être étendu au scénario longitudinal et transversal. Dans les expériences, cet effet peut être utile pour détecter l'apparition d'une aimantation orbitale hors équilibre, qui à son tour indiquerait l'apparition de l'effet Hall du second ordre en le champ électrique.

Enfin, au Chapitre 5, nous dérivons par l'analyse de symétries une série de réponses hors équilibre autorisées dans les systèmes magnétiques à symétrie trigonale. D'une part, nous nous intéressons à un effet de couple de spin-orbite en présence d'une perturbation linéaire du champ électrique, un effet prometteur pour la réalisation de dispositifs de mémoire. En nous fondant sur la théorie des invariants, nous obtenons plusieurs corrections qui apparaissent lors de l'expansion jusqu'au troisième ordre en magnétisation. En particulier, l'un de ces termes de correction est susceptible d'induire le renversement de l'aimantation en l'absence de champ magnétique extérieur. D'autre part, en corrigeant au même ordre les composantes magnétiques,

nous analysons la variété des effets Hall associés à cette symétrie. Ici, l'un d'eux a la particularité d'être antisymétrique en aimantation et en champ magnétique appliqué, ce qui permet l'apparition d'un courant transversal même lorsque les champs électrique et magnétique sont alignés l'un avec l'autre. Nous appelons cette réponse l'effet Hall chiral. D'un point de vue microscopique, on pourrait attribuer ces observables à la distortion trigonale [trigonal warping] de la surface de Fermi, qui se produit pour une valeur d'énergie suffisamment élevée.

b. Résultats Principaux

Le contrôle des degrés de liberté de l'électron dans les applications technologiques est l'un des principaux sujets d'attention en Physique de la Matière Condensée. Dans le cas de la réponse linéaire, où la dynamique des électrons est contrôlée par une perturbation linéaire du champ électrique, l'effet Hall est l'un des phénomènes les plus riches et les plus emblématiques. Au premier ordre en champ électrique, l'effet Hall nécessite que le matériau soit magnétique, ce qui laisse de côté un large spectre de systèmes où la symétrie d'inversion temporelle est conservée. Ainsi, à des ordres élevés en la perturbation, il est possible de modifier une série de restrictions dans la réponse, ce qui garantit que le spectre des matériaux où l'effet Hall est observé est élargi. De cette manière, les effets Hall non linéaires fournissent également des informations sur la structure électronique du matériau considéré. L'un des principaux exemples se produit lorsque l'on considère un système non magnétique dont la symétrie d'inversion est brisée. Ici, l'effet Hall du premier ordre est interdit par symétrie, mais une nouvelle contribution du second ordre en champ électrique apparaît. Une illustration de cette différence est présentée dans la Figure 1.

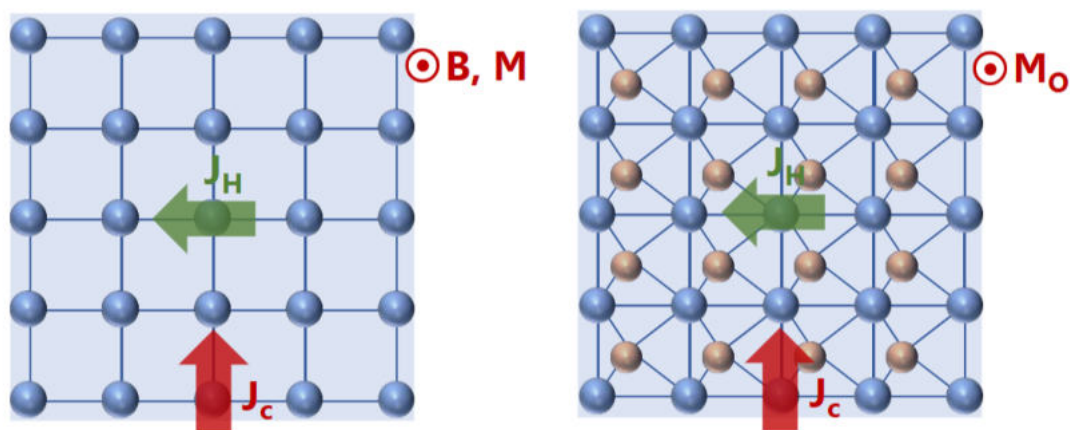


Figure 1. – Esquisse des effets Hall linéaires (a) et (b) du second ordre (J_H) en réponse à un courant de charge injecté (J_c). (a) L'effet Hall linéaire émerge en présence d'un champ magnétique (B) ou d'une aimantation (M) perpendiculaire au plan. (b) L'effet Hall du second ordre apparaît dans les matériaux avec rupture de symétrie d'inversion et s'accompagne d'une aimantation orbitale (M_o) hors équilibre (c'est-à-dire linéaire en E) perpendiculaire au plan.

Dans ce contexte, alors que l'effet Hall du premier ordre en l'absence de champ magnétique extérieur dépend de la courbure de Berry, qui est une grandeur géométrique présentant les mêmes symétries qu'un champ magnétique dans l'espace réciproque, l'effet Hall du second ordre est proportionnel à la dérivée de la courbure de Berry, également appelée dipôle de Berry. De plus, alors que l'effet Hall linéaire s'accompagne d'un champ magnétique ou d'une aimantation interne dans le système, l'effet Hall de second ordre s'accompagne d'une aimantation hors équilibre qui rompt la symétrie d'inversion temporelle dans le processus. Il est à noter que bien que l'effet soit associé à une quantité géométrique qui ne dépend pas du désordre, la conductivité totale est proportionnelle au temps de collision entre les impuretés. A un ordre supérieur en champ électrique, une série d'effets peut se produire en fonction des symétries du système. Beaucoup d'entre eux, par exemple au troisième ordre en champ électrique, sont hors du champ d'application de la courbure de Berry et font partie des études que je suis en train de réaliser.

Dans le cadre de l'effet Hall du second ordre dû au dipôle de la courbure de Berry, un grand nombre de candidats ont été proposés au cours de la dernière décennie pour présenter de grandes amplitudes de conductivité. Parmi eux, l'un des plus importants est celui des semi-métaux de Weyl. La principale raison est que leurs bandes se touchent en des points "diaboliques" où leur courbure Berry tend vers l'infini. De plus, leurs bandes sont exceptionnellement dispersives. Les semi-métaux de Weyl sont considérés comme des matériaux topologiques car ils possèdent des états de bord protégés par une symétrie. De plus, ils peuvent manifester des états non topologiques qui sont dus à leur géométrie ; dans ce cas, ils sont généralement sensibles à l'inclinaison du cône de Weyl qui se forme autour du point de Weyl. S'il est vrai que l'influence de ces états sur la conductivité linéaire a été étudiée précédemment, rien n'est connu à ce jour quant à leur impact sur l'effet de second ordre. Dans ce contexte, il a été documenté dans la littérature que les calculs basés sur des modèles continus ne sont pas capables de décrire correctement ce qui se passe au niveau de la zone de Brillouin, montrant la nécessité d'approfondir cette question.

Dans un récent article publié dans *Physical Review B* [1], avec mon équipe nous avons démontré l'influence des états de surface sur l'effet Hall de second ordre induit par le dipôle de Berry (BCD). Pour cela, notre travail est divisé en 2 parties : d'une part, je me suis concentré sur l'application d'un modèle à 2 bandes qui imite les principales caractéristiques d'un semi-métal de Weyl, qui a une symétrie d'inversion temporelle et n'a pas de symétrie d'inversion spatiale. La courbure de Berry du modèle dans le plan des arcs de Fermi et leurs nœuds de Weyl correspondants sont représentés dans le Figure 2. Sur la base du modèle, nous avons d'abord calculé le dipôle de Berry pour les géométries de dalles dans les directions de courant pertinentes, en fonction des symétries de réflexion présentes, grâce à une méthode de discrétisation précédemment utilisée [2]. Les résultats numériques sont présentés à la Figure 3 pour une valeur fixe du potentiel chimique. Plus de détails sur l'analyse du système et les paramètres utilisés peuvent être trouvés dans le corps principal du document. De

là, nous avons conclu que dans un système fini avec des cônes de Weyl légèrement inclinés (appelé régime de type I), il est capable d'avoir un dipôle qui évolue avec le nombre de couches, ce qui a également été précédemment démontré analytiquement [3].

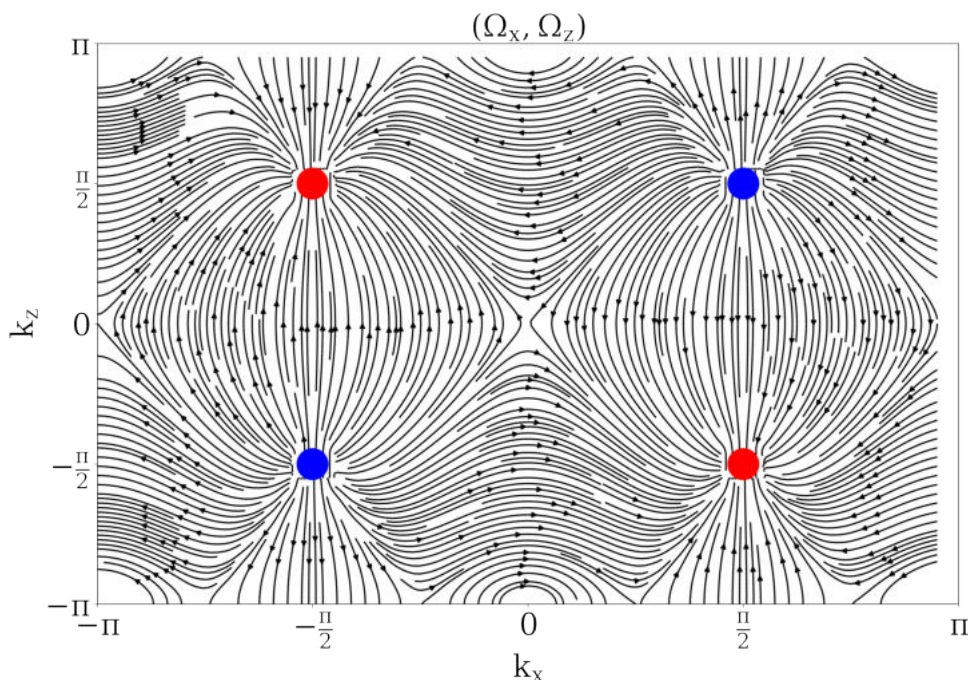


Figure 2. – Champ vectoriel de la courbure de Berry dans le plan des arcs de Fermi. Nous fixons les paramètres intrinsèques. Les monopôles de la courbure de Berry sont représentés par des points rouges et bleus, indiquant les sources (bleu) ou les puits (rouge) du flux de courbure de Berry. Dans le contexte des semi-métaux de Weyl, ils sont généralement étiquetés comme des points de Weyl et, dans ce cas, ils sont disposés dans un espace réciproque obéissant à une symétrie d'inversion du temps.

D'autre part, lorsque l'inclinaison des cônes de Weyl est suffisamment grande (également connu sous le nom de régime de type II), la réponse du dipôle de Berry est amplifiée, conduisant à un effet Hall de second ordre en fonction du nombre de couches. Après une analyse de la densité d'états, dans chacune des limites concernées, nous avons conclu que l'augmentation de la réponse non linéaire correspondante est le conséquence du grand nombre d'états de surface qui ne sont pas liés à la topologie du système. Techniquement, cette augmentation est principalement liée à l'augmentation de la taille des poches de Fermi qui entourent les noeuds de Weyl dans cette frontière. D'autre part, les simulations réalistes réalisées par Dr. Armando Pezo, chercheur postdoctorant dans mon groupe de travail, représentent un ingrédient supplémentaire qui corrobore les prédictions faites grâce à la modélisation théorique. Ici, on observe également une dépendance au nombre de couches du dipôle de Berry

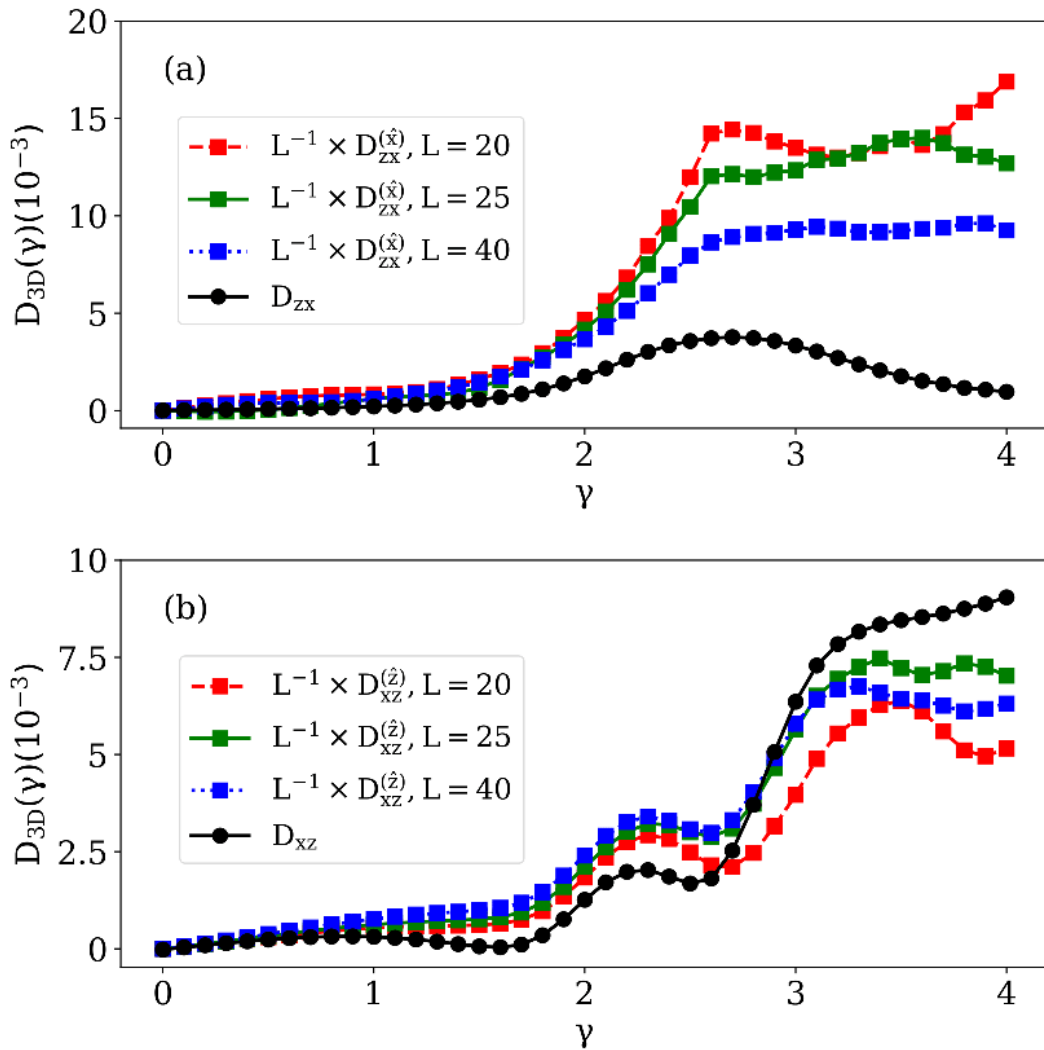


Figure 3. – Considérant le cas $\mu = 0.2$, nous reportons en (a) le BCD d’une dalle avec un vecteur normal aligné avec \hat{x} , pour différents nombres de couches et en fonction du paramètre d’inclinaison. Nous montrons la situation similaire pour une géométrie de dalle normale à \hat{z} (b), en prenant dans les deux cas le profil du coefficient dipolaire en lignes noires comme référence.

pour l’un des systèmes construits à base du semi-métal Weyl type II WTe_2 . Le travail développé est une invitation à explorer d’autres systèmes similaires, avec des états de surface qui peuvent même être topologiquement triviaux, et où l’effet Hall non linéaire peut être amplifié.

Comme mentionné ci-dessus, par analogie avec l'effet Hall du premier ordre en champ électrique dans un système magnétique, l'effet Hall du second ordre en champ électrique doit être accompagné d'une aimantation qui brise la symétrie d'inversion du temps. Dans le cas de l'effet non linéaire induit par le dipôle de Berry, le candidat parfait est l'aimantation orbitale induite par le champ électrique. Cela vient du moment magnétique orbital, qui a les mêmes symétries que la courbure de Berry et qui caractérise la rotation propre du paquet d'ondes électroniques à l'intérieur de la cellule unitaire.

Dans ce travail, nous avons mis en évidence un effet Kerr non linéaire dans les systèmes symétriques et non magnétiques sans inversion, qui est un indicateur de l'effet Hall non linéaire induit par le dipôle de Berry. De plus, dans la limite de fréquence nulle, l'aimantation orbitale hors équilibre peut se décomposer en deux parties : une qui est proportionnelle au dipôle de Berry et une autre qui dépend d'un champ supplémentaire, avec les mêmes symétries que les termes détaillés ci-dessus. En particulier, nos calculs sur une bicouche de WTe_2 et sur la classe de matériaux $Nb_{2n+1}Si_nTe_{4n+2}$ montrent que la relation $M_{Orb} \simeq \mu D$ est valide près du gap ou de cônes inclinés de matériaux de Dirac.

L'angle de Kerr obtenu dans ce type de système constitue non seulement une signature de l'effet Hall du second ordre qui dépend du dipôle de Berry, mais il peut aussi être une preuve d'accumulation orbitale hors équilibre car en principe il ne nécessite pas d'interaction spin-orbite. D'une part, les effets calculés dans le travail sont similaires aux estimations faites sur des expériences qui détectent l'accumulation de spin dans W et Pt [4], et GaAs[5]. La différence entre l'accumulation de spin et l'accumulation orbitale, qui est liée à l'effet Hall du second ordre, est illustrée dans le Figure 4. De plus, les résultats obtenus sont également comparables au cas documenté d'une monocouche de MoS_2 [6], mais sans contraintes.

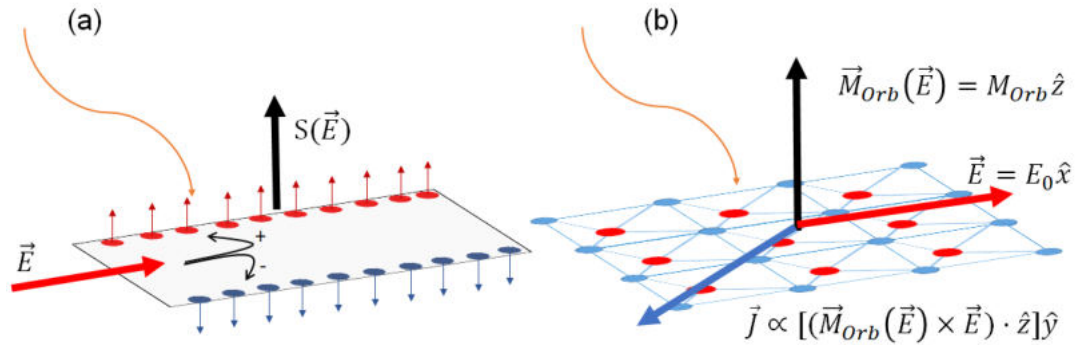


Figure 4. – (a) Dans un matériau bidimensionnel avec couplage spin-orbite et en présence d'un champ électrique externe, une accumulation de spin hors équilibre est générée en raison d'un flux net d'électrons de spins opposés, qui peut être détecté par MOKE. (b) Si le système est non-magnétique et non-centrosymétrique, et même en l'absence de couplage spin-orbite, un effet Hall du second ordre est autorisé par symétrie et sa contribution principale est proportionnelle au dipôle de la courbure de Berry. En utilisant la magnéto-optique, on peut montrer que le courant Hall non linéaire est également proportionnel à l'aimantation orbitale hors équilibre.

Les symétries du matériau peuvent en outre révéler une série d'effets qui, bien que linéaires en champ électrique, sont non linéaires en l'aimantation ou en champ magnétique. Ils sont capables d'induire des processus qui ne sont pas conventionnels et qui sont utiles non seulement pour comprendre la structure électronique du système, mais aussi comme méthodes efficaces applicables aux nanotechnologies. Parmi eux, l'un des plus prometteurs est la génération d'un couple spin-orbite qui peut induire le renversement d'aimantation en l'absence de champ magnétique externe. En supposant maintenant que nous nous intéressons à une réponse linéaire en champ électrique, mais à des ordres non linéaires en les composants de l'aimantation ou de champ magnétique, nos recherches suggèrent que des effets dépendant de la symétrie peuvent se produire. Dans ce contexte, les cristaux à symétrie trigonale sont particulièrement intéressants car sous certaines conditions la surface de Fermi se déforme. Ce phénomène est connu sous le nom de "warping" ou distorsion et a été identifié grâce à des modèles continus qui peuvent être appliqués à des matériaux topologiques tels que Bi_2Te_3 [7].

Le travail est divisé en deux parties : D'une part, nous analysons la réponse hors équilibre de la densité de spin dans des cristaux ferromagnétiques trigonaux. Cet article, qui a été publié dans *Physical Review B* [8], montre qu'il existe une série de termes associés à la densité de spin qui peuvent être obtenus par l'analyse du groupe ponctuel du cristal et la méthode des invariants [9]. Ces champs participent au couple spin-orbite [Spin-Orbit Torque], qui est un élément crucial dans le développement des dispositifs de mémoire modernes. L'une des contributions les plus remarquables de l'expansion est le couple dit "3m", qui permet le renversement de l'aimantation du système en l'absence d'un champ magnétique externe pour l'assister. Le terme "3m" a déjà été vérifié dans le système CoPt/CuPt [10], et il a également été prédit dans Fe_3GeTe_2 [11]. De plus, nous avons pu conclure que les couples spin-orbite prédits ont leur origine dans la distorsion trigonale de la surface de Fermi.

D'un point de vue pratique, ma participation à la recherche s'est concentrée sur la dérivation des termes d'ordre supérieur, en tenant compte de la symétrie du cristal, et à la confirmation de nos prédictions par le calcul explicite des coefficients, par la méthode de la fonction de Green, en utilisant un modèle à 2 bandes défini en 2 dimensions et qui respecte la symétrie du cristal. Le Hamiltonian microscopique du système contient un terme Rashba linéaire qui rompt la symétrie d'inversion dans le plan, et un autre terme qui représente une correction cubique du terme Rashba linéaire. C'est ce dernier qui est lié à la distorsion trigonale, qui nécessite un potentiel chimique suffisamment élevé pour se manifester, et qui est crucial pour l'émergence de couples spin-orbite non linéaires en aimantation. De plus, nous corroborons notre théorie avec des simulations numériques réalistes réalisées par le Dr. Armando Pezo, qui sont détaillées dans le corps de ce document. Dans le cas du modèle de liaisons fortes, nous présentons une illustration avec l'évolution de la surface de Fermi sur la Figure 5. C'est l'élément crucial pour comprendre la réponse du couple spin-orbite détaillée ci-dessus.

Dans le même contexte, en appliquant la même logique et organisation du travail que dans le cas du couple spin-orbite, nous avons pu montrer qu'un effet Hall impair en aimantation et en champ magnétique émerge dans ces cristaux ferromagnétiques, lorsque les champs électrique et magnétique sont colinéaires. En plus d'identifier que cette réponse est extrinsèque (ou en d'autres termes, cela dépend du désordre), nous pouvons en déduire que, comme dans le cas du couple de spin-orbite, l'effet est causé par des contributions cubiques au couplage spin-orbite et est dominant à un niveau d'énergie suffisamment élevé. A ce niveau, on observe à nouveau la distorsion trigonale de la surface de Fermi.

c. Conclusion et Perspectives

D'un point de vue général, il est important de souligner que l'exploration des effets d'ordre élevé en champ électrique et/ou magnétique est un outil qui ouvre non seulement des opportunités d'optimisation des composants électroniques actuels,

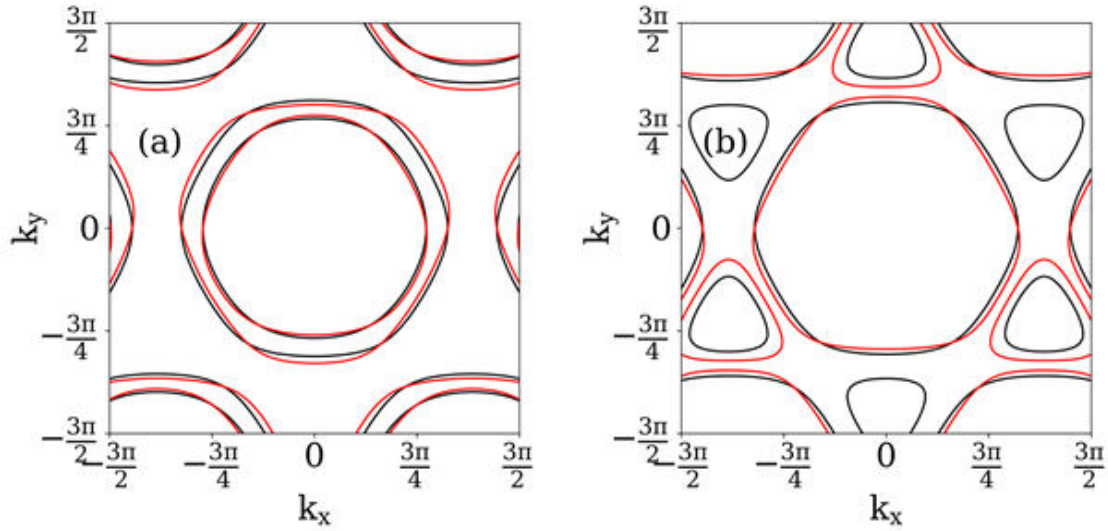


Figure 5. – Evolution des surfaces de Fermi avec le remplissage de bande (inférieur en (a) et supérieur en (b)), pour les cas sans (lignes noires) et avec (lignes rouges) couplage spin-orbite cubique lorsque l'aimantation est hors plan.

mais donne également accès à de nouveaux détails dans la structure électronique des matériaux à étudier.

Pour clore ce résumé, il convient de mentionner que notre principale perspective d'étude à court terme est l'effet Hall du troisième ordre dans le domaine électrique. Ici, l'accent est mis sur la compréhension de l'apparition d'une conductivité non nulle en fonction de la polarisabilité de la courbure de Berry [12], dont le comportement n'est cependant pas lié à la présence de symétries d'inversion temporelles ou spatiales. Cet effet prend sa source au-delà de la courbure de Berry, en impliquant le tenseur métrique quantique. De plus, bien que certains travaux soient apparus à cet égard et que de nouvelles extensions de la théorie aient été proposées pour prendre en compte les matériaux magnétiques, une explication complète est nécessaire sur l'origine de cet effet, pour comprendre quelles sont ses principales limites et comment augmenter la réponse à une stimulation extérieure. La compréhension de cet effet élargira non seulement notre vision de certains matériaux où les effets de premier et de second ordre en le champ électrique sont interdits par symétrie, mais approfondira également notre compréhension de la structure de ces systèmes au-delà de la courbure de Berry. Ce scénario est potentiellement l'occasion de s'intéresser à des systèmes électroniques plus complexes (par exemple, des systèmes hautement corrélés) ou des isolants topologiques d'ordre élevé, pour ne citer que quelques exemples.

Contents

Affidavit	2
Acknowledgements	3
List of Publications and Participation in Conferences	4
Résumé	6
Abstract	7
Résumé Etendu	8
Contents	17
List of Figures	20
List of Tables	22
1. State of the Art on Electronic Transport and Spintronics	24
1.1. Preliminaries	24
1.2. Anomalous Hall Effect	26
1.2.1. Symmetry Considerations	26
1.2.2. Materials of Contemporary Interest	28
1.3. Second Order Hall Effect	33
1.3.1. Symmetries of the Conductivity Tensor	33
1.3.2. Materials Under Study	34
1.4. Third order Hall Effect	38
1.4.1. Symmetry Relations	38
1.5. Nonlinear Physics in Spin-Orbitronics	39
1.5.1. Spin and Orbital Currents	39
1.5.2. Spin-Orbit Torques	40
1.6. Invariant Theory in a Nutshell	41
1.7. Motivation and Scope of the Work	45
2. A Pedagogical Introduction to Electronic Transport Theory	47
2.1. Linear Response in Electric Field	48
2.1.1. Semiclassical Formalism	48
2.1.2. Green Function Formalism	53

2.2. Quadratic Response in Electric Field	56
2.2.1. Semiclassical Description	56
2.2.2. Green Function Formula	58
2.2.3. Current-Induced Magnetization	62
2.3. Cubic Response in Electric Field	63
3. Influence of the Surface States on the Nonlinear Hall Effect in Weyl Semimetals	65
3.1. Motivation	65
3.2. Lattice and Slab Model Hamiltonians	68
3.3. Model Calculations and Discussion	73
3.4. Realistic Simulations in WTe ₂ Slabs	81
3.5. Main Conclusions and Prospects	84
4. Magneto-optical Probe of Non-Equilibrium Orbital Magnetism via the Second-Order Hall effect	86
4.1. Introduction	86
4.2. General Theory	89
4.2.1. Magneto-Optics	89
4.2.2. Decomposition of the Non-Equilibrium Orbital Magnetization	91
4.3. WTe ₂ Bilayer	91
4.3.1. Definition of the Model System	91
4.3.2. Model Calculations	93
4.3.3. Comparison With Experiments	96
4.3.4. Orbital Edelstein Coefficients Versus Berry Curvature Dipole in WTe ₂	97
4.4. Nb _{2n+1} Si _n Te _{4n+2} Monolayer	99
4.4.1. Model System	99
4.4.2. Model Calculations and Discussion	100
4.4.3. Orbital Edelstein Coefficients Versus Berry Curvature Dipole in Nb _{2n+1} Si _n Te _{4n+2}	104
4.5. Conclusions and Prospects	105
5. Unconventional Responses in Trigonal Crystals	106
5.1. Spin-Orbit Torque for Field Free Switching in C _{3v} crystals	106
5.1.1. Motivation	106
5.1.2. Symmetry Analysis	109
5.1.3. Transport Formalism and C _{3v} Model	113
5.1.4. Numerical Results and Discussion	118
5.1.5. First Principles Case Study: CuPt(111)/Co	120
5.2. Chiral Hall Effect	124
5.2.1. Symmetry Analysis	124
5.2.2. Model Calculations	126
5.2.3. Realistic Simulations	128

5.3. Conclusions and Prospects	130
6. General Conclusion	132
Appendices	170
A. Berry Phase Theory in Quantum Mechanics	170

List of Figures

1.1. Sketch of First and Second Order Hall Transport	26
1.2. Anomalous Hall Conductivity in the Magnetic Weyl Semimetal $\text{Co}_3\text{Sn}_2\text{S}_2$	29
1.3. Anomalous Hall Conductivity in Thin Films of Mn_3Sn	30
1.4. Anomalous Hall Conductivity in RuO_2	31
1.5. Planar Hall Effect in GdPtBi	32
1.6. Second order Hall effect detected in bilayer WTe_2	34
1.7. Schematics on the Generation of BCD in MoS_2 Under Strain.	36
1.8. Experimental and Theoretical Results About the Second Order Hall Effect in MoS_2 Under Strain.	37
1.9. Illustration of Field-Free Switching of the Magnetization	41
3.1. Berry Curvature Field in the Plane of the Fermi Arcs	67
3.2. Band Structures of the Slab Systems	70
3.3. Density of States in the Plane of the Fermi Arcs	72
3.4. Layer Resolution for the Density of States	74
3.5. Tilting Dependence of the Berry Curvature Dipole for the Slab Geome- tries and Dipole to Density of States Ratio	76
3.6. Layer Resolution of the Berry Curvature Dipole	78
3.7. Energy Dependence of the Berry Curvature Dipole	79
3.8. Berry Curvature Dipole as a Function of the Layer Number	80
3.9. Band Structure of WTe_2	81
3.10. Density of States of WTe_2	82
3.11. Band Structure and Berry curvature Dipole Calculations in WTe_2	83
4.1. Illustration of Non-Equilibrium Spin Accumulation and Second Order Hall Effect Accompanied by Non-Equilibrium Orbital Magnetization	89
4.2. Band Structures and Berry Curvature Distribution in WTe_2 Bilayer	92
4.3. a.c. Transport in Bilayer WTe_2	94
4.4. Kerr Angle in Bilayer WTe_2	95
4.5. Orbital Magnetization Coefficients in WTe_2	98
4.6. Lattice Structure for a Model of $\text{Nb}_{2n+1}\text{Si}_n\text{Te}_{4n+2}$ Monolayer	99
4.7. Band Structure for a Model of $\text{Nb}_{2n+1}\text{Si}_n\text{Te}_{4n+2}$ Monolayer	100
4.8. d.c. BCD in $\text{Nb}_{2n+1}\text{Si}_n\text{Te}_{4n+2}$ Monolayer as a Function of the Band Filling	101
4.9. a.c. Transport Quantities and Kerr angle in $\text{Nb}_{2n+1}\text{Si}_n\text{Te}_{4n+2}$ Monolayer as a Function of the Energy	102
4.10. a.c. Transport Quantities and Kerr angle in $\text{Nb}_{2n+1}\text{Si}_n\text{Te}_{4n+2}$ Monolayer as a Function of the Interchain Hopping	103

4.11. Orbital Edelstein Coefficient in $\text{Nb}_{2n+1}\text{Si}_n\text{Te}_{4n+2}$ Monolayer	104
5.1. Experimental Setup and Magnetization Switching in CuPt/CoPt Heterostructure	108
5.2. Examples of Basic Torque Configurations	112
5.3. Properties of the Lattice Hamiltonian	115
5.4. Angular Dependence of the Effective Field Components for the Model Hamiltonian	118
5.5. Behavior of the Different Contributions to the Spin-Orbit Torque	120
5.6. Spin Texture of CuPt(111)/Co	121
5.7. Angular Dependence of the Effective Field Components for Realistic Scenario	122
5.8. Chiral Hall Effect for $\phi_I = 0^\circ$	127
5.9. Chiral Hall Effect for $\phi_I = \phi_M$	127
5.10. Extrinsic Hall Conductivity in CuPt/Co for Fixed Electric Field Angle.	128
5.11. Extrinsic Hall Conductivity in CuPt/Co for $\phi_I = \phi_B$	129

List of Tables

5.1. Character table for C_{3v} point group	110
5.2. Summary of the minimal model analysis.	121

List of acronyms

BC Berry curvature. [24](#), [25](#), [28](#), [29](#), [32](#), [36](#), [38](#), [45](#), [50–53](#), [56–58](#), [62](#), [63](#), [65](#), [67–69](#), [75](#), [90](#), [91](#), [93](#), [101](#), [130](#)

BCD Berry curvature dipole. [33–37](#), [45](#), [46](#), [57](#), [58](#), [62](#), [63](#), [65–68](#), [71](#), [73–80](#), [82–85](#), [88–91](#), [93](#), [94](#), [96–98](#), [100–104](#), [133](#)

BCP Berry connection polarizability. [63](#), [64](#)

CHE chiral Hall effect. [124](#), [126–131](#)

MOKE magneto-optical Kerr effect. [87](#), [89](#), [96](#), [100](#), [101](#), [104](#), [132](#), [133](#)

NLHE nonlinear Hall effect. [35](#), [36](#), [45](#), [58](#), [62](#), [65–67](#), [75](#), [77](#), [81](#), [83–85](#)

TOHE third order Hall effect. [63](#)

WSM Weyl semimetal. [29](#), [31–33](#), [45](#), [58](#), [65–68](#), [70](#), [73](#), [75](#), [77](#), [79](#), [81](#), [84](#), [85](#), [87](#)

1. State of the Art on Electronic Transport and Spintronics

Summary

1.1. Preliminaries	24
1.2. Anomalous Hall Effect	26
1.2.1. Symmetry Considerations	26
1.2.2. Materials of Contemporary Interest	28
1.3. Second Order Hall Effect	33
1.3.1. Symmetries of the Conductivity Tensor	33
1.3.2. Materials Under Study	34
1.4. Third order Hall Effect	38
1.4.1. Symmetry Relations	38
1.4.1.1. Investigations on Different Platforms	38
1.5. Nonlinear Physics in Spin-Orbitronics	39
1.5.1. Spin and Orbital Currents	39
1.5.2. Spin-Orbit Torques	40
1.6. Invariant Theory in a Nutshell	41
1.7. Motivation and Scope of the Work	45

1.1. Preliminaries

Historically, the manipulation of the electron's degrees of freedom in condensed matter has been an active field of research, both theoretically and experimentally. In this context, the generation of transverse charge flows under external longitudinal perturbations pointed out by Edwin Hall [13, 14] is considered as a milestone finding due to the underlying mechanisms behind it. Since this discovery, the so-called Hall effect has opened the door to important repercussions in the development of new theories and applications in industry and the daily life [15, 16, 17]. With the raise of the quantum theory, the investigation of the Hall effect at the microscopic level led to the boosting on the generation of innovative electronic devices and modernizing their electric capabilities and functionalities [18, 19, 20, 21, 22, 23, 24, 25, 26].

When an external electric field \vec{E} is applied to a material, the electronic wavepacket acquires a positional shift that in the linear response regime is conducted by the [Berry](#)

curvature (BC) [27, 28]. Usually interpreted as a magnetic field in reciprocal space, the BC emerged naturally as a geometric quantity behind the anomalous Hall velocity imprinted on the electron. Moreover, in selected cases the flux of the BC in a closed loop takes a quantized value, in complete analogy to the geometrical phase related to the wavefunction when a particle moves around a magnetized cylinder. Such a peculiar behavior manifests itself in a wide class of systems called topological materials, including insulators and semimetals [29, 30]. Irrespective of the topological nature of the material though, the properties of its non-equilibrium tensors are governed by the crystal symmetries. Besides, in the linear response regime, the response tensor also fulfils Onsager reciprocity. As a result, to the first order of the electric field, a Hall current only develops in the presence of time-reversal symmetry breaking, i.e., either in the presence of an external magnetic field or in materials with a net magnetic moment...or so it was thought until very recently.

Recent progress has revealed that the interplay between the geometry of the Bloch states and the symmetry properties of the crystal can lead to higher order effects that are notably different from the ones usually obtained in the linear regime [31, 12]. A remarkable paradigm is the Hall effect. As stated above, it was believed for more than a century that anomalous Hall currents arise in materials with net magnetization, such as ferromagnets or ferrimagnets, and vanish in the absence of magnetization [15]. Although the limitation of linear anomalous Hall effect to ferromagnets was challenged about twenty years ago with the emergence of the topological Hall effect in non-collinear antiferromagnets [32, 33], 2015 has greatly shook this conception with the experimental observation of linear anomalous Hall effect in compensated, coplanar antiferromagnets [34, 35] (see below), and most importantly for the present Thesis, with the realization that the anomalous Hall effect can emerge at the second order in the electric field in materials that do not display any magnetism but possess inversion symmetry breaking [31, 36, 37]. These two effects, linear and second order Hall effects, are sketched in Fig.1.1. Therefore, higher order electronic response not only opens avenues for the exploitation of materials that do not accommodate linear response, but also appears are a powerful tool to probe the impact of the crystal symmetries on the geometry of the Bloch states.

In this Chapter, we attempt to provide a pedagogical introduction to quantum transport theory, highlighting the way crystal symmetries impact the response tensor at various orders in the external excitation. Let us begin by considering a system subjected to an external stimulus that is typically an electric field \vec{E} (and possibly, a magnetic field \vec{B}). In addition, we can suppose that the system can display a magnetic ordering with magnetization \vec{m} . We also assume that the adiabatic limit holds, or in other words, that the evolution of the system is slow enough to be only deviated from its equilibrium state. The induced current \vec{j} follows a constitutive relation of the form

$$j_a = \sigma_{ab}^{(I)}(\vec{B}, \vec{m})E_b + \sigma_{abc}^{(II)}(\vec{B}, \vec{m})E_bE_c + \sigma_{abcd}^{(III)}(\vec{B}, \vec{m})E_bE_cE_d + \dots, \quad (1.1)$$

We will give more details below and in Chapter 2.

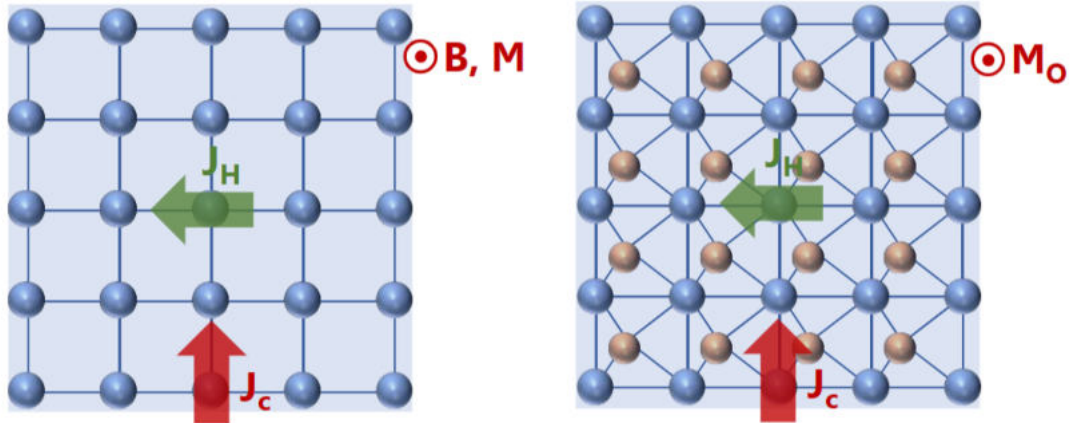


Figure 1.1. – Sketch of the (a) linear and (b) second order Hall effects (J_H) as a response to an injected charge current (J_c). (a) Linear Hall effect emerges in the presence of either magnetic field (B) or magnetization (M) perpendicular to the plane. (b) Second order Hall effect emerges in materials with inversion symmetry breaking and is accompanied by non-equilibrium (i.e., linear in E) orbital magnetization (M_o) perpendicular to the plane.

1.2. Anomalous Hall Effect

1.2.1. Symmetry Considerations

Let us presume first that our sample is subjected to a linearly dependent perturbation in \vec{E} and \vec{B} . In that case, expanding Eq.(1.1) up to first order in \vec{E} we obtain

$$j_a \simeq \sigma_{ab}^{(0)} E_b + \sigma_{abc}^{(1)} E_b B_c + \dots, \quad (1.2)$$

where σ is a tensor that has to be determined. Here, $\sigma_{ab}^{(0)}$ is the conductivity in presence of the electric field solely and $\sigma_{ab}^{(1)}$ is the conductivity when both \vec{E} and \vec{B} hold. Besides, subscripts with latin indexes indicate cartesian components. A priori, the Taylor expansion in Eq.(1.2) is valid as long as the electric and magnetic fields are small. It is clear that the second term in the right hand side of Eq.(1.2) corresponds to the ordinary Hall effect for $a \neq b$: The generation of a transverse in-plane current in the presence of an in-plane external electric field and an out-of plane magnetic field. On the other hand, the first term does not require an external magnetic field.

At this point, an essential ingredient of the analysis of the linear response regime in electric field is Onsager reciprocity [38], which is a direct consequence of the second law of thermodynamics. In his seminal work Onsager demonstrates that "*The entire motion may be reversed by reversing the magnetic field together with the velocities of all the particles composing a dynamical system*". Consider the average fluctuation of two dynamical variables α_i and α_j in a time interval τ as

1. State of the Art on Electronic Transport and Spintronics – 1.2. Anomalous Hall Effect

$$A_{ji}(\tau) = \lim_{t'' \rightarrow \infty} \int_{t=t'}^{t=t''} \alpha_j(t) \alpha_i(t+\tau) dt \quad (1.3)$$

and a set of constitutive relations for their average flows $\partial_t \alpha_r^{av} = G_{rs} \partial_{\alpha_s} S$, where $S = S(\alpha_1, \dots, \alpha_n)$. For a system in the presence of an external magnetic field \vec{B} , we have [39] $A_{ji}(\vec{B}, \tau) = A_{ji}(-\vec{B}, -\tau) = A_{ij}(-\vec{B}, \tau)$. Then, applying the symmetry relations of A_{ij} with the set of linear relations for an irreversible process

$$A_{ji}(\vec{B}, \Delta t) = A_{ji}(\vec{B}, 0) - k_B \Delta t G_{ij}(\vec{B}), \quad (1.4)$$

$$A_{ij}(-\vec{B}, \Delta t) = A_{ij}(-\vec{B}, 0) - k_B \Delta t G_{ji}(-\vec{B}), \quad (1.5)$$

it can be deduced that $G_{ij}(\vec{B}) = G_{ji}(-\vec{B})$ [39]. Consequently, the conductivity coefficients σ_{ab} such that $j_a = \sigma_{ab} E_b$ obey:

$$\sigma_{ab}(\vec{m}) = \sigma_{ba}(-\vec{m}). \quad (1.6)$$

We combine Eq.(1.6) with the antisymmetric part of the total conductivity tensor

$$\sigma_{ab}(\vec{m}) = -\sigma_{ba}(\vec{m}), \quad (1.7)$$

from which

$$\sigma_{ab}(\vec{m}) = -\sigma_{ab}(-\vec{m}). \quad (1.8)$$

Notice that Onsager reciprocity only holds at the linear response regime. As such, one can expect unforeseen behavior beyond this limit. In addition, the Hall effect is non-dissipative in the sense that the current related to Joule heating is parallel to the electric field. Then, the Joule heat for the Hall effect is $\vec{J}_H \cdot \vec{E} = 0$. Last but not least, the symmetries of the crystal also play a crucial role on the determination of the allowable responses. In this way, the outgoing current follows Neumann principle, i.e., it is invariant under a given symmetry operation \mathcal{A} of a point group \mathcal{G} (For more details about the symmetry analysis of linear response tensors, see [40, 41, 42, 43, 44]). For $\sigma^{(0)}$, for instance, we have

$$(\vec{j})' = \mathcal{A} \vec{j} = \vec{j}. \quad (1.9)$$

Then

$$\begin{aligned} (\sigma \vec{E})' &= \mathcal{A} \sigma \mathcal{A}^{-1} \mathcal{A} \vec{E} \\ \mathcal{A} \sigma \mathcal{A}^{-1} \vec{E} &= \sigma \vec{E} \rightarrow \mathcal{A} \sigma \mathcal{A}^{-1} = \sigma. \end{aligned}$$

At the microscopic scale, early predicted in the work of Karplus and Luttinger [45] and years later refined in terms of the Berry phase theory [28, 46], the anomalous Hall effect reveals the role of the material's band structure and the geometry of the

electronic Bloch states on the transport properties. In simple words, the transverse current generated in the presence of the perturbative electric field is a consequence of an anomalous velocity term that is perpendicular to the electric field. As we mentioned earlier, this expression plays the role of a magnetic field in reciprocal space and is commonly known as the Berry curvature. This object is responsible of the Aharonov-Bohm effect in Quantum Mechanics, which at the same time is the first concrete evidence of the influence of topology in the physics of the wave-function [28] (For a derivation of the Berry phase, see Appendix A). Importantly, the BC described is an intrinsic property of a given material that does not depend on any particular form of disorder. In contrast, there are other extrinsic terms based on similar Gauge independent quantities that are mediated by impurities such as side jump and skew-scattering (See, for example, [15, 47]). Nevertheless, these disorder considerations are out of the scope of this work.

Coming back to Eq.(1.2) and in absence of magnetic fields, we have $j_a \simeq \sigma_{ab}E_b$. While applying inversion symmetry ($x \rightarrow -x$) leaves the conductivity coefficients invariant, time reversal symmetry forbids any chance of Hall currents. Indeed, if we look for a current that is invariant under time reversal, hence $-\sigma_{ab} = \sigma_{ab}$. The Hall conductivity σ_H is the antisymmetric part of the conductivity tensor, which leads to $2\sigma_H = \sigma_{ab} - \sigma_{ba} = -\sigma_{ab} + \sigma_{ab} = 0$. Consequently, we deduce that in any non-magnetic material the anomalous Hall effect completely vanishes. This criteria also applies for any system where a combination between a crystal symmetry operation \mathcal{A} and the time reversal symmetry operation restores time reversal effectively. For instance, the case of coplanar [32] and non-coplanar antiferromagnets [33]. With the rapid innovation in quantum materials, a natural question is whether the symmetry restrictions presented here can be challenged at higher order in external impulses. Because of this reason, whereas in the next section we will introduce higher order responses in electric fields through basic symmetry considerations and the different materials under scrutiny, we will delve on the microscopic theory concerning those effects in Chapter 2.

1.2.2. Materials of Contemporary Interest

The anomalous Hall effect has been extensively explored in a wide variety of magnetic materials, and here we are going to exemplify a few interesting cases. In this context, the effort has been concentrated not only on the intrinsic part arising from the BC, but also on the extrinsic contributions coming from side jump and skew-scattering processes. Whereas the former originates from the deflection of the average velocity when the electron interacts with the impurity and it is independent of the scattering time τ [48, 15], the latter arises on the interaction between the electrons and the impurity in the presence of spin-orbit coupling [49].

Within the frame of ferromagnets, and besides of the well-known instances in magnetic semiconductors [50] and Co, Fe, Ni based-materials, the latter explored

experimentally to get an insight of its temperature dependence [51], topological systems have gained strong attention of the community due to their peculiar band structure properties. In Weyl materials, for instance, where the electronic bands touch at "diaboloic" points known as Weyl points, the anomalous Hall effect tends to be large because the BC diverges at these points, enhancing the overall linear response. One of the trending systems in this context is the Kagome semimetal $\text{Co}_3\text{Sn}_2\text{S}_2$ [52], where the intrinsic contribution has been argued as the main mechanism for the Hall conductivity, just as in the ferromagnetic Weyl semimetal (WSM) candidate PrAlGe [53]. Nonetheless, experiments in the Van Der Waals material CrTe_2 [54] display a skew scattering anomalous Hall effect that is one order of magnitude larger than the Berry contribution observed in $\text{Co}_3\text{Sn}_2\text{S}_2$. Concerning the latter, it is expected that the direction of the magnetization [55] and the Fermi level with respect to the Weyl point energy plays a substantial role, enhancing the anomalous Hall conductivity when they lie at the same energy. This has been demonstrated from theoretical predictions by tight-binding model calculations with out-of plane magnetization, keeping a few bands close to the Fermi level for simplicity [56]. The calculation of the band structure and the anomalous Hall conductivity relying on the tight binding model is illustrated in Fig.1.2.

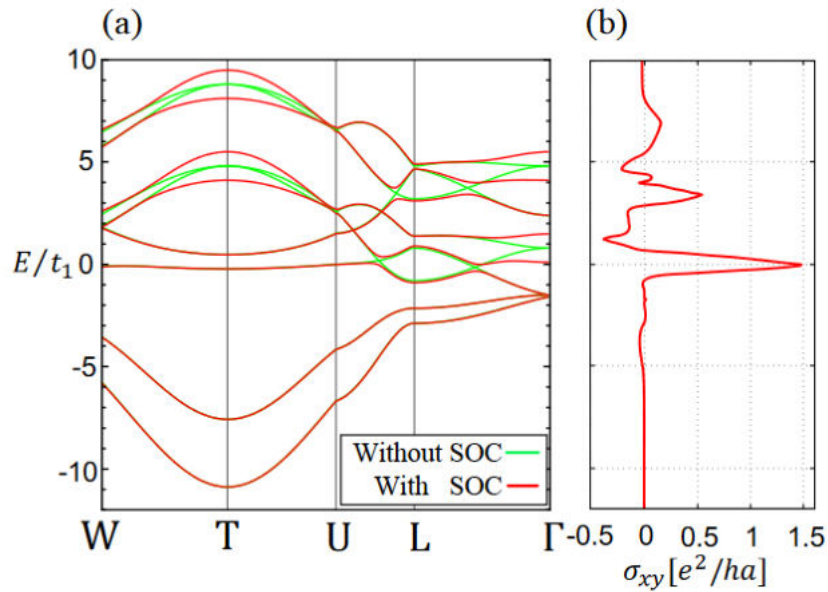


Figure 1.2. – (a) Band structure of the tight binding Hamiltonian representing effectively the $\text{Co}_3\text{Sn}_2\text{S}_2$ system. (b) Anomalous Hall conductivity for the tight binding Hamiltonian, exhibiting a peak in the signal at the energy of the Weyl points. Figure extracted and modified from [56].

In the same context, an ongoing research demonstrates the strong tunability of the chemical potential in $\text{Co}_3\text{Sn}_2\text{S}_2$ by substituting Co by Fe or Ni [57]. To the best of our knowledge, the modulation of the anomalous Hall conductivity through the Fermi level has not been proved experimentally, but a signature of this property has been

communicated in EuCd_2S_2 thin films [58]. Surprisingly, the combined action of topology and disorder can contribute substantially to the Hall conductivity, even though there is no clear magnetic ordering in the sample. In this line, a giant anomalous Hall effect induced by skew scattering has been detected in the frustrated magnet KV_3Sb_5 , having a Hall ratio of one order of magnitude larger than Fe [59]. Inspired by the Haldane model, the quantum anomalous Hall effect has also been anticipated in Kagome magnets displaying flat bands [60], as in the milestone occurrence in twisted bilayer Graphene [61].

Another ongoing compelling scenario pertains antiferromagnetic materials. In light of what we explained earlier, in certain types of antiferromagnets the magnetic ordering is such that an effective time reversal symmetry cannot be restored when it is combined with a lattice symmetry, giving rise to a Hall current. This was verified in certain classes of antiferromagnets with non-collinear structure [33, 62, 63], with remarkable instances including Mn_3Sn [34], Mn_5Si_3 [64] and Mn_3Ge [35]. By ab-initio simulations and symmetry considerations, a complementary study of the anomalous Hall conductivity has been developed in the antiferromagnetic compounds Mn_3X ($\text{X}=\text{Ge}, \text{Sn}, \text{Ga}, \text{Ir}, \text{Rh}$ and Pt) [65]. Thin films of Mn_3Sn represents a stimulating scenario, offering large Hall responses such as an anomalous Hall effect that is comparable to ferromagnetic materials [66]. A picture with the results of the original experiment is depicted in Fig.1.3.

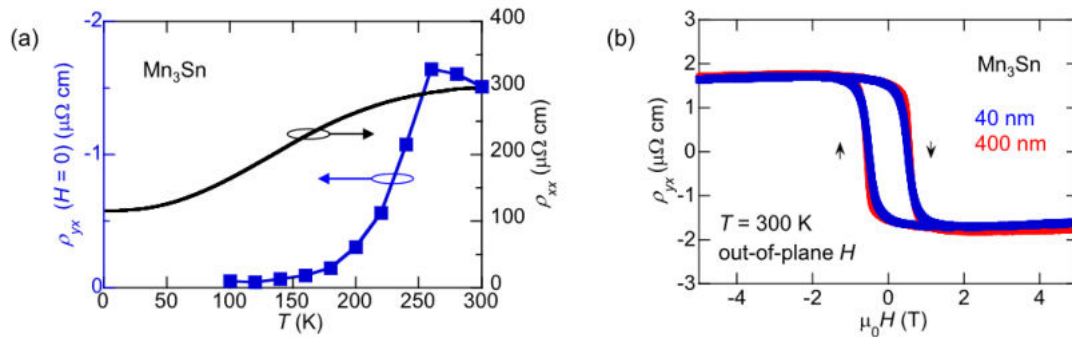


Figure 1.3. – (a) Temperature dependence of the longitudinal and the Hall resistivity, for a film of Mn_3Sn with 40nm. (b) Field dependence of the Hall resistivity, for two films of Mn_3Sn with different thickness, when the magnetic field is applied perpendicular to the surface. Figure extracted and modified from [66].

The anomalous Hall effect is not limited to non-collinear antiferromagnets. In fact, a spontaneous Hall effect has also been predicted and then verified experimentally in RuO_2 [67, 68], a collinear antiferromagnet that is capable to break time reversal effectively by the interaction between the non-magnetic atoms, which are located in non-centrosymmetric positions. A sketch with the crystal structure and the anomalous Hall conductivity obtained from the experimental data are given in Fig.1.4

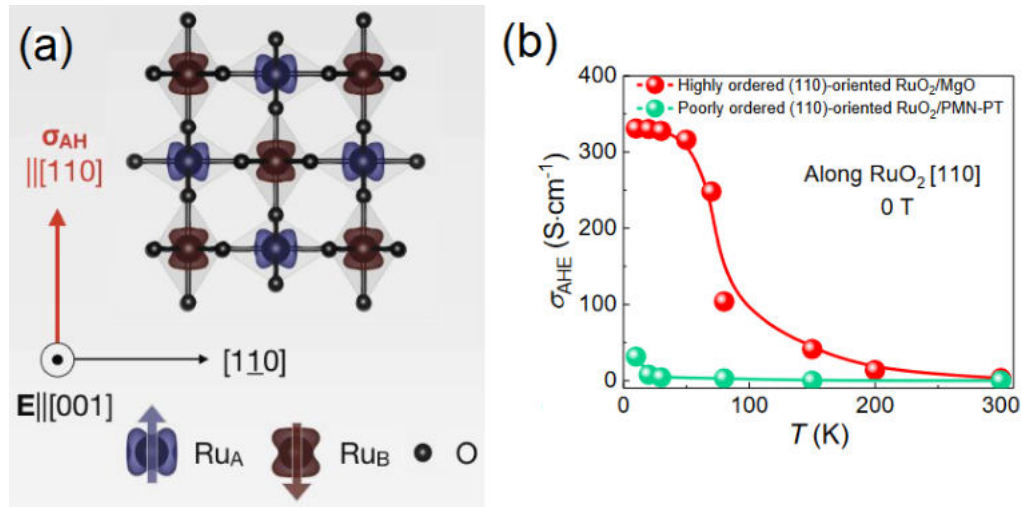


Figure 1.4. – (a) Crystalline structure of RuO₂. (b) Temperature dependence of the anomalous Hall conductivity of RuO₂ synthesized on two distinct substrates. Panels (a) and (b) extracted and modified from [67] and [68], respectively.

As a distinct paradigm, a large anomalous Hall conductivity can also be induced by the presence of a non-trivial magnetic texture in the system, as it has been inspected in the chiral antiferromagnet CoNb₃S₆ [69] and in the half-Heusler antiferromagnet GdPtBi [70]. Last but not least, exotic expressions of the anomalous Hall conductivity as a function of temperature have been reported in the centrosymmetric antiferromagnet EuAl₄ [71], in an identical fashion to what was documented for Fe₃GeTe₂ [72].

Linear response to an external electric field is not limited to the absence of applied magnetic fields or higher order magnetic contributions. In fact, the higher order magnetotransport can be amazingly enhanced from the right coaction between the applied fields and the internal magnetization configuration. In topological materials, the Hall field has been pointed out as a major factor in the giant magnetoresistance of the Dirac semimetal TiBiSSe [73]. In order to explain this outcome and other experiments in Co₃Sn₂S₂, it was claimed that the transport properties observed in presence of a magnetic field should a priori not only have a classical but also an anomalous origin [74]. When time reversal is broken and inversion is preserved the Dirac system becomes a WSM, and in this case the giant anomalous conductivity observed does not need to be related to the existence of Weyl nodes. A new experiment in the magnetic WSM EuCd₂S₂ [75] assures that the pronounce peaks in the nonlinear magnetotransport could be explained by the evolution of the band structure due to spin canting, which at the same time can be induced by an external magnetic field. The transport properties of the WSM in presence of a magnetic field can also be dictated by the presence of a large hole pocket, as it was recently checked experimentally in SrAgBi [76]. Transport measurements have also been developed in ZrTe₅ in order to

understand the connection between the orientation of the applied magnetic field and the underlying Weyl physics [77]. Beyond the appearance of Weyl points, the materials' topology could be encoded in curves in reciprocal space where the BC diverges. These systems are tagged as nodal line semimetals and have been disclosed experimentally by means of magnetotransport measurements in YbCdGe [78] and CaCdSn [79].

Let us finally comment on the planar Hall effect that arises when the electric field, magnetic field and output current are coplanar. In fact, planar Hall effect is almost as old as anomalous Hall effect itself. It is rather weak and has been widely studied in transition metal alloys in the 70s [80]. The planar Hall effect is usually associated with spin-orbit scattering and is a companion of anisotropic magnetoresistance. Interest in planar Hall effect (and anisotropic magnetoresistance) has been recently revived with the emergence of topological materials. In WSMs, theoretical works have connected the planar Hall effect with the chiral anomaly [81] (the pumping of Weyl fermions from one cone to another when both electric and magnetic fields are aligned). A schematics of the planar Hall effect and experimental results on GdPtBi [82] are presented in Fig.1.5.

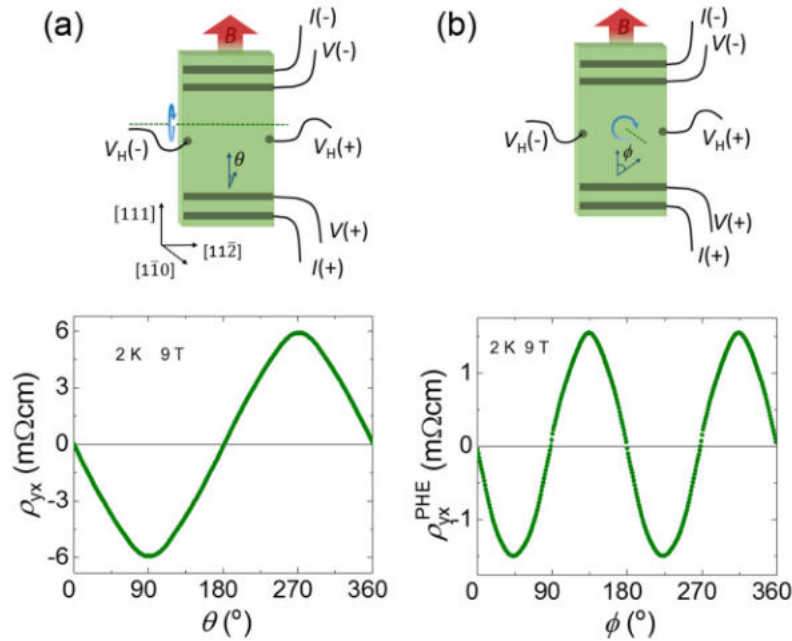


Figure 1.5. – Illustration of the regular and planar Hall effect measurements in the upper panels (a) and (b), respectively. Whereas θ denotes the angle of the magnetic field with respect to the out-of plane axis, ϕ lies always in the plane. On the other hand, the lower panels of (a) and (b) are the Hall measurements of both configurations, for a temperature $T = 2K$ and a magnetic field $B = 9T$. Figure extracted and modified from [82].

As we will see in Chapter 5, trigonal crystals are able to display unconventional pla-

nar Hall effect and other contributions that can be predicted by symmetry arguments. One of them, in which the electric and magnetic field are parallel between each other, has also been attributed to the chiral anomaly in magnetic WSMs [83]. In this context, we will justify that a suitable microscopic source of higher order magnetotransport effects in trigonal crystals is the trigonal warping of the Fermi surface [7].

1.3. Second Order Hall Effect

1.3.1. Symmetries of the Conductivity Tensor

Second order Hall transport has emerged as a new avenue to explore a wide variety of non-magnetic materials. The charge current can be non-zero as soon as the system is not inversion symmetric. From the symmetry standpoint, we can understand this phenomenologically by looking at a second order current in a system that is time reversal symmetric:

$$j_a^{(2)} = \sigma_{abc}^{(2)} E_b E_c. \quad (1.10)$$

Applying inversion symmetry on both sides of Eq.(1.10), we see that the left side changes sign while the right one does not, leading to the absence of second-order transport in materials with inversion symmetry. In fact, the inversion symmetry breaking must be accompanied by a mirror symmetry breaking. Next, if we apply time reversal, it is straightforward to understand that the conductivity tensor should change sign in order to obtain a non-vanishing current. For that reason, the system must induce a magnetization term out-of-equilibrium that *breaks time reversal in the process*. This idea is sketched in Fig. 1.1. Then, Eq.(1.10) must be modified qualitatively to

$$j_a^{(2)} = \sigma_{ab}(\vec{m}(\vec{E})) E_b. \quad (1.11)$$

Throughout the last decade, a plethora of explanations have been proposed as the microscopic origin of second order Hall transport based on Eq.(1.11). A pioneering step on this road is the definition of the **Berry curvature dipole (BCD)** in 2015 [31], relying on semiclassical principles that we will discuss in Chapter 2. This perspective has been extended to study systems where particular forms of disorder are considered [84]. In 2016, Morimoto et al. [85] deduced that the **BCD** is the leading order contribution to the second-harmonic generation in time reversal invariant materials for frequencies smaller than the band gap. In 2021, a Green function formalism was published, separating explicitly the contributions ascribed to extrinsic (side jump, skew-scattering) and intrinsic origins [86]. One year later, a systematic study of nonlinear response tensors has been communicated, which has also helped to figure it out the genesis of second order Hall transport [87]. Based on this research, in 2022, the intrinsic contribution to the second order Hall effect has been studied in PT antiferromagnets [88], i.e., antiferromagnetic systems that are invariant under the combination of inversion

(parity) and time reversal symmetry. We will focus on the BCD contribution to the Hall transport in Chapter 2, with an application to Weyl semimetals in Chapter 3. In addition, we will study the connection between BCD and non-equilibrium orbital magnetization in Chapter 4.

1.3.2. Materials Under Study

In view of Eq.(1.10) and the research developed in the context of the anomalous Hall effect, it has been necessary to construct a theory to estimate the second-order conductivity coefficients and apply these formulas to several material candidates and model systems, with the objective of tracking down the perfect conditions for experimental realizations. While in this section we give a few examples of the experimental and numerical studies on different materials and their features, in Chapter 2 we explain how the semiclassical theory gives rise to the second order conductivity coefficient and its limitations. Besides, we will also mention the extension to more complex (multiband) systems.

Taking note of these elements, several material candidates have been proposed as suitable options to obtain nonlinear Hall effect at the second order in electric field. The pioneering experiments were performed in bilayers and few layers of WTe₂ [37, 36]. The nonlinear Hall voltage from the experiment performed in bilayer WTe₂ [36] is shown in Fig.1.6.

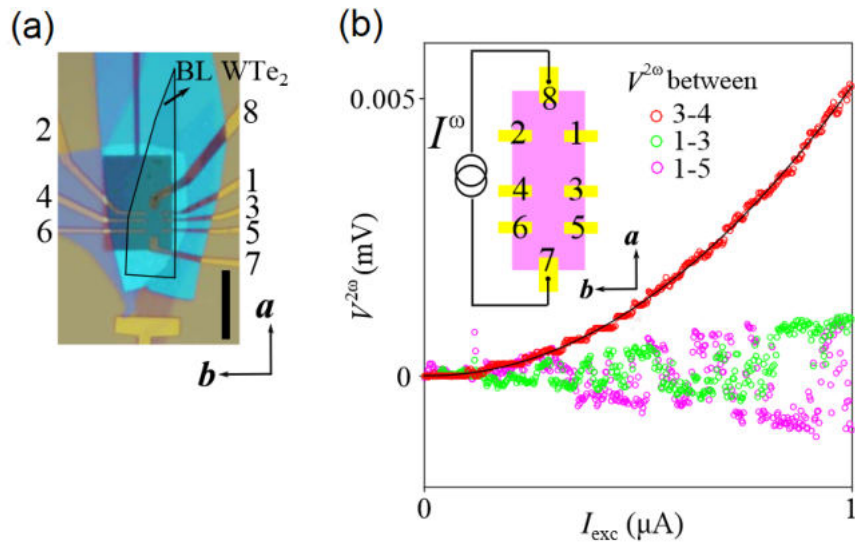


Figure 1.6. – (a) Optical image of the experimental setup, with the electrodes labelled with numbers. The crystalline directions are denoted by **a** and **b**. (b) Measure of the nonlinear Hall and longitudinal voltages $V^{2\omega}$ if an a.c. current flows parallel to **a** at $\omega \sim 177$ Hz, or in other words, between electrodes 7 and 8. Figure extracted and modified from [36].

Within the same frame, if an a.c. electric field is applied to generate the second order current, one can control its magnitude and direction with a direct current in WTe_2 [89]. Then, new efficient platforms have been discovered through numerical simulations in Transition Metal Dichalcogenides [90, 91, 92, 93, 94, 95], strained Graphene [96, 97, 98], Dirac [99] and Weyl semimetals [100, 101]. The investigation of new materials able to reach large values of nonlinear Hall effect (NLHE) has even reached non-centrosymmetric superconductors; giant nonlinear transport results have been published based on experiments in $PbTaSe_2$. The measurements expose the probable role of vortex-antivortex pairs in the origin of such responses [102]. Although non-magnetic systems are the immediate options to seek for second-order currents, antiferromagnets can also exhibit such a behavior. Certain classes of antiferromagnetic materials, where time reversal is broken but can be effectively restored with a combination with a lattice translation symmetry, can also produce nonlinear transport. This fact has been suggested as a new mean to detect the Néel vector, for example, in $CuMnSb$ [103]. The corresponding BCD can be used to identify the antiferromagnetic ordering in this classes of antiferromagnets.

A key ingredient of the emergence on second-order NLHE is the engineering of inversion symmetry breaking in non-magnetic materials through mirror symmetry breaking. In a first stage, this can be identified with the space group of the crystal under study, and more specifically, by asking for a proper combination of mirror symmetries. Viewed in this way, material interfaces and heterostructures are the immediate options for this objective due to structural asymmetry. For instance, strong signatures of NLHE have been disclosed in bilayers of WTe_2 [90], which are attributed to the interplay between the geometrical properties of the band structure and the inversion symmetry breaking produced by a gate voltage applied normal to the sample. From a microscopic perspective, the gate voltage is commonly encoded in a Rashba spin-orbit coupling term in our Hamiltonian system. In addition, the atomic structure of the system is also an essential factor that triggers inversion asymmetry in periodic crystals. Under such circumstances, for example, a polar structure is by far the simplest scenario where the NLHE can be detected both theoretically and experimentally. Indeed, researchers have been using the NLHE to uncover the polar ordering in ferroelectric materials such as $LiOsO_3$ [104], where the combination of a polar structure and electrically switchable electrical polarization establishes ferroelectric materials as remarkable prospects for optimizing the second order Hall effect. Moreover, the ferroelectricity can even promote a finite Hall current, for example, in $Bi(110)$ monolayer [105].

Another alternative to architect second-order nonlinear transport is the application of strain. In 2D non-centrosymmetric materials with certain C_n rotational symmetries, the implementation of strain immediately permits the BCD as long as the electric field is injected along the remaining mirror symmetry line. For example, experiments have been developed in monolayer MoS_2 under strain [6] in which this system is capable to create an orbital magnetization that can be detected even at room temperature. The intensity of the second-order transverse conductivity depends on the magnitude

of the applied strain and the orientation of the external electric field. A sketch of the generation of the second order Hall effect and a plot with the main experimental results are given by Figs.1.7-1.8.

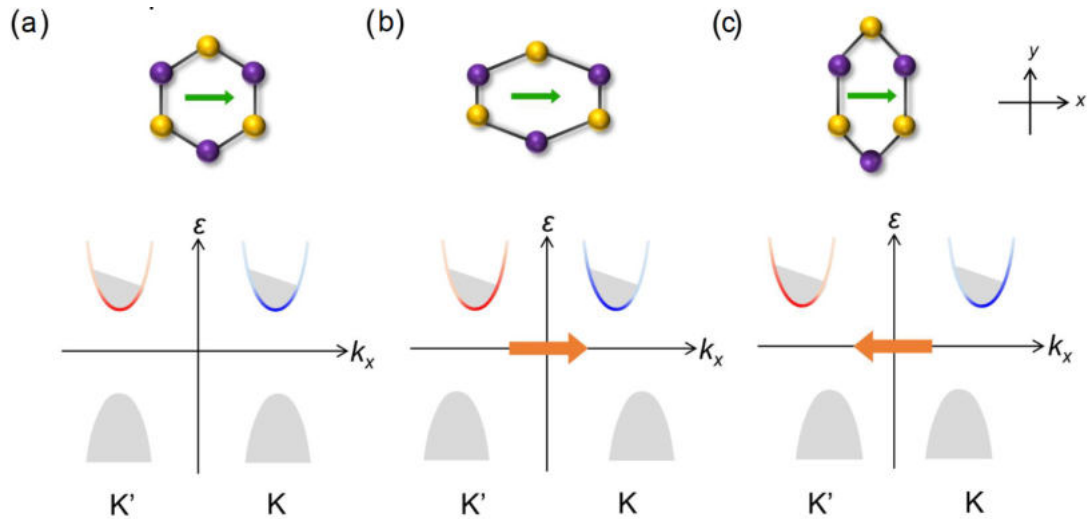


Figure 1.7. – Nonlinear Hall effect in Transition Metal Dichalcogenide monolayers under strain. When the electric field is applied along the mirror symmetry line (green arrows), there are 3 options: (a) For a monolayer without strain, the **BCD** is forbidden due to the 3-fold rotation. In the case of uniaxial strain along \hat{x} (b) or \hat{y} (c), the 3-fold rotation is subsequently broken and the distribution of the **BC** around the valleys K and K' (red and blue solid lines) produces a sizable **BCD** (orange arrows). Figure extracted and modified from [6].

Similar nonlinear effects have been studied in strained polar Transition Metal Dichalcogenides [95], where the **NLHE** is initially forbidden without strain. The assistance of the strain is particularly useful in materials with 3-fold rotation subjected to an in-plane electric field, emphasizing the role of the crystal deformation subjected to strong spin-orbit coupling. Disregarding the latter and lowering the crystal rotation to C_6 , for example in Graphene, non-zero Hall effects can be reached with the aid of hexagonal warping [96]. The elongation of the crystal is on top of that an ever-present effect in moiré systems - e.g. twisted bilayer Graphene, whereby a topological transition can be captured through the geometry of the quantum states [106, 107].

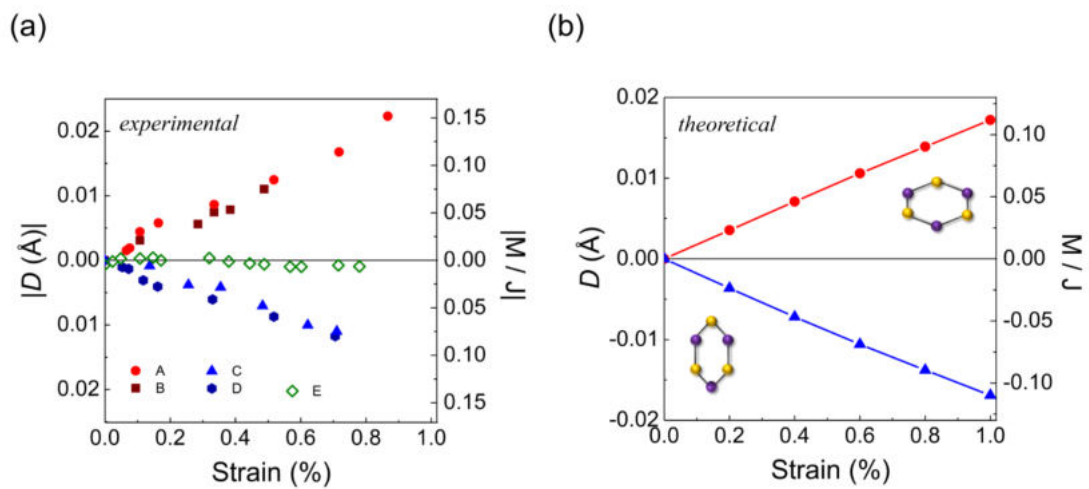


Figure 1.8. – BCD and normalized (valley) magnetization with respect to the total Hall current (M/J). (a) D and M/J measured for 5 different devices. Devices A and B (C and D) are strained along \hat{x} (\hat{y}) when the electric field is injected along \hat{x} . In device E, the strain is along \hat{x} when the electric field is applied along \hat{y} . (b) Calculated D and M/J when the strain is applied along \hat{x} (red circles) and \hat{y} (blue circles). Figure extracted and modified from [6].

1.4. Third order Hall Effect

1.4.1. Symmetry Relations

With the same reasoning for the quadratic current, the third order response must follow an analogous pattern in the absence of magnetism:

$$j_a = \sigma_{abcd} E_b E_c E_d. \quad (1.12)$$

In a system with time reversal symmetry the intrinsic third order vanishes, as in the case of the linear current, because the left side of Eq.(1.12) changes sign but the right one does not. Nevertheless, the extrinsic contribution is the leading order term of the transport. As we can see in Eq.(1.12), unlike the second order Hall effect in non-magnetic materials, inversion symmetry breaking is not the prerequisite of the third order Hall effect. As such, one does not expect the physical origin of the third order Hall effect to be simply related to the BC of the Bloch state, in contrast with its linear and second-order counterparts. Nonetheless, one of the popular (although quite recent) theories of third order Hall transport in non-magnetic centrosymmetric materials conjectures that the conductivity is driven by a quantity known as the Berry connection polarizability (BCP), which is at the same time a correction to the quantum geometric tensor [12]. What makes third order Hall effect particularly interesting in our view is that it emerges in centrosymmetric, non-magnetic materials, i.e., in systems when neither linear nor second-order Hall exist. This opens exciting perspectives for the study of materials with very high crystal symmetries.

1.4.1.1. Investigations on Different Platforms

From an experimental standpoint, the third order current was experimentally verified in bulk Td - MoTe₂ [108] and Td - TaIrTe₄ [109]. In fact, it has also been related with the orbital polarization in nanoflakes of WTe₂ [110], showing the possible role of the angular momentum on third-order Hall transport. In addition, the third order Hall effect has been observed in multiterminal devices as a tool to investigate higher order quantum effects at the nanoscale level [111].

It is interesting to observe that most experimental efforts (and theoretical predictions for that matter) focus on quantum materials, i.e., materials that display peculiarities in their band structures such as Weyl or Dirac nodes. In fact, the nonlinear effects we address in this Thesis do not necessarily require such behavior to be observable.

The benefits on investigating nonlinear effects are not limited to higher order responses in the electric field. Indeed, the charge transport is only one of the multiple roads where nonlinear responses can take place. In the next section, we summarize a variety nonlinear phenomena that can emanate from the flow of spin and/or angular momentum of the electron, and how their understanding can impact the magnetic properties of a vast selection of materials.

1.5. Nonlinear Physics in Spin-Orbitronics

1.5.1. Spin and Orbital Currents

Spin-Orbitronics is devoted to study intrinsic degrees of freedom of the electron that are beyond its charge, namely, its angular momentum and spin properties, in order to be utilized for nanoelectronics. A central concept in this field is the spin (orbital) current, i.e., a pure, charge-neutral current of angular momentum that carries information without carrying a charge. The efficient generation of spin (orbital) current via spin (orbital) Hall effect has been a major research focus over the past decade [112, 113, 26, 114, 115].

Symmetry analysis suggests that the spin Hall effect could persist in almost any material with spin-orbit coupling and the orbital Hall effect should prevail in systems with the right atomic configuration; none of them is bound to a time reversal or inversion restriction. Moreover, Onsager reciprocity imposes that the injected current direction, the collected current direction and its spin (orbital) polarization form an orthogonal triad. Since Onsager reciprocity does not apply at the second order in electric field, the nonlinear spin (orbital) current at this level can have a polarization that is not orthogonal to the input and output current directions.

Even though the spin and orbital Hall effects are essentially ubiquitous phenomena in terms of symmetry requirements, initial investigations in 2D crystals pointed out that valley and spin currents can be produced at second order in electric field, which depends on the anisotropy of the Fermi pockets [116]. Likewise, Araki in 2018 [117] has asserted that the nonlinear spin Hall effect can even reach values comparable to that of the linear spin Hall effect when a topological Dirac semimetal is subjected to strain, highlighting the cooperation between the axial effective magnetic field created by strain and the momentum space topology.

Collinear antiferromagnets have also been tested theoretically as an efficient platform for second-order spin Hall effects: The origin of this phenomenon has been ascribed to a spin dependent band geometric quantity related to the antiferromagnetic ordering. This mechanism seems to not require any kind of spin-orbit coupling or spin-split band structure [118]. In addition, nonlinear orbital currents have been signalled as an instrument to identify topological transitions in non-magnetic centrosymmetric structures[119].

In the case that the injected and output current are parallel, the longitudinal spin or orbital current are zero at the first order in electric field in systems with time reversal symmetry. In other words, there is no way to create a longitudinal spin (orbital) current by simply applying an electric field to a non-magnetic metal. Here, and in a similar fashion as the second order Hall effect in time reversal invariant materials, a second order longitudinal current is permitted in materials with additional inversion symmetry breaking (For example, in samples with Rashba spin-orbit coupling [120,

[121]). In this context, the assumption of the relaxation time approximation has also been reformulated up to the second order correction in the distribution function, with a particular application to identify nonlinear spin current in quantum wells with arbitrary Rashba and Dresselhaus coupling interactions [122].

Besides their ability to convey angular momentum information, the spin and orbital Hall effects are instrumental for the electrical manipulation of the magnetization in non-magnetic/ferromagnetic bilayers via the so-called spin-orbit torque [26]. In the next subsection, we show that lowering the crystal symmetry of such a bilayer can lead to unconventional forms of spin-orbit torques by introducing nonlinear effects not only in electric field, but also in the magnetization direction.

1.5.2. Spin-Orbit Torques

In the course of this PhD, and keeping on sight our interest for nonlinear effects, we made a short detour through the field of spin-orbitronics, a field of research that exploits spin-orbit coupling for spin-charge interconversion and current-driven magnetization control. The workhorse of spin-orbitronics is, as discussed in the previous paragraph, the spin Hall effect and the interfacial Rashba effect. Both effects both give rise to the spin-orbit torques in non-magnetic/ferromagnetic bilayers [123], as sketched in Fig.1.9(a) for instance. Until recently, most of the attention has been paid on the two the conventional components of the spin-orbit torque [124], called the field-like and the damping-like components. It turns out that these components, which are responsible for current-driven magnetization switching, are only the tip of the iceberg, i.e., the leading terms of the spin-orbit torque. It was realized recently that lowering the symmetry of the crystals composing the non-magnetic/ferromagnetic bilayers can lead to additional torque components of highest interest for applications such as magnetic memories.

Although linear in electric field and demanding inversion symmetry breaking, these torque components can be obtained by symmetry analysis of low symmetry crystals. In this frame, the re-evaluation of spin-orbit torques due to the symmetry of certain ferromagnets has been discussed earlier [126]. Later experiments verified the magnetization switching due to unexpected spin accumulations in FePt ferromagnets [127]. Further, low symmetry crystals captivated the attention due to numerous spin-orbit torques measured to achieve field-free switching, as illustrated in 1.9(b): Cr- based heterostructures [128], WTe₂ [129] and CoPt/CuPt bilayers [10]. The latter exhibits what is known as the "3m" torque, a crystalline dependent term that enables field-free switching in these systems. This torque has also been predicted in Fe₃GeTe₂ [11]. Besides, an unusual contribution has been identified in proximity to a magnetic interface [130], where the spin-polarization produced is able to rotate about the magnetization. In the same spirit, the angular dependencies of the spin-orbit torques obtained in Pt/Co/MgO trilayers [131] served as a complement to the previous work of Garello et al. [132], and thus motivating the subsequent observation of a spin-orbit field

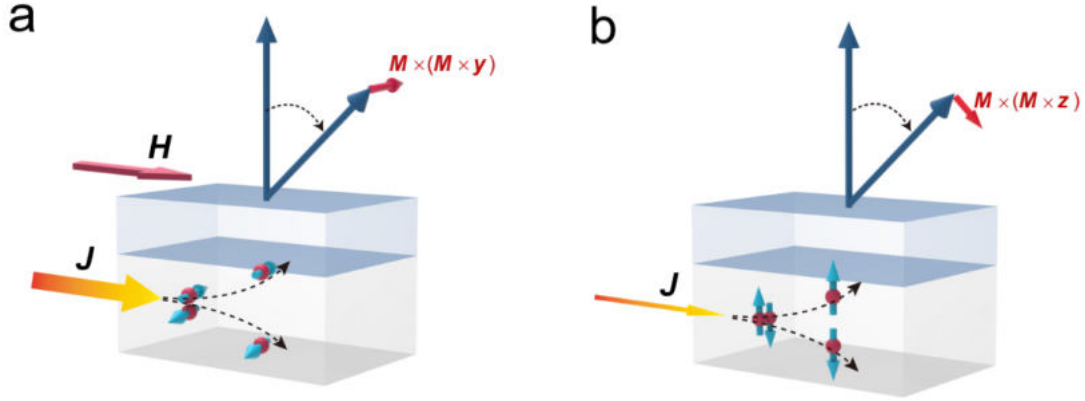


Figure 1.9. – Let us consider, without loss of generality, the field-free switching scheme throughout the Spin Hall effect in one of its common forms. (a) Injecting a current in a normal metal along \hat{x} creates an out-of plane spin current that is polarized along \hat{y} . Then, the torque exerted on the magnetization at the top layer $\sim \hat{m} \times (\hat{m} \times \hat{y})$ is not apt to perform the switching process, so an external magnetic field is mandatory. (b) In contrast, if the polarization of the spin current is along \hat{z} , the corresponding torque $\sim \hat{m} \times (\hat{m} \times \hat{z})$ allows the deterministic switching. Figure extracted and modified from [125].

arising on a planar Hall current [133]. Finally, a recent article reveals higher order angular dependencies in W/CoTeB bilayer, paying specific attention to the fact that its magnitude is way larger than in the cases of Pt/Co or Ta/CoFeB [134]. In Chapter 5 we will discuss broadly the spin-orbit torques allowed by symmetry in trigonal crystals, and how one can complete the switching process of perpendicular magnet without the assistance of a magnetic field.

1.6. Invariant Theory in a Nutshell

Physical quantities related to periodic systems, such as the Hamiltonian, the charge or spin current tensor, follow Neumann principle and thus they must remain invariant under a set of symmetry operations fulfilled by the material. An efficient way to explore the new effects allowed at higher order in the external stimuli to determine the most general form of the nonlinear response tensor that obeys the symmetry operations of the system. Here we introduce the so-called Invariant Theory [9], a method that allows for expressing the expansion coefficients of the response tensor in terms of "invariant functions".

As an illustration, let us begin by considering a Hamiltonian \mathcal{H} that describes (for example) a crystal subjected to certain symmetry operations that could be time reversal, inversion, mirror, rotations, etc, denoted as A_i for $i = 1 \dots N$. Then, if \mathcal{H} properly describes the system, it must be invariant under the corresponding set of

operations $\mathcal{G} := \{A_i\}_{i=1}^N$. In this case, since the Hamiltonian commutes with all the elements of \mathcal{G}

$$[\mathcal{H}, A_i] = 0 \quad \forall i \in [1, N], \quad (1.13)$$

then \mathcal{G} is a group. Indeed, we just need to check that these elements fulfil the properties of a group. The existence of the identity is trivial and the associative property comes directly from standard Quantum Mechanics. Next,

$$[\mathcal{H}, A_i] = 0 \rightarrow \mathcal{H} = A_i^{-1} \mathcal{H} A_i = A_i \mathcal{H} A_i^{-1} \forall i \in \mathcal{G}, \quad (1.14)$$

thus $[\mathcal{H}, A_i^{-1}] = 0$ and A_i^{-1} is an element of the group. Finally, taking A_1 and A_2 in \mathcal{G} , we have

$$\begin{aligned} (A_1 A_2)^{-1} \mathcal{H} (A_1 A_2) &= A_2^{-1} (A_1^{-1} \mathcal{H} A_1) A_2, \\ &= A_2^{-1} \mathcal{H} A_2, \\ &= \mathcal{H}. \end{aligned} \quad (1.15)$$

Having in mind that a group related to a given crystal contains elements that leave the Hamiltonian invariant, the next step is to find a way to represent them. In general, a group is completely determined by its multiplication table, showing us the way that the symmetry elements of the group are related between them. Going one step forward, each one of these operations can be characterized by a matrix, and the full set of elements in a given group is a matrix representation of the symmetry group under consideration. This is also called an algebra and is a set of matrices $D(R)$ that follows the multiplication table of the group:

$$D(R)D(S) = \lambda(R, S)D(RS). \quad (1.16)$$

where $\lambda(R, S)$ are numerical factors compatible with the associativity of the elements of the group. For example, the case $\lambda = 1$ defines an ordinary group. As we expect at this point, there are an infinite set of matrices that are equivalent representations of the group. Explicitly, if X is *any* square matrix with the same dimension as $D(R)$, then $XD(R)X^{-1}$ respects the same algebra as $D(R)$. This is also called an equivalent representation of the group, and a series of these transformations could lead to an irreducible representation of the group $D_j(R)$ for each j , being $D(R) = D_1(R) \otimes D_2(R) \otimes D_3(R) \otimes \dots$ written in a diagonal form and \otimes referring to the direct sum. For practical applications, we require to elucidate how to represent a given group in terms of a set of basis functions. Let us take an arbitrary group \mathcal{G} with symmetry operators E, A, B, C , etc., and a function $\psi(\vec{x})$ on which the operators can act. The set of g functions $E\psi(\vec{x}), A\psi(\vec{x}), B\psi(\vec{x})$, etc. are invariant under \mathcal{G} thinking that any operation $R \in \mathcal{G}$ just rearrange the previous set of functions. Moreover, the space ρ of functions

$$\phi = c_1 E\psi + c_2 A\psi + c_3 B\psi + \dots \quad (1.17)$$

is invariant under \mathcal{G} , keeping in mind that $R\phi \in \rho \forall R \in \mathcal{G}$. This set of functions may not be all independent between each other and thus they do not form a basis, but we can choose a smaller set of μ independent functions ψ_μ , with $\mu \leq g$, such that

$$\phi = \sum_{\mu} c_{\mu} \psi_{\mu}. \quad (1.18)$$

Again, if we use the invariance of ρ under \mathcal{G} , one can prove that any element $S \in \mathcal{G}$ over a function ψ_ν can be written as a linear combination of the functions ψ_μ :

$$S\psi_\nu = \psi_\mu D_{\mu\nu}(S), \quad (1.19)$$

being $D_{\mu\nu}(S)$ coefficients that are functions of S . In view of Eq.(1.19), it can be stated that any set of functions ψ_μ spanning a space ρ that is invariant under \mathcal{G} constitutes a matrix representation of the group through $D_{\mu\nu}(S)$. Following the algebraic properties of the group, we just need to show that the operator RS can be represented by the matrix $D(R)D(S)$. Applying the operator R to the left side of Eq.(1.19), we have

$$\begin{aligned} RS\psi_\nu &= (R\psi_\nu)D_{\mu\nu}(S) \\ &= \psi_\lambda D_{\lambda\mu}(R)D_{\mu\nu}(S) \\ &= \psi_\lambda D_{\lambda\nu}(RS), \end{aligned} \quad (1.20)$$

and then $D_{\lambda\nu}(RS) = D_{\lambda\mu}(R)D_{\mu\nu}(S)$. In fact, if we want to fix that the basis functions are orthonormal (which assumes that the space gathering the functions are accompanied by a dot product), hence

$$D_{\mu\nu}(S) = \langle \psi_\mu | S\psi_\nu \rangle. \quad (1.21)$$

Basis functions are a representation of a subspace in a given symmetry group, and they are summarized in the different character tables that can be found in the literature. Nevertheless, it is important to understand where they come from, specially because they play a pivotal role on determining the general form of a response tensor up to a given order in external impulses. We want to illustrate what we learned in order to obtain basis functions for the different representations of the symmetry group C_{3v} , which indeed will be relevant for the discussion of the physics of trigonal crystals in Chapter 5. The aforementioned group only involves a 3 fold rotation C_3 and a mirror symmetry normal to (\hat{x}, \hat{z}) or (\hat{y}, \hat{z}) σ_v . As a first scenario, in regular cylindrical coordinates (r, θ, z) it is clear that r and z are invariant under C_3 and σ_v . Consequently, any function ψ of the form $f(r, z)$ can only be accounted for by a function $f(r, z)$. Since $S\psi = \psi$ we arrive at the identity representation that can be expressed as $D_{\mu\nu}(S) = \delta_{\mu\nu}$.

Secondly, let us take a function of the form $\psi = x^2 e^{-r}$. It is straightforward to notice that e^{-r} is invariant under C_3 and σ_v , so it can be excluded from the upcoming analysis. Under the operation R , we notice that the polynomials of degree 2 $R\psi$ can

be expressed as combinations of $\psi_1 = x^2$, $\psi_2 = y^2$ and $\psi_3 = xy$. Taking into account the matrix representation for C_3 and σ_ν normal to, say, \hat{x} :

$$T(C_3) = \frac{1}{2} \begin{pmatrix} 1 & -\sqrt{3} \\ \sqrt{3} & -1 \end{pmatrix}, \quad (1.22)$$

$$S(\sigma_\nu) = \begin{pmatrix} -1 & 0 \\ 0 & 1 \end{pmatrix}, \quad (1.23)$$

and the transformations $\vec{x}' = \vec{x}T$ and $\vec{x}' = \vec{x}S$, a three dimensional representation can be written in the form $[(x')^2, (y')^2, 2x'y'] = [x^2, y^2, 2xy][D(R)]$, where

$$D[S] = \begin{pmatrix} 1 & 0 & 0 \\ 0 & 1 & 0 \\ 0 & 0 & -1 \end{pmatrix}, \quad (1.24)$$

$$D[T] = \frac{1}{4} \begin{pmatrix} 1 & 3 & 2\sqrt{3} \\ 3 & 1 & -2\sqrt{3} \\ -\sqrt{3} & \sqrt{3} & -2 \end{pmatrix}. \quad (1.25)$$

Let us try to write a representation that can be expressed in a diagonal form. In its normalized version, we can take the mapping $[x, y] \rightarrow [\cos\phi, \sin\phi]$, $\phi \in [0, 2\pi]$. Then, $x^2 \rightarrow \cos^2\phi$ and $y^2 \rightarrow \sin^2\phi$, which are not orthogonal in the sense of the dot product $\langle f(\phi) | g(\phi) \rangle = \int_0^{2\pi} f^*(\phi)g(\phi)d\phi$. Within the same context, on the contrary, $x^2 + y^2 \rightarrow 1$ and $x^2 - y^2 \rightarrow \cos 2\phi$ are. Moreover, $x^2 + y^2$ is invariant under $T(C_3)$ and $S(\sigma_\nu)$. Therefore, we can use the vectors $2xy \rightarrow \sin 2\phi$ and $x^2 - y^2 \rightarrow \cos 2\phi$ to span a subspace that is orthogonal to $x^2 + y^2$. Our full representation is given by

$$[(x')^2 + (y')^2, 2x'y', (x')^2 - (y')^2] = [x^2 + y^2, 2xy, x^2 - y^2]D[R] \quad (1.26)$$

with

$$D[S] = \begin{pmatrix} 1 & 0 & 0 \\ 0 & -1 & 0 \\ 0 & 0 & -1 \end{pmatrix}, \quad (1.27)$$

$$D[T] = \frac{1}{2} \begin{pmatrix} 1 & 0 & 0 \\ 0 & -1 & -\sqrt{3} \\ 0 & \sqrt{3} & -1 \end{pmatrix}. \quad (1.28)$$

The generators defined in Eqs.(1.27-1.28) are a direct sum of the identity representation related to $x^2 + y^2$ and a 2x2 representation identical to $[x, y]$. In conclusion, $[2xy, x^2 - y^2]$ transforms in the same way that $[x, y]$, hence creating an identical representation. A representation of a group that is written in the form of Eq.(1.27-1.28) is

tagged as irreducible.

In the definition of a character table, the behavior of the basis function under different classes of symmetry operations are classified by their so-called "characters". For a given representation $D(R)$, its character is defined as its trace:

$$\chi(R) = \sum_{\mu} D_{\mu\mu}(R). \quad (1.29)$$

Having in mind all these ingredients, we can read a character table by following a few rules. Here, each row indicates an irreducible representation of the group. Since the group can be divided in classes, each column of the table is related to a class and the characters assign a number for each representation in that class. For instance, in Table 5.1 for the C_{3v} point group, A_1 , A_2 and E are the irreducible representations of the group. E , C_3 and σ_v are the classes in which the group is subdivided and they give us the different symmetry operations concerning the group. In addition, the number accompanied them symbolizes the number of elements in the class. Then, since the character of the identity representation is the trace of a unit matrix, we can read the dimension of the representation from the character table. For the sake of the invariance of a given physical quantity, the remaining terms that are relevant have characters that are 1 or -1 .

1.7. Motivation and Scope of the Work

The fundamental symmetries observed in the distinct classes of quantum materials are imprinted on their electronic properties. As such, nonlinear effects provide new information about these features because they obey different symmetry constraints. Moreover, The emergent characteristics obtained through these quantities are not only applicable to offer new functionalities in nano-electronics, but they also expand our knowledge on the electronic structure of quantum materials. For all of these reasons, in this doctoral Thesis we aim to explore two categories of nonlinear effects: anomalous Hall and magnetotransport, which are currently relevant in electronic transport and spintronics, and that stem from higher order contributions in electric fields and magnetization (or magnetic fields).

Firstly, due to the ongoing interest on the second-order NLHE driven by the BCD, we investigate the corresponding conductivity coefficients in a lattice model that describes a WSM. It was expected that large values of BCD appear here because of the divergencies in the BC and the highly dispersive energy bands, but there was a lack of understanding about the contribution of Fermi arcs and other surfaces states to the BCD, and whether topology is a crucial factor to enhance the NLHE. In Chapter 3, we demonstrate how the surface states at the different faces of our system impact the BCD, putting a special emphasis on the interplay between the Weyl cone tilting and the band filling. The BCD components are strongly related to the mirror symmetries of the system, but as we will see in Chapter 3, it is possible to retrieve the contribution

1. State of the Art on Electronic Transport and Spintronics – 1.7. Motivation and Scope of the Work

of the topological states' projections even though the BCD in the plane of the Fermi arcs can be forbidden by symmetry.

Secondly, in Chapter 4 we explain the generation of the second order non-equilibrium orbital magnetization in non-magnetic materials with non-centrosymmetric structure through the magneto-optical Kerr effect, showing that is proportional to a frequency dependent BCD. Since it only requires inversion symmetry breaking, this magneto-optical can be considered as a probe of the orbital accumulation, even in the absence of spin-orbit coupling. Finally, In Chapter 5 we study unconventional spin-orbit torques and anomalous Hall effects in trigonal crystals that can be predicted from the Invariant Theory. We demonstrate the emergence of these responses and their corresponding origin at the microscopic level, showing the relevance of cubic contributions to the spin-orbit coupling and a proper band filling.

2. A Pedagogical Introduction to Electronic Transport Theory

Summary

2.1. Linear Response in Electric Field	48
2.1.1. Semiclassical Formalism	48
2.1.2. Green Function Formalism	53
2.2. Quadratic Response in Electric Field	56
2.2.1. Semiclassical Description	56
2.2.2. Green Function Formula	58
2.2.3. Current-Induced Magnetization	62
2.3. Cubic Response in Electric Field	63

Having in mind the repercussions of the theoretical studies to the discovery of new material platforms and innovative electro-optical effects for the ongoing and future nanoscience, in this chapter we introduce the electronic transport theory for the instances of first, second and third order in the electric field. We concentrate our treatment on semiclassical considerations combined with a simplified description of the disorder. For the sake of completeness, we also summarize the main results obtained from the equations of motion of the wave-packet center, and a multiband formalism arising on the Green function formula. We will carry on our arguments in the context of the generation of charge currents, but as we will see, this can be easily extended to other non-equilibrium properties such as the spin polarization, which has enormous implications in memory and logic devices.

As a first step, we will address linear response in electric field, and discuss how the inclusion of magnetic fields or an intrinsic magnetic ordering permits to unlock new physics related to the behavior of the electrons in the sample. Then, we address the nonlinear response regime keeping on sight our motivation to overcome the barriers imposed by the symmetry constraints of the linear regime. Then, throughout this report we will illustrate how this knowledge has been uncovered in the last 10 years, the way these effects can be enhanced and under which conditions they could take place. We present plethora of scenarios where a higher order effect in electric or magnetic field can offer unprecedented opportunities for the evolution of material science and nanotechnology.

2.1. Linear Response in Electric Field

2.1.1. Semiclassical Formalism

Let us consider a periodic system subjected to an external electric field \vec{E} in the adiabatic limit. Here, the ground state of the system is slightly corrected, which can be explained from Bloch theory's point of view [135]. Then, the output current in periodic crystals can be readily computed from the so-called Bloch Hamiltonian $\mathcal{H}_{\mathbf{k}}$, whose electronic eigenstates are Bloch states $|u_{n\mathbf{k}}\rangle$ satisfying Schrodinger equation $\mathcal{H}_{\mathbf{k}}|u_{n\mathbf{k}}\rangle = \epsilon_{n\mathbf{k}}|u_{n\mathbf{k}}\rangle$, where $\epsilon_{n\mathbf{k}}$ are the eigenenergies of the system. In general, the Bloch Hamiltonian is described through its eigenenergies and eigenvectors as a function of the crystal momentum and the band index n . The velocity operator, in the absence of any external perturbation, reads

$$\hat{v}_{\mathbf{k}} = \vec{\nabla}_{\mathbf{k}} \mathcal{H}_{\mathbf{k}}. \quad (2.1)$$

Subsequently, the electronic current in the material is the average value of the velocity operator after summing over all the energy bands:

$$\vec{j} = -\frac{e}{\hbar} \int_{BZ} \frac{d^D k}{(2\pi)^D} \sum_n \langle u_{n\mathbf{k}} | \hat{v}_{\mathbf{k}} | u_{n\mathbf{k}} \rangle g_{n\mathbf{k}}(\epsilon_{n\mathbf{k}} - \mu), \quad (2.2)$$

where D is the dimension of our crystal ($D = 2, 3$), μ is the chemical potential, $e > 0$ is the magnitude of the electronic charge and $g_{n\mathbf{k}}(\epsilon_{n\mathbf{k}} - \mu)$ is the Fermi distribution function. Throughout this manuscript we fix our calculations in the zero temperature limit, implying that the equilibrium distribution $f_{n\mathbf{k}}(\epsilon_{n\mathbf{k}} - \mu) \rightarrow -\Theta(\epsilon_{n\mathbf{k}} - \mu)$, being $\Theta(x)$ the Heaviside step function. Within this assumption we neglect all possible effects arising from thermal fluctuations. Now let us suppose that an external electric field \vec{E} is applied to the sample. Since the Bloch eigenstates are slightly perturbed from their equilibrium value, an additional shift in the average current will be induced in Eq.(2.2). We can take into account this modification by applying time independent perturbation theory with respect to the equilibrium Bloch eigenstates, say, $|u_{n\mathbf{k}}\rangle$. Setting the perturbation as $\delta\mathcal{H} = e\vec{E} \cdot \hat{x}$ in the length gauge, where \hat{x} is the position operator, the first order perturbation to the Bloch eigenstates under the presence of this electric field is

$$|u_{n\mathbf{k}}^{(1)}\rangle = \sum_{m \neq n} \frac{\langle u_{m\mathbf{k}} | \delta\mathcal{H} | u_{n\mathbf{k}} \rangle}{(\epsilon_{n\mathbf{k}} - \epsilon_{m\mathbf{k}})} |u_{m\mathbf{k}}\rangle. \quad (2.3)$$

Next, we need to evaluate the terms related to the position operator coming from the perturbative expansion coming from Eq.(2.2). That being said, we write the position operator as $\hat{x} = \hat{x}_i + \hat{x}_e$, where \hat{x}_i (\hat{x}_e) is the intraband (interband) part of the position operator. Its matrix elements in the Bloch basis are [136]

2. A Pedagogical Introduction to Electronic Transport Theory – 2.1. Linear Response in Electric Field

$$\langle u_{n\mathbf{k}} | \hat{x}_i | u_{m\mathbf{k}} \rangle = \delta_{nm} [\vec{A}_{nn} + i \vec{\nabla}_{\mathbf{k}}], \quad (2.4)$$

$$\langle u_{n\mathbf{k}} | \hat{x}_e | u_{m\mathbf{k}} \rangle = (1 - \delta_{nm}) \vec{A}_{nm}, \quad (2.5)$$

where \vec{A}_{nm} is called the Berry connection

$$\vec{A}_{nm} = i \langle u_{n\mathbf{k}} | \vec{\nabla}_{\mathbf{k}} | u_{m\mathbf{k}} \rangle. \quad (2.6)$$

Setting the position operator in Eqs.(2.4-2.5), a fundamental ambiguity becomes visible for the intraband part [136]. As we can see from Eq.(2.4), this is because of the ambivalence in the Berry connection for $n = m$. We can obtain a representation of Eq.(2.6) for $n \neq m$ in the parallel transport Gauge with the identity:

$$\begin{aligned} \mathcal{H}_{\mathbf{k}} | u_{n\mathbf{k}} \rangle &= \epsilon_{n\mathbf{k}} | u_{n\mathbf{k}} \rangle, \\ \vec{\nabla} \mathcal{H}_{\mathbf{k}} | u_{n\mathbf{k}} \rangle + \mathcal{H}_{\mathbf{k}} | \vec{\nabla} u_{n\mathbf{k}} \rangle &= \vec{\nabla} \epsilon_{n\mathbf{k}} | u_{n\mathbf{k}} \rangle + \epsilon_{n\mathbf{k}} | \vec{\nabla} u_{n\mathbf{k}} \rangle. \end{aligned}$$

Applying $\langle u_{m\mathbf{k}} |$ on both sides of the previous equation, we have

$$\langle u_{m\mathbf{k}} | \vec{\nabla} \mathcal{H}_{\mathbf{k}} | u_{n\mathbf{k}} \rangle + \epsilon_{m\mathbf{k}} \langle u_{m\mathbf{k}} | \vec{\nabla} u_{n\mathbf{k}} \rangle = \vec{\nabla} \epsilon_{n\mathbf{k}} \langle u_{m\mathbf{k}} | u_{n\mathbf{k}} \rangle + \epsilon_{n\mathbf{k}} \langle u_{m\mathbf{k}} | \vec{\nabla} u_{n\mathbf{k}} \rangle$$

If $n = m$, we retrieve the identity for the velocity operator

$$\langle u_{n\mathbf{k}} | \hat{v}_{\mathbf{k}} | u_{n\mathbf{k}} \rangle = \vec{\nabla}_{\mathbf{k}} \epsilon_{n\mathbf{k}}. \quad (2.7)$$

In contrast, for $n \neq m$, we obtain

$$\langle u_{m\mathbf{k}} | \vec{\nabla}_{\mathbf{k}} u_{n\mathbf{k}} \rangle = \frac{\langle u_{m\mathbf{k}} | \hat{v}_{\mathbf{k}} | u_{n\mathbf{k}} \rangle}{\epsilon_{n\mathbf{k}} - \epsilon_{m\mathbf{k}}}. \quad (2.8)$$

This Gauge is effective in situations where we can avoid band degeneracies, being capable to capture the essential physics of the system [135]; If that is not possible, such as in more realistic scenarios, a different Gauge should be used (In general, the velocity Gauge is quite instrumental).

Regarding $g_{n\mathbf{k}}$, it is clear that it also deviates from the equilibrium as we apply the perturbation. The modification in the distribution can be taken into account by means of the Boltzmann equation, which we consider in the relaxation time approximation for simplicity. Here, the corrections to $g_{n\mathbf{k}}$ follow the identity

$$\tau \partial_t g_{n\mathbf{k}} + \tau \dot{\vec{k}} \cdot \vec{\nabla} g_{n\mathbf{k}} = f_{n\mathbf{k}} - g_{n\mathbf{k}}, \quad (2.9)$$

where $\tau = \frac{\hbar}{2\Gamma}$ is the constant scattering time and Γ is a homogeneous disorder parameter related to random impurities. The electron experiences a force $\dot{\vec{k}} = -\frac{e\vec{E}}{\hbar}$. At the first order, we apply the ansatz

2. A Pedagogical Introduction to Electronic Transport Theory – 2.1. Linear Response in Electric Field

$$g_{n\mathbf{k}} = f_{n\mathbf{k}} - f_{n\mathbf{k}}^{(1)} \quad (2.10)$$

and we assume that $f_{n\mathbf{k}}^{(1)}$ vanishes as \vec{E} . Therefore, we deduce that

$$f_{n\mathbf{k}}^{(1)} = -\frac{e\tau\vec{E}\cdot\vec{\nabla}f_{n\mathbf{k}}}{\hbar}. \quad (2.11)$$

With all these ingredients, the current at linear order in \vec{E} is given by

$$\begin{aligned} \vec{j} &= -\frac{e}{\hbar} \int_{BZ} \frac{d^D k}{(2\pi)^D} \sum_n \left[\langle u_{n\mathbf{k}} | \hat{v}_{\mathbf{k}} | u_{n\mathbf{k}} \rangle f_{n\mathbf{k}}^{(1)} + \left\langle \left\langle u_{n\mathbf{k}}^{(1)} | \hat{v}_{\mathbf{k}} | u_{n\mathbf{k}} \right\rangle + \langle u_{n\mathbf{k}} | \hat{v}_{\mathbf{k}} | u_{n\mathbf{k}}^{(1)} \right\rangle f_{n\mathbf{k}} \right] \\ &= \vec{j}_I + \vec{j}_{II}. \end{aligned} \quad (2.12)$$

Let us discuss about the two terms in Eq.(2.12) and the physics behind them. First, \vec{j}_I is a current proportional to τ , thus diverging in the weak disorder limit. We can write \vec{j}_I in the form

$$\vec{j}_I = \frac{e^2\tau}{\hbar} \int_{BZ} \frac{d^D k}{(2\pi)^D} \sum_n \langle u_{n\mathbf{k}} | \hat{v}_{\mathbf{k}} | u_{n\mathbf{k}} \rangle [\langle u_{n\mathbf{k}} | \vec{E} \cdot \hat{v}_{\mathbf{k}} | u_{n\mathbf{k}} \rangle] \partial_{\epsilon_{n\mathbf{k}}} f(\epsilon_{n\mathbf{k}} - \mu). \quad (2.13)$$

The previous equation is considered as the extrinsic contribution to the current, being also a Fermi surface quantity. Besides, it is responsible for the longitudinal conductivity, which is a part of the total outgoing current that is parallel to the direction of the injected one, constituting a dissipative part of the current; nevertheless, and as we will check in Chapter 5, we can demonstrate that it can play a role in magnetotransport phenomena under certain symmetry constraints. An exemplary case for the latter is the planar Hall effect. Second, under the same assumptions about scattering time and disorder on \vec{j}_{II} , we have for the velocity along the a direction when the \vec{E} is along b :

$$\begin{aligned} & \langle u_{n\mathbf{k}} | \hat{v}_{\mathbf{k}} | u_{n\mathbf{k}}^{(1)} \rangle_a + \langle u_{n\mathbf{k}}^{(1)} | \hat{v}_{\mathbf{k}} | u_{n\mathbf{k}} \rangle_a \\ &= eE_b \sum_{m \neq n} \frac{\langle u_{n\mathbf{k}} | \hat{v}_{\mathbf{k}} | u_{m\mathbf{k}} \rangle_a \langle u_{m\mathbf{k}} | x_b | u_{n\mathbf{k}} \rangle + \langle u_{m\mathbf{k}} | \hat{v}_{\mathbf{k}} | u_{n\mathbf{k}} \rangle_a \langle u_{n\mathbf{k}} | x_b | u_{m\mathbf{k}} \rangle}{\epsilon_{n\mathbf{k}} - \epsilon_{m\mathbf{k}}} \\ &= eE_b \sum_{m \neq n} \frac{\langle u_{n\mathbf{k}} | \hat{v}_{\mathbf{k}} | u_{m\mathbf{k}} \rangle_a \langle u_{m\mathbf{k}} | i\partial_b | u_{n\mathbf{k}} \rangle + \langle u_{m\mathbf{k}} | \hat{v}_{\mathbf{k}} | u_{n\mathbf{k}} \rangle_a \langle u_{n\mathbf{k}} | i\partial_b | u_{m\mathbf{k}} \rangle}{\epsilon_{n\mathbf{k}} - \epsilon_{m\mathbf{k}}} \\ &= ieE_b \sum_{m \neq n} \frac{\langle u_{n\mathbf{k}} | \hat{v}_{\mathbf{k}} | u_{m\mathbf{k}} \rangle_a \langle u_{m\mathbf{k}} | \hat{v}_{\mathbf{k}} | u_{n\mathbf{k}} \rangle_b - \langle u_{m\mathbf{k}} | \hat{v}_{\mathbf{k}} | u_{n\mathbf{k}} \rangle_a \langle u_{n\mathbf{k}} | \hat{v}_{\mathbf{k}} | u_{m\mathbf{k}} \rangle_b}{(\epsilon_{n\mathbf{k}} - \epsilon_{m\mathbf{k}})^2} \\ &= e\epsilon_{abc} E_b [\Omega_{n\mathbf{k}}]_c, \end{aligned} \quad (2.14)$$

where $\vec{\Omega}_{n\mathbf{k}}$ is the electronic BC of band n [15]

2. A Pedagogical Introduction to Electronic Transport Theory – 2.1. Linear Response in Electric Field

$$\vec{\Omega}_{n\mathbf{k}} = i \sum_{m \neq n} \frac{\langle u_{n\mathbf{k}} | \hat{v}_{\mathbf{k}} | u_{m\mathbf{k}} \rangle \times \langle u_{m\mathbf{k}} | \hat{v}_{\mathbf{k}} | u_{n\mathbf{k}} \rangle}{(\epsilon_{n\mathbf{k}} - \epsilon_{m\mathbf{k}})^2}. \quad (2.15)$$

Remarkably, in Eq.(2.15) only interband elements of the Berry connection participate because $m \neq n$. Then, we can directly choose the parallel transport Gauge. Therefore, the so-called anomalous Hall current, which is linear in the applied electric field, is given by

$$\vec{j}_{II} = -\frac{e^2}{\hbar} \int_{BZ} \frac{d^D k}{(2\pi)^D} \sum_n (\vec{E} \times \vec{\Omega}_{n\mathbf{k}}) f(\epsilon_{n\mathbf{k}} - \mu). \quad (2.16)$$

At this point, we should mention that the BC is a band structure quantity that emerges when the electric field perturbs the initial ground state(at least, when linear contributions in the electric field are taken into account. Let us maintain the question of higher order responses on hold for a moment). From a geometrical viewpoint, the BC leads to the non-commutativity of the position operator in periodic structures, which is at the heart of our ongoing knowledge of electronic transport theory [137]. The previous equation states that the anomalous Hall conductivity at the first order in electric field is a Fermi sea property, just requiring an integration below the Fermi surface. In addition, it is intrinsic because it produces a finite conductivity in the weak disorder limit. One can treat this term without considering any particular mechanism such as side-jump or skew scattering, by including a constant broadening term at the denominator of Eq.(2.15). From a microscopic perspective, let us mention a few symmetry properties about the behavior of the BC: the electronic BC is an axial vector in reciprocal space, and hence it is odd under time reversal symmetry \mathcal{T} and even under inversion symmetry \mathcal{P} :

$$\mathcal{P} \Omega_{n\mathbf{k}} \mathcal{P}^{-1} = \Omega_{n-\mathbf{k}}, \quad (2.17)$$

$$\mathcal{T} \Omega_{n\mathbf{k}} \mathcal{T}^{-1} = -\Omega_{n-\mathbf{k}}. \quad (2.18)$$

As we discussed in the previous section, the Hall current emerges if time reversal symmetry is effectively broken. Then, it is natural to associate some sort of equilibrium magnetization to the anomalous Hall effect. Although magnetization possesses both spin and orbital contributions, the part that is intimately connected to the anomalous Hall effect is the orbital magnetization, i.e., the magnetic moment associated with the rotational motion of the electron wave packet in the unit cell. The orbital magnetization is defined in the Bloch eigenbasis as [138, 139]

$$\begin{aligned} \vec{m}_{n\mathbf{k}} &= -\frac{e}{2\hbar} \langle u_{n\mathbf{k}} | \hat{x} \times \hat{v} | u_{n\mathbf{k}} \rangle \\ &= \frac{ie}{2\hbar} \sum_{m \neq n} \frac{\langle u_{n\mathbf{k}} | \hat{v}_{\mathbf{k}} | u_{m\mathbf{k}} \rangle \times \langle u_{m\mathbf{k}} | \hat{v}_{\mathbf{k}} | u_{n\mathbf{k}} \rangle}{\epsilon_{n\mathbf{k}} - \epsilon_{m\mathbf{k}}}. \end{aligned} \quad (2.19)$$

2. A Pedagogical Introduction to Electronic Transport Theory – 2.1. Linear Response in Electric Field

Notice that the Kubo identities for the orbital magnetic moment and the BC just differ by a factor proportional to the energy $\sim (\epsilon_{n\mathbf{k}} - \epsilon_{m\mathbf{k}})^{-1}$. In systems with particle-hole symmetry, or near the band gap in selected cases, the orbital moment can be explicitly connected to the BC [140]. In fact, both objects resemble a magnetic field or an angular velocity in reciprocal space.

For the sake of completeness, we point out that another, formally equivalent, approach to model Hall transport is the semiclassical transport theory that tracks the equation of motion of the center of mass of the electron wave packet. The theory was initialized by Sundaram and Niu in 1999 [46] and refined by Xiao and coworkers in 2005 [138], involving a lagrangian formulation of the electron's motion. The equations of motion of the wavepacket center, neglecting non-abelian contributions and to the first order in electric field, can be written in the following form for a given band n

$$\dot{\vec{x}}_n = \frac{D(\vec{B}, \vec{\Omega}_{n\mathbf{k}})}{\hbar} \left(\vec{v}_{n\mathbf{k}} + e\vec{E} \times \vec{\Omega}_{n\mathbf{k}} + \frac{e}{\hbar} (\vec{v}_{n\mathbf{k}} \cdot \vec{\Omega}_{n\mathbf{k}}) \vec{B} \right), \quad D(\vec{B}, \vec{\Omega}_{n\mathbf{k}}) = \left(1 + \frac{e\vec{B} \cdot \vec{\Omega}_{n\mathbf{k}}}{\hbar} \right)^{-1}, \quad (2.20)$$

$$\dot{\vec{k}}_n = \frac{D(\vec{B}, \vec{\Omega}_{n\mathbf{k}})}{\hbar} \left(-e\vec{E} - \frac{e}{\hbar} \vec{v}_{n\mathbf{k}} \times \vec{B} - \frac{e^2 (\vec{E} \cdot \vec{B}) \vec{\Omega}_{n\mathbf{k}}}{\hbar} \right), \quad (2.21)$$

where $\dot{\vec{x}}_n$ is the electron's velocity and $\dot{\vec{k}}_n$ is the force experienced by the electron subjected to an external electric and/or magnetic field. An interesting element of this theory is the inclusion of the function $D(\vec{B}, \vec{\Omega}_{n\mathbf{k}})$ that describes the modification of the density of states in the crystal, maintaining the validity of Liouville's theorem [138]. Remarkably, this term vanishes when the magnetic field and the BC are orthogonal between them. The average current formula thus incorporates a scaling factor $D^{-1}(\vec{B}, \vec{\Omega}_{n\mathbf{k}})$, which turns out to be relevant for the studies of magnetotransport phenonema and unconventional responses in quantum materials:

$$\vec{j} = -\frac{e}{\hbar} \sum_n \int_{BZ} \frac{d^D k}{(2\pi)^D} D^{-1}(\vec{B}, \vec{\Omega}_{n\mathbf{k}}) f_{n\mathbf{k}} \vec{v}_{n\mathbf{k}}. \quad (2.22)$$

Let us now concentrate on the so-called orbital magnetization \vec{M}_{orb} . In the grand-canonical ensemble we have $\epsilon_M = \epsilon_{\mathbf{k}} - \vec{m}_{\mathbf{k}} \cdot \vec{B} - \mu$ for every n in the Bloch basis, and thus the average energy is

$$E = \int \frac{d^D k}{(2\pi)^D} \left(1 + \frac{e\vec{B} \cdot \vec{\Omega}_{n\mathbf{k}}}{\hbar} \right) (\epsilon_0 - \vec{m}_{\mathbf{k}} \cdot \vec{B} - \mu). \quad (2.23)$$

Then, taking the Maxwell relation, it can be demonstrated that

$$\begin{aligned}
\vec{m} &= -\lim_{\vec{B} \rightarrow 0} \frac{\partial E}{\partial \vec{B}} \\
&= -\lim_{\vec{B} \rightarrow 0} \int \frac{d^D k}{(2\pi)^D} \left[\frac{e\vec{\Omega}_{\mathbf{k}}}{\hbar} (\epsilon_0 - \vec{m}_{\mathbf{k}} \cdot \vec{B} - \mu) - \left(1 + \frac{e\vec{B} \cdot \vec{\Omega}_{\mathbf{k}}}{\hbar} \right) \vec{m}_{\mathbf{k}} \right] \\
&= \int \frac{d^D k}{(2\pi)^D} \left[\frac{e\vec{\Omega}_{\mathbf{k}}}{\hbar} (\mu - \epsilon_0) + \vec{m}_{\mathbf{k}} \right].
\end{aligned} \tag{2.24}$$

Subsequently, the previous equation can be easily extended to a system of n bands [138, 139]

$$\vec{m}_{orb} = \sum_n \int_{BZ} \frac{d^D k}{(2\pi)^D} \left[\frac{e\vec{\Omega}_{n\mathbf{k}}}{\hbar} (\mu - \epsilon_{n\mathbf{k}}) + \vec{m}_{n\mathbf{k}} \right] f_{n\mathbf{k}}. \tag{2.25}$$

From Eq.(2.25), the equilibrium orbital magnetization accompanies the anomalous Hall effect because the orbital magnetic moment and the BC share the same symmetry constraints. As we will also see in section 2.2 for the second order Hall effect, a current-induced magnetization will also coexist with the Hall current as long as inversion symmetry is broken. In this way, the non-equilibrium orbital magnetization created (among others) by the electric field can be applied as a probe of the second-order Hall effect for a non-magnetic material without inversion symmetry.

2.1.2. Green Function Formalism

Whereas the semiclassical transport theory can explain several observables (including disorder effects) when the collision integral is computed appropriately, the Green function formalism contains the information about the extrinsic contributions through the self-energy Σ . Since it is written in terms of matrices and we do not deal with an explicit representation of the diagonal terms of the Berry connection, this representation is particularly suitable to multi-band problems, where band degeneracies are more likely to appear in the band structure. In the context of linear response theory, this approach is based on the Green function formalism [141]. A suitable way to get the identities is through the Keldysh technique, which we summarize here by starting with the Dyson equations in the presence of a uniform electric field [142, 143]:

$$G^R \otimes (\epsilon - H - \Sigma_R) = 1, \tag{2.26}$$

$$G^R \otimes (\Sigma^< \otimes G^A) = G^<, \tag{2.27}$$

where $G^{R(A)}$ are the retarded and advanced Green functions, ϵ is the transport energy, H is the Hamiltonian and $\Sigma_{R(A)}$ are the corresponding self-energies, which contain information about the disorder in our system. Here our objective is to find $G^<$ up to the first order in perturbation. Fixing the calculation in the Gauge invariant setup for

2. A Pedagogical Introduction to Electronic Transport Theory – 2.1. Linear Response in Electric Field

the coordinates (x, p) , \otimes is defined as the Moyal product between two operators \mathcal{A} and \mathcal{B} :

$$\mathcal{A} \otimes \mathcal{B}(x, p) = \mathcal{A}(x, p) e^{i\frac{\hbar}{2}(\overleftarrow{\partial}_{x\mu}\overrightarrow{\partial}_{p\mu} - \overleftarrow{\partial}_{p\mu}\overrightarrow{\partial}_{x\mu} - eF_{\mu\nu}\overleftarrow{\partial}_{p\mu}\overrightarrow{\partial}_{p\nu})} \mathcal{B}(x, p) \quad (2.28)$$

through the convolution between the spatial and temporal variables of the problem. In Eq.(2.28), $F_{\mu\nu}$ is the Maxwell tensor and $\overleftarrow{\partial}$ ($\overrightarrow{\partial}$) indicates the derivative applied to \mathcal{A} (\mathcal{B}). For the case of a constant electric field, the Moyal product in the energy-momentum space (ϵ, \vec{p}) takes the form [143]

$$\mathcal{A}(\epsilon, p) \otimes \mathcal{B}(\epsilon, p) = \mathcal{A}(\epsilon, p) e^{-i\frac{eE\hbar}{2}(\overleftarrow{\partial}_\epsilon\overrightarrow{\partial}_p - \overleftarrow{\partial}_p\overrightarrow{\partial}_\epsilon)} \mathcal{B}(\epsilon, p), \quad (2.29)$$

which at the linear order can be approximated to

$$\mathcal{A}(\epsilon, p) \otimes \mathcal{B}(\epsilon, p) \simeq \mathcal{A}(\epsilon, p) \left[1 - \frac{ieE\hbar}{2}(\overleftarrow{\partial}_\epsilon\overrightarrow{\partial}_p - \overleftarrow{\partial}_p\overrightarrow{\partial}_\epsilon) \right] \mathcal{B}(\epsilon, p). \quad (2.30)$$

Besides, we expand the Green function in the form

$$G^{R(A)} = G_0^{R(A)} + G_E^{R(A)}. \quad (2.31)$$

keeping terms proportional to \hbar . At zeroth order and setting $\Sigma = \Sigma(\epsilon)$, assuming that the scattering is governed by delta impurities, we have

$$G_0^< = G_0^R \Sigma_0^< G_0^A = (G_0^A - G_0^R) f(\epsilon), \quad (2.32)$$

$$G_0^R = (\epsilon - H - \Sigma_0^R)^{-1}, \quad (2.33)$$

$$\Sigma_0^< = (\Sigma_0^A - \Sigma_0^R) f(\epsilon), \quad (2.34)$$

where $f(\epsilon)$ is the equilibrium distribution function. At the first order and defining $\partial_p H = \hbar^{-1} \hat{v}_0$, we deduce that

$$\begin{aligned} G_E^R &= -\frac{ieE\hbar}{2} [\partial_p(G_0^R) \partial_\epsilon(G_0^R)^{-1} - \partial_\epsilon(G_0^R) \partial_p(G_0^R)^{-1}] G_0^R \\ &= \frac{ieE}{2} G_0^R [G_0^R, \hat{v}_0] G_0^R, \end{aligned} \quad (2.35)$$

$$\begin{aligned} G_E^< &= G_E^R \Sigma_0^< G_0^A + G_0^R \Sigma_0^< G_E^A - \frac{ieE\hbar}{2} G_0^R (\overleftarrow{\partial}_\epsilon\overrightarrow{\partial}_p - \overleftarrow{\partial}_p\overrightarrow{\partial}_\epsilon) \Sigma_0^< G_0^A \\ &= G_E^R \Sigma_0^< G_0^A + G_0^R \Sigma_0^< G_E^A - \frac{ieE\hbar}{2} [(\partial_\epsilon G_0^R) \Sigma_0^< (\partial_p G_0^A) - (\partial_p G_0^R) \Sigma_0^< (\partial_\epsilon G_0^A)] \\ &\quad - \frac{ieE\hbar}{2} [G_0^R (\partial_\epsilon \Sigma_0^<) (\partial_p G_0^A) - (\partial_p G_0^R) (\partial_\epsilon \Sigma_0^<) G_0^A]. \end{aligned} \quad (2.36)$$

Taking into account that the current along the a direction is given by

2. A Pedagogical Introduction to Electronic Transport Theory – 2.1. Linear Response in Electric Field

$$j_a = -\frac{e}{4\pi i\hbar} \int d\epsilon \text{Tr} [\{\hat{v}_a, G^<\}] \quad (2.37)$$

and in light of Eq.(2.36), the Fermi surface contribution to the the non-equilibrium current coming from $G^<$ ($\sim \partial_\epsilon f(\epsilon)$), up to first order in electric field applied into the b direction, is

$$\begin{aligned} G_{Ext}^< &= -\frac{ieE\hbar}{2} [G_0^R(\partial_\epsilon \Sigma_0^<)(\partial_p G_0^A) - (\partial_p G_0^R)(\partial_\epsilon \Sigma_0^<)G_0^A] \\ &= -\frac{ieE}{2} [G_0^R \hat{v}_0(G_0^R - G_0^A) + (G_0^A - G_0^R) \hat{v}_0 G_0^A] \partial_\epsilon f(\epsilon), \end{aligned} \quad (2.38)$$

hence the Fermi surface conductivity is

$$\begin{aligned} \sigma_{ab}^{Ext} &= \frac{e^2}{8\pi\hbar} \int d\epsilon \partial_\epsilon f(\epsilon) \text{Tr} [\{\hat{v}_a, G_0^R \hat{v}_b(G_0^R - G_0^A) + (G_0^A - G_0^R) \hat{v}_b G_0^A\}] \\ &= \frac{e^2}{4\pi\hbar} \int d\epsilon \partial_\epsilon f(\epsilon) \text{Tr} \{\hat{v}_a, \text{Re}(G_0^R \hat{v}_b(G_0^R - G_0^A))\} \\ &= \frac{e^2}{2\pi\hbar} \int d\epsilon \partial_\epsilon f(\epsilon) \text{Re} (\text{Tr} \{\hat{v}_b G_0^R \hat{v}_a(G_0^R - G_0^A)\}) \end{aligned} \quad (2.39)$$

If we focus on the Fermi sea terms ($\sim f(\epsilon)$), its $G^<$ part turns out to be

$$\begin{aligned} G_{Int}^< &= G_p^R \Sigma_0^< G_0^A + G_0^R \Sigma_0^< G_p^A - \frac{ieE\hbar}{2} [(\partial_\epsilon G_0^R) \Sigma_0^< (\partial_p G_0^A) - (\partial_p G_0^R) \Sigma_0^< (\partial_\epsilon G_0^A)] \\ &= \frac{ieE\hbar}{2} [\partial_\epsilon G_0^R - G_0^R \hat{v}_0 \partial_\epsilon G_0^R - \partial_\epsilon G_0^A \hat{v}_0 G_0^A + G_0^A \hat{v}_0 \partial_\epsilon G_0^A] \\ &\quad - \frac{ieE}{2} [G_0^R G_0^R \hat{v}_0 G_0^A + G_0^R \hat{v}_0 G_0^A G_0^A - G_0^R \hat{v}_0 G_0^R G_0^A - G_0^R G_0^A \hat{v}_0 G_0^A]. \end{aligned} \quad (2.40)$$

Therefore, after discarding the resulting imaginary terms from Eq.(2.40), the corresponding conductivity is

$$\sigma_{ab}^{Int} = \frac{e^2}{2\pi\hbar} \int d\epsilon f(\epsilon) \text{Re} (\text{Tr} \{\hat{v}_b G_0^R \hat{v}_a \partial_\epsilon G_0^R - \hat{v}_b \partial_\epsilon G_0^R \hat{v}_a G_0^R\}). \quad (2.41)$$

During this work, we consider a symmetrized version of these formulas for the linear conductivities [144], which are given by

2. A Pedagogical Introduction to Electronic Transport Theory – 2.2. Quadratic Response in Electric Field

$$\sigma_{ab}^{Ext} = \frac{e^2}{4\pi\hbar} \int d\epsilon \partial_\epsilon f(\epsilon) \text{Re}[\text{Tr}\{\hat{v}_b(G^R - G^A)\hat{v}_a(G^R - G^A)\}], \quad (2.42)$$

$$\sigma_{ab}^{Int} = \frac{e^2}{2\pi\hbar} \int d\epsilon \text{Re}[\text{Tr}\{\hat{v}_b(G^R - G^A)\hat{v}_a\partial_\epsilon(G^R + G^A)\}]. \quad (2.43)$$

Let us comment about the physics behind Eqs.(2.42-2.43). The first equation is the extrinsic contribution to the conductivity. In the relaxation time approximation combined with a weak disorder limit Γ , Eq.(2.42) can be written in the form of a Kubo identity by using Eq.(5.26) [144]. It converges to Eq.(2.13), which is inversely proportional to the homogeneous disorder Γ . Under the same assumptions about scattering time and disorder, the intrinsic contribution to the conductivity in Eq.(2.43) converges to the BC identity, which is insensitive to Γ .

Regarding the orbital magnetization, it has been demonstrated that the Green function formula is given by [145]

$$M_{orb}^z = -ie\hbar \int \frac{d\epsilon}{2\pi} \text{Tr}[(H - \mu)(G_B^A(\epsilon, \vec{p}) - G_B^R(\epsilon, \vec{p}))] f(\epsilon), \quad (2.44)$$

where

$$G_B^{R(A)} = G_0^{R(A)} \Sigma_B^{R(A)} G_0^{R(A)} + \frac{i}{2} \left[G_0^{R(A)} \hat{v}_x \partial_{p_y} G_0^{R(A)} - \partial_{p_y} G_0^{R(A)} \hat{v}_x G_0^{R(A)} \right] \quad (2.45)$$

and $\Sigma_B^{R(A)}$ is the retarded (advanced) self-energy in the presence of a magnetic field.

2.2. Quadratic Response in Electric Field

2.2.1. Semiclassical Description

Inspired by Eq.(2.12), in principle the current in this situation must contain all possible contributions available when we expand the Bloch state and the distribution function in terms of the electric field. If we assume the relaxation time approximation, the total current is

$$\begin{aligned} \vec{j} &= -\frac{e}{\hbar} \int_{BZ} \frac{d^D k}{(2\pi)^D} \sum_n \left[\left\{ \langle u_{n\mathbf{k}}^{(0)} | \hat{v}_{\mathbf{k}} | u_{n\mathbf{k}}^{(0)} \rangle \right\} f_{n\mathbf{k}}^{(2)} + \left\{ \langle u_{n\mathbf{k}}^{(1)} | \hat{v}_{\mathbf{k}} | u_{n\mathbf{k}}^{(0)} \rangle + \langle u_{n\mathbf{k}}^{(0)} | \hat{v}_{\mathbf{k}} | u_{n\mathbf{k}}^{(1)} \rangle \right\} f_{n\mathbf{k}}^{(1)} \right] \\ &\quad - \frac{e}{\hbar} \int_{BZ} \frac{d^D k}{(2\pi)^D} \sum_n \left[\langle u_{n\mathbf{k}}^{(1)} | \hat{v}_{\mathbf{k}} | u_{n\mathbf{k}}^{(1)} \rangle + \langle u_{n\mathbf{k}} | \hat{v}_{\mathbf{k}} | u_{n\mathbf{k}}^{(2)} \rangle + \langle u_{n\mathbf{k}}^{(2)} | \hat{v}_{\mathbf{k}} | u_{n\mathbf{k}}^{(0)} \rangle \right] f_{n\mathbf{k}}^{(0)} \\ &= \vec{j}_I + \vec{j}_{II} + \vec{j}_{III}, \end{aligned} \quad (2.46)$$

where $|u_{n\mathbf{k}}^{(i)}\rangle$ and $f_{n\mathbf{k}}^{(i)}$ are the i^{th} correction to the Bloch state and the Fermi distri-

2. A Pedagogical Introduction to Electronic Transport Theory – 2.2. Quadratic Response in Electric Field

bution, respectively, for $i \geq 0$. Besides the first order corrections for both quantities depicted in Eqs.(2.3-2.11), the second order contributions are given by

$$\left| u_{n\mathbf{k}}^{(2)} \right\rangle = \sum_{m \neq n} \left(\sum_{p \neq n} \frac{\langle u_{m\mathbf{k}} | \delta \hat{H} | u_{p\mathbf{k}} \rangle \langle u_{p\mathbf{k}} | \delta \hat{H} | u_{n\mathbf{k}} \rangle}{(\epsilon_{n\mathbf{k}} - \epsilon_{m\mathbf{k}})(\epsilon_{n\mathbf{k}} - \epsilon_{p\mathbf{k}})} - \frac{\langle u_{n\mathbf{k}} | \delta \hat{H} | u_{n\mathbf{k}} \rangle \langle u_{m\mathbf{k}} | \delta \hat{H} | u_{n\mathbf{k}} \rangle}{(\epsilon_{n\mathbf{k}} - \epsilon_{m\mathbf{k}})^2} \right) | u_{m\mathbf{k}} \rangle \quad (2.47)$$

$$f_{n\mathbf{k}}^{(2)} = -\frac{e\tau}{2\hbar} \vec{E} \cdot \vec{\nabla}_{\mathbf{k}} f_{n\mathbf{k}}^{(1)}. \quad (2.48)$$

In the case of a crystal with time reversal symmetry and inversion symmetry breaking only the second term in Eq.(2.46) \vec{j}_{II} survives since \vec{j}_I and \vec{j}_{III} are odd under time reversal. This matches accordingly with the previous symmetry principles sketched in section 1.3, because the material must generate an object that breaks time reversal out-of-equilibrium. As discussed below, this is achieved by the onset of non-equilibrium (orbital) magnetization, also called the orbital Edelstein effect.

The expression for \vec{j}_{II} given by

$$\vec{j}_{II} = -\frac{e}{\hbar} \int_{BZ} \frac{d^D k}{(2\pi)^D} \sum_n \left[\langle u_{n\mathbf{k}}^{(1)} | \hat{v}_{\mathbf{k}} | u_{n\mathbf{k}} \rangle + \langle u_{n\mathbf{k}} | \hat{v}_{\mathbf{k}} | u_{n\mathbf{k}}^{(1)} \rangle \right] f_{n\mathbf{k}}^{(1)} \quad (2.49)$$

thus corresponds to the leading order contribution to the BCD if time reversal is preserved and inversion is absent. The explicit derivation of the expression was performed by I. Sodemann and L.Fu [31], indicating that the leading order contribution to the Hall current is an extrinsic term driven by a higher order moment of the BC, which they tagged as the BCD. The idea has been even extended to higher orders in the electric field, where it has been proposed that the n^{th} BC multipole is the key mechanism for a Hall current proportional to E^n in the low-frequency limit [146, 147] (We can see that the integration by parts reveals the multipole nature of the BC terms through its derivatives).

As we capture from the first and second order currents presented in Eqs.(2.12-2.46), the BC multipole is one of many terms that could appear in a proper expansion of the current, where other band geometric terms can emerge depending on the symmetries of the crystal. Explicitly, the expression in square parenthesis in Eq.(2.49) is the BC given by Eq.(2.15) and $f_{n\mathbf{k}}^{(1)}$ is given by Eq.(2.11) in the relaxation time approximation. Therefore, we can recast the current as $j_a = \frac{e^3 \tau}{\hbar^2} \epsilon_{adc} D_{bd}$, where D_{bd} is the BCD

$$D_{bd} = \int_{BZ} \frac{d^D k}{(2\pi)^D} \sum_n [\hat{v}_{n\mathbf{k}}]_b [\Omega_{n\mathbf{k}}]_d \partial_{\epsilon_{n\mathbf{k}}} f_{n\mathbf{k}}. \quad (2.50)$$

The conductivity induced by the BCD is an extrinsic quantity since it depends on τ , but arises on the geometry of the quantum states that are related to the electronic band structure itself. Moreover, whereas the BCD is not constrained to Onsager's reciprocity (which only applies in linear response regime), it is subjected to the crystalline

symmetries of the sample. In this context, Nandy and Sodemann suggested a general rule for the BCD under the symmetry operations of a given space group. They also analyzed possible corrections to the nonlinear Hall tensor in presence of disorder that goes beyond the constant rate, something that is out of the scope of this work [84]. A few years later, intraband and interband BCDs have been taken into account as precursors of nonlinear optical effects in insulators [148]. Bearing in mind Eq.(2.50), the NLHE driven by the BCD should be enhanced in systems with large BC or with highly dispersive energy bands. As we will explain in Chapter 3, this is expected to occur in WSMs. Nonlinear photocurrents and second-order NLHE have been predicted in WSMs by applying many-body quantum techniques [149] and perturbation theory [150], noticing the sensitivity of this Hall transport to intraband processes, the chemical potential and the tilting of the Weyl cones.

If we change the perspective to systems with PT symmetry (a combination of time reversal and inversion symmetry), second order effects has been proposed as techniques to identify properties of quantum materials. In addition to what was reported by D.Shao et al. [103], if PT is preserved but time reversal is broken, the intrinsic second order anomalous Hall effect has been studied in certain classes of noncollinear antiferromagnets [88]. These second order contributions have been derived by means of quantum kinetic theory [151]. In addition, the proper cooperation between the BC and skew-scattering is capable to produce second-order Hall responses in PT-antiferromagnets [152]. Last but not least, it has been shown that nonlinear orbital responses can be used as a tool to identify topological transitions in centrosymmetric systems [119].

2.2.2. Green Function Formula

Recently, a full Green function theory of the second order Hall effect has been proposed [86], pointing out the differences between extrinsic and intrinsic contributions. The complete formulas are [86]

$$\chi_{abc}^I = -\frac{e^3}{4\pi\hbar} \int_{BZ} \frac{d^d k}{(2\pi)^d} \int d\epsilon \partial_\epsilon f(\epsilon) \text{Im} [\text{Tr} \{ \hat{v}_a \partial_\epsilon G^R \hat{v}_b G^R \hat{v}_c G^A \}] + b \leftrightarrow c, \quad (2.51)$$

$$\chi_{abc}^{II} = -\frac{e^3}{8\pi\hbar} \int_{BZ} \frac{d^d k}{(2\pi)^d} \int d\epsilon \partial_\epsilon f(\epsilon) \text{Im} [\text{Tr} \{ \hat{v}_a \partial_\epsilon G^R \partial_b \hat{v}_c G^A \}] + b \leftrightarrow c, \quad (2.52)$$

$$\chi_{abc}^{III} = -\frac{e^3}{8\pi\hbar} \int_{BZ} \frac{d^d k}{(2\pi)^d} \int d\epsilon \partial_\epsilon f(\epsilon) \text{Im} [\text{Tr} \{ \hat{v}_a \partial_\epsilon^2 G^R \partial_b \hat{v}_c G^R + 2 \hat{v}_a \partial_\epsilon (\partial_\epsilon G^R \hat{v}_b G^R) \hat{v}_c G^R \}] + b \leftrightarrow c. \quad (2.53)$$

In this context, the authors refined the symmetry analysis performed by Sodemann and Fu by detailing the allowed components in an extensive range of crystallographic point groups. This table is presented below [86] for the relevant point group symmetries with nonzero terms. The conductivity tensor is defined as

2. A Pedagogical Introduction to Electronic Transport Theory – 2.2. Quadratic Response in Electric Field

$$(j_x, j_y, j_z)^T = \begin{pmatrix} \chi_{xxx}^{ex} & \chi_{xxy}^{ex} & \chi_{xyy}^{ex} & \chi_{xxz}^{ex} & \chi_{xyz}^{ex} & \chi_{xzz}^{ex} \\ \chi_{yxx}^{ex} & \chi_{yyx}^{ex} & \chi_{yyy}^{ex} & \chi_{yzx}^{ex} & \chi_{yyz}^{ex} & \chi_{yzz}^{ex} \\ \chi_{zxx}^{ex} & \chi_{zxy}^{ex} & \chi_{zyy}^{ex} & \chi_{zzx}^{ex} & \chi_{zzy}^{ex} & \chi_{zzz}^{ex} \end{pmatrix} (E_x^2, 2E_x E_y, E_y^2, 2E_x E_z, 2E_y E_z, E_z^2)^T \quad (2.54)$$

Space Group	Extrinsic	Intrinsic
C_1	$\begin{pmatrix} \chi_{xxx}^{ex} & \chi_{xxy}^{ex} & \chi_{xyy}^{ex} & \chi_{xxz}^{ex} & \chi_{xyz}^{ex} & \chi_{xzz}^{ex} \\ \chi_{yxx}^{ex} & \chi_{yyx}^{ex} & \chi_{yyy}^{ex} & \chi_{yzx}^{ex} & \chi_{yyz}^{ex} & \chi_{yzz}^{ex} \\ \chi_{zxx}^{ex} & \chi_{zxy}^{ex} & \chi_{zyy}^{ex} & \chi_{zzx}^{ex} & \chi_{zzy}^{ex} & \chi_{zzz}^{ex} \end{pmatrix}$	$\begin{pmatrix} 0 & -\chi_{yxx}^{in} & \chi_{xyy}^{in} & -\chi_{zxx}^{in} & \chi_{xyz}^{in} & \chi_{xzz}^{in} \\ \chi_{yxx}^{in} & -\chi_{xyy}^{in} & 0 & \chi_{yzx}^{in} & -\chi_{zyy}^{in} & \chi_{yzz}^{in} \\ \chi_{zxx}^{in} & -\chi_{xyz}^{in} - \chi_{yzx}^{in} & \chi_{zyy}^{in} & -\chi_{xzz}^{in} & -\chi_{yzz}^{in} & 0 \end{pmatrix}$
C_{1v}	$\begin{pmatrix} 0 & \chi_{xxy}^{ex} & 0 & \chi_{xxz}^{ex} & 0 & 0 \\ \chi_{yxx}^{ex} & 0 & \chi_{yyy}^{ex} & 0 & \chi_{yyz}^{ex} & \chi_{yzz}^{ex} \\ \chi_{zxx}^{ex} & 0 & \chi_{zyy}^{ex} & 0 & \chi_{zzy}^{ex} & \chi_{zzz}^{ex} \end{pmatrix}$	$\begin{pmatrix} 0 & -\chi_{yxx}^{in} & 0 & -\chi_{zxx}^{in} & 0 & 0 \\ \chi_{yxx}^{in} & 0 & 0 & 0 & -\chi_{zyy}^{in} & \chi_{yzz}^{in} \\ \chi_{zxx}^{in} & 0 & \chi_{zyy}^{in} & 0 & -\chi_{yzz}^{in} & 0 \end{pmatrix}$
C_2	$\begin{pmatrix} 0 & 0 & 0 & \chi_{xxz}^{ex} & \chi_{xyz}^{ex} & 0 \\ 0 & 0 & 0 & \chi_{yzx}^{ex} & \chi_{yyz}^{ex} & 0 \\ \chi_{zxx}^{ex} & \chi_{zxy}^{ex} & \chi_{zyy}^{ex} & 0 & 0 & \chi_{zzz}^{ex} \end{pmatrix}$	$\begin{pmatrix} 0 & 0 & 0 & -\chi_{zxx}^{in} & \chi_{xyz}^{in} & 0 \\ 0 & 0 & 0 & \chi_{yzx}^{in} & -\chi_{zyy}^{in} & 0 \\ \chi_{zxx}^{in} & -\chi_{xyz}^{in} - \chi_{yzx}^{in} & \chi_{zyy}^{in} & 0 & 0 & 0 \end{pmatrix}$
C_{2v}	$\begin{pmatrix} 0 & 0 & 0 & \chi_{xxz}^{ex} & 0 & 0 \\ 0 & 0 & 0 & 0 & \chi_{yyz}^{ex} & 0 \\ \chi_{zxx}^{ex} & 0 & \chi_{zyy}^{ex} & 0 & 0 & \chi_{zzz}^{ex} \end{pmatrix}$	$\begin{pmatrix} 0 & 0 & 0 & -\chi_{zxx}^{in} & 0 & 0 \\ 0 & 0 & 0 & 0 & -\chi_{zyy}^{in} & 0 \\ \chi_{zxx}^{in} & 0 & \chi_{zyy}^{in} & 0 & 0 & 0 \end{pmatrix}$

2. A Pedagogical Introduction to Electronic Transport Theory – 2.2. Quadratic
Response in Electric Field

Space Group	Extrinsic	Intrinsic
D_2	$\begin{pmatrix} 0 & 0 & 0 & 0 & \chi_{xyz}^{ex} & 0 \\ 0 & 0 & 0 & \chi_{yzx}^{ex} & 0 & 0 \\ 0 & \chi_{zxy}^{ex} & 0 & 0 & 0 & 0 \end{pmatrix}$	$\begin{pmatrix} 0 & 0 & 0 & 0 & \chi_{xyz}^{in} & 0 \\ 0 & 0 & 0 & \chi_{yzx}^{in} & 0 & 0 \\ 0 & -\chi_{xyz}^{in} - \chi_{yzx}^{in} & 0 & 0 & 0 & 0 \end{pmatrix}$
C_4	$\begin{pmatrix} 0 & 0 & 0 & \chi_{xxz}^{ex} & \chi_{xyz}^{ex} & 0 \\ 0 & 0 & 0 & -\chi_{xyz}^{ex} & \chi_{xxz}^{ex} & 0 \\ \chi_{zxx}^{ex} & 0 & \chi_{zxx}^{ex} & 0 & 0 & \chi_{zzz}^{ex} \end{pmatrix}$	$\begin{pmatrix} 0 & 0 & 0 & -\chi_{zxx}^{in} & \chi_{xyz}^{in} & 0 \\ 0 & 0 & 0 & -\chi_{xyz}^{in} & -\chi_{zxx}^{in} & 0 \\ \chi_{zxx}^{in} & 0 & \chi_{zxx}^{in} & 0 & 0 & 0 \end{pmatrix}$
C_{4v}	$\begin{pmatrix} 0 & 0 & 0 & \chi_{xxz}^{ex} & 0 & 0 \\ 0 & 0 & 0 & 0 & \chi_{xxz}^{ex} & 0 \\ \chi_{zxx}^{ex} & 0 & \chi_{zxx}^{ex} & 0 & 0 & \chi_{zzz}^{ex} \end{pmatrix}$	$\begin{pmatrix} 0 & 0 & 0 & -\chi_{zxx}^{in} & 0 & 0 \\ 0 & 0 & 0 & 0 & -\chi_{zxx}^{in} & 0 \\ \chi_{zxx}^{in} & 0 & \chi_{zxx}^{in} & 0 & 0 & 0 \end{pmatrix}$
D_4	$\begin{pmatrix} 0 & 0 & 0 & 0 & \chi_{xyz}^{ex} & 0 \\ 0 & 0 & 0 & -\chi_{xyz}^{ex} & 0 & 0 \\ 0 & 0 & 0 & 0 & 0 & 0 \end{pmatrix}$	$\begin{pmatrix} 0 & 0 & 0 & 0 & \chi_{xyz}^{in} & 0 \\ 0 & 0 & 0 & -\chi_{xyz}^{in} & 0 & 0 \\ 0 & 0 & 0 & 0 & 0 & 0 \end{pmatrix}$
S_4	$\begin{pmatrix} 0 & 0 & 0 & \chi_{xxz}^{ex} & \chi_{xyz}^{ex} & 0 \\ 0 & 0 & 0 & \chi_{xyz}^{ex} & -\chi_{xxz}^{ex} & 0 \\ \chi_{zxx}^{ex} & \chi_{zxy}^{ex} & -\chi_{zxx}^{ex} & 0 & 0 & 0 \end{pmatrix}$	$\begin{pmatrix} 0 & 0 & 0 & -\chi_{zxx}^{in} & \chi_{xyz}^{in} & 0 \\ 0 & 0 & 0 & \chi_{xyz}^{in} & \chi_{zxx}^{in} & 0 \\ \chi_{zxx}^{in} & -2\chi_{xyz}^{in} & -\chi_{zxx}^{in} & 0 & 0 & 0 \end{pmatrix}$
D_{2d}	$\begin{pmatrix} 0 & 0 & 0 & 0 & \chi_{xyz}^{ex} & 0 \\ 0 & 0 & 0 & \chi_{xyz}^{ex} & 0 & 0 \\ 0 & \chi_{zxy}^{ex} & 0 & 0 & 0 & 0 \end{pmatrix}$	$\begin{pmatrix} 0 & 0 & 0 & 0 & \chi_{xyz}^{in} & 0 \\ 0 & 0 & 0 & \chi_{xyz}^{in} & 0 & 0 \\ 0 & -2\chi_{xyz}^{in} & 0 & 0 & 0 & 0 \end{pmatrix}$
T	$\begin{pmatrix} 0 & 0 & 0 & 0 & \chi_{xyz}^{ex} & 0 \\ 0 & 0 & 0 & \chi_{xyz}^{ex} & 0 & 0 \\ 0 & \chi_{xyz}^{ex} & 0 & 0 & 0 & 0 \end{pmatrix}$	$\begin{pmatrix} 0 & 0 & 0 & 0 & 0 & 0 \\ 0 & 0 & 0 & 0 & 0 & 0 \\ 0 & 0 & 0 & 0 & 0 & 0 \end{pmatrix}$
T_d	$\begin{pmatrix} 0 & 0 & 0 & 0 & \chi_{xyz}^{ex} & 0 \\ 0 & 0 & 0 & \chi_{xyz}^{ex} & 0 & 0 \\ 0 & \chi_{xyz}^{ex} & 0 & 0 & 0 & 0 \end{pmatrix}$	$\begin{pmatrix} 0 & 0 & 0 & 0 & 0 & 0 \\ 0 & 0 & 0 & 0 & 0 & 0 \\ 0 & 0 & 0 & 0 & 0 & 0 \end{pmatrix}$

2. A Pedagogical Introduction to Electronic Transport Theory – 2.2. Quadratic
Response in Electric Field

Space Group	Extrinsic	Intrinsic
C_3	$\begin{pmatrix} \chi_{xxx}^{ex} & -\chi_{yyy}^{ex} & -\chi_{xxx}^{ex} & -\chi_{xxx}^{ex} & \chi_{xyz}^{ex} & 0 \\ -\chi_{yyy}^{ex} & -\chi_{xxx}^{ex} & \chi_{yyy}^{ex} & -\chi_{xyz}^{ex} & -\chi_{xxx}^{ex} & 0 \\ \chi_{zxx}^{ex} & 0 & \chi_{zxx}^{ex} & 0 & 0 & \chi_{zzz}^{ex} \end{pmatrix}$	$\begin{pmatrix} 0 & 0 & 0 & 0 & \chi_{xyz}^{in} & 0 \\ 0 & 0 & 0 & -\chi_{xyz}^{in} & 0 & 0 \\ \chi_{zxx}^{in} & 0 & \chi_{zxx}^{in} & 0 & 0 & 0 \end{pmatrix}$
C_{3v}	$\begin{pmatrix} 0 & -\chi_{yyy}^{ex} & 0 & 0 & 0 & 0 \\ -\chi_{yyy}^{ex} & 0 & \chi_{yyy}^{ex} & 0 & 0 & 0 \\ \chi_{zxx}^{ex} & 0 & \chi_{zxx}^{ex} & 0 & 0 & \chi_{zzz}^{ex} \end{pmatrix}$	$\begin{pmatrix} 0 & 0 & 0 & 0 & 0 & 0 \\ 0 & 0 & 0 & 0 & 0 & 0 \\ \chi_{zxx}^{in} & 0 & \chi_{zxx}^{in} & 0 & 0 & 0 \end{pmatrix}$
D_3	$\begin{pmatrix} \chi_{xxx}^{ex} & 0 & -\chi_{xxx}^{ex} & 0 & \chi_{xyz}^{ex} & 0 \\ 0 & -\chi_{xxx}^{ex} & 0 & -\chi_{xyz}^{ex} & 0 & 0 \\ 0 & 0 & 0 & 0 & 0 & 0 \end{pmatrix}$	$\begin{pmatrix} 0 & 0 & 0 & 0 & \chi_{xyz}^{in} & 0 \\ 0 & 0 & 0 & -\chi_{xyz}^{in} & 0 & 0 \\ 0 & 0 & 0 & 0 & 0 & 0 \end{pmatrix}$
C_6	$\begin{pmatrix} 0 & 0 & 0 & \chi_{xxz}^{ex} & \chi_{xyz}^{ex} & 0 \\ 0 & 0 & 0 & -\chi_{xyz}^{ex} & \chi_{xxz}^{ex} & 0 \\ \chi_{zxx}^{ex} & 0 & \chi_{zxx}^{ex} & 0 & 0 & \chi_{zzz}^{ex} \end{pmatrix}$	$\begin{pmatrix} 0 & 0 & 0 & -\chi_{zxx}^{in} & \chi_{xyz}^{in} & 0 \\ 0 & 0 & 0 & -\chi_{xyz}^{in} & -\chi_{zxx}^{in} & 0 \\ \chi_{zxx}^{in} & 0 & \chi_{zxx}^{in} & 0 & 0 & 0 \end{pmatrix}$
C_{6v}	$\begin{pmatrix} 0 & 0 & 0 & \chi_{xxz}^{ex} & 0 & 0 \\ 0 & 0 & 0 & 0 & \chi_{xxz}^{ex} & 0 \\ \chi_{zxx}^{ex} & 0 & \chi_{zxx}^{ex} & 0 & 0 & \chi_{zzz}^{ex} \end{pmatrix}$	$\begin{pmatrix} 0 & 0 & 0 & -\chi_{zxx}^{in} & 0 & 0 \\ 0 & 0 & 0 & 0 & -\chi_{zxx}^{in} & 0 \\ \chi_{zxx}^{in} & 0 & \chi_{zxx}^{in} & 0 & 0 & 0 \end{pmatrix}$
D_6	$\begin{pmatrix} 0 & 0 & 0 & 0 & \chi_{xyz}^{ex} & 0 \\ 0 & 0 & 0 & -\chi_{xyz}^{ex} & 0 & 0 \\ 0 & 0 & 0 & 0 & 0 & 0 \end{pmatrix}$	$\begin{pmatrix} 0 & 0 & 0 & 0 & \chi_{xyz}^{in} & 0 \\ 0 & 0 & 0 & -\chi_{xyz}^{in} & 0 & 0 \\ 0 & 0 & 0 & 0 & 0 & 0 \end{pmatrix}$
C_{3h}	$\begin{pmatrix} \chi_{xxx}^{ex} & -\chi_{yyy}^{ex} & -\chi_{xxx}^{ex} & 0 & 0 & 0 \\ -\chi_{yyy}^{ex} & -\chi_{xxx}^{ex} & \chi_{yyy}^{ex} & 0 & 0 & 0 \\ 0 & 0 & 0 & 0 & 0 & 0 \end{pmatrix}$	$\begin{pmatrix} 0 & 0 & 0 & 0 & 0 & 0 \\ 0 & 0 & 0 & 0 & 0 & 0 \\ 0 & 0 & 0 & 0 & 0 & 0 \end{pmatrix}$
D_{3h}	$\begin{pmatrix} 0 & -\chi_{yyy}^{ex} & 0 & 0 & 0 & 0 \\ -\chi_{yyy}^{ex} & 0 & \chi_{yyy}^{ex} & 0 & 0 & 0 \\ 0 & 0 & 0 & 0 & 0 & 0 \end{pmatrix}$	$\begin{pmatrix} 0 & 0 & 0 & 0 & 0 & 0 \\ 0 & 0 & 0 & 0 & 0 & 0 \\ 0 & 0 & 0 & 0 & 0 & 0 \end{pmatrix}$

Here, the C_n axis is along \hat{z} , the mirror plane σ_v is normal to \hat{y} and the mirror plane σ_h is assumed as the (\hat{x}, \hat{y}) plane.

The extrinsic terms obtained in this article could explain the frequency doubling observed in Bi_2Se_3 [153]. Along the same line of disorder-induced nonlinear transport, skew-scattering has been stipulated as the origin of second order NLHE in graphene superlattices [154]. This has the potential to be responsible for high-frequency rectifiers in graphene multilayers and Transition Metal Dichalcogenides [155]. Second harmonic generation measurements along the out-of plane axis in Td-MoTe₂ and WTe₂ multilayer geometries display giant values of NLHE [156], which likewise has been attributed to extrinsic contributions coming from skew-scattering.

2.2.3. Current-Induced Magnetization

Based on qualitative symmetry arguments, one can postulate that the nonlinear current at the second order in electric field must be produced by a non-equilibrium magnetization that must be compatible with the inversion symmetry breaking. In other words, the second order Hall current could be interpreted as a two step-process: an anomalous Hall effect driven by a magnetization created by an electric field. An article published last year [87] explains that this statement can be verified from tight-binding modelling in SnTe. Therefore, the NLHE must be complemented with a current-induced orbital magnetization commonly tagged as the orbital Edelstein effect. In general, the Edelstein effect [157, 158, 159] depends linearly on the electric field, viz., $\vec{m} = \alpha \vec{E}$ [158], whether coming from the orbital magnetic moment, intra-atomic angular momentum or spin features. In the same way that the second-order Hall effect, it requires inversion symmetry breaking and follows from an identical rationale to what we deduce for the expression of the BCD: Expanding the Fermi distribution function up to first order in electric field, we conclude that the current-induced coefficients α_{ab} produced by an operator \hat{O} related to spin or orbital momenta are [160, 161, 162]

$$\alpha_{ab} = \frac{e\tau}{\hbar} \sum_n \int_{BZ} \frac{d^D k}{(2\pi)^D} \langle u_{n\mathbf{k}} | \hat{O} | u_{n\mathbf{k}} \rangle \langle u_{n\mathbf{k}} | \hat{v}_b | u_{n\mathbf{k}} \rangle \partial_{\epsilon_{n\mathbf{k}}} f_{n\mathbf{k}}. \quad (2.55)$$

We must remark that if $\langle u_{n\mathbf{k}} | \hat{O} | u_{n\mathbf{k}} \rangle$ is replaced by the argument in Eq.(2.25), we converge to the Edelstein effect ascribed to the physics of the unit cell [163, 164]. Analogously, for the orbital magnetization coming from the BC, we use the Kubo formulas for both $\vec{m}_{n\mathbf{k}}$ and $\vec{\Omega}_{n\mathbf{k}}$ in Eqs.(2.19) and (2.15). Then Eq.(2.55) becomes [163]

$$\begin{aligned} \alpha_{ab} &= \frac{ie^2\tau\epsilon_{abc}}{\hbar^2} \sum_{m \neq n, n} \int_{BZ} \frac{d^D k}{(2\pi)^D} \left[\frac{(\mu - \epsilon_{n\mathbf{k}})}{(\epsilon_{n\mathbf{k}} - \epsilon_{m\mathbf{k}})^2} + \frac{(\epsilon_{n\mathbf{k}} - \epsilon_{m\mathbf{k}})}{2(\epsilon_{n\mathbf{k}} - \epsilon_{m\mathbf{k}})^2} \right] \partial_{\epsilon_{n\mathbf{k}}} f_{n\mathbf{k}} \\ &\times \{ \langle u_{n\mathbf{k}} | \hat{v}_b | u_{m\mathbf{k}} \rangle \times \langle u_{m\mathbf{k}} | \hat{v}_c | u_{n\mathbf{k}} \rangle \langle u_{n\mathbf{k}} | \hat{v}_b | u_{n\mathbf{k}} \rangle \} \\ &= \frac{ie^2\tau}{2\hbar^2} \sum_{m \neq n, n} \int_{BZ} \frac{d^D k}{(2\pi)^D} \left\{ \frac{2\mu - \epsilon_{n\mathbf{k}} - \epsilon_{m\mathbf{k}}}{(\epsilon_{n\mathbf{k}} - \epsilon_{m\mathbf{k}})^2} \right\} \langle u_{n\mathbf{k}} | \hat{v}_b | u_{m\mathbf{k}} \rangle \langle u_{m\mathbf{k}} | \hat{v}_c | u_{n\mathbf{k}} \rangle \langle u_{n\mathbf{k}} | \hat{v}_b | u_{n\mathbf{k}} \rangle \partial_{\epsilon_{n\mathbf{k}}} f_{n\mathbf{k}}. \end{aligned} \quad (2.56)$$

An illustration about the similarities between BCD and the magnetoelectric effect is the generation of the BCD under strain in monolayer MoS₂ [6], as illustrated in Fig. 1.8, where the authors proved that the BCD can be considered as a magnetization induced by the electric field. In this case, we have $\vec{J} = \vec{m}(\vec{E}) \times \vec{E} = (\vec{D} \cdot \vec{E}) \hat{z} \times \vec{E}$ [31], with \vec{D} the BCD created by an orbital magnetization \vec{m}_{orb} and that can be linked to the BC closed to the energy gap.

2.3. Cubic Response in Electric Field

The third order Hall effect (TOHE) is the perfect scenario where our modern understanding of electronic transport is challenged. We include it in this work since it is a source of multiple ongoing prospects, inspired by second-order Hall effect, where the physical mechanisms that provide the current are still under debate and more investigation is needed. Whereas at first and second order in electric field, the leading contributions are related to the BC itself or the BCD, at the third order in the perturbation the absence of time reversal or inversion is not required anymore. Moreover, the current-induced magnetization at the first order in electric field requires inversion symmetry breaking and hence it is automatically absent in these materials. If we also consider that the Hall effect in this situation cannot be attributed to the Berry physics, the main points of ongoing discussion aim to elucidate the conditions for which the TOHE takes place and how it can be enhanced by external manipulation. Regarding the crystalline symmetries, the research has been restricted to 2D materials, where the TOHE vanishes in systems with C_{3v} , C_{6v} , D_3 , D_{3h} , D_{3d} , D_6 and D_{6h} .

An explanation for the third order conductivity has been presented by Liu et al. [12], based on semiclassical considerations, claiming that it arises from a correction due to the quantum geometry tagged as the Berry connection polarizability (BCP). In this context, the semiclassical equations presented in Eq.(2.20-2.21) are not valid anymore since they are accurate up to first order in electric field. Up to second order in electric field, a semiclassical analysis of the motion of the electronic wave-packet shows that [12]

$$\dot{\vec{x}} = \frac{1}{\hbar} \left\{ \tilde{v}_{\mathbf{k}} + e\vec{E} \times \tilde{\Omega}_{\mathbf{k}} \right\}, \quad (2.57)$$

$$\dot{\vec{k}} = \frac{1}{\hbar} \left\{ -e\vec{E} - \frac{e}{\hbar} \dot{\vec{x}} \times \vec{B} \right\}. \quad (2.58)$$

Here, $\tilde{v}_{\mathbf{k}}$ and $\tilde{\Omega}_{\mathbf{k}}$ are

$$\tilde{v}_{n\mathbf{k}} = \frac{\partial \tilde{\epsilon}_{n\mathbf{k}}}{\partial \mathbf{k}}, \quad (2.59)$$

$$\tilde{\Omega}_{n\mathbf{k}} = \tilde{\Omega}_{n\mathbf{k}} + \tilde{\Omega}_{n\mathbf{k}}^{(1)}, \quad (2.60)$$

2. A Pedagogical Introduction to Electronic Transport Theory – 2.3. Cubic Response in Electric Field

where

$$\tilde{\epsilon}_{n\mathbf{k}} = \epsilon_{n\mathbf{k}} - \sum_{m \neq n} \frac{(\vec{E} \cdot \vec{A}_{nm\mathbf{k}})(\vec{E} \cdot \vec{A}_{mn\mathbf{k}})}{\epsilon_{n\mathbf{k}} - \epsilon_{m\mathbf{k}}}, \quad (2.61)$$

$$\vec{\Omega}_{n\mathbf{k}}^{(1)} = \partial_{\mathbf{k}} \times A_{n\mathbf{k}}^{(1)}. \quad (2.62)$$

Besides, $\vec{A}_{nm\mathbf{k}} = i \langle u_{n\mathbf{k}} | \partial_{\mathbf{k}} | u_{m\mathbf{k}} \rangle$ the interband Berry connection, $A_{n\mathbf{k},a}^{(1)} = G_{n\mathbf{k},ab} E_b$ and $G_{n\mathbf{k},ab}$ is the BCP

$$G_{n\mathbf{k},ab} = 2 \operatorname{Re} \sum_{m \neq n} \frac{(\vec{E} \cdot \vec{A}_{nm\mathbf{k}})(\vec{E} \cdot \vec{A}_{mn\mathbf{k}})}{\epsilon_{n\mathbf{k}} - \epsilon_{m\mathbf{k}}}. \quad (2.63)$$

In the parallel transport gauge, using Eq.(2.8), Eq.(2.63) yields to

$$G_{n\mathbf{k},ab} = \sum_{m \neq n} \frac{\langle u_{n\mathbf{k}} | \hat{v}_a | u_{m\mathbf{k}} \rangle \langle u_{m\mathbf{k}} | \hat{v}_b | u_{n\mathbf{k}} \rangle + \langle u_{n\mathbf{k}} | \hat{v}_b | u_{m\mathbf{k}} \rangle \langle u_{m\mathbf{k}} | \hat{v}_a | u_{n\mathbf{k}} \rangle}{(\epsilon_{n\mathbf{k}} - \epsilon_{m\mathbf{k}})^3}. \quad (2.64)$$

Expanding the distribution function in the relaxation time approximation, the third order conductivity reads (In the original paper, $e = \hbar = 1$):

$$\begin{aligned} \chi_{abcd}^{(I)} &= \tau \int \frac{d^D k}{(2\pi)^D} \{ -\partial_a \partial_b G_{n\mathbf{k},cd} + \partial_a \partial_d G_{n\mathbf{k},bc} - \partial_b \partial_d G_{n\mathbf{k},ac} \} f_{n\mathbf{k}} \\ &+ \frac{\tau}{2} \int \frac{d^D k}{(2\pi)^D} v_{n\mathbf{k},a} v_{n\mathbf{k},b} G_{n\mathbf{k},cd} \partial_{\epsilon_{n\mathbf{k}}}^2 f_{n\mathbf{k}}, \end{aligned} \quad (2.65)$$

$$\chi_{abcd}^{(II)} = -\tau^3 \int \frac{d^D k}{(2\pi)^3} v_{n\mathbf{k},a} \partial_b \partial_c \partial_d f_{n\mathbf{k}}. \quad (2.66)$$

such that $j \propto (\chi_{abcd}^{(I)} + \chi_{abcd}^{(II)}) E_b E_c E_d$.

3. Influence of the Surface States on the Nonlinear Hall Effect in Weyl Semimetals

Summary

3.1. Motivation	65
3.2. Lattice and Slab Model Hamiltonians	68
3.3. Model Calculations and Discussion	73
3.4. Realistic Simulations in WTe_2 Slabs	81
3.5. Main Conclusions and Prospects	84

3.1. Motivation

The emergence of nonlinear dissipationless currents in systems where the linear order vanishes, such as non-magnetic materials and antiferromagnets with effective time reversal symmetry, has drawn a great deal of attention over the last decade. In this chapter we focus on the second order NLHE driven by the intrinsic BCD, which constitutes one of the mechanisms of second order d.c. transport [86]. As we briefly discussed in Chapter 2, the BCD is expected to reach large values in materials with large BC and highly dispersive energy bands and thus WSMs have been identified as promising sources of large BCD. This behavior has been verified in ab-initio numerical simulations [165].

Non-magnetic WSMs such as TaAs or WTe_2 are particularly interesting platforms for the realization of NLHE because inversion symmetry is necessarily broken and BC diverges at the Weyl nodes. WSMs possess pairs of doubly degenerate linearly dispersive states, forming Weyl cones at Fermi level [166]. According to the Nielsen-Ninomiya theorem [167], each pair of nodes carries BC monopoles of opposite chirality which are connected via Fermi arcs lying at opposite surfaces of the slab [30]. Type I WSMs such as Janus superlattices [168] and mononictide transition metal compounds [169, 170, 171] are characterized by point-like Fermi surface in the bulk and vanishing density of states. Looking at the band structure, the conical shape with apexes at the Weyl points is slightly tilted with respect to a given symmetry axis. Type II WSMs, such as $MoTe_2$ [172, 173] and WTe_2 [174, 175] but also the magnetic candidate $Co_3Sn_2S_2$ [176, 177, 178, 179, 180, 181], offer a slightly different paradigm as the Weyl cone spectrum is

3. Influence of the Surface States on the Nonlinear Hall Effect in Weyl Semimetals – 3.1. Motivation

strongly tilted in momentum space, breaking Lorentz invariance. As a result, the Weyl points arise at the boundary between electron and hole pockets. Notice that certain compounds can support type I as well as type II Weyl nodes [182, 183].

A remarkable aspect of WSMs is the nature of their surface states. As mentioned above, alike topological insulators WSMs possess topologically protected surface states in the form of spin-momentum locked Fermi arcs that connect bulk Weyl nodes of opposite chirality. In type I WSMs, the Fermi arcs coexist with the projection of electron (or hole) pockets when the chemical potential lies away from the neutrality point. In type II WSMs, the Fermi arcs coexist with projected electron and hole pockets irrespective of the value of the chemical potential, as well as with trivial closed loops called "track states" [184]. As a consequence, surface states of WSMs can be rich, resulting in enhanced Edelstein effect [160], and unconventional patterns in quantum oscillation experiments [185, 186, 187] (see also Ref. [188]). Previous works pointed out that topological materials defined in slab geometries can exhibit interesting transport properties due to finite size effects and the behavior of surface states inside the samples. In this context, it has been shown that the anomalous Hall conductivity is highly influenced by surface states such as Fermi arcs in Weyl systems without time-reversal symmetry [189], even in presence of disorder [190]. Additional studies have been performed in confined geometries to clarify, among others, the behavior of chiral magnetic effects [191], the magnetoresistance [192] and the quantum Hall effect in Dirac semimetals [193]. The surface disorder has also been analyzed as a possible factor that can impact the linear conductivity in WSMs, particularly regarding to the geometry of the Fermi arcs [194], and hence it is also interesting to extend its proper impact on the NLHE. We leave this aspect for future studies.

Despite of all the research developed to show the impact of the surface states in linear response phenomena, their influence on the nonlinear conductivity coefficients is still unclear. In this Chapter we aim to understand how the surface states influence the NLHE driven by the BCD. To do so, we start by studying a minimal 2-band spinless model of a time reversal invariant WSM without inversion symmetry in a slab geometry, in such a way that bulk and surface states are treated on equal footing [184]. This model exhibits four Weyl points: the minimum number of degeneracies due to time-reversal symmetry. These four points are associated with local divergencies of the Berry curvature, as depicted on Fig. 3.1. After neglecting the vanishing components of the BCD tensor due to mirror symmetries in the 3D lattice, Zeng et al. [100] recently reported that NLHE requires Weyl cone tilting and an asymmetric Fermi surface when the nodes lie at the same energy. The NLHE is also influenced by the distance between nodes. In fact, this lattice model confirms that BCD could behave differently whether we retain this configuration or we compute in the continuum regime. Accordingly, our study gives further insight about the implications of the Fermi arc configurations on the BCD. Remarkably, it also complements a recent study that comprises a surface BCD due to the projection of Fermi arcs in type I WSMs [3].

3. Influence of the Surface States on the Nonlinear Hall Effect in Weyl Semimetals – 3.1. Motivation

In this Chapter we present our findings related to the impact of the surface states on the NLHE in WSMs, which has recently been published in Physical Review B [1]. Particularly, my work is focused on the minimal model that leads to the main conclusions of the article. The Density Functional Theory simulations were developed by Dr. Armando Pezo, postdoctoral fellow in my research group, and they served as a tool to validate our predictions in a more realistic scenario. In Section 3.2 we show the lattice model that we consider for our study and the methodology for the generation of the slab geometries. Second, in Section 3.3 we report our main results and an extense discussion of the physics involved in the problem. In Section 3.4 we show the realistic simulations, comparing these outcomes with the results obtained from the lattice model calculations. Finally, in Section 3.5, we deliver our main conclusions of the study, interesting perspectives of the idea developed and prospects about the engineering of second order Hall effect driven by the BCD.

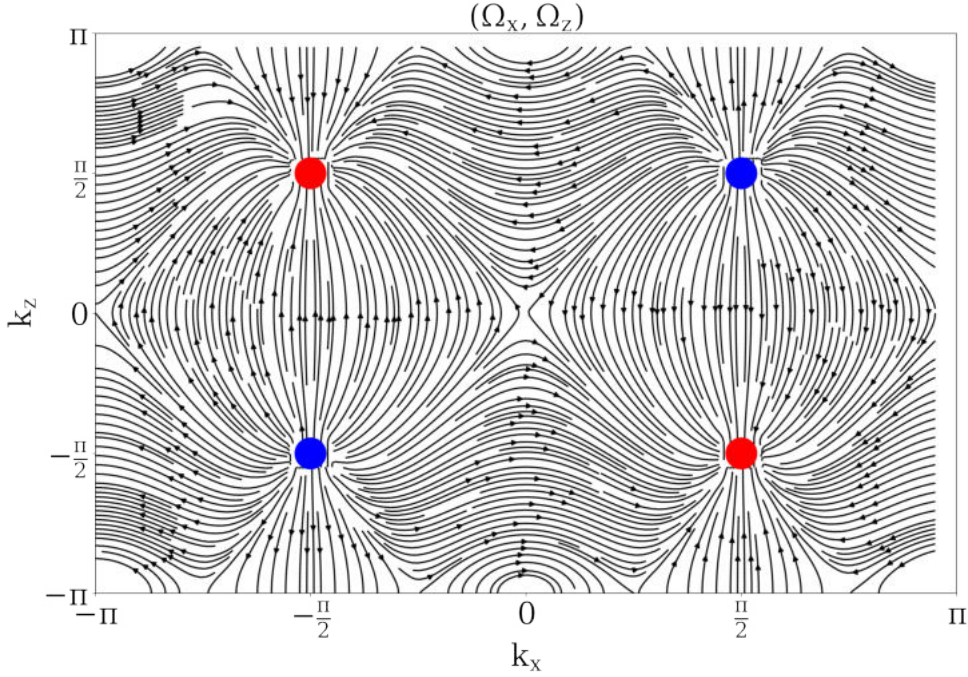


Figure 3.1. –BC vector field (Ω_x, Ω_z) of the Hamiltonian presented in Eq.(3.1), in the plane of the Fermi arcs with $k_y = 0$. We set the intrinsic parameters $k_0 = \frac{\pi}{2}$, $m = 2$, $t_x = \frac{1}{2}$, $\gamma = 1$ and $t = 1$. The BC is not sensitive to the value of γ [184], and then one specific value is enough to illustrate this vector field. The monopoles of BC are depicted by red and blue points, indicating sources (blue) or sinks (red) of BC flux. In the context of WSMs they are commonly tagged as Weyl points, and in this case they are arranged in reciprocal space obeying time reversal symmetry.

3.2. Lattice and Slab Model Hamiltonians

The minimal Hamiltonian under study is a 2-band spinless frame in the cubic lattice $\mathcal{C} = [-\pi, \pi]^3$ that mimics the essential features of a time reversal invariant Weyl semimetal with non-centrosymmetric structure [184]:

$$\begin{aligned} \mathcal{H}_B &= \gamma(\cos 2k_z - \cos k_0)(\cos k_x - \cos k_0)\hat{\sigma}_0 \\ &- [m(1 - \cos^2 k_x - \cos k_y) + 2t_x(\cos k_z - \cos k_0)]\hat{\sigma}_1 \\ &- 2t \sin k_y \hat{\sigma}_2 - 2t \cos k_x \hat{\sigma}_3, \end{aligned} \quad (3.1)$$

with $\hat{\sigma}_i$, $i = 1 \dots 3$ the 2×2 Pauli matrices and $\hat{\sigma}_0 = \mathbb{1}_{2 \times 2}$. Each node can be assigned to a topological charge of $n = \pm 1$. Currently, the BCD has also been investigated in WSMs with topological charges of $n = \pm 2, \pm 3$ [195], claiming that the intensity of the BCD obtained is mainly due to the magnitude of the topological charge and the energy dispersion. For the next calculations arising on Eq.(3.1), the essential parameters are set to be $k_0 = \frac{\pi}{2}$, $m = 2$, $t_x = \frac{1}{2}$ and $t = 1$. In this frame, the system exhibits four Weyl nodes at $\vec{k}_* = \pm \frac{\pi}{2}(\hat{x} + \hat{z})$. In addition, with the previous set of system parameters the transition point between type I and type II regime is fixed at $\gamma = 2$. The evolution of the system from type I to type II reveals the emergence of closed surface states tagged as track states. They are not topological, but degenerated in energy with respect to the states forming the Fermi arcs.

The lattice Hamiltonian presented in Eq.(3.1) is constrained by the mirror symmetries

$$\mathcal{M}_x^\dagger \mathcal{H}_B(k_x, k_y, k_z) \mathcal{M}_x = \mathcal{H}_B(-k_x, k_y, k_z), \quad (3.2)$$

$$\mathcal{M}_z^\dagger \mathcal{H}_B(k_x, k_y, k_z) \mathcal{M}_z = \mathcal{H}_B(k_x, k_y, -k_z), \quad (3.3)$$

and thus only D_{zx} and D_{xz} are non-zero components of BCD. Then, the transverse current is along \hat{y} . The mirror symmetries presented above constrain the non-zero elements of the dipole tensor, as it was mentioned earlier, generating a second order Hall current that is orthogonal to the mirror planes. Hence they will also forbid direct information of the second-order conductivity coefficients from the plane of the Fermi arcs; nonetheless, the study of the other planes remaining gives valuable information about the surface states in the system, independently of their topological nature.

Keeping in mind our objective to describe the surface contribution to the nonlinear transport, let us begin with a slab construction method based on a previous work that implemented the same procedure for the study of spin-orbit torques [2]. This technique is particularly useful for the investigation of the transport properties arising on the out-of-plane Berry curvature of a given plane; however, and since the Hamiltonian loses the periodicity in the direction of the slab, the BC is ill-defined in this direction.

3. Influence of the Surface States on the Nonlinear Hall Effect in Weyl Semimetals –
3.2. Lattice and Slab Model Hamiltonians

It is worth mentioning that up to now several attempts have been developed to explain the transport and magnetization properties driven by in-plane contributions of the BC and the orbital magnetic moment, especially in polar configurations [163, 196].

The slab Hamiltonian for a slab geometry normal to the \hat{n} direction is defined as follows:

$$\mathcal{H}_S^{\hat{n}} = \begin{pmatrix} \mathcal{H}_0^{\hat{n}} & \mathcal{H}_1^{\hat{n}} & \mathcal{H}_2^{\hat{n}} & 0 & \dots & 0 \\ \mathcal{H}_1^{\hat{n}\dagger} & \mathcal{H}_0^{\hat{n}} & \mathcal{H}_1^{\hat{n}} & \mathcal{H}_2^{\hat{n}} & \ddots & \vdots \\ \mathcal{H}_2^{\hat{n}\dagger} & \mathcal{H}_1^{\hat{n}\dagger} & \ddots & \ddots & \ddots & 0 \\ 0 & \mathcal{H}_2^{\hat{n}\dagger} & \ddots & \ddots & \ddots & \mathcal{H}_2^{\hat{n}} \\ \vdots & \ddots & \ddots & \ddots & \ddots & \mathcal{H}_1^{\hat{n}} \\ 0 & \dots & 0 & \mathcal{H}_2^{\hat{n}\dagger} & \mathcal{H}_1^{\hat{n}\dagger} & \mathcal{H}_0^{\hat{n}} \end{pmatrix}. \quad (3.4)$$

For the block matrices in Eq. (3.4), $\mathcal{H}_0^{\hat{n}}$ is the intralayer Hamiltonian that retains in-plane periodicity after the cut, while $\mathcal{H}_1^{\hat{n}}$ and $\mathcal{H}_2^{\hat{n}}$ are the nearest neighbor and second nearest neighbor interlayer Hamiltonian, respectively. For the cut along \hat{x} , the block matrices are given by

$$\begin{aligned} \mathcal{H}_0^{\hat{x}} &= -\gamma \cos k_0 (\cos 2k_z - \cos k_0) \hat{\sigma}_0 \\ &\quad - \left[m \left(\frac{1}{2} - \cos k_y \right) + 2t_x (\cos k_z - \cos k_0) \right] \hat{\sigma}_1 \\ &\quad - 2t \sin k_y \hat{\sigma}_2, \end{aligned} \quad (3.5)$$

$$\mathcal{H}_1^{\hat{x}} = \frac{\gamma}{2} (\cos 2k_z - \cos k_0) \hat{\sigma}_0 - t \hat{\sigma}_3, \quad (3.6)$$

$$\mathcal{H}_2^{\hat{x}} = \frac{m}{4} \hat{\sigma}_1. \quad (3.7)$$

A cut along \hat{y} leads to

$$\begin{aligned} \mathcal{H}_0^{\hat{y}} &= \gamma (\cos 2k_z - \cos k_0) (\cos k_x - \cos k_0) \hat{\sigma}_0 \\ &\quad - [m \sin^2 k_x + 2t_x (\cos k_z - \cos k_0)] \hat{\sigma}_1 \\ &\quad - 2t \cos k_x \hat{\sigma}_3, \end{aligned} \quad (3.8)$$

$$\mathcal{H}_1^{\hat{y}} = \frac{m}{2} \hat{\sigma}_1 + i t \hat{\sigma}_2. \quad (3.9)$$

Finally, a cut along \hat{z} gives

3. Influence of the Surface States on the Nonlinear Hall Effect in Weyl Semimetals –
 3.2. Lattice and Slab Model Hamiltonians

$$\begin{aligned}\mathcal{H}_0^{\hat{z}} &= -\gamma \cos k_0 (\cos k_x - \cos k_0) \hat{\sigma}_0 \\ &- [m(1 - \cos^2 k_x - \cos k_y) - 2t_x \cos k_0] \hat{\sigma}_1 \\ &- 2t \sin k_y \hat{\sigma}_2 - 2t \cos k_x \hat{\sigma}_3,\end{aligned}\quad (3.10)$$

$$\mathcal{H}_1^{\hat{z}} = -t_x \hat{\sigma}_1, \quad (3.11)$$

$$\mathcal{H}_2^{\hat{z}} = \frac{\gamma}{2} (\cos k_x - \cos k_0) \hat{\sigma}_0. \quad (3.12)$$

The band structures for slab geometries of 25 layers are presented in Fig.3.2, when the original Hamiltonian is cut along \hat{x} (a-d), \hat{y} (b-e) and \hat{z} (c-f). We take the instances for a type I and a type II WSM by fixing the value of γ at $\gamma = 1$ (upper panels) and $\gamma = 3$ (lower panels). We plot the bands for the \hat{x} (\hat{z}) cut for $k_y = 0$ and k_z (k_x) $\in [-\pi, \pi]$, while the \hat{y} cut is plotted in the path $A_1 = (-\pi, 0, \pi) \rightarrow \Gamma = (0, 0, 0) \rightarrow A_2 = (\pi, 0, \pi)$. In this case, the cuts along \hat{x} and \hat{z} reflects the exponentially localized states at the surface of each slab, whereas the central panels reveals more dispersive surface states in the plane of the Fermi arcs.

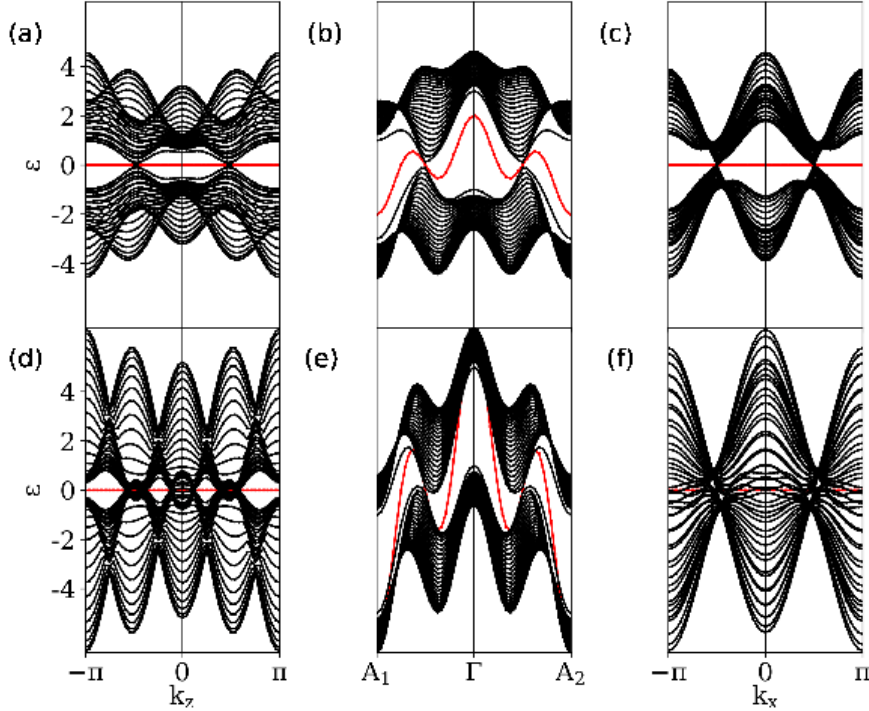


Figure 3.2. – Band structure for slab configurations with 25 layers in type I (upper panels, $\gamma = 1$) and type II (lower panels, $\gamma = 3$) regime, when the slab is normal to \hat{x} (a-d), \hat{y} (b-e) and \hat{z} (c-f). We denote the surface states with red lines.

3. Influence of the Surface States on the Nonlinear Hall Effect in Weyl Semimetals – 3.2. Lattice and Slab Model Hamiltonians

Next, the layer resolution for the slab geometries defined above give us more details about the surface states' diversity and its impact on the second order Hall transport. To do so, and since the periodic part of the Bloch function can be written in terms of the complete layer basis as $|u_{n\mathbf{k}}\rangle = \sum_{l=1}^L |\omega_{l\mathbf{k}}\rangle \langle \omega_{l\mathbf{k}}|u_{n\mathbf{k}}\rangle$, one can extract the contribution of layer l by applying the projection operator $\mathcal{S}_l = |\omega_{l\mathbf{k}}\rangle \langle \omega_{l\mathbf{k}}|$, $l \in [1, L]$ to an observable \mathcal{O} . In this way, it is straightforward to see that $\mathcal{O} = \sum_{l=1}^L \mathcal{S}_l \mathcal{O}$ and $\sum_{l=1}^L \mathcal{S}_l = \mathbb{1}_{2L \times 2L}$. We use this description to separate the contribution of a given layer to the density of states of a slab with a fixed number of layers L ,

$$\mathcal{D}_{l\mathbf{k}} = -\frac{1}{\pi} \text{Im} [\text{Tr}(\mathcal{S}_l G_{\mathbf{k}}^R)], \quad (3.13)$$

with the retarded Green's function defined as

$$G_{\mathbf{k}}^R = \lim_{\eta \rightarrow 0^+} [(\epsilon + i\eta) \mathbb{1} - \mathcal{H}_S^{\hat{n}}]^{-1}. \quad (3.14)$$

We start by confirming the Fermi arc recombination of the system and its surface states' evolution as a function of γ by computing the layer resolution density of states when the slab is normal to the plane of the Fermi arcs (\hat{y}). This is performed for a slab geometry of 25 layers for the case $\mu = 0.2$, illustrating the top (upper panels), middle (central panels) and bottom layers (lower panels), for different values of γ going from $\gamma = 1$ to $\gamma = 3$ (left to right panels). The outcomes are reported in Fig.3.3. From the evolution of the density of states given by the top ($l = 1$) and bottom ($l = 25$) layers, it is clear that the Fermi arcs change direction from k_z to k_x , when the system goes through the transition between $\gamma = 1$ and $\gamma = 3$. Furthermore, as the value of γ increases trivial surface states and an enlargement of the Fermi pockets surrounding the Weyl nodes emerge at the Brillouin zone, joining the track states that appear with centers at $(k_x, k_z) = (0, \pm\pi)$. Last but not least, the mismatch between the top and bottom surfaces is in agreement to what is reported in [184], and we assign this behavior to the absence of mirror symmetry along \hat{y} in the original Hamiltonian given by Eq. (3.1).

In the next section of this chapter, we address the transport properties and discuss them by looking at the density of states projected on the relevant faces due to the mirror symmetries of the 2-band original Hamiltonian. We apply the same layer decomposition that leads to Eqs.(3.13-3.14), but now paying specific attention to the \hat{x} and \hat{z} cut. In fact, the same procedure is applied later to resolve the BCD across the slabs in Fig.3.6. In order to obtain the contribution of layer l to the response along, say, \hat{y} , one simply needs to perform the substitution $\hat{v}_y \rightarrow \mathcal{S}_l \hat{v}_y$ into Eq. (2.15) and then into Eq.(2.50).

3. Influence of the Surface States on the Nonlinear Hall Effect in Weyl Semimetals –
 3.2. Lattice and Slab Model Hamiltonians

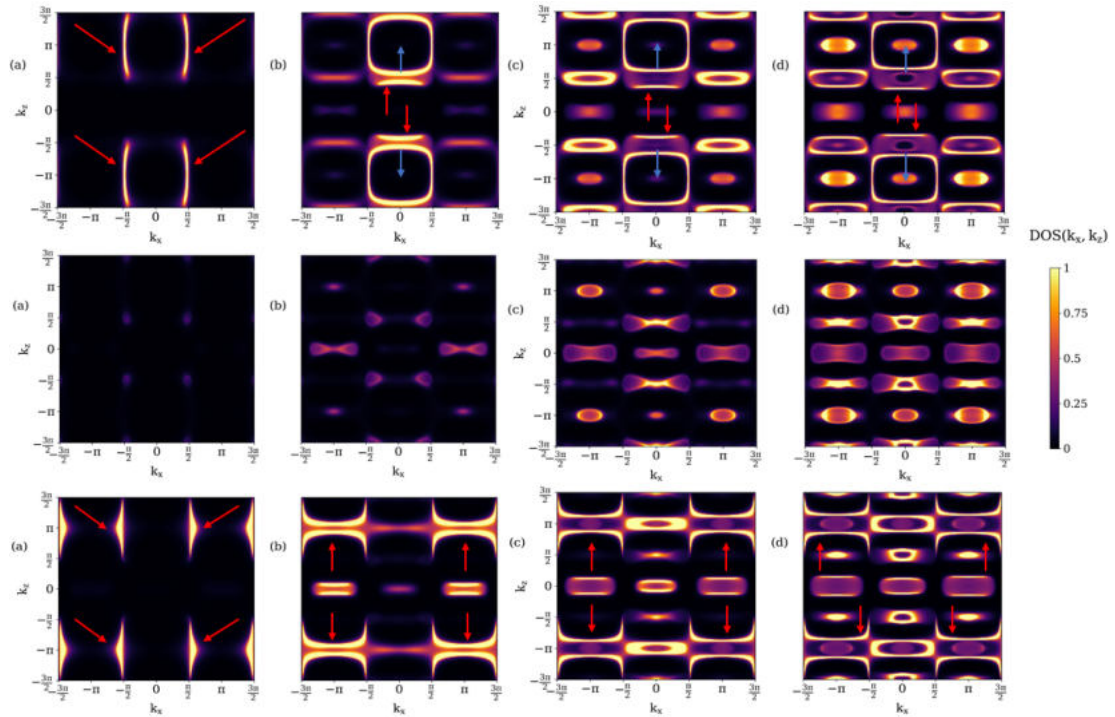


Figure 3.3. – Density of states for a slab system with $L = 25$ layers, when the growth direction is along \hat{y} . We take the same parameters as in Fig.3.1 and $\mu = 0.2$, exemplifying the top (upper panels), central (central panels) and bottom layers (lower panels) for the system described above. We show the transition between type I and type II by varying the tilting parameter γ , labeling the instances $\gamma = 1, 2, 2.5, 3$ with indexes (a-d), respectively. Finally, the Fermi arcs and the center of the track states are indicated with red and blue arrows, respectively.

3.3. Model Calculations and Discussion

We support our conclusions on the BCD for the slabs based on an analysis of the density of states, which reveals the main differences regarding the tilting of the Weyl cones and the corresponding distribution of the surface states of the pertinent systems. We compute the corresponding BCDs by using Eq.(2.50) in Chapter 2. Our results are reported in Figs. 3.4. For an exemplary system of 25 layers and fixing the energy at $\mu = 0.2$, we perform a surface resolution for selected layers $l = 1, 7, 13, 19, 25$, being $l = 1$ ($l = 25$) the bottom most (uppermost) surface, in the case of a slab geometry normal to \hat{x} [Fig.3.4 (a-c)] and when the growth direction is along \hat{z} [Fig.3.4 (b-d)].

When the growth direction is normal to \hat{x} , two situations occur depending on whether the system is in type I or type II regime: If the system is a type I WSM ($\gamma = 1$) as in Fig. 3.4 (a), the density of states projected in this direction displays degenerate Fermi arcs connected along k_z . Indeed, this scenario shows two copies of the time reversal breaking case where two Weyl nodes are connected by one Fermi arc. On the other hand, if the tilting of the Weyl cones increases to the type II regime ($\gamma = 3$) in Fig.3.4(c), large Fermi pockets' projections emerge in the system as a result of the reorientation of the Fermi arcs along the k_x direction. Nonetheless, as the value of γ continuously increases, the enlargement of the Fermi pockets surrounding the nodes leads to a merging of two pockets in a trivial state, screening out the effect of the Fermi arc connection as we corroborated in Fig.3.3. In contrast, a slab developed with normal along \hat{z} illustrates a complementary situation: On one side, when we take a type I WSM as in Fig.3.4(b), the two Weyl nodes are disconnected since the Fermi arc connects points along k_z rather than k_x . In contrast, when we consider the type II regime as in Fig. 3.4(d) the density of states increases surrounding the center of the track state's projections, but its magnitude is in average notably smaller than in Fig.3.4(c). The density of states in the type II regime depicted in Figs.3.4 (c-d) is basically a result of a high contribution coming from trivial states (Fermi pockets, track states, etc) whose origin is the change in connectivity of the Weyl nodes going from k_z to k_x .

3. Influence of the Surface States on the Nonlinear Hall Effect in Weyl Semimetals –
 3.3. Model Calculations and Discussion

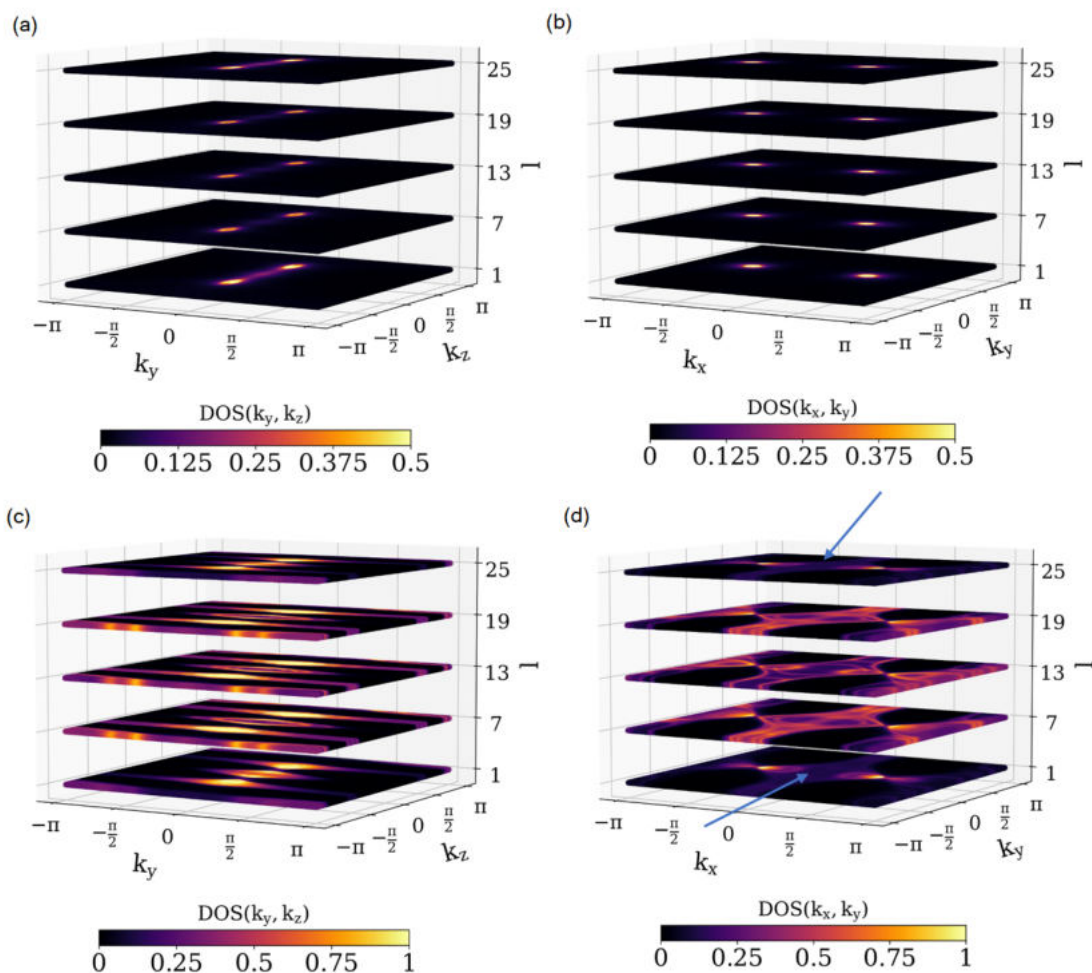


Figure 3.4. – Layer resolved density of states for the relevant configurations with non-vanishing **BCD**. Here we consider a system of 25 layers in two different scenarios, revealing the difference between type I ($\gamma = 1$) and type II ($\gamma = 3$) regime: When the growth direction is along \hat{x} , we illustrate the density of states for a given layer l in the case of $\gamma = 1$ (a) and $\gamma = 3$ (c). In the same form, we report the projected density of states when the slab is normal to \hat{z} , emphasizing on the differences between $\gamma = 1$ (b) and $\gamma = 3$ (d). We indicate the center of the track states in Fig.3.4(d) with blue arrows.

3. Influence of the Surface States on the Nonlinear Hall Effect in Weyl Semimetals – 3.3. Model Calculations and Discussion

In the following we present the second order conductivity normalized by the number of layers. For systems consisting of $L = 20, 25, 40$ layers and fixing $\mu = 0.2$ we compute the BCDs $D_{zx}^{(\hat{x})}$ ($D_{xz}^{(\hat{z})}$), when the growth direction is along \hat{x} (\hat{z}), as a function of the tilting parameter. We add our bulk calculations for the model as a reference, which matches qualitatively to previous reports on the same model [100]. Furthermore, we also compute the ratio between the BCD and the density of states for the same instances described earlier. A summary of our findings is given in Fig.3.5. In the bulk system, which is depicted in black lines, the BCDs allowed by symmetry are evidently different. When the electric field is applied along \hat{z} and we compute the BC along \hat{x} , the corresponding dipole D_{zx} follows a Gaussian behavior in the γ range. It is very small at small γ since the tilting of the nodes is very small. Besides, it reaches a peak close to $\gamma = 3$ and decreases towards zero when we increase γ . This pattern can be assigned by the implicit symmetry on the tilting of the Weyl cones as we increase γ .

From Fig.3.5 (a-b) is clear that for a type I WSM the ratio between the Berry curvature dipole in the bulk and in the slab is proportional to the number of layers, which was previously predicted from geometrical considerations [197]. In contrast, for a type II WSM the BCD displays an enhancement of its magnitude depending on the slab under consideration: Whereas in Fig.3.5(b) the profiles of the dipole in both slab and bulk converges reasonably well even for a small number of layers, they substantially differ when considering a slab normal to \hat{x} as depicted in Fig.3.5(a). The density of states plotted accordingly in Fig.3.4 suggests that the difference between the BCD profiles rely on the number of states displayed on each surface. Whereas a type I WSM displays the projections of the Weyl nodes and Fermi arcs (if there is any) on each surface, the type II regime experiences a dramatic increase on the density of states due to the enlargement of the Fermi pockets surrounding the nodes and the emergence of trivial track states and other surface states. For these reasons, the increase on the BCD in a slab normal to \hat{x} compared to a slab normal to \hat{z} can be attributed to the Fermi pocket's projections on the system. On the other hand, the track states' projections and other trivial states do not affect abruptly the behavior of the dipole in comparison with the bulk. This phenomenology leads to a thickness dependence on the NLHE depending on the slab chosen, when the WSM is in type II regime.

We support our argument by showing the ratio between the dipole and the density of states for each slab under consideration. If our slab is normal to \hat{x} , this ratio decreases with the number of layers [Fig.3.5(c)], corroborating that the increase on the BCD in type II WSM is accompanied by a magnification on the relative number of states at the surface rather than the bulk. In contrast, if the slab is normal to \hat{z} [Fig.3.5(d)] the ratio becomes essentially a constant, revealing that the impact of the number of states in the second-order transport is negligible in comparison with its \hat{x} -cut sibling. The previous arguments show a thickness dependence on the NLHE driven by the BCD when the slab under consideration exhibits strong surface states. This behavior is induced by the transition between type I and type II regime in WSMs, which at the same time is the origin of the reconnection of Fermi arcs in this system.

3. Influence of the Surface States on the Nonlinear Hall Effect in Weyl Semimetals –
 3.3. Model Calculations and Discussion

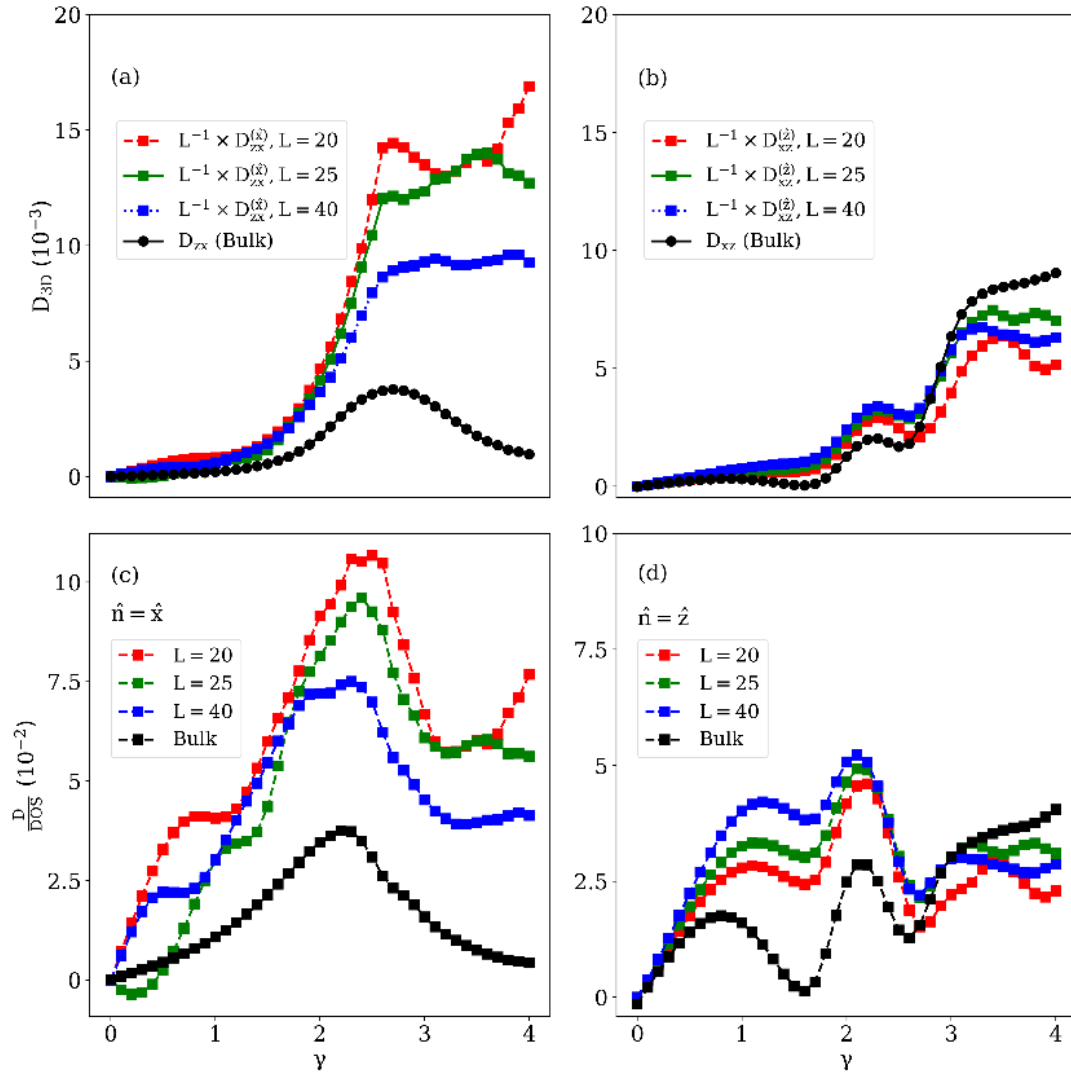


Figure 3.5. – Considering the case $\mu = 0.2$, we report in (a) the BCD of a slab with normal along \hat{x} , for different number of layers and as a function of the tilting parameter. We show the similar situation for a slab geometry normal to \hat{z} (b), putting on black lines the profiles for the dipole coefficients in the bulk case as a reference. (c) Ratio between the dipole and the density of states for the slab systems built with normal $\hat{n} = \hat{x}$, with its counterpart when the growth direction is along \hat{z} in panel (d).

3. Influence of the Surface States on the Nonlinear Hall Effect in Weyl Semimetals – 3.3. Model Calculations and Discussion

Further insight on the behavior of the NLHE can be extracted from a layer resolution on this system. Our results are reported in Fig.3.6 for the slabs normal to \hat{x} (black lines) and \hat{z} (red lines), taking into account the two exemplary cases $\gamma = 1$ (a) and $\gamma = 3$ (b) for a slab geometry of $L = 25$ layers. As we notice from Fig.3.6(a), the slab geometries offer a strong difference on the NLHE at the edges, i.e, at the top $l = 1$ and bottom $l = 25$ layers, when the system is in the type I regime. In view of Fig.3.4(a-b), we attribute this outcome to the presence (or absence) of degenerate Fermi arcs. On the other hand, for a type II WSM, the Berry dipole coefficient at the central layer ($l = 13$) is larger in the \hat{x} -cut rather than the \hat{z} -cut. Moreover, the maximum magnitudes of the conductivity are reached at layers underneath the surfaces ($l = 5$ and $l = 21$) instead of the surfaces itself. It is worth mentioning that topologically trivial surface states should be sensitive to the presence of surface disorder. In contrast, topological surface states such as Fermi arcs should be weakly affected by it. We leave the development of this inquiry for future studies.

We have taken the transport calculations in our model away from the neutrality point, for a fixed value of the chemical potential at $\mu = 0.2$. Hence, we might also wonder about the dipole profiles as a function of the energy, for a fixed value of the tilting parameter. In Fig.3.7 we plot the BCD for different number of layers, when the system is in type I (a-b) or type II (c-d) for the \hat{x} (a-c) and \hat{z} (b-d) cut. As we can verify from Figs.3.7 (a-b), the profiles follow qualitatively the tendency proposed by the reference calculation of the 3D configuration. Nevertheless, the difference is abrupt as we move to the type II regime in Fig.3.7(c), which is not appearing in Fig.3.7(d). Therefore, our model computations in the energy range holds in the same way as in the γ range. We will add realistic simulations in WTe₂ in the next pages that corroborate our predictions based on our model outcomes.

Finally, let us comment on the possible techniques adopted to detect the NLHE in experiments. Since the surface states enhance the conductivity in finite slab geometries when we cut along \hat{x} and the system is in the type II regime, a large value of the conductivity is expected to be measured experimentally in this case, in comparison with the \hat{z} cut. As we can verify from Fig.3.8 when we compute the dipole coefficient as a function of the thickness, for the exemplary case $\gamma = 3$ and $\mu = 0.2$, the \hat{x} - cut reaches large values at small thicknesses, whereas the \hat{z} -cut profile converges monotonously to the bulk value and its maximum is smaller than the \hat{x} -cut for the range of thicknesses explored.

3. Influence of the Surface States on the Nonlinear Hall Effect in Weyl Semimetals –
 3.3. Model Calculations and Discussion

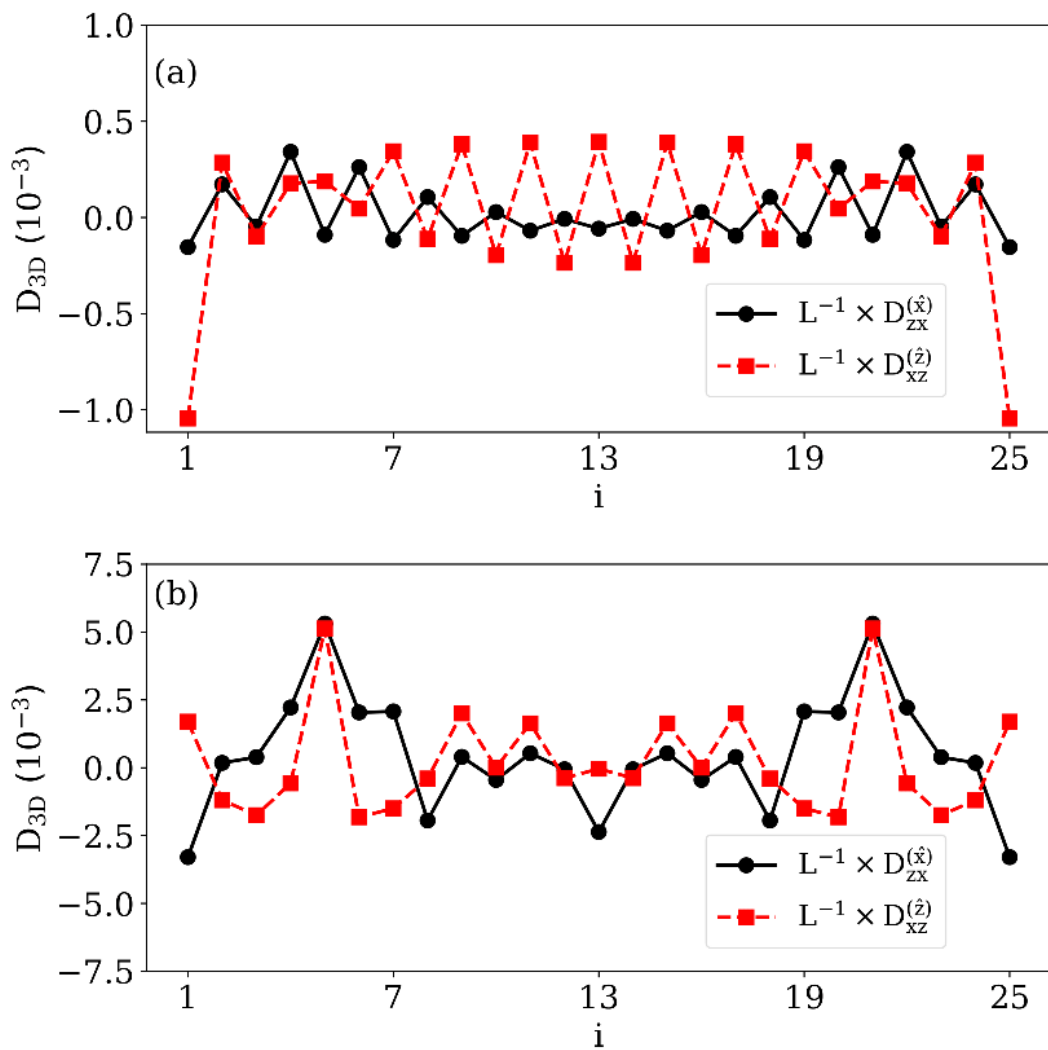


Figure 3.6. – Layer resolution of the BCD for a system of 25 layers for a slab normal to \hat{x} (black lines) or \hat{z} (red lines), fixing the chemical potential at $\mu = 0.2$. We depict the cases $\gamma = 1$ in panel (a) and $\gamma = 3$ in panel (b).

3. Influence of the Surface States on the Nonlinear Hall Effect in Weyl Semimetals –
 3.3. Model Calculations and Discussion

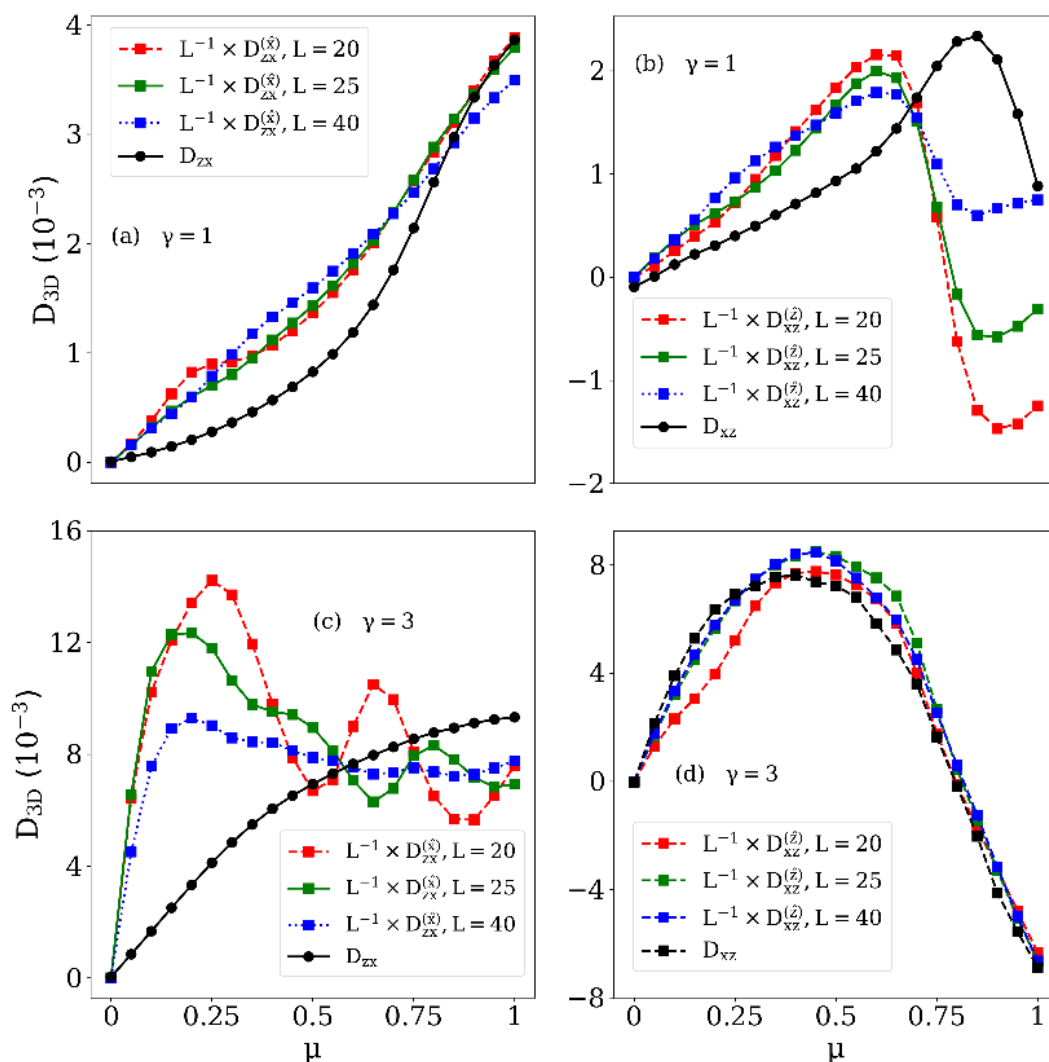


Figure 3.7. – Energy dependence of the BCD in the slab geometries, for different numbers of layers. For the type I regime ($\gamma = 1$), we follow the dipole coefficient for a slab normal to \hat{x} in (a) and normal to \hat{z} in (b). Similarly, the nonlinear response is plotted as a function of the energy for a type II WSM when the growth direction is along \hat{x} (c) and along \hat{z} (d). We include the corresponding dipole components for the 3D configuration in black lines.

3. Influence of the Surface States on the Nonlinear Hall Effect in Weyl Semimetals –
 3.3. Model Calculations and Discussion

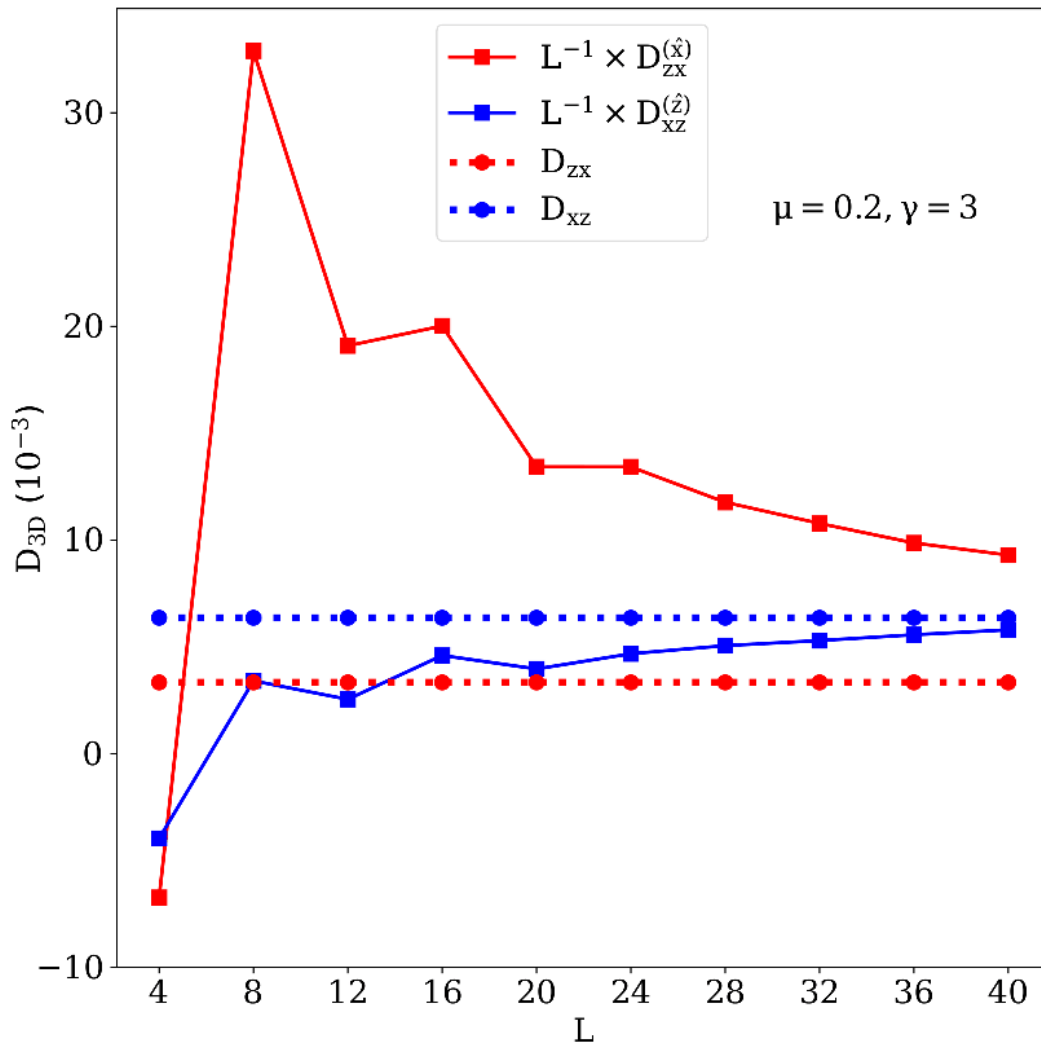


Figure 3.8. – For the exemplary case $\mu = 0.2$ and $\gamma = 3$, we present the BCD as a function of the number of layers of the slab, for the slab geometries with normal along \hat{x} (solid red lines) and along \hat{z} (solid blue lines). The dotted lines refer to the value of the dipole in the 3D configuration: D_{zx} in red lines and D_{xz} in blue lines.

3.4. Realistic Simulations in WTe_2 Slabs

For the sake of completeness, I now present the results obtained from first principles calculations. These calculations were performed by Dr. Armando Pezo, postdoc in the team. Although I did not perform the calculations myself, I participated actively in the development of this aspect of the project and in the discussion of the data. Let us now consider a realistic system, WTe_2 in its orthorhombic phase, and compute the NLHE from first principles. WTe_2 is a well-known type II WSM [198, 199], in which NLHE has been originally reported [200, 36]. For the density functional theory simulations [201, 202], the Perdew-Burke-Ernzerhof [203] exchange correlation functional was used. The geometry optimizations were performed using a plane-wave basis as implemented in the Vienna Ab-initio Simulation Package (VASP) [204, 205]. Besides, 400 eV for the plane-wave expansion cutoff was employed, with a force criterion of $5 \mu eV \text{ \AA}^{-1}$ and a reciprocal space sampling containing $16 \times 16 \times 14$ k-points within the Brillouin zone. The ionic potentials were described using the projector augmented-wave (PAW) method [206], post-processing calculations were performed using WannierTools [207]. The band structure is sketched at Fig.3.9 with the inset displaying the unit cell. The band crossings are located within the X- Γ path in momentum space, such that the Fermi level was set to zero near this region. With this consideration, the Weyl points were projected on selected surfaces, i.e., \hat{z} (corresponding to the (001) direction) and \hat{x} (corresponding to the (100) direction).

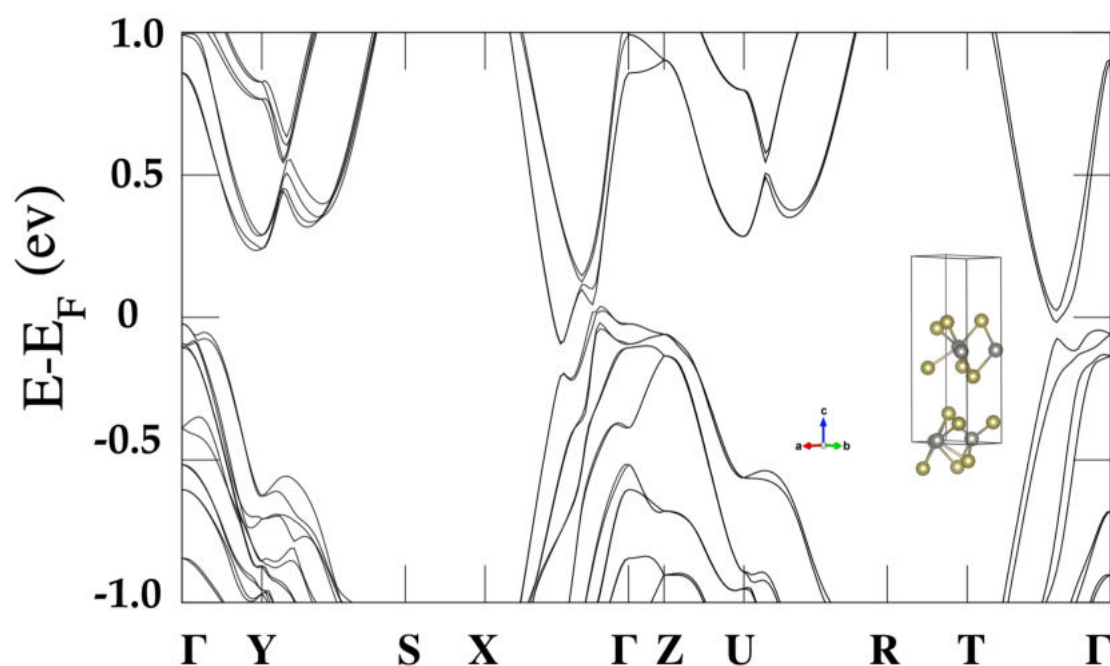


Figure 3.9. – Bulk band structure for the type II WSM obtained from first principle calculations, where the inset displays the unit cell.

3. Influence of the Surface States on the Nonlinear Hall Effect in Weyl Semimetals –
 3.4. Realistic Simulations in WTe_2 Slabs

In the same way as we did it for the model calculations, the density of states was obtained in the middle (bulk) layer and the uppermost layer of slab geometries containing 25 layers. In Fig.3.10 we illustrate the cuts along \hat{z} (a-b) and \hat{x} (c-d). As we can see from Figs.3.10(a-b), the projected density of states is larger at the surface than the bulk, especially close to the Γ point. Furthermore, based on the findings given in Figs.3.10(c-d), the opposite situation can be deduced in the slab with normal along \hat{x} . In view of the lattice model calculations, we infer that the conductivity coefficients for the slab along \hat{z} should exhibit an enhancement due to the influence of the surface states, whereas the geometry normal to \hat{x} should be less sensitive to the Fermi arc diversity in the sample.

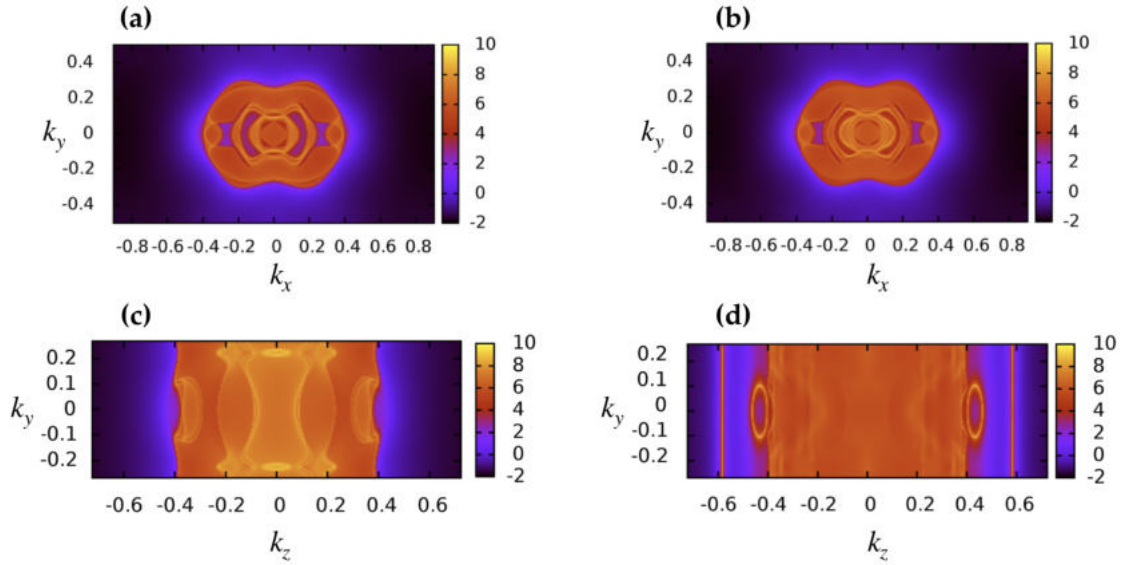


Figure 3.10. – Density of states at the Fermi level projected on the bulk (a,c) and top surfaces (b,d) for a slab geometry of 25 layers. Upper panels are related to a slab normal to \hat{z} and lower panels to a slab normal to \hat{x} .

Knowing the projected density of states for each slab relevant to the problem, the BCD was computed within a grid of 500×500 in the Brillouin zone as a function of the energy, for three exemplary cases moving between $L = 15$ and $L = 25$ layers. The profile computed in the bulk (dashed lines) is included for the sake of comparison. In addition, these results are accompanied with their corresponding band structures in Fig.3.11 as well. For a slab normal to \hat{z} direction [3.11(a-b)], we observe that the BCD strikingly depends on the slab thickness, reflecting the influence of the surface states. In fact, for an infinite thick slab the peaks presented below the Fermi level and associated with the surface states disappear. When the slab is normal to \hat{x} [3.11(c-d)], the surface states cannot be clearly distinguished in the band structure, which, at the same time, is dominated by the bulk states. Regarding the dipole calculations in panel (d) of the figure mentioned above, it is interesting to notice that the BCD follows the same behavior as a function of the layer number, revealing its low sensitivity to the slab thickness. Moreover, for an infinitely thick slab the BCD preserves the overall

3. Influence of the Surface States on the Nonlinear Hall Effect in Weyl Semimetals –
 3.4. Realistic Simulations in WTe_2 Slabs

structure. The results presented here corroborate our predictions developed through the model analysis and confirms a thickness dependence related to the surface states on the NLHE in realistic materials.

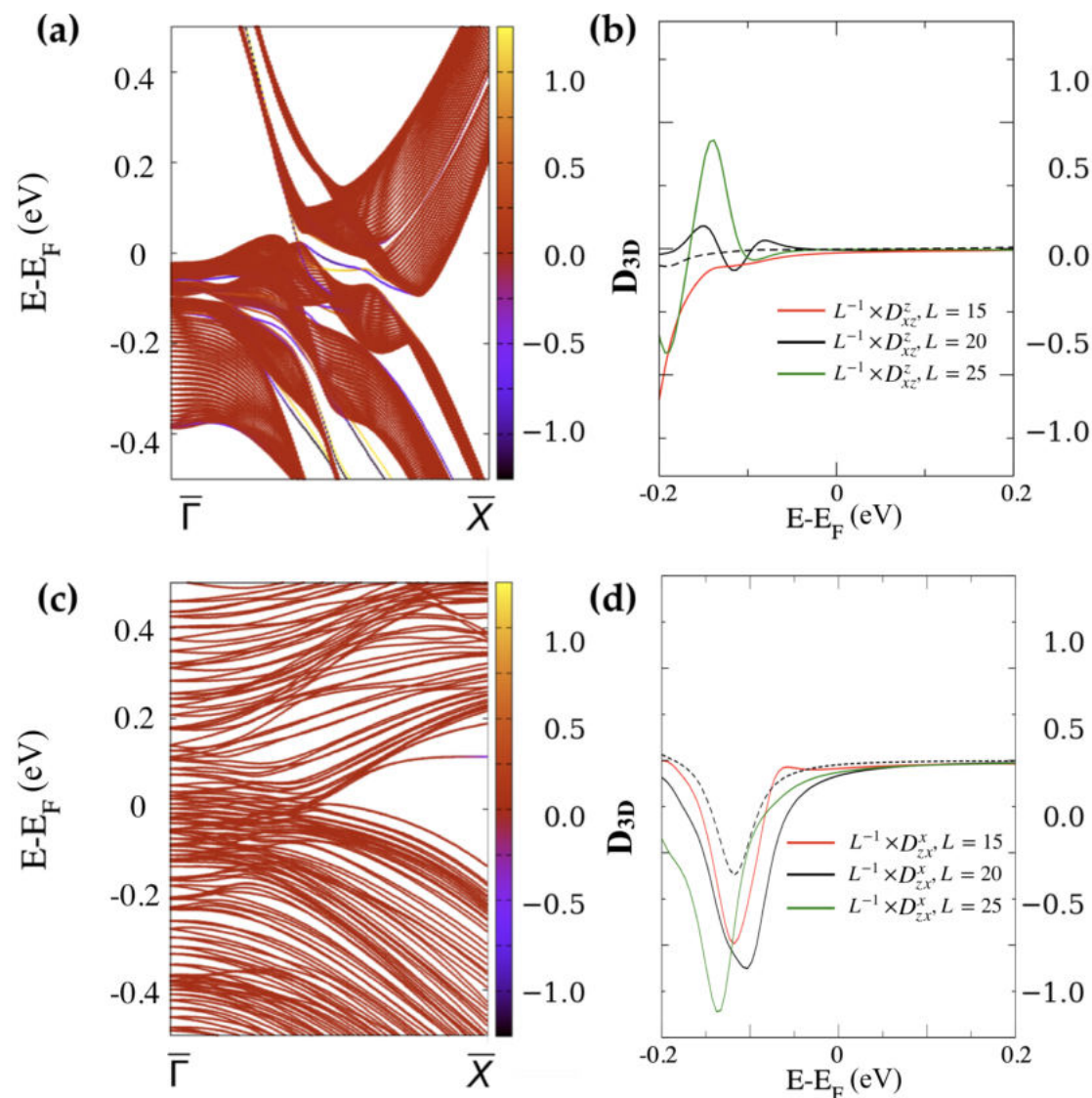


Figure 3.11. – Band structure for a system of 25 layers (a-c) and BCD calculations in the energy range and for different thicknesses in terms of their number of layers (b-d), when the slab is normal to \hat{z} (upper panels) and \hat{x} (lower panels). The color bar in (a-c) represents the projections on the bottom (-1) and top (+1) layers.

3.5. Main Conclusions and Prospects

We demonstrate that in the context of non-magnetic WSMs the NLHE driven by the BCD is strongly impacted by its surface states, independently of their topological nature. Moreover, the WSM model analyzed here suggests that a key ingredient to enhance the value of the second-order conductivity coefficient is the relative number of states at the surface compared to the bulk, which is mainly produced by the enlargement of the trivial Fermi pockets surrounding the nodes in the slabs created. Besides, although they do not influence severely the NLHE, the emergence of track states are a signature of the transition between type I and type II regimes that exhibit profound differences in terms of Hall transport: Whereas in type I regime the BCDs allowed by symmetry scale with the number of layers, as predicted by [197], the type II regime displays a stronger thickness dependence on the NLHE in the slab that possesses a large number of surface states. The thickness dependence on the NLHE in realistic materials is corroborated by computations in thin films of WTe₂, establishing a remarkable feature that could be useful for experimental applications.

The knowledge established in this work opens interesting perspectives and raises new questions: First, one could ask about a suitable model or realistic system offering a BCD that lies in the plane of the Fermi arcs directly. If that would be the case, it would be interesting to create a slab geometry in the plane of the Fermi arcs and compute a layer resolution of the BCD across the different layers, comparing the contribution of the surface with respect to the bulk. We expect to observe similar results to the ones presented in this Chapter, namely, that the most relevant contributions would come from non-topological surface states. Nevertheless, we would be able to obtain a direct measurement on how the Fermi arcs impact the BCD. Second, since the BCD is extremely sensitive to the relative number of states at the surface, more than their topology, it is worth a new exploration of suitable candidates for larger values of NLHE. It is quite intriguing that the topological surface states do not dramatically affect the NLHE in WSMs, since the transition between type I and type II regime is a process that involves a tilting in the Weyl cones, whose apexes are indeed topological objects. Therefore, one valid question is how to artificially generate these surface states away from topological matter and whether one can control it. Is it possible to elaborate a mechanism to produce a large number of states in slab geometries?

If we look at the broader picture concerning second order Hall transport, plethora of topics are still unclear. In general, inversion symmetry breaking is accompanied by a ferroelectric polarization, opening a wide class of interesting materials with switchable NLHE. In addition, since inversion symmetry breaking can arise at the interface, one can envisage to design multilayers with optimal NLHE. This latter aspect is discussed in Chapter 1. When we look at topological materials, a Dirac material with inversion symmetry breaking and NLHE as the leading order response remains difficult, specially because they preserve PT symmetry in general. A proper example would be new antiferromagnets with non-symmorphic symmetries that indeed would be able to display topologically protected Dirac surface states, going one step forward from the

3. *Influence of the Surface States on the Nonlinear Hall Effect in Weyl Semimetals –*
3.5. *Main Conclusions and Prospects*

case of CuMnSb [103]. Although it was already documented that topological materials with Dirac surface states show quantum frequency doubling [153], for instance, it has also been explained that this effect should arise from extrinsic mechanisms, thus inviting us to propose that a Dirac material with BCD could represent a striking novelty in the field. In the context of WSMs, our thought goes in the direction of nodal line materials and similar systems. Last but not least, the temperature dependence of the Hall coefficients is something worth to explore in order to identify new materials that could achieve NLHE at room temperature. The question has been addressed from the experimental standpoint by designing new measurements on the Dirac material BaMnSb₂ [208] and MoTe₂ [209] during this year, but a profound understanding of this avenue is still in progress.

4. Magneto-optical Probe of Non-Equilibrium Orbital Magnetism via the Second-Order Hall effect

Summary

4.1. Introduction	86
4.2. General Theory	89
4.2.1. Magneto-Optics	89
4.2.2. Decomposition of the Non-Equilibrium Orbital Magnetization	91
4.3. WTe ₂ Bilayer	91
4.3.1. Definition of the Model System	91
4.3.2. Model Calculations	93
4.3.3. Comparison With Experiments	96
4.3.4. Orbital Edelstein Coefficients Versus Berry Curvature Dipole in WTe ₂	97
4.4. Nb _{2n+1} Si _n Te _{4n+2} Monolayer	99
4.4.1. Model System	99
4.4.2. Model Calculations and Discussion	100
4.4.3. Orbital Edelstein Coefficients Versus Berry Curvature Dipole in Nb _{2n+1} Si _n Te _{4n+2}	104
4.5. Conclusions and Prospects	105

4.1. Introduction

Modern spintronics is based on the interconversion between charge and spin currents, either achieved via conventional ferromagnetic polarizers [210] or mediated by spin-orbit coupling [26, 123]. The latter mechanism is currently the center of attention of a research field called spin-orbitronics and that intends to harvest the spin-momentum locking present in materials with heavy elements, including 5d metals and topological materials. In recent years, it has been proposed that most of the flagship phenomena of spin-orbitronics, spin Hall effect [26] and Rashba-Edelstein effect [159], also exist at the level of the orbital moment, although not necessitating any spin-orbit coupling [211, 112, 212, 213]. This prediction opens wide perspectives

4. Magneto-optical Probe of Non-Equilibrium Orbital Magnetism via the Second-Order Hall effect – 4.1. Introduction

for materials research and device development as entire families of metallic compounds made of light elements, often cheap and abundant, could in principle host interconversion phenomena between charge currents and orbital currents [213, 214, 215, 216]. As a matter of fact, very recent experiments have demonstrated orbital phenomena of highest interest for microelectronics such as orbital torque [217, 218] and orbital magnetoresistance in materials such as CuOx.

A central difficulty that has not been solved to date concerns the means to detect orbital currents and accumulations. Ideally, since the orbital accumulation of electrons produces a non-equilibrium orbital magnetization, it can be detected by converting this non-equilibrium orbital signal into a chemical potential using a proximate magnetic layer for instance. This technique is typically used to detect spin accumulation in magnetic bilayers [219] or in nonlocal geometries [220]. When it comes to detect the orbital accumulation though, a difficulty arises. Indeed, assuming that this proximate ferromagnet is made out of transition metals, its magnetization mostly comes from the spin angular momentum because of orbital quenching [221, 222]. Therefore, one needs to first convert the orbital signal into a spin signal, typically via spin-orbit coupling, as achieved in Ref. [223]. In other words, the electrical detection of non-equilibrium orbital magnetization using a bilayer configuration requires the coexistence of spin-orbit coupling and magnetism. As a result, it is virtually impossible to selectively probe the orbital accumulation using electrical means only.

A promising alternative would be to use magneto-optical methods to directly probe the orbital accumulation without relying on any magnetic material or non-locality. As it is well known, the **magneto-optical Kerr effect (MOKE)** is routinely used to describe the electronic properties of magnetic materials (See [224, 225, 226, 227, 228] for a few examples) and image magnetic domains [229]. As a matter of fact, a large Kerr angle is highly desired to the fabrication of efficient optical memory devices. Within this frame, a large Kerr angle has been estimated in the family of compounds FeX (X= Co, Ni, Pd, Pt) [230, 231] and MnBi [232]. In topological materials such as **WSMs**, it has been proved the sensitivity of the Kerr angle to the location of the Weyl points [233]. This can be interpreted as a signature of the chiral anomaly when a non-magnetic Weyl system is subjected to a magnetic field [234]. Certain classes of antiferromagnets are also capable to break time reversal symmetry effectively, and thus they can exhibit linear **MOKE**. An example of this feature has been reported in the class of non-collinear antiferromagnets Mn₃X (X= Rh, Ir, Pt), where a large Kerr angle has been detected and compared to bcc Fe [235]. Moreover, sizable polar and longitudinal Kerr angles have been discovered in measurements of Mn₃Ge [236] (See also [66, 237]). Numerical simulations further agree that a large polar Kerr angle does not require a non-collinear structure, for instance, in the paradigmatic instance of bilayer MnPSe₃ [238].

A precise interpretation of the **MOKE** spectrum remains difficult as it is highly sensitive to the hybridization of the electronic states, the distribution of magnetic and non-magnetic elements and on the spin-orbit coupling. Nonetheless, **MOKE** has been successfully used to detect the nonequilibrium spin accumulation in GaAs [5],

4. Magneto-optical Probe of Non-Equilibrium Orbital Magnetism via the Second-Order Hall effect – 4.1. Introduction

Cu, Ag and Au [239, 240], Pt and W thin films [4] and Bi₂O₃ surface [241]. In these experiments, the spin-orbit coupling enters in two steps: (i) it enables the creation of non-equilibrium spin accumulation and (ii) it couples the circularly polarized light to the non-equilibrium spin magnetization.

In the case of a light metal, i.e., in the absence of spin-orbit coupling, orbital magnetization can be generated by two means: either through orbital Hall effect [211, 112], leading to orbital accumulation at the surface, or through orbital Rashba-Edelstein effect when inversion symmetry is broken [212, 164]. We propose that magneto-optical Kerr effect can be used to probe this non-equilibrium orbital magnetization, even in the absence of spin-orbit coupling, via the nonlinear anomalous Hall effect [31].

Before entering in further details, we emphasize that in ferromagnets the magneto-optical Kerr effect does not directly probe the magnetization itself, but it rather probes the anomalous Hall effect of magnetic materials. Indeed, as discussed in more details below, the Kerr angle is directly proportional to the anomalous Hall conductivity $\theta_k + i\phi_k \sim \sigma_{xy}/\sigma_{xx}$. Since the anomalous Hall effect is itself proportional to the magnetization component perpendicular to the plane of the sample, the Kerr rotation provides a hallmark of this measurement magnetization. A similar process occurs in antiferromagnets with broken effective time reversal symmetry such as Mn₃Sn for instance, that exhibits both anomalous Hall effect [34, 35] and magneto-optical Kerr effect [66]. In non-magnetic materials, the anomalous Hall effect vanishes due to the absence of a net magnetization. Nonetheless, as discussed in this Thesis, as long as inversion symmetry is broken, an anomalous Hall effect can emerge at *the second order* in the electric field [31, 36, 37], where the leading order contribution is proportional to the BCD (See Chapter 2). As discussed below, this second order Hall effect is in fact a companion effect to the non-equilibrium orbital magnetization [6]. Indeed, both effects only require inversion symmetry breaking and can emerge in the absence of spin-orbit coupling. Therefore, the existence of the second order Hall effect is an indirect signature of non-equilibrium orbital magnetization. Moreover, non-equilibrium orbital magnetization can be probed by magneto-optical Kerr effect via the second order Hall effect, even in the absence of spin-orbit coupling. The difference between the non-equilibrium spin accumulation and the second order Hall effect accompanied by a non-equilibrium orbital magnetization in two dimensional materials is illustrated in Fig.4.1

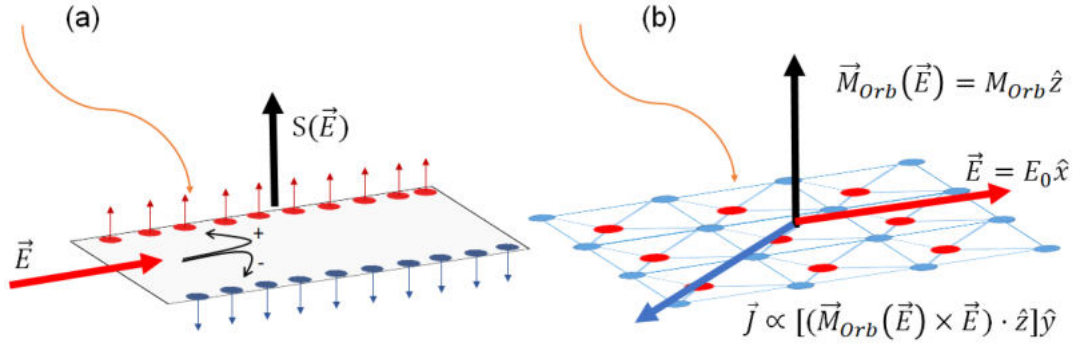


Figure 4.1. – (a) In a two dimensional material with spin-orbit coupling and under the presence of an external electric field, a non-equilibrium spin accumulation is generated due to a net flow of electrons with opposite spins, which can be detected through **MOKE**. (b) If the system is non-magnetic and non-centrosymmetric, and even in absence of spin-orbit coupling, a second order Hall effect is allowed by symmetry and its leading contribution is proportional to the **BCD**. Using magneto-optics one can probe that in fact the nonlinear Hall current is also proportional to the non-equilibrium orbital magnetization, which can serve as an evidence of non-equilibrium orbital accumulation in the material.

In this Chapter we analyze the current-driven magneto-optical Kerr effect in its polar configuration, considering two different platforms: A bilayer WTe_2 [90] and the newly introduced family of compounds $\text{Nb}_{2n+1}\text{Si}_n\text{Te}_{4n+2}$ [242]. Besides, we aim at understanding the connection between non-equilibrium orbital magnetization and second-order Hall effect driven by the **BCD** in the aforementioned two dimensional systems. Since these two materials are extended in the (x, y) plane, the second-order anomalous Hall effect is driven by the **BCD** elements D_{xz} and D_{yz} , associated with an orbital magnetization perpendicular to the plane.

4.2. General Theory

4.2.1. Magneto-Optics

Without loss of generality, let us take into account the magneto-optical Kerr effect in its polar version [229]. For this case, the electric permittivity tensor has the following form in two dimensions [231]

$$\epsilon = \begin{pmatrix} \epsilon_{xx} & \epsilon_{xy} \\ -\epsilon_{xy} & \epsilon_{xx} \end{pmatrix}, \quad (4.1)$$

using $\epsilon_0 = 1$ to ease the notation. Under the application of a perpendicularly incident

4. Magneto-optical Probe of Non-Equilibrium Orbital Magnetism via the Second-Order Hall effect – 4.2. General Theory

light $\vec{E}_{ac} = \mathcal{E}_0 e^{i(\vec{k}\cdot\hat{z} - \omega t)}$ with frequency ω and circular polarization, the Kerr rotation angle θ_k and the ellipticity ϕ_k can be approximated in terms of the longitudinal (σ_{xx}) and transverse (σ_{xy}) optical conductivity [231]:

$$\theta_k + i\phi_k = \frac{\sigma_{xy}}{\sigma_{xx} \left(1 + \frac{4\pi i}{\omega} \sigma_{xx}\right)^{\frac{1}{2}}}. \quad (4.2)$$

The longitudinal conductivity in Eq.(4.2) can be accounted for through the Green function formula in Eq.(2.42)[144] with the substitution $\epsilon \rightarrow \epsilon + \hbar\omega$. On the other hand, the transverse optical conductivity can be defined as [243]

$$\sigma_{xy} = \frac{e^2}{\hbar} \int \frac{d^2k}{(2\pi)^2} \sum_{nm} \tilde{\Omega}_{nm\mathbf{k}}^{(z)} (f_{n\mathbf{k}}^{(0)} - f_{m\mathbf{k}}^{(0)}), \quad (4.3)$$

where $\tilde{\Omega}_{n\mathbf{k}}$ is the BC,

$$\tilde{\Omega}_{n\mathbf{k}}(\omega) = i \sum_{m \neq n} \frac{\langle u_{n\mathbf{k}} | \hat{v}_{\mathbf{k}} | u_{m\mathbf{k}} \rangle \times \langle u_{m\mathbf{k}} | \hat{v}_{\mathbf{k}} | u_{n\mathbf{k}} \rangle}{(\epsilon_{n\mathbf{k}} - \epsilon_{m\mathbf{k}})^2 - (\hbar\omega + i\Gamma)^2} = \sum_{m \neq n} \tilde{\Omega}_{nm\mathbf{k}}. \quad (4.4)$$

In the limit $\hbar\omega \rightarrow 0$ Eq.(4.4) converges to the BC presented in Chapter 2, which is given by Eq.(2.15) [15]. From Eq.(4.3) it is clear that if the system is time-reversal symmetric then $\sigma_{xy} \rightarrow 0$ and thus the magneto-optical Kerr effect completely vanishes at equilibrium. Notwithstanding, when time reversal is preserved and inversion symmetry is absent, a non-equilibrium magneto-optical Kerr effect is allowed by symmetry, revealing the underlying generation of a non-equilibrium magnetization in the process. Now, let us suppose that an additional d.c. electric field \vec{E}_0 is applied in the sample. As a matter of fact, the inclusion of an auxiliary d.c. electric field has been utilized recently to prove second-harmonic generation, rather than magneto-optical effects, in inversion symmetric Dirac and Weyl semimetals [244]. Following the rationale developed by Sodemann and Fu [31] for the second order anomalous Hall effect and Yoda and Murakami [164] for the non-equilibrium orbital magnetization, within the relaxation time approximation, we deduce that [47]

$$\sigma_{xy} = \frac{e^3 \tau \vec{E}_0}{\hbar^2} \int \frac{d^2k}{(2\pi)^2} \sum_{nm} \Omega_{nm\mathbf{k}}^{(z)} (\partial_{\mathbf{k}} f_{n\mathbf{k}}^{(0)} - \partial_{\mathbf{k}} f_{m\mathbf{k}}^{(0)}). \quad (4.5)$$

Therefore, the combination of Eqs.(4.5) and (4.1) indicates that the non-equilibrium magneto-optical Kerr effect is proportional to an a.c. Berry curvature dipole [31] [the integral in Eq.(4.5)], which in fact is the leading order contribution to the second order optical conductivity at small frequencies [85]. As such, non-equilibrium magnetization, second-order Hall currents and non-equilibrium magneto-optical Kerr effects are companion phenomena in non-centrosymmetric non-magnetic materials and heterostructures. In the calculations below, we apply this theory on two instances defined in two dimensions. In addition, we complement the Kerr angle obtained with an analysis of the compatibility between the symmetries of the non-equilibrium orbital magnetization and the nonlinear Hall effect driven by the BCD.

4.2.2. Decomposition of the Non-Equilibrium Orbital Magnetization

As a complementary evidence of the connection between the non-equilibrium orbital magnetization and the second order Hall effect driven by the BCD, let us consider those quantities in the limit $\omega \rightarrow 0$. From Eqs.(2.19,2.25,2.11), the orbital Edelstein coefficients can be written as follows:

$$\begin{aligned}
 \alpha_{ij}(\mu) &= \int_{BZ} \frac{d^2k}{(2\pi)^2} \sum_n m_{nk}^j v_{nk}^i \partial_{\epsilon_{nk}} f_{nk} \\
 &= - \int_{BZ} \frac{d^2k}{(2\pi)^2} \sum_{m \neq n, n} i(\epsilon_{nk} - \epsilon_{mk}) \left(\frac{\langle u_{nk} | \hat{v}_{\mathbf{k}} | u_{mk} \rangle \times \langle u_{mk} | \hat{v}_{\mathbf{k}} | u_{nk} \rangle}{(\epsilon_{nk} - \epsilon_{mk})^2} \right)_i v_{nk}^j \delta(\epsilon_{nk} - \mu) \\
 &= - \int_{BZ} \frac{d^2k}{(2\pi)^2} \sum_n \left(\epsilon_{nk} [\vec{\Omega}_{nk}]_i - [\vec{b}_{nk}]_i \right) v_{nk}^j \delta(\epsilon_{nk} - \mu), \\
 &= \mu D_{ji}(\mu) + \mathcal{B}_{ji}(\mu),
 \end{aligned} \tag{4.6}$$

where

$$\vec{b}_{nk} = i \sum_{m \neq n} \frac{\epsilon_{mk} \langle u_{nk} | \hat{v}_{\mathbf{k}} | u_{mk} \rangle \times \langle u_{mk} | \hat{v}_{\mathbf{k}} | u_{nk} \rangle}{(\epsilon_{nk} - \epsilon_{mk})^2}. \tag{4.7}$$

As we can see from Eq.(4.6), the non-equilibrium orbital magnetization can be divided in two contributions: A term linear in the chemical potential and proportional to the BCD, and a term that is nonlinear in μ arising from an effective magnetic field with the same symmetries as the BC and the orbital magnetic moment. Remarkably, this expression goes one step forward from previous studies relating BC and orbital magnetic moment in the vicinity of the gap [90] and for two-band systems with particle hole symmetry [140]. In the next sections, we also analyze this decomposition for the electric-induced orbital magnetization in the instances of the minimal model of WTe₂ Bilayer and in the Nb_{2n+1}Si_nTe_{4n+2} monolayer.

4.3. WTe₂ Bilayer

4.3.1. Definition of the Model System

In order to illustrate our theory, we start by computing θ_k and ϕ_k in the exemplary case of a model system describing a WTe₂ bilayer [90]. From an experimental viewpoint, it has been observed that this material displays strong signatures of non-linear Hall effect at the second order in electric field [36, 37]. The minimal model is composed of four tilted Dirac Hamiltonians in the form [90]

4. Magneto-optical Probe of Non-Equilibrium Orbital Magnetism via the Second-Order Hall effect – 4.3. WTe₂ Bilayer

$$\mathcal{H}_{\mathbf{k}} = \begin{pmatrix} \mathcal{H}_{\mathbf{k}}^{d1} & \mathcal{P}_{\mathbf{k}} & 0 & \gamma \\ \mathcal{P}_{\mathbf{k}}^\dagger & \mathcal{H}_{\mathbf{k}}^{d1} & \gamma & 0 \\ 0 & \gamma & \mathcal{H}_{\mathbf{k}}^{d2} & \mathcal{P}_{\mathbf{k}} \\ \gamma & 0 & \mathcal{P}_{\mathbf{k}}^\dagger & \mathcal{H}_{\mathbf{k}}^{d2} \end{pmatrix}, \quad (4.8)$$

where $\mathcal{H}_{\mathbf{k}}^{di}$ describes the tilted Dirac cone located at \vec{K}_i (In the simulations below, we will consider that the Dirac cones are located at $\vec{K}_1 = 0.1\pi\text{\AA}^{-1}\hat{x}$ and $\vec{K}_2 = 0.15\pi\text{\AA}^{-1}\hat{x}$)

$$\mathcal{H}_{\mathbf{k}}^{di} = [E_i + t_i(k_x + K_i)]\hat{\sigma}_0 + v_i[k_y\hat{\sigma}_1 + \eta_i(k_x + K_i)\hat{\sigma}_2] + \frac{m_i\hat{\sigma}_3}{2}, \quad (4.9)$$

being $\hat{\sigma}_i$, $i = 1..3$ and $\hat{\sigma}_0$ is the identity matrix in two dimensions. In addition,

$$\mathcal{P}_{\mathbf{k}} = \begin{pmatrix} v_x k_x - i v_y k_y & 0 \\ 0 & -v_x k_x - i v_y k_y \end{pmatrix}, \quad (4.10)$$

is a matrix that contains the spin-orbit coupling strength v_x (v_y) along \hat{x} (\hat{y}), with γ an inter-layer coupling between the layers. We report the band structures of the model in Fig.4.2 for different values of v_x .

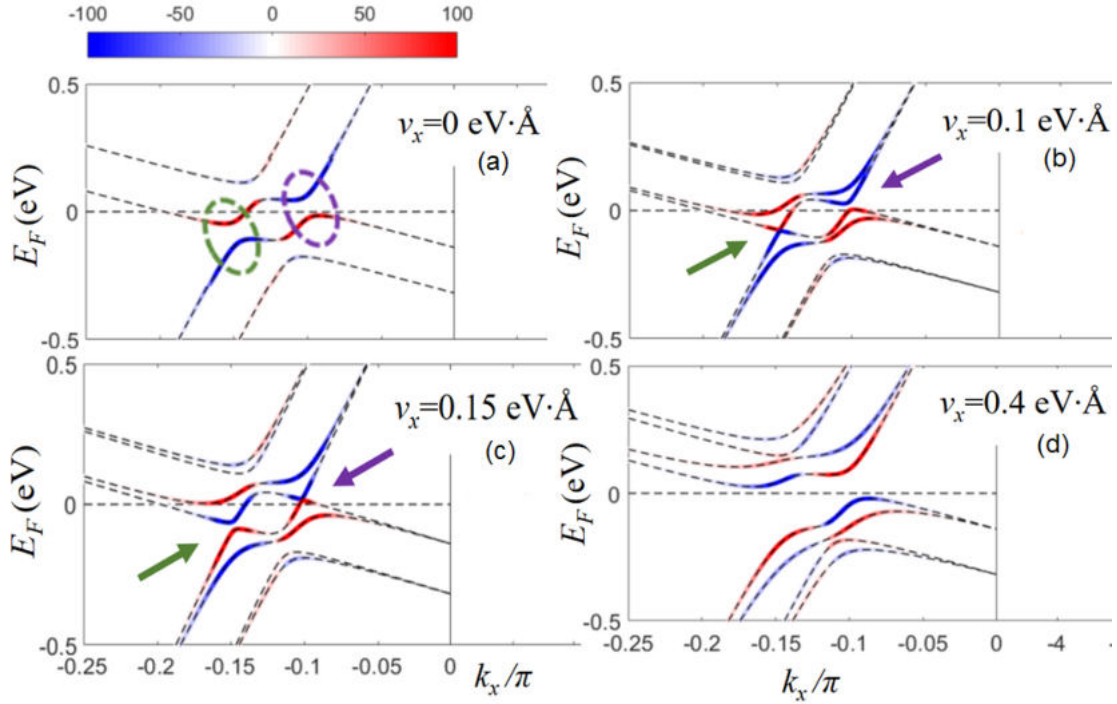


Figure 4.2. – Band structures and Berry curvature distributions of the model system defined by Eq.(4.8) for $k_y = 0$, with the representative values $v_y = 0$, $\gamma = 0.05$ eV, $K_1 = 0.1\pi \text{\AA}^{-1}$, $K_2 = 0.15\pi \text{\AA}^{-1}$, $v_1 = v_2 = 2$ eVÅ, $t_1 = t_2 = 1.5$ eV Å, $m_1 = m_2 = 0.1$ eV, $\eta_1 = -\eta_2 = -1$, $E_1 = 0.02$ eV, $E_2 = -0.08$ eV. The cases considered here are (a) $v_x = 0$, (b) $v_x = 0.1$ eV Å, (c) $v_x = 0.15$ eV Å and (d) $v_x = 0.4$ eV Å. Figure extracted and modified from [90].

4. Magneto-optical Probe of Non-Equilibrium Orbital Magnetism via the Second-Order Hall effect – 4.3. WTe₂ Bilayer

In this context, the BC related to the Hamiltonian defined in Eq.(4.8) is highly concentrated around the Dirac cones [90], thus we will perform our calculations in the rectangle $\mathcal{C} = [-\pi, \pi] \times [-\pi, \pi]$ for simplicity. The BC and the non-equilibrium orbital moment are perpendicular to the (k_x, k_y) plane and the system also has a mirror symmetry along k_y , thus only D_{xz} and α_{zx} are non-zero. Therefore, when the electric field is applied along \hat{x} and the BC is along \hat{z} , the resulting orbital magnetization is along \hat{z} and the Hall current flows along \hat{y} . From the symmetry perspective, we can interpret the second order Hall current along \hat{y} as the interplay between the non-equilibrium orbital magnetization along \hat{z} and the external electric field applied along \hat{x} . In the following calculations, we study the validity of this assertion by inspecting Eq.(4.6). As a complement, we compute the Kerr angle in a polar configuration as an additional evidence of the intimate connection between non-equilibrium orbital magnetization and second-order Hall effect driven by the BCD.

4.3.2. Model Calculations

In order to verify numerically the relation between electric-induced orbital magnetization and second order Hall effect driven by the BCD through magneto-optics, we perform the calculations of the a.c. BCD, the longitudinal conductivity and the Kerr angle for the model system defined in Eq.(4.8). We fix the electric field at 45° with respect to the \hat{x} axis to retain a polar configuration. Our results are depicted in Fig.4.3-4.4 as a function of the incoming light energy, for different values of v_x .

Firstly, as we can see from Figs.4.3(a-b), whereas the real part of the BCD converges to a finite but nonzero value at $\hbar\omega \rightarrow 0$, the imaginary part of the BCD goes to zero at zero frequency. Secondly, $\text{Re}(D)$ and $\text{Im}(D)$ are concentrated at energies $\hbar\omega \leq 250$ meV, approximately, because the distribution of the BC is enhanced around the degeneracy points of the bands, as it can be seen in Fig.4.2. Upon increasing the energy, the BC signal vanishes as well as the BCD. On the other hand, whereas the maximum values in the real and the imaginary parts of the BCD occur at $v_x = 0$, where the Dirac model exhibits two Dirac nodes around $\mu = 0$, at $v_x \neq 0$ the (smaller) local peaks move instead to the left side of the light energy range as we turn on spin-orbit coupling. We have to remark that from the definitions in Eqs.(4.4,4.5), although $\text{Re}(D)$ displays the same average magnitude as its d.c. counterpart [90], its behavior and that of $\text{Im}(D)$ are not precisely related to the peculiarities of the band structure (avoided band crossing and BC maxima). Indeed, we fixed the value of the chemical potential in the equilibrium distribution function at $\mu = 0$, and in the conductivity formula only the BC depends on the frequency. In the case of the longitudinal conductivity in Fig.4.3(c), we observe identical responses independently of the values of v_x , and all of them are increasing functions of the signal in terms of $\hbar\omega$.

From the BCD coefficients and the longitudinal conductivity reported in Figs.4.3, we can compute the Kerr angle and ellipticity for the same range of frequencies. Our results are displayed in Fig.4.4.

4. Magneto-optical Probe of Non-Equilibrium Orbital Magnetism via the Second-Order Hall effect – 4.3. WTe_2 Bilayer

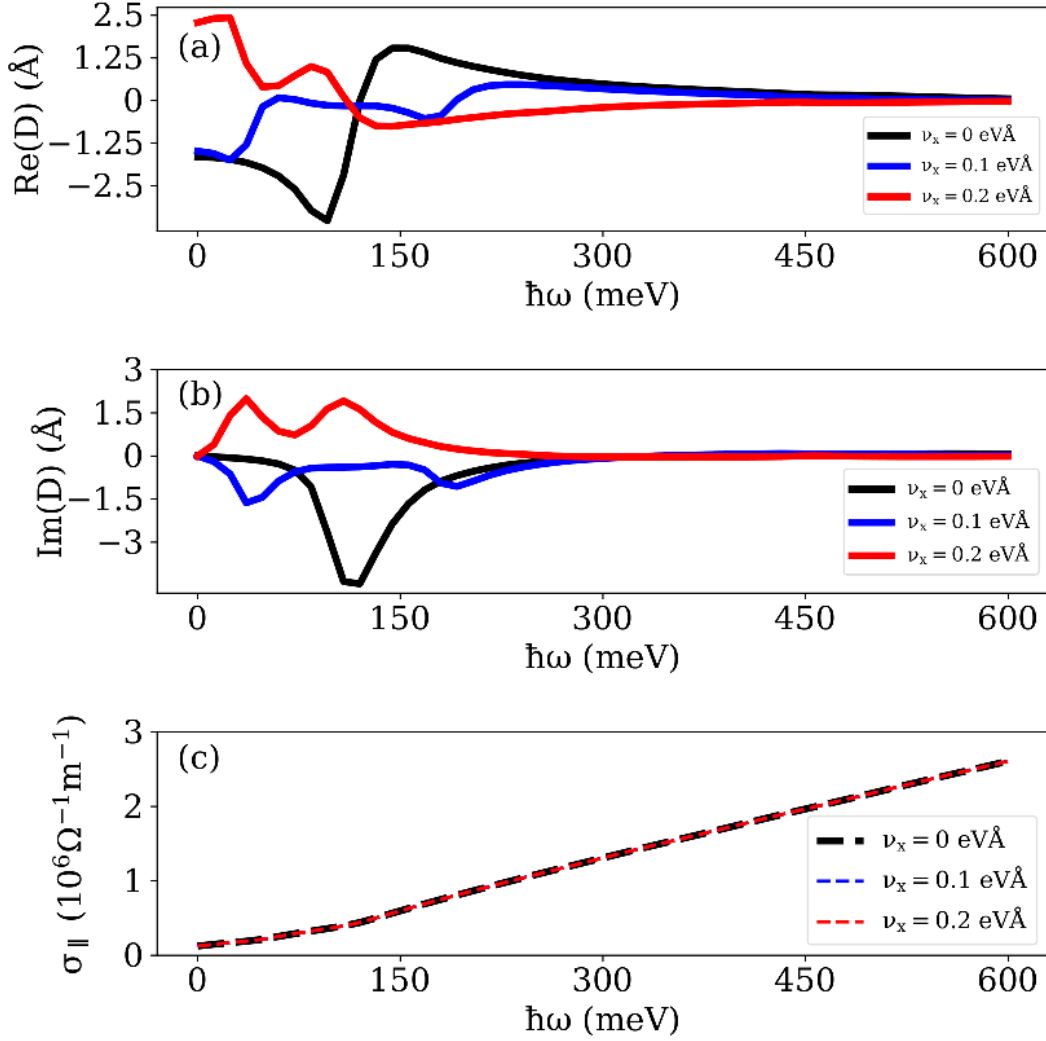


Figure 4.3. – Real (a) and imaginary (b) part of the a.c. BCD as a function of the light energy, for different values of ν_x and taking $\mu = 0$. (c) Corresponding longitudinal conductivity for the cases indicated in panels (a) and (b). For this simulation, we consider the representative values $\nu_y = 0$, $\gamma = 0.05$ eV, $K_1 = 0.1\pi \text{ \AA}^{-1}$, $K_2 = 0.15\pi \text{ \AA}^{-1}$, $\nu_1 = \nu_2 = 2$ eVÅ, $t_1 = t_2 = 1.5$ eV Å, $m_1 = m_2 = 0.1$ eV, $\eta_1 = -\eta_2 = -1$, $E_1 = 0.02$ eV, $E_2 = -0.08$ eV. In addition, we suppose an homogeneous disorder $\Gamma = 0.01$ eV.

4. Magneto-optical Probe of Non-Equilibrium Orbital Magnetism via the Second-Order Hall effect – 4.3. WTe_2 Bilayer

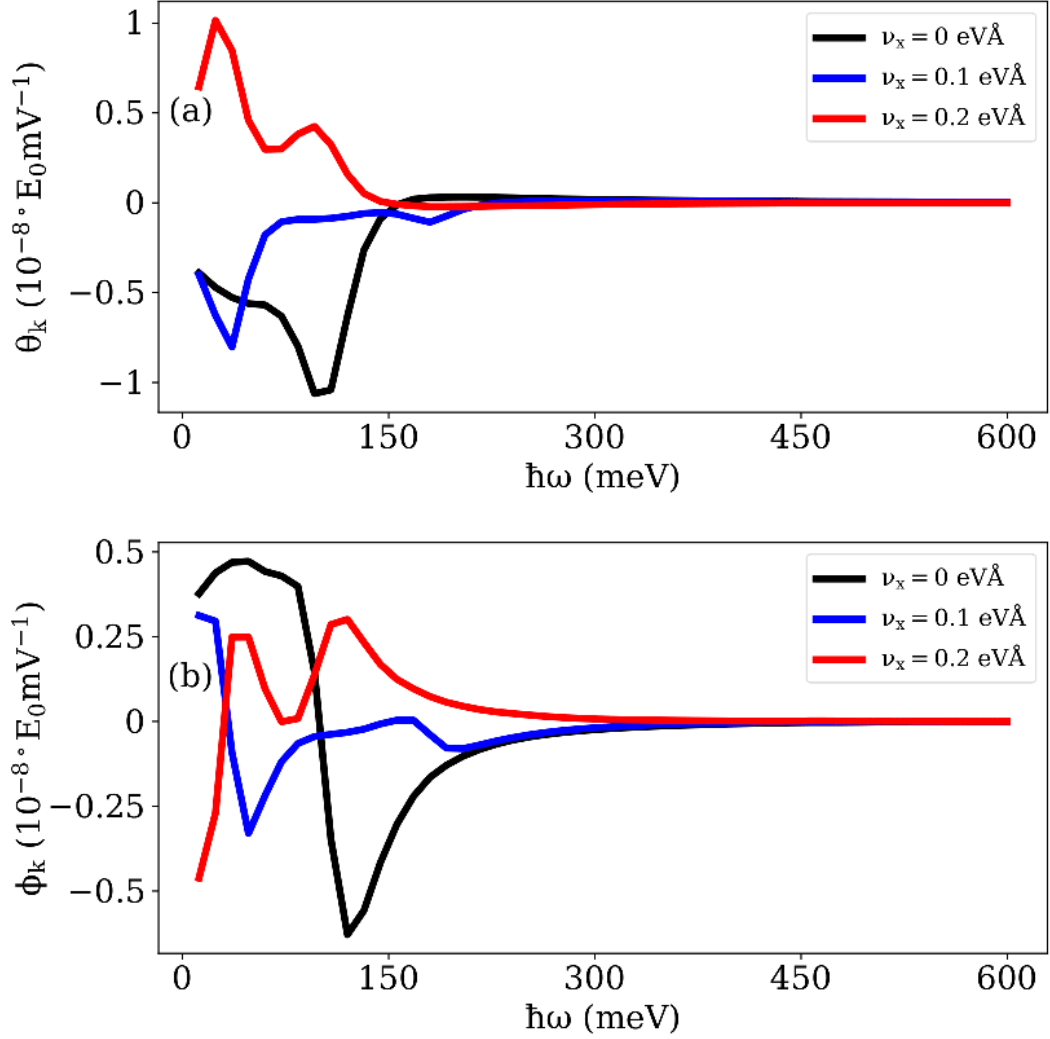


Figure 4.4. – Kerr rotation (a) and ellipticity (b) for the model Hamiltonian in Eq. (4.8), for different values of ν_x when $\mu = 0$. We take the same microscopic parameters that in Fig.4.3.

As we can see in the plots for the Kerr rotation [Fig.4.4(a)] and ellipticity [Fig.4.4(b)], at $\nu_x = 0$ the peak around 125 meV corresponds to the maximum of $\text{Re}(D)$ and $\text{Im}(D)$ for the same energy. For $\nu_x \neq 0$, the average value of θ_k and ϕ_k becomes large by increasing the spin-orbit coupling, suggesting that the Kerr angle can be controlled externally with a gate voltage.

4.3.3. Comparison With Experiments

In order to assess whether **MOKE** can be used in realistic experiments to probe the non-equilibrium orbital accumulation (and thus, non-equilibrium orbital magnetization and **BCD**), we now compare our results with experimental data obtained on different material platforms.. Our calculations show that WTe₂ exhibits an electrical **MOKE** efficiency of $\Theta_{WTe_2}/E \simeq 10^{-10}$ rad m V⁻¹, corresponding to a current **MOKE** efficiency of $\theta_{WTe_2}/j \simeq 10^{-11} - 10^{-12}$ rad cm² A⁻¹ (we took $\sigma_{WTe_2} \simeq 10^5 - 10^6$ Ω⁻¹m⁻¹ [200]).

Let us start by comparing these values with the results obtained in the seminal work of Kato et al. [5]. In their pioneering experiment, the authors performed the **MOKE** detection of spin Hall-induced spin accumulation in n-GaAs. Based on their data, they obtained an electrical **MOKE** efficiency of $\theta_{GaAs}/E \simeq 2 \times 10^{-10}$ rad m V⁻¹, which is comparable to our numerical results for WTe₂. This is rather surprising considering the very small spin-orbit coupling of GaAs. Although the present remark would require further investigation, we speculate that this unexpected value – among the largest reported to date -, could perhaps be related to the non-equilibrium orbital accumulation. We now turn our attention to MoS₂ monolayer under stress, studied by Son et al. [6]. They obtained a current **MOKE** efficiency of $\theta_{MoS_2}/j \simeq 9.1 \times 10^{-11}$ rad cm² A⁻¹, again comparable to our calculations for WTe₂ bilayer, although without strain.

We now complete the present analysis by considering non-equilibrium **MOKE** measurements in heavy metals, as achieved by Stamm et al. [4]. The authors found that for Pt, the current **MOKE** efficiency is $\theta_{Pt}/j \simeq 2 \times 10^{-15}$ rad cm² A⁻¹, whereas in W, $\theta_W/j \simeq 6 \times 10^{-15}$ rad cm² A⁻¹. More recently, **MOKE** has been used to detect the non-equilibrium orbital magnetization in a Ti layer [245], where the authors reported a current **MOKE** efficiency surprisingly similar to the case of heavy metals $\theta_{Ti}/j \simeq 10^{-15}$ rad cm² A⁻¹. Strikingly, the non-equilibrium **MOKE** effect is much smaller in these materials, in spite of their very strong spin-orbit coupling. Similarly, the electrical **MOKE** efficiency is $\theta_{Pt}/E \simeq 10^{-12}$ rad m V⁻¹, whereas in W, $\theta_W/E \simeq 3 \times 10^{-13}$ rad m V⁻¹, which remains two orders of magnitude smaller than in semiconductors.

As a conclusion, it appears that the non-equilibrium **MOKE** effect is much larger in semiconductors than in metals, no matter the spin-orbit coupling strength, suggesting that this effect is remarkably suited to detect non-equilibrium orbital accumulation and the related **BCD** in these materials.

4.3.4. Orbital Edelstein Coefficients Versus Berry Curvature Dipole in WTe₂

As an additional probe of the connection between non-equilibrium orbital magnetization and second order Hall effect driven by the BCD, in the d.c. limit $\hbar\omega \rightarrow 0$ we evaluate the decomposition of the orbital magnetization given by Eq.(4.6) in order to obtain an explicit relation between the non-equilibrium orbital magnetization (through its Edelstein coefficients) and the BCD. As we explain earlier, the model couples four tilted Dirac models where the on-site energy is defined as $h_0 = E_i + t_i(k_x + K_i)$. In the case of two bands, the constant function $E_i + t_i K_i$ is a rigid shift in the energy of each band and $t_i k_x$ is an odd function in k_x , thus we expect that the first term in Eq.(4.6) must dominate over \mathcal{B} . Therefore, the non-equilibrium orbital magnetization of the minimal model described by Eq.(4.8) must follow a similar relation $\alpha_{zx} \simeq \mu D_{zx}$. Because of this reason, we compare the quantities α_{zx} and μD_{zx} of the model, for different values of v_x and as a function of the chemical potential. Our results are shown in Fig.4.5.

As we can see from Fig.4.5 and from the band structure adapted from [90] in Fig.4.2, when $v_x = 0$ [Fig.4.5(a)] we have two tilted Dirac cones and $\alpha_{zx} \simeq \mu D_{zx}$ is in qualitative agreement with the calculations. As we increase v_x to the cases presented in Figs.4.5(b-c), the system exhibits band inversions and anticrossings, and \mathcal{B} becomes more dominant. Then, at $v_x = 0.4 \text{ eV \AA}$ a gap is open and the linear relation between α_{zx} and D_{zx} tends to be accurate again. It is clear that $\alpha \simeq \mu D$ is in good agreement with our calculations as long as we are in the vicinity of the gap or when $v_x \rightarrow 0$, where we observe two tilted Dirac cones.

4. Magneto-optical Probe of Non-Equilibrium Orbital Magnetism via the Second-Order Hall effect – 4.3. WTe_2 Bilayer

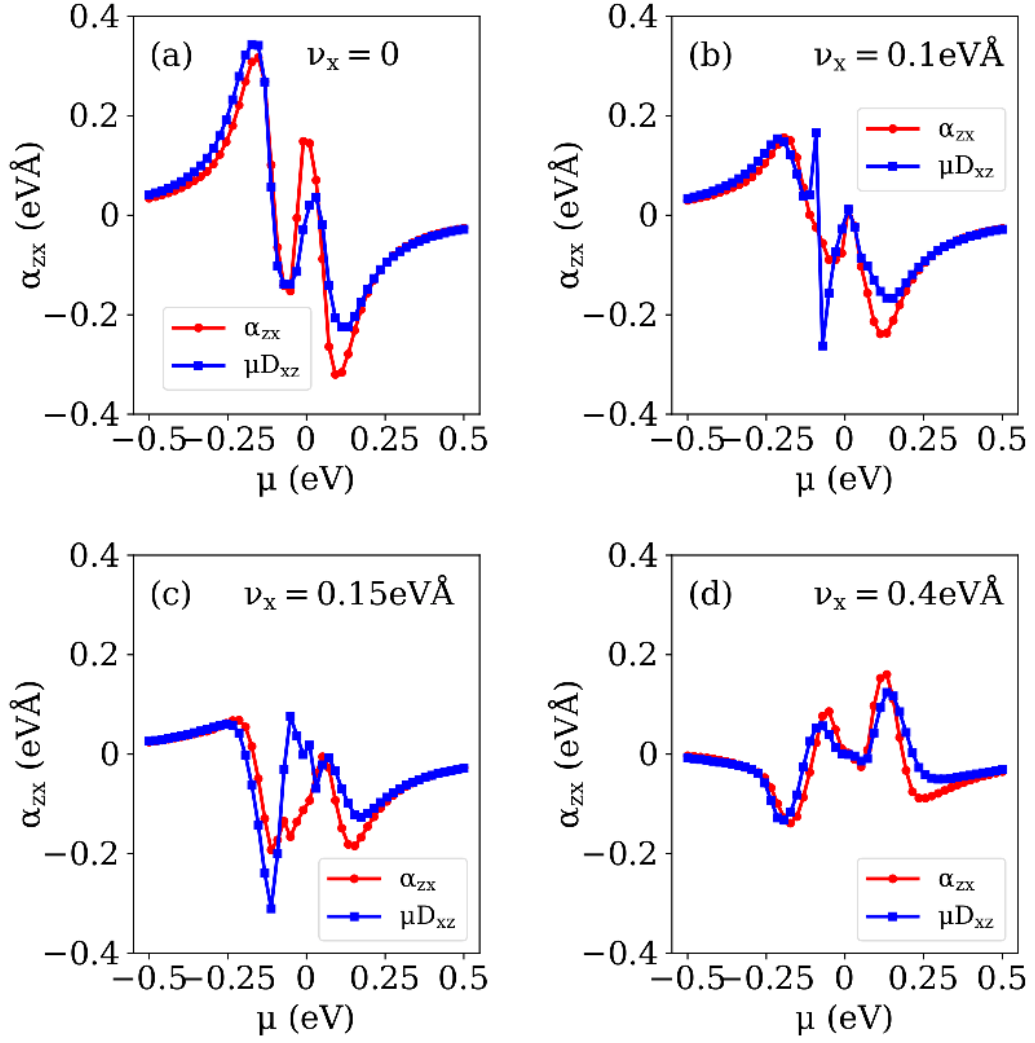


Figure 4.5. – Comparison between the orbital Edelstein coefficients and the BCD for the minimal model of WTe_2 bilayer, for different values of ν_x and as a function of μ . We fix the same microscopic parameters that in Fig.4.3, exemplifying the cases (a) $\nu_x = 0$, (b) $\nu_x = 0.1 \text{ eV \AA}$, (c) $\nu_x = 0.15 \text{ eV \AA}$ and (d) $\nu_x = 0.4 \text{ eV \AA}$.

4.4. $\text{Nb}_{2n+1}\text{Si}_n\text{Te}_{4n+2}$ Monolayer

4.4.1. Model System

As another example, we apply the theory to the family of compounds $\text{Nb}_{2n+1}\text{Si}_n\text{Te}_{4n+2}$ modelled with a minimal tight-binding Hamiltonian. The Hamiltonian is given by $\mathcal{H}_{\mathbf{k}} = \mathcal{H}_{\mathbf{k}}^{(0)} + \mathcal{H}_{\mathbf{k}}^{(soc)}$, where [242]

$$\begin{aligned} \mathcal{H}_{\mathbf{k}}^{(0)} &= t \begin{pmatrix} 0 & 1 + e^{-ik_x} \\ 1 + e^{ik_x} & 0 \end{pmatrix} \otimes \hat{\sigma}_0 \\ &+ \delta t \begin{pmatrix} 0 & e^{-ik_y}(1 + e^{-ik_x}) \\ e^{ik_y}(1 + e^{ik_x}) & 0 \end{pmatrix} \otimes \hat{\sigma}_0, \end{aligned} \quad (4.11)$$

$$\begin{aligned} \mathcal{H}_{\mathbf{k}}^{(soc)} &= t \begin{pmatrix} \lambda_1 \sin k_x & 0 \\ 0 & -2\lambda_1 \sin k_x \end{pmatrix} \otimes \hat{\sigma}_3 + \\ &+ \delta t \begin{pmatrix} 2\lambda_3 \sin k_y & i\lambda_2 e^{ik_y}(1 + e^{-ik_x}) \\ -i\lambda_2 e^{-ik_y}(1 + e^{ik_x}) & 2\lambda_3 \sin k_y \end{pmatrix} \otimes \hat{\sigma}_3. \end{aligned} \quad (4.12)$$

being $\hat{\sigma}_i$, $i = 1..3$ Pauli matrices and $\hat{\sigma}_0$ the identity in two dimensions. In the Hamiltonian defined by Eqs. (4.11-4.12), t and δt are intra and inter-chain hoppings, respectively. Besides, $\{\lambda_j\}_{j=1}^3$ are Rashba parameters contributing when $\mathcal{H}_{\mathbf{k}}^{(soc)}$ is active: Whereas λ_1 is related to intrachain processes, λ_2 and λ_3 are related to interchain processes. A scheme with the lattice structure of the system is reported in Figs.4.6. In addition, our calculation of the band structure of the model, which agrees qualitatively with [242], is presented in Fig.4.7.

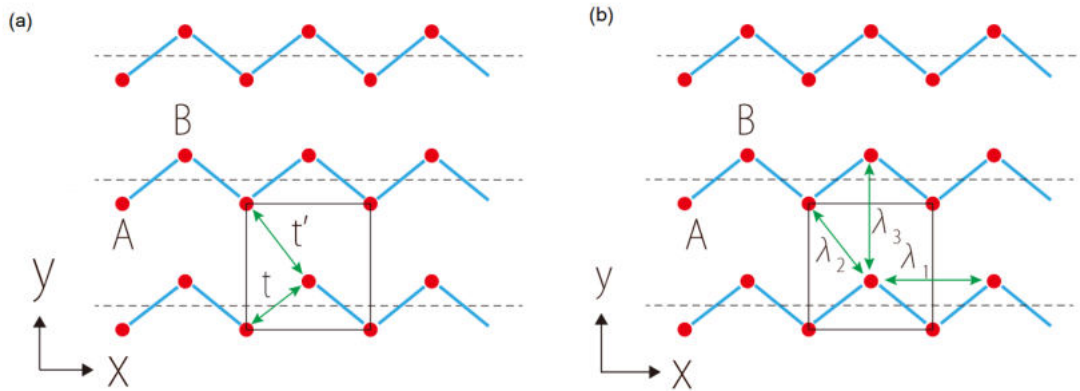


Figure 4.6. – (a) Lattice structure of the model consisting on zigzag chains. The primitive cell has two sites A and B, and the hoppings t and $t' = \delta t$ are intrachain and interchain, respectively. (b) denotes the three hoppings related to spin-orbit coupling. Figure modified from [242].

4. Magneto-optical Probe of Non-Equilibrium Orbital Magnetism via the Second-Order Hall effect – 4.4. $Nb_{2n+1}Si_nTe_{4n+2}$ Monolayer

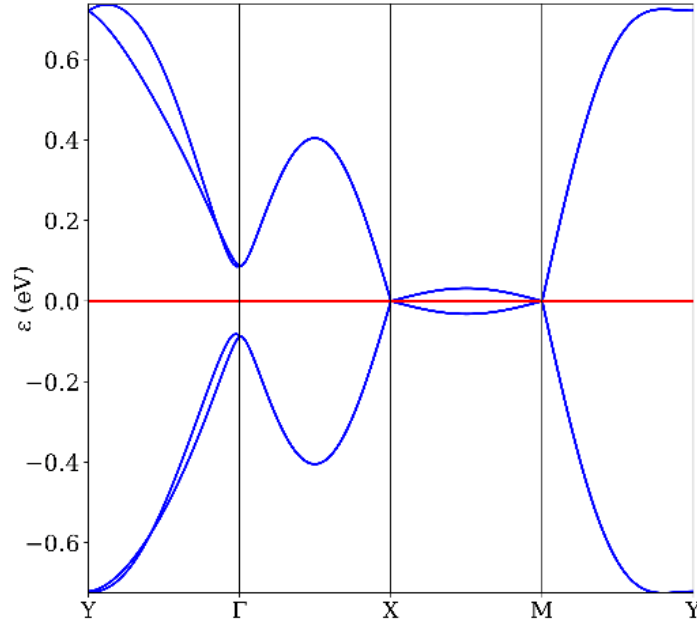


Figure 4.7. – Band structure of the model in Eqs.(4.11-4.12), computed with the microscopic parameters $t = -0.2$ eV, $t' = \delta t = 0.16$ eV, $\lambda_1 = 1$ and $\lambda_2 = \lambda_3 = 0.1$.

4.4.2. Model Calculations and Discussion

For the **MOKE** response, we fix the value of the band filling at the peak of the d.c. **BCD** signal (see Chapter 2 for more details) when the electric field is applied along \hat{y} , finding that the maximum is reached at $\mu \approx \pm 0.028$ eV. Our result agrees qualitatively with [242] and our outcome is communicated in Fig.4.8.

4. Magneto-optical Probe of Non-Equilibrium Orbital Magnetism via the Second-Order Hall effect – 4.4. $Nb_{2n+1}Si_nTe_{4n+2}$ Monolayer

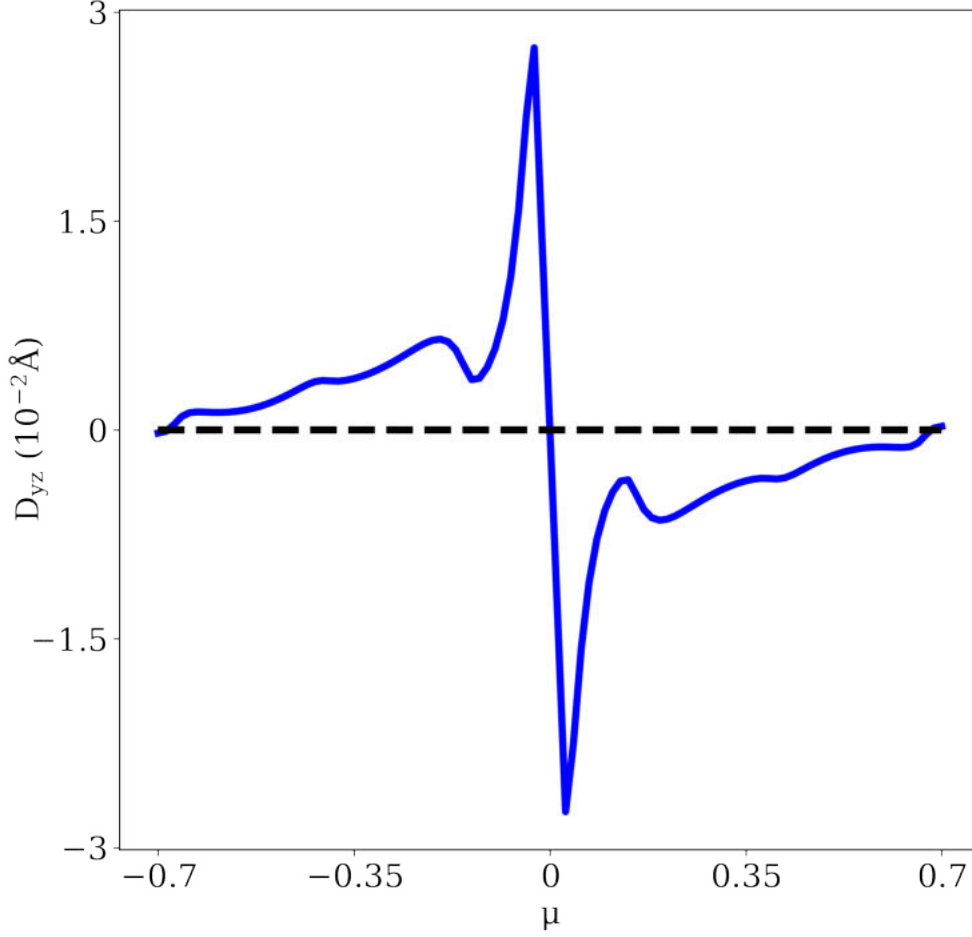


Figure 4.8. – d.c. BCD for the model system defined by Eqs.(4.11-4.12), taking the microscopic parameters as $t = -0.2$ eV, $t' = \delta t = -0.16$ eV, $\lambda_1 = 1$ and $\lambda_2 = \lambda_3 = 0.1$.

In this case, considering the fact that the BC and the orbital moment are parallel to \hat{z} , the non-equilibrium orbital magnetization is along \hat{z} . Therefore, the setup for the second-order Hall current here is identical to WTe_2 presented earlier: On one side, the Hall current flows along \hat{x} when the BCD D_{yz} is generated by the out-of plane BC and an electric field that is applied along \hat{y} . From a symmetry perspective, the second order Hall current flowing along \hat{x} should be related to an external electric field applied along \hat{y} and a non-equilibrium orbital magnetization along \hat{z} . With this in mind, let us first study the nonlinear MOKE effect in this system, showing the behavior of the BCD, the longitudinal conductivity and the Kerr angle as a function of the energy of the incoming light and interchain hopping. Our results are reported in Figs.4.9-4.10 for an electric field applied 45° with respect to the \hat{x} axis in order to retain the polar

4. Magneto-optical Probe of Non-Equilibrium Orbital Magnetism via the Second-Order Hall effect – 4.4. $Nb_{2n+1}Si_nTe_{4n+2}$ Monolayer

configuration.

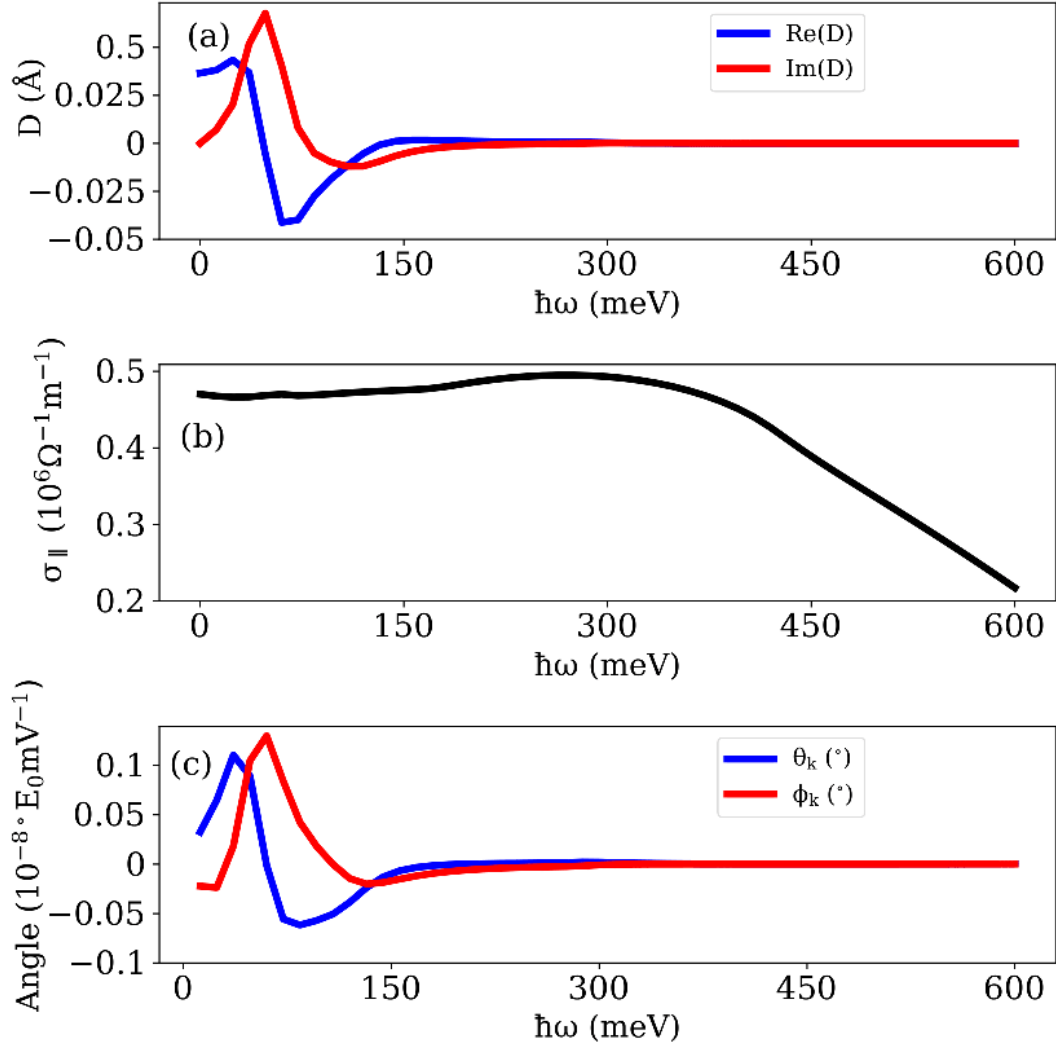


Figure 4.9. – For the model system defined by Eqs.(4.11-4.12), taking the microscopic parameters as $t = -0.2$ eV, $t' = \delta t = -0.16$ eV, $\lambda_1 = 1$, $\lambda_2 = \lambda_3 = 0.1$, $\mu = 0.028$ eV and $\Gamma = 0.01$ eV. (a) Real (solid blue line) and imaginary (solid red line) part of the a.c. BCD as a function of the energy of the incoming light $\hbar\omega$. (b) Longitudinal conductivity of the system. (c) Kerr angle (solid blue line) and ellipticity (solid red line) of the model.

Following Fig.4.9(a), we verify that at zero frequency the real part of the BCD is finite and the imaginary part of the BCD vanishes as expected. The coefficients also tend to zero as we increase the frequency, with peaks close to $\hbar\omega \rightarrow 100$ meV. Besides, the longitudinal conductivity is almost a constant for the region $\hbar\omega \leq 300$ meV [Fig.4.9(b)] and then decreases slowly with the frequency. This signal has the same order of magnitude of the response reported in previous experiments on Nb_3SiTe_6 [246, 247].

4. Magneto-optical Probe of Non-Equilibrium Orbital Magnetism via the Second-Order Hall effect – 4.4. $Nb_{2n+1}Si_nTe_{4n+2}$ Monolayer

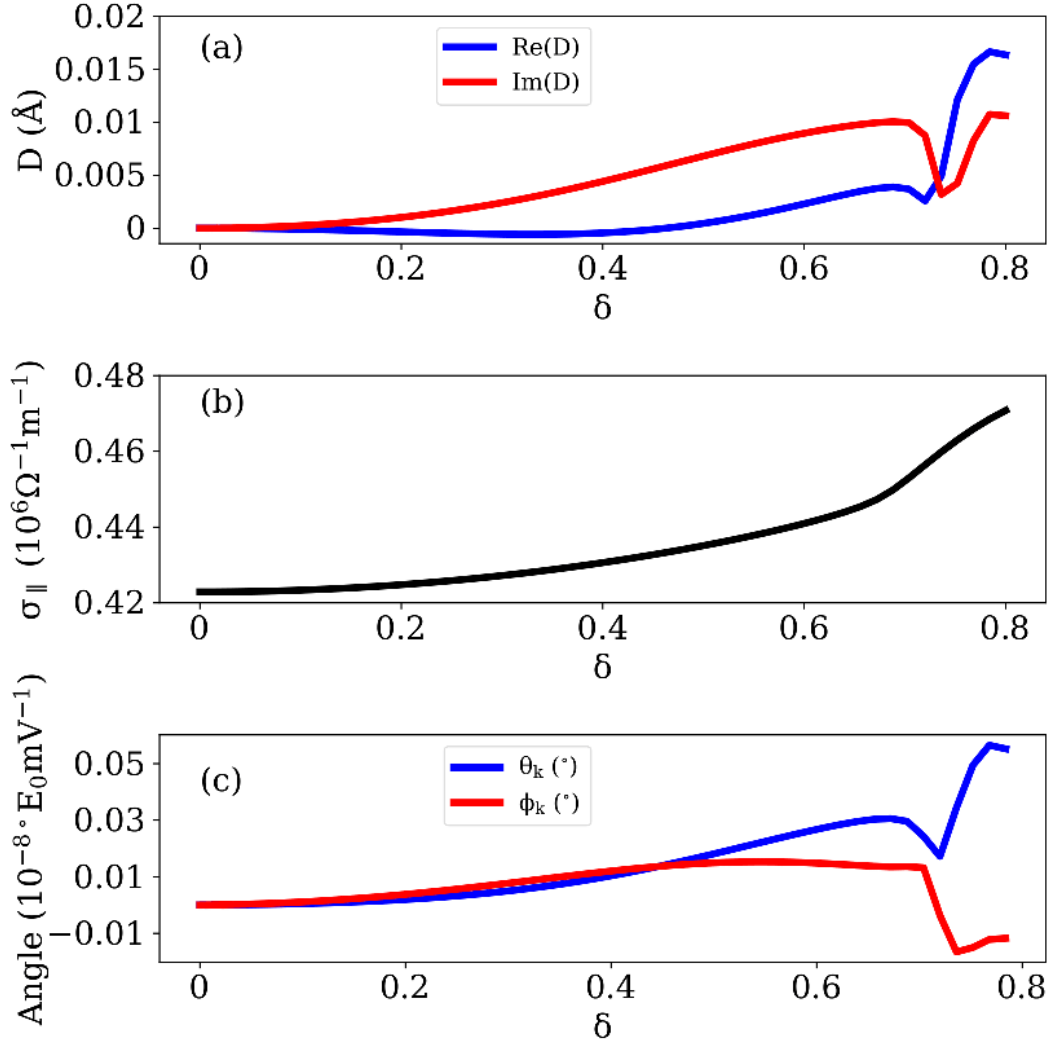


Figure 4.10. – For the model system defined by Eqs.(4.11-4.12), taking the microscopic parameters as $t = -0.2$ eV, $t' = \delta t = -0.16$ eV, $\lambda_1 = 1$, $\lambda_2 = \lambda_3 = 0.1$, $\mu = -0.028$ eV, $\hbar\omega = 100$ meV and $\Gamma = 0.01$ eV: (a) Real (solid blue line) and imaginary (solid red line) part of the a.c. BCD as a function of the interchain parameter δ . (b) Longitudinal conductivity of the system. (c) Kerr angle (solid blue line) and ellipticity (solid red line) of the model.

Identical to the case of Fig.4.9, in this instance we corroborate that both $\text{Re}(D)$ and $\text{Im}(D)$ tend to zero as long as $\delta \rightarrow 0$, because we reinstall inversion symmetry. In the same frame, from Fig.4.10(a) we notice that $\text{Re}(D)$ takes a larger value than $\text{Im}(D)$ as $\delta \rightarrow 0.8$. Moreover, the notorious local minimum of $\text{Im}(D)$ at $\delta = 0.75$ [Fig.4.10(a)] makes ϕ_k in Fig.[Fig.4.10(c)] decreases and changes sign around the same value of δ .

Let us comment about the magnitude of the Kerr angle and contrast with the previous case on WTe_2 . From Fig.4.9(c), we notice that the magnitude of the nonlinear

4. Magneto-optical Probe of Non-Equilibrium Orbital Magnetism via the Second-Order Hall effect – 4.4. $\text{Nb}_{2n+1}\text{Si}_n\text{Te}_{4n+2}$ Monolayer

MOKE response is of the order of nrad, which is one order of magnitude smaller than the case of WTe_2 . This difference can be explained by the magnitudes of the corresponding BCD and longitudinal conductivity. The BCD reaches values two orders of magnitude smaller in this system, and the longitudinal conductivity is one order of magnitude smaller as well.

4.4.3. Orbital Edelstein Coefficients Versus Berry Curvature Dipole in $\text{Nb}_{2n+1}\text{Si}_n\text{Te}_{4n+2}$

As it was illustrated for the case of WTe_2 bilayer in section 4.3.4, in the following we perform a similar analysis to the non-equilibrium orbital magnetization, comparing it with the BCD function in the d.c. limit. Our findings are presented in Fig.4.11.

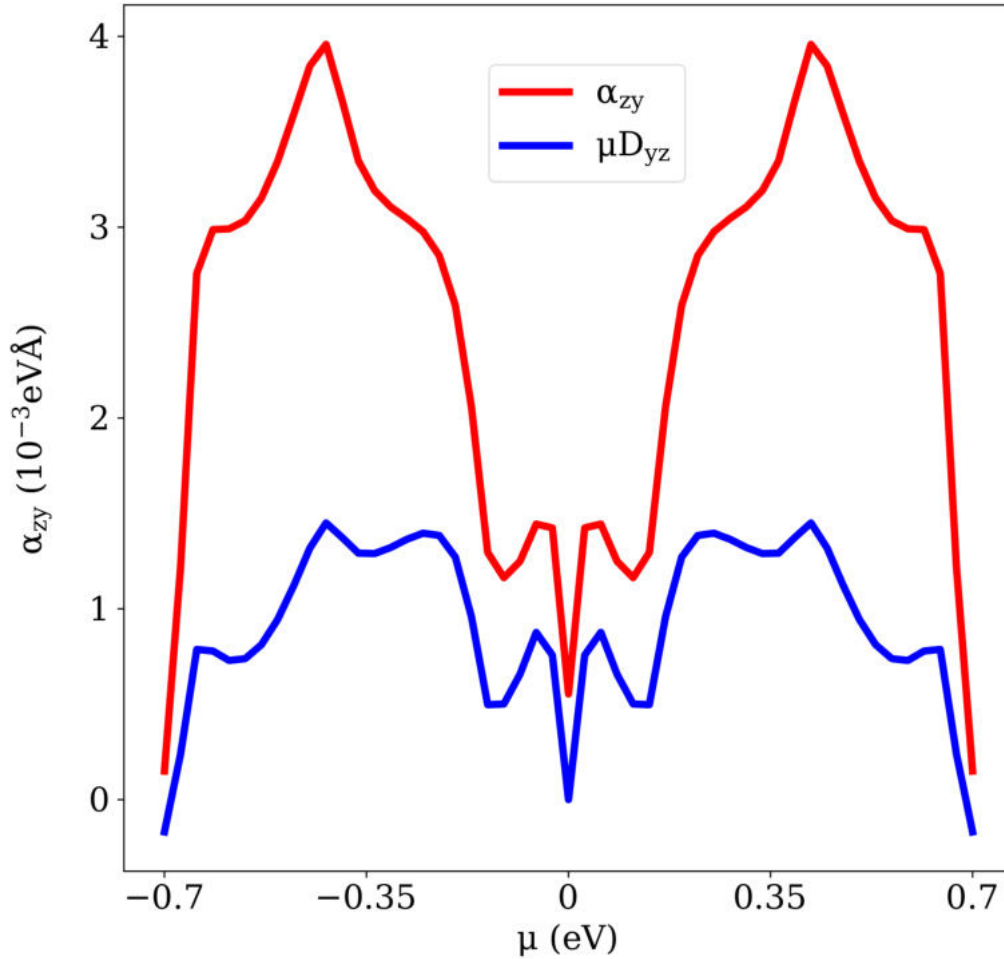


Figure 4.11. – Orbital Edelstein coefficient α_{zy} and the function for the model system defined by Eqs.(4.11-4.12), taking the microscopic parameters as $t = -0.2$ eV, $t' = \delta t = -0.16$ eV, $\lambda_1 = 1$, $\lambda_2 = \lambda_3 = 0.1$ and $\mu = -0.028$ eV.

4. Magneto-optical Probe of Non-Equilibrium Orbital Magnetism via the Second-Order Hall effect – 4.5. Conclusions and Prospects

As we can identify from Fig.4.11 and following Eq.(4.6), although both functions α_{zy} and μD_{yz} have similar behavior their magnitude is notably different. Then, the non-equilibrium orbital magnetization has a sizable contribution arising on $\mathcal{B}(\mu)$. This example points out the fact that $\alpha \simeq \mu D$ is not general, and its accuracy is only valid close to gapped and tilted Dirac and related systems.

4.5. Conclusions and Prospects

In conclusion, we investigate the nonlinear magneto-optical Kerr effect as a probe of non-equilibrium magnetization in non-magnetic materials without inversion symmetry, when the system is assisted with a d.c electric field. As a consequence, the Kerr rotation is proportional to an a.c. Berry curvature dipole. In the case of a minimal model of a bilayer WTe_2 , we infer that the Kerr angle reaches sizable values at small frequencies that can be controlled under the presence of a gate voltage. We suggest to apply this principle to other interesting platforms such as in ferroelectrics and time reversal invariant Weyl semimetals, in order to prove the induction of the magnetization and obtain a potential candidate for second order Hall effect. Besides, in the SSH model we infer that the Kerr angle is controlled by the interchain coupling that breaks inversion symmetry. The theory presented here can be extended to detect current-induced magnetization in the transverse and longitudinal configuration.

An interesting prospect points to explore whether the nonlinear Hall effect mediated by disorder mechanisms, such as side jump or skew-scattering, could be explained through the same processes but at the level of the spin or orbital angular momentum. In other words, one could wonder about the conditions where the second order Hall effects mediated by disorder can be related to the spin Edelstein effect and/or the orbital Edelstein effect mediated by the orbital angular momentum. These perspectives are not limited to second-order in electrical perturbation, and in fact one avenue concerns the theory for the emergence of the orbital polarization accompanying the third order Hall effect. This has been proposed recently in order to explain the signal in WTe_2 [110], but this effects lacks a proper theoretical study. In the same way as in this research, we also expect a magneto-optical effect relating third-order transport and second-order magnetization, where the symmetry considerations are completely different. We consider to investigate this topic in future studies.

5. Unconventional Responses in Trigonal Crystals

Summary

5.1. Spin-Orbit Torque for Field Free Switching in C_{3v} crystals	106
5.1.1. Motivation	106
5.1.2. Symmetry Analysis	109
5.1.3. Transport Formalism and C_{3v} Model	113
5.1.4. Numerical Results and Discussion	118
5.1.5. First Principles Case Study: CuPt(111)/Co	120
5.2. Chiral Hall Effect	124
5.2.1. Symmetry Analysis	124
5.2.2. Model Calculations	126
5.2.3. Realistic Simulations	128
5.3. Conclusions and Prospects	130

5.1. Spin-Orbit Torque for Field Free Switching in C_{3v} crystals

5.1.1. Motivation

Electrical manipulation of the magnetization in single magnetic thin films using spin-orbit torques has become routinely available in the past decade [123]. In perpendicularly magnetized systems, the most suitable configuration for memory applications, achieving reversible current-driven switching necessitates the combination of spin-orbit torque with an external magnetic field [248, 249]. As a matter of fact, whereas the spin-orbit torque tends to bring the magnetization in the plane, applying an additional external field along the current direction provides the necessary force that completes the reversal process in a deterministic manner. The need for this external field is considered as a hurdle for memory applications and several strategies have been proposed to circumvent this difficulty. Field-free current-driven switching has been realized using exchange bias from a neighboring antiferromagnet [250, 251], exchange coupling [252, 253] or anomalous Hall torque from a proximate ferromagnet [254, 255]. The latter takes advantage of an interfacial spin rotation of the incoming spin current [256], sometimes called spin swapping [257, 258] (see also Refs. [259, 260]).

5. Unconventional Responses in Trigonal Crystals – 5.1. Spin-Orbit Torque for Field Free Switching in C_{3v} crystals

In addition, structural engineering has been successfully exploited to design lateral [116, 261, 262, 263, 264] and geometrical [265] symmetry breaking, tilted anisotropy [266, 267, 268] and longitudinal (compositional or structural) gradient [269, 270].

Whereas most of these works considered multilayers made out of polycrystalline materials, recent experiments demonstrated that low symmetry crystals are endowed with unconventional spin-orbit torques that can play the role of an external field, thereby completing the current-driven switching process. The impact of the crystalline symmetries on the spin-orbit torque is well-known since its initial observation in the non-centrosymmetric magnetic semiconductors (Ga,Mn)As [271, 272] and in the Heusler alloy MnNiSb [273], where the bulk inversion symmetry breaking promotes a so-called Dresselhaus-like spin-orbit torque. In fact, further lowering of the crystalline symmetries can lead to unusual torques that turn out to be instrumental to achieve field-free switching. For instance, WTe₂ has been shown to display a "perpendicular damping-like torque" [129, 274] that enables field-free switching, an effect confirmed in several experiments [275, 276, 277]. This torque, also present in MoTe₂ [278] and NbSe₂ [279], is associated with a crystalline mirror symmetry breaking perpendicular to the interface plane. When a current is injected along this mirror, it may generate a nonequilibrium spin density contained in this mirror plane and normal to the interface. Antiferromagnets are also currently attracting attention from this standpoint. Indeed, the combination of crystalline and magnetic symmetries tend to produce spin currents with a polarization different from what is dictated by the conventional spin Hall effect [280, 281], an effect sometimes called "magnetic" spin Hall effect [282, 283]. These spin currents can in turn exert "unconventional" torques on an adjacent ferromagnet, as observed in collinear (Mn₂Au [284], RuO₂[285, 286]), and non-collinear antiferromagnets (Mn₃GaN [287], Mn₃Pt [288] and Mn₃Sn [289]).

Recently, Liu et al. [10] studied the current-driven magnetization reversal in a crystalline CuPt/CoPt bilayer in the L1₁ phase grown along the (111) direction. They reported that field-free switching could be achieved when the current was applied along low-symmetry crystallographic directions. Intriguingly, the polarity of the magnetization reversal loop displayed a periodic pattern depending on the crystallographic direction along which the current was applied (See Fig.5.1). This unusual behavior was interpreted as arising from an unconventional torque, tagged "3m" torque, which appears in crystals with C_{3v} point group [44]. Nonetheless, no microscopic explanation was proposed to explain the emergence of the "3m" torque in this bilayer. Such an explanation is highly desired, especially with the acceleration of the research in two-dimensional van der Waals magnets [290]. As a matter of fact, most of the van der Waals magnets possess a hexagonal or trigonal point group and are therefore entitled to display such a torque. For instance, the "3m" torque was identified in Fe₃GeTe₂ monolayer [11, 291] and is associated with an unconventional form of Dzyaloshinskii-Moriya interaction [292]. Nonetheless, mere symmetry consideration is not sufficient and a microscopic description is needed. Indeed, recent first principles calculation in the Janus monolayer VSeTe demonstrated that although this material possesses

5. Unconventional Responses in Trigonal Crystals – 5.1. Spin-Orbit Torque for Field Free Switching in C_{3v} crystals

the C_{3v} symmetry, no "unconventional" torque can be obtained and only the usual field-like and damping-like torques are present [293]. Therefore, understanding the physical origin of the "3m" torque in C_{3v} crystals and suggesting guidelines to enhance it is of crucial interest.

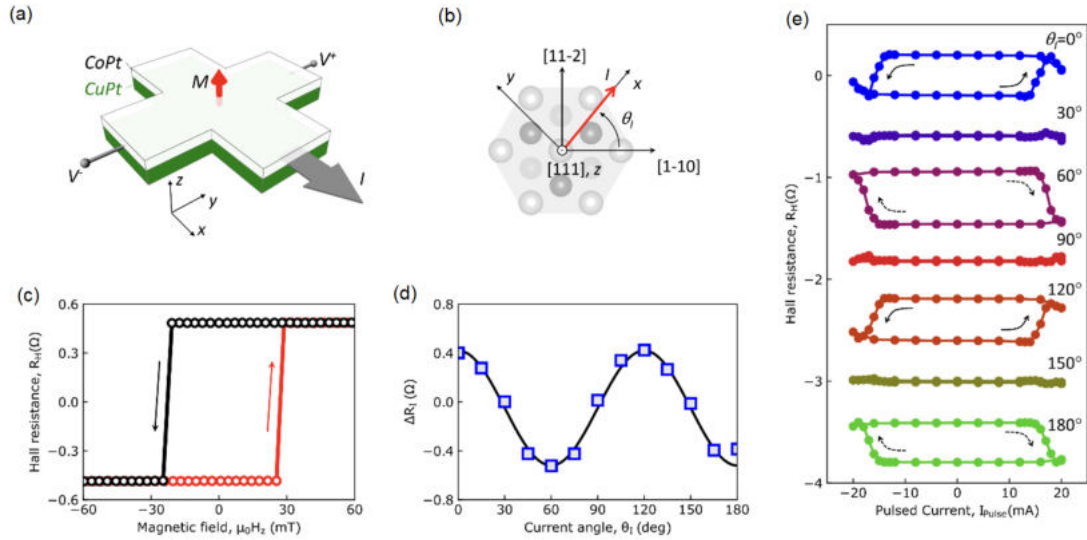


Figure 5.1. – (a) Setup of the experiment in CuPt/CoPt heterostructure for the transport measurement. The red arrow denotes the magnetization M and the grey arrow symbolizes the current I flowing along x . Here, the x and y axis are the same as in (b). (b) The definition of the current direction in terms of θ_I . The current is applied along the Hall bar, with an azimuthal angle of θ_I with respect to the $[110]$ direction. (c) Anomalous Hall effect of the bilayer for $\theta_I = 0^\circ$. (d) Current angle dependence of the spin-orbit torque induced magnetization switching. The solid line is a cosine fit to the data. (e) Current-induced magnetization switching for Hall bars with different θ_I . The dashed (solid) arrows indicate clockwise (anti-clockwise) switching polarity. The loops were manually shifted for better visualization. The pulse width is $30 \mu\text{s}$. Illustration extracted and modified from [10].

5. Unconventional Responses in Trigonal Crystals – 5.1. Spin-Orbit Torque for Field Free Switching in C_{3v} crystals

In this Chapter, we intend to clarify the nature of the spin-orbit torque in crystals with C_{3v} point group, i.e., its vectorial form and its microscopic origin. In subsection 5.1.2 we first determine the general form of the spin-orbit torque up to the third order in magnetization using the Invariant Theory applied on the C_{3v} character table. We then consider a minimal model for a magnetic gas with C_{3v} symmetries. In this model, the spin texture is governed by the cooperation between linear (Rashba) and cubic spin-momentum locking terms. The Fermi surface is characterized by trigonal warping that appears close to the top of the band structure. We show that the unconventional "3m" torque is associated with the cubic spin-momentum locking when the Fermi surface displays strong trigonal warping. We therefore suggest that trigonal warping can be used as a good indicator for the search of "3m" torques in C_{3v} crystals and two-dimensional van der Waals magnets. In subsection 5.1.5 we compare our findings from the tight-binding calculations with the realistic case of CuPt/Co, confirming the strong interplay between cubic-Rashba coupling and the warping of the Fermi surface for the observation of such unconventional torques.

5.1.2. Symmetry Analysis

In this section we first indicate the main ingredients inherited from the representation theory [294, 9], aiming to obtain a proper expansion for the unconventional spin-orbit torques in trigonal crystals. To do so, we first need to identify the point group symmetry for the system of interest. In the present case, it is the C_{3v} point group, which is characterized by three symmetry operations: The identity E , a three-fold rotation along \hat{z} and a mirror symmetry normal to \hat{y} . Moreover, it has three irreducible representations A_1 , A_2 and E that can be represented by matrices, which at the same time reveal the action of the symmetry operations mentioned earlier. Although a given symmetry operation can be defined by an infinite number of matrices, the trace of these matrices is unique for a given operation. Therefore, each irreducible representation can be identified by a unique set of traces called "characters". Table 5.1 gives the character table of the C_{3v} point group. The (equilibrium and nonequilibrium) properties of a given crystal are written as the combination of polar and axial vectors. For instance, in the case of the spin-orbit torque these vectors are the electric field (E_x, E_y, E_z) (polar vector) and the magnetization (m_x, m_y, m_z) (axial vector). When applying the symmetry operations on these vectors, they transform according to the irreducible representations A_1 , A_2 and E so that one can define basis functions for each representation. In Table 5.1, we give the basis functions of the irreducible representation of the C_{3v} point group up to the third order in magnetization. Concretely, they transform in the following way,

$$(E_x, E_y) \xrightarrow{\sigma_v} (E_x, -E_y), \quad (5.1)$$

$$(E_x, E_y) \xrightarrow{C_3} \left(-\frac{1}{2}E_x - \frac{\sqrt{3}}{2}E_y, \frac{\sqrt{3}}{2}E_x - \frac{1}{2}E_y\right), \quad (5.2)$$

5. Unconventional Responses in Trigonal Crystals – 5.1. Spin-Orbit Torque for Field Free Switching in C_{3v} crystals

and

$$(m_x, m_y, m_z) \xrightarrow{\sigma_v} (-m_x, m_y, -m_z), \quad (5.3)$$

$$(m_x, m_y, m_z) \xrightarrow{C_3} \left(-\frac{1}{2}m_x - \frac{\sqrt{3}}{2}m_y, \frac{\sqrt{3}}{2}m_x - \frac{1}{2}m_y, m_z\right). \quad (5.4)$$

	E	$2C_3$	$3\sigma_v$	Linear	Quadratic	Cubic
A ₁	1	1	1	z	$x^2 + y^2, z^2$ $m_x^2 + m_y^2, m_z^2$	$z^3, z(x^2 + y^2), x(x^2 - 3y^2)$ $m_y(3m_x^2 - m_y^2)$
A ₂	1	1	-1	m_z	-	$y(3x^2 - y^2)$ $m_x(m_x^2 - 3m_y^2)$
E	2	-1	0	(x, y)	$(x^2 - y^2, xy), (xz, yz)$	$(z(x^2 - y^2), xyz), (xz^2, yz^2),$ $(x(x^2 + y^2), y(x^2 + y^2))$
				(m_x, m_y)	$(m_x^2 - m_y^2, m_x m_y)$ $(m_x m_z, m_y m_z)$	$(m_z(m_x^2 - m_y^2), m_x m_y m_z), (m_x m_z^2, m_y m_z^2)$ $(m_x(m_x^2 + m_y^2), m_y(m_x^2 + m_y^2))$

Table 5.1. – Character table for the C_{3v} point group symmetry. We show the generating polynomials for each irreducible representation in both polar and axial versions.

Within this frame, we first determine the general form of the spin-orbit field from the invariant theory [294, 9], which will be later compared to model and realistic calculations. The spin-orbit torque $\vec{\tau}$ arises on an effective field \vec{h} such that $\vec{\tau} = -\gamma \vec{m} \times \vec{h}$. Since the latter plays the role of a magnetic field it is an axial vector, which is crucial to develop a proper expansion of \vec{h} by applying the basis functions in Table 5.1. For example, \vec{E} is a polar vector that belongs to the A_1 representation since it is invariant under C_3 and σ_v . Then, by looking at Table 5.1 we deduce that the only way to construct an axial vector is by taking basis functions in A_2 . Therefore, the only possible combinations in magnetization with \vec{E} that are invariant under the symmetries of the group are m_z, m_z^3 and $m_x(m_x^2 - 3m_y^2)$. Conversely, $\hat{z} \times \vec{E}$ is an axial vector that belongs to A_2 , hence its allowed combinations with A_1 are 1, m_z and $m_y(3m_x^2 - m_y^2)$. The same reasoning should be applied to the basis functions in E . Accounting for all combinations involving polar vector components at the first order and axial vector components up to the third order in magnetization, the effective field invariant under the C_{3v} point group symmetry is

5. Unconventional Responses in Trigonal Crystals – 5.1. Spin-Orbit Torque for Field Free Switching in C_{3v} crystals

$$\begin{aligned}
h_{\parallel} = & h_{FL}^{\parallel}(1 + \eta_{FL}m_z^2 + \delta_{FL}m_y(3m_x^2 - m_y^2))\hat{z} \times \vec{E} \\
& + h_{DL}^{\parallel}((1 + \eta_{DL}m_z^2)m_z + \delta_{DL}m_x(m_x^2 - 3m_y^2))\vec{E} \\
& + h_{3m}^{\parallel}(1 + \eta_{3m}m_z^2)[(m_xE_x - m_yE_y)\hat{x} - (m_yE_x + m_xE_y)\hat{y}] \\
& + h_{PH}^{\parallel}[(m_x^2 - m_y^2)E_y - 2m_xm_yE_x]\hat{x} + ((m_x^2 - m_y^2)E_x + 2m_xm_yE_y)\hat{y}] \\
& + h_{\chi}^{\parallel}m_z[(m_x^2 - m_y^2)E_x + 2m_xm_yE_y]\hat{x} - ((m_x^2 - m_y^2)E_y - 2m_xm_yE_x)\hat{y}] \\
& + h_{3m}^z m_z \{(m_yE_x + m_xE_y)\hat{x} + (m_xE_x - m_yE_y)\hat{y}\}
\end{aligned} \tag{5.5}$$

and

$$\begin{aligned}
h_{\perp} = & \left[h_{DL}^z(1 + \eta_z m_z^2)\vec{E} \cdot \vec{m} + h_{FL}^z m_z \vec{m} \cdot (\hat{z} \times \vec{E}) + h_{PH}^z((m_x^2 - m_y^2)E_y + 2m_xm_yE_x) \right. \\
& \left. + h_{\chi}^z m_z \{E_x(m_x^2 - m_y^2) - 2E_y m_x m_y\} \right] \hat{z}.
\end{aligned} \tag{5.6}$$

Here, we describe in a first stage the variety of terms appearing in our expansion; the formulas are completely general and they do not rely on any specific mechanism. We will address this question in the next sections. In addition to the regular field-like (h_{FL}) and damping-like (h_{DL}) components, we recognize the "3m" one reported in Ref.[10] for Pt-based heterostructures and in Ref.[11], the latter in F_3GeTe_2 with D_{3h} symmetry. In fact, D_{3h} contains the same symmetry operations that C_{3v} plus a two-fold rotation around \hat{x} . At higher orders in the magnetization, h_{FL}^{\parallel} and h_{DL}^{\parallel} are sensitive to planar (η_{α}) and trigonal (δ_{α}) anisotropies. Furthermore, the magnitudes of the field-like and damping-like components are different in-plane ($h_{FL}^{\parallel}, h_{DL}^{\parallel}$) and out-of plane (h_{FL}^z, h_{DL}^z). We also identify two additional components referred as in-plane (h_{PH}^{\parallel}) and out-of plane (h_{PH}^z) planar Hall torque, and the chiral torques ($h_{\chi}^{\parallel}, h_{\chi}^z$). The planar Hall torque terms have symmetries comparable to the planar Hall effect, in the sense that it is active when the magnetization lies in the (x,y) plane. Moreover, its magnitude depends on the relative angle between the electric field and the magnetization. The chiral torque necessitates to cant the magnetization away from the plane and it changes sign when reversing the magnetization ($m_z \rightarrow -m_z$).

To clarify the impact of the torque on the magnetization dynamics, we analyze its expression in two illustrative situations. When the magnetization lies out-of-plane ($\vec{m} = m_z \hat{z}$), which is typical of perpendicularly magnetized systems at rest [see Fig. 5.2(a)], the two torque components up to first order in magnetization read

$$\tau_{\parallel} = -\gamma h_{FL}^{\parallel} \hat{z} \times (\hat{z} \times \vec{E}), \tag{5.7}$$

$$\tau_{\perp} = -\gamma h_{DL}^{\parallel} \hat{z} \times \vec{E} \tag{5.8}$$

We see that only the conventional field-like and damping-like torques are active in this configuration. One can also notice that the field-like torque is always along the

5. Unconventional Responses in Trigonal Crystals – 5.1. Spin-Orbit Torque for Field Free Switching in C_{3v} crystals

electric field, $\sim \vec{m} \times (\hat{z} \times \vec{E})$, whereas the damping-like torque is perpendicular to it $\sim \vec{m} \times [(\hat{z} \times \vec{E}) \times \vec{m}]$. These two torques are the ones that destabilize the magnetization from its rest position and tend to bring it in the plane, normal to the applied electric field [see Fig. 5.2(b)].

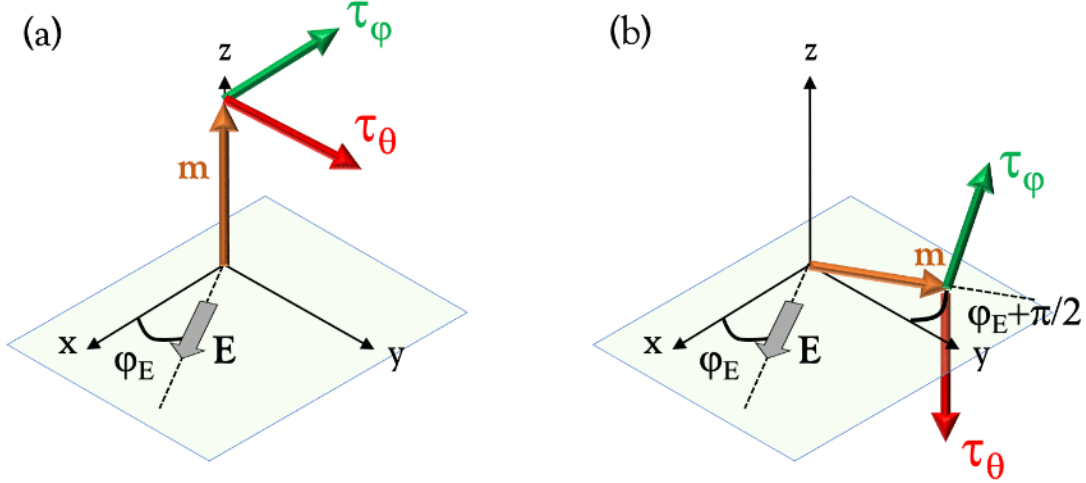


Figure 5.2. – Instances for the spin-orbit torque, when the magnetization is perpendicular to the plane (a) and in the case where the applied electric field and the magnetization differ by 90° .

Once the magnetization is in-plane, at $\phi = \varphi_E + \frac{\pi}{2}$, where φ_E is the in-plane angle of the electric field with respect to \hat{x} and (θ, ϕ) are the polar and azimuthal angles of the magnetization unit vector, the torques $\vec{\tau} = -\gamma \vec{m} \times \vec{h} = \tau_\theta \hat{\theta} + \tau_\phi \hat{\phi}$ in regular spherical coordinates are

$$\tau_\theta / E = \gamma [h_{DL}^\parallel \delta_{DL} - h_{3m}^\parallel] \sin 3\varphi_E, \quad (5.9)$$

$$\tau_\phi / E = \gamma h_{PH}^z \cos 3\varphi_E. \quad (5.10)$$

In this configuration, the conventional field-like and damping-like torques are quenched, and the only active torques are the "3m" torque (h_{3m}^\parallel), identified in Ref. [10], the trigonal anisotropy correction to the damping-like torque ($h_{DL}^\parallel \delta_{DL}$), and the perpendicular planar Hall torque (h_{PH}^z). Here, only τ_θ induces the deterministic switching, which means that the "3m" torque and the trigonal anisotropy correction to the damping-like torque are the active contributions in this process. Remarkably, in this frame the two other torques identified in Eqs. (5.7-5.8), i.e. the planar Hall torque ($h_{PH}^{\parallel,z}$) and the chiral torque ($h_\chi^{\parallel,z}$), are only active when $\theta \neq 0, \pi/2$ and should therefore impact the magnetization dynamics itself. Their influence could modify the current-driven auto-oscillation[295, 296], a phenomenon that we leave to future studies.

The impact of Fermi surface warping on the spin-orbit torque has been addressed

5. Unconventional Responses in Trigonal Crystals – 5.1. Spin-Orbit Torque for Field Free Switching in C_{3v} crystals

theoretically in the context of the topological insulator surfaces. Kurebayashi et al. and Imai et al. [297, 298] investigated the influence of warping on the spin-transfer torque and spin-orbit torque, respectively, in magnetic domain walls and skyrmions to the first order of the magnetization gradient. The spin-orbit torque discussed presently is not addressed in these works. Zhou et al. [299] investigated the appearance of a damping-like torque that is nonlinear in electric field and directly induced by the warping. Li et al. [300] investigated the impact of the hexagonal warping on the spin-orbit torque, linear in electric field, and observed that the torque does not vanish when the magnetization lies in the plane. This is consistent with the analysis performed in the previous section, although a direct connection with the general form provided in Eqs. (5.5)-(5.6) remains difficult.

5.1.3. Transport Formalism and C_{3v} Model

In this section we present the tight-binding model and the transport formalism, in order to explain the physical origin of the unconventional spin-orbit torques and asses their different magnitudes. Besides, we will be able to contrast our tight-binding calculations with the symmetry predictions described earlier. We consider a tight-binding model defined in an hexagonal lattice with Hamiltonian

$$\mathcal{H}_0 = \varepsilon_{\mathbf{k}} + \Delta \vec{\sigma} \cdot \vec{m} + \mathcal{H}_R + \mathcal{H}_{R3}, \quad (5.11)$$

with

$$\mathcal{H}_R = -i \frac{t_R}{a} \sum_{\mathbf{u}, s=\pm} s \vec{\sigma} \cdot (\hat{z} \times \vec{u}) e^{i s \vec{k} \cdot \vec{u}} = \frac{t_R}{a} \eta_{\mathbf{k}} \cdot (\vec{\sigma} \times \hat{z}), \quad (5.12)$$

$$\mathcal{H}_{R3} = -i t_{R3} \sum_{\mathbf{u}, s=\pm} s \vec{\sigma} \cdot \hat{z} e^{i s \vec{k} \cdot \vec{u}} = t_{R3} \lambda_{\mathbf{k}} \sigma_z. \quad (5.13)$$

The sum is taken over the nearest neighbors (NN), i.e., $\vec{u} = \vec{a}, \vec{b}, \vec{c}$, sketched on Fig. 5.3(a), and a is the lattice parameter. Explicitly, $\varepsilon_{\mathbf{k}} = -2t(\cos \vec{k} \cdot \vec{a} + \cos \vec{k} \cdot \vec{b} + \cos \vec{k} \cdot \vec{c})$, $\eta_{\mathbf{k}} = 2(\vec{a} \sin \vec{k} \cdot \vec{a} + \vec{b} \sin \vec{k} \cdot \vec{b} + \vec{c} \sin \vec{k} \cdot \vec{c})$ and $\lambda_{\mathbf{k}} = 2(\sin \vec{k} \cdot \vec{a} + \sin \vec{k} \cdot \vec{b} + \sin \vec{k} \cdot \vec{c})$, where $\vec{a} = \frac{a(\sqrt{3}\hat{x} - \hat{y})}{2}$, $\vec{b} = -\frac{a(\sqrt{3}\hat{x} + \hat{y})}{2}$ and $\vec{c} = a\hat{y}$. Here, \mathcal{H}_0 represents the nearest neighbor hopping Hamiltonian between the atoms, plus an additional term that quantifies the ferromagnetic exchange in the system. In addition, \mathcal{H}_R is the Rashba spin-orbit coupling Hamiltonian that breaks inversion symmetry due to the out-of plane Rashba field, being a common element to explain the inversion asymmetry in the majority of heterostructures. Most importantly, \mathcal{H}_{R3} is a cubic correction to the Rashba term. Let us fix the path for computing the band structure in the case of this Rashba system. The lattice structure of this model is shown in Fig. 5.3 (a). Following the definition of the model, we take the lattice vectors

5. Unconventional Responses in Trigonal Crystals – 5.1. Spin-Orbit Torque for Field Free Switching in C_{3v} crystals

$$\vec{a}_1 = \frac{\sqrt{3}\hat{x} - \hat{y}}{2}, \quad (5.14)$$

$$\vec{a}_2 = \hat{y}. \quad (5.15)$$

The corresponding primitive vectors are

$$\vec{b}_1 = \frac{4\pi\hat{k}_x}{\sqrt{3}}, \quad (5.16)$$

$$\vec{b}_2 = \frac{4\pi}{\sqrt{3}} \left(\frac{\hat{k}_x}{2} + \frac{\sqrt{3}\hat{k}_y}{2} \right), \quad (5.17)$$

Now we can compute the band structure by following the path Γ -M-K- Γ , such that the symmetry points are $\Gamma = (0, 0, 0)$, M = $(\frac{1}{2}, 0, 0)$ and K = $(\frac{1}{3}, \frac{1}{3}, 0)$. Since $\vec{k} = u\vec{b}_1 + v\vec{b}_2 + w\vec{b}_3$, the corresponding symmetry points in reciprocal space are

$$\Gamma = \vec{0}, \quad (5.18)$$

$$M = \frac{2\pi\hat{x}}{\sqrt{3}}, \quad (5.19)$$

$$K = \left(\frac{2\pi\hat{x}}{\sqrt{3}} + \frac{2\pi\hat{y}}{3} \right). \quad (5.20)$$

Then, the curves for each segment are given by

$$\mathcal{C}_1 = \frac{2\pi t\hat{k}_x}{\sqrt{3}}, \quad (5.21)$$

$$\mathcal{C}_2 = \frac{2\pi}{\sqrt{3}} \left(\hat{k}_x + \frac{t\hat{k}_y}{\sqrt{3}} \right), \quad (5.22)$$

$$\mathcal{C}_3 = \frac{2\pi(1-t)}{\sqrt{3}} \left[\hat{k}_x + \frac{\hat{k}_y}{\sqrt{3}} \right], \quad (5.23)$$

for $t \in [0, 1]$. For the integration, we can take $R := [0, \frac{2\pi}{\sqrt{3}}] \times [-2\pi, 2\pi]$. The band structure of the model is presented in Fig.3.2(b) for the situations with (red lines) and without (black lines) cubic spin-orbit coupling.

As we can see from Fig.5.3(b), aside of the conventional splitting of the bands when $t_R \neq 0$, an extra modification can be observed around the K point (top of the band) if $t_{R3} \neq 0$. Indeed, the hexagonal symmetry and the cubic spin-orbit coupling term improve our existing knowledge on the pure free-electron Rashba physics, also inducing further modifications on the Fermi surface. According to Fig.5.3(c-e), the

5. Unconventional Responses in Trigonal Crystals – 5.1. Spin-Orbit Torque for Field Free Switching in C_{3v} crystals

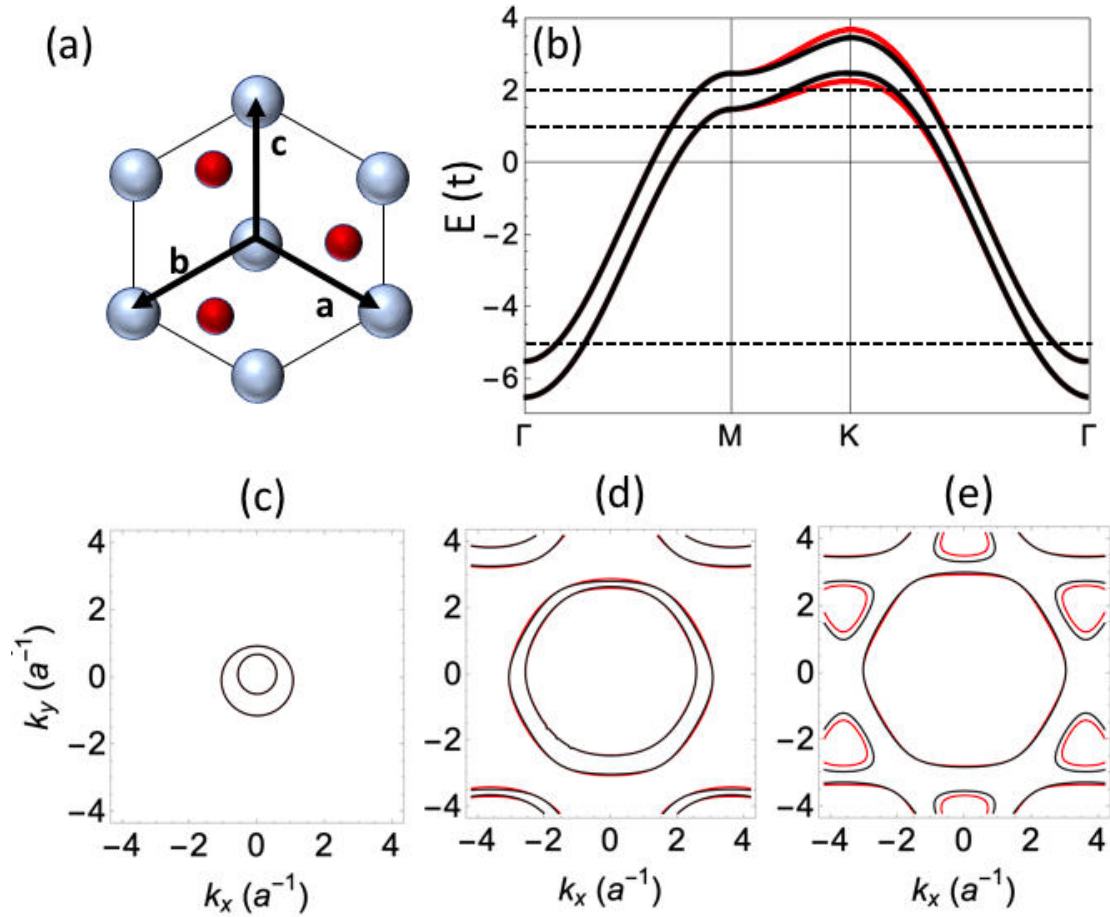


Figure 5.3. – (a) Lattice structure of the Hamiltonian. Here the grey atoms represent the hexagonal lattice sites, while the red atoms preserve the rotational symmetry along \hat{z} and the mirror symmetry normal to \hat{y} . (b) Band structure for the Hamiltonian set up with Eqs.(5.11-5.13), setting the intrinsic parameters as $t_R = 0.1t$ and $\Delta = 0.5t$ for the cases $t_{R3} = 0$ (black lines) and $t_{R3} = 0.1t$ (red lines). In addition, the magnetization angles are set to be $\theta = 90^\circ$ and $\phi = 0^\circ$. The horizontal dashed lines correspond to $\mu = -5t$, $\mu = t$ and $\mu = 2t$, respectively. Besides, we report the Fermi surfaces with ($t_{R3} = 0.1t$ -red lines) and without ($t_{R3} = 0$ -black lines) for (c) $\mu = -5t$, (d) $\mu = t$ and (e) $\mu = 2t$.

5. Unconventional Responses in Trigonal Crystals – 5.1. Spin-Orbit Torque for Field Free Switching in C_{3v} crystals

inclusion of cubic spin-orbit coupling impacts the evolution of the Fermi surface in the band-filling range: at low chemical potential [5.3(c)], where the energy dispersion is quadratic, the Fermi surface remains spherical and the cubic spin-orbit coupling has almost no impact. Upon increasing the band filling [5.3(d-e)], the Fermi surface experiences hexagonal warping and the cubic spin-orbit coupling modifies the energy contours. In this context, the Fermi surface acquires Fermi pockets away from the Γ point progressively and at high band filling the system manifests trigonal warping. In the next sections we will discuss how the combined action of the cubic spin-orbit coupling and a proper band filling allow the appearance of unconventional responses in charge transport and spin-orbit torques due to the modification of the Fermi surface. In the sections below, we complement the calculations performed based on the tight-binding Hamiltonian presented here with realistic simulations in CuPt/Co developed by Dr. Armando Pezo, aiming to confirm our theoretical findings and put them in a more realistic viewpoint. Our paper is published in Physical Review B [8].

We compute the effective fields based on the symmetrized decomposition of Kubo-Bastin formula[144], where the intrinsic and extrinsic contributions are explicitly given by

$$(\hat{\sigma}_i)_{Int} = -\frac{e\hbar}{4\pi} \int f(\epsilon) d\epsilon \operatorname{Re} [\operatorname{Tr} \{ \hat{\mathbf{v}}(G^{R-A}) \hat{\sigma}_i (\partial_\epsilon G^{R+A}) \}], \quad (5.24)$$

$$(\hat{\sigma}_i)_{Ext} = -\frac{e\hbar}{8\pi} \int \partial_\epsilon f(\epsilon) d\epsilon \operatorname{Re} [\operatorname{Tr} \{ \hat{\mathbf{v}}(G^{R-A}) \hat{\sigma}_i (G^{R-A}) \}], \quad (5.25)$$

where a momentum-space integration is implicit. Notice that Eqs.(5.24-5.25) are equivalent to Eqs.(2.42-2.43) for the charge transport, but here we obtain an electric-induced spin density rather than a current. The effective field and the spin-orbit torque read $\vec{h} = \Delta V^{-1} M_s^{-1}(\vec{\sigma})$ and $\vec{\tau} = \vec{h} \times \vec{m}$. Here, V is the volume of the unit cell and M_s is the saturation magnetization of the ferromagnet. In order to improve its time efficiency for numerical calculations, we develop an analogue identity of Eq.(5.24) in the Bloch basis. Integrating by parts the argument of the integral in Eq.(5.24) and using the following identities for the Green functions

$$G^{R(A)} = \sum_n \frac{|u_{n\mathbf{k}}\rangle \langle u_{n\mathbf{k}}|}{\epsilon - \epsilon_{n\mathbf{k}} \pm i\Gamma}, \quad (5.26)$$

we infer that

$$\operatorname{Tr} \{ \hat{\mathbf{v}}(G^{R-A}) \hat{\sigma}_i (\partial_\epsilon G^{R+A}) \} = \sum_n \{ \langle u_{n\mathbf{k}} | \hat{\mathbf{v}}(G^{R-A}) \hat{\sigma}_i (\partial_\epsilon G^{R+A}) | u_{n\mathbf{k}} \rangle \},$$

5. Unconventional Responses in Trigonal Crystals – 5.1. Spin-Orbit Torque for Field Free Switching in C_{3v} crystals

$$\begin{aligned}
&= \sum_{n,m,p,q} \{ \langle u_{n\mathbf{k}} | \hat{\mathbf{v}} | u_{m\mathbf{k}} \rangle \langle u_{m\mathbf{k}} | (G^R - G^A) | u_{p\mathbf{k}} \rangle \langle u_{p\mathbf{k}} | \hat{\sigma}_i | u_{q\mathbf{k}} \rangle \langle u_{q\mathbf{k}} | (\partial_\epsilon G^{R+A}) | u_{n\mathbf{k}} \rangle \} \\
&= - \sum_{n,m,p,q} \delta_{mp} \delta_{nq} \langle u_{n\mathbf{k}} | \hat{\mathbf{v}} | u_{m\mathbf{k}} \rangle \langle u_{p\mathbf{k}} | \hat{\sigma}_i | u_{q\mathbf{k}} \rangle \\
&\times \left\{ \frac{1}{\epsilon - \epsilon_{m\mathbf{k}} + i\Gamma} - \frac{1}{\epsilon - \epsilon_{m\mathbf{k}} - i\Gamma} \right\} \left\{ \frac{1}{(\epsilon - \epsilon_{n\mathbf{k}} + i\Gamma)^2} + \frac{1}{(\epsilon - \epsilon_{n\mathbf{k}} - i\Gamma)^2} \right\} \\
&= - \sum_{m \neq n} \langle u_{n\mathbf{k}} | \hat{\mathbf{v}} | u_{m\mathbf{k}} \rangle \langle u_{m\mathbf{k}} | \hat{\sigma}_i | u_{n\mathbf{k}} \rangle \left\{ \frac{1}{\epsilon - \epsilon_{m\mathbf{k}} + i\Gamma} - \frac{1}{\epsilon - \epsilon_{m\mathbf{k}} - i\Gamma} \right\} \left\{ \frac{1}{(\epsilon - \epsilon_{n\mathbf{k}} + i\Gamma)^2} + \frac{1}{(\epsilon - \epsilon_{n\mathbf{k}} - i\Gamma)^2} \right\} \\
&= - \sum_{m \neq n} \langle u_{n\mathbf{k}} | \hat{\mathbf{v}} | u_{m\mathbf{k}} \rangle \langle u_{m\mathbf{k}} | \hat{\sigma}_i | u_{n\mathbf{k}} \rangle g'(\epsilon) \tag{5.27}
\end{aligned}$$

Then, for $f'(\epsilon) \rightarrow -\delta(\epsilon - \mu)$ and integrating by parts, we deduce that

$$\begin{aligned}
h_i^{Int} &= \frac{e\hbar}{4\pi} \text{Re} \left[\sum_{m \neq n} \langle u_{n\mathbf{k}} | \hat{\mathbf{v}} | u_{m\mathbf{k}} \rangle \langle u_{m\mathbf{k}} | \hat{\sigma}_i | u_{n\mathbf{k}} \rangle \int f(\epsilon) g'(\epsilon) d\epsilon \right], \\
&= -\frac{e\hbar}{4\pi} \text{Re} \left[\sum_{m \neq n} \langle u_{n\mathbf{k}} | \hat{\mathbf{v}} | u_{m\mathbf{k}} \rangle \langle u_{m\mathbf{k}} | \hat{\sigma}_i | u_{n\mathbf{k}} \rangle \int f'(\epsilon) g(\epsilon) d\epsilon \right], \\
&= \frac{e\hbar}{4\pi} \text{Re} \left[\sum_{m \neq n} \langle u_{n\mathbf{k}} | \hat{\mathbf{v}} | u_{m\mathbf{k}} \rangle \langle u_{m\mathbf{k}} | \hat{\sigma}_i | u_{n\mathbf{k}} \rangle g(\mu) \right], \tag{5.28}
\end{aligned}$$

where

$$\begin{aligned}
g(\epsilon) &= I(\epsilon_{m\mathbf{k}} - i\Gamma, \epsilon_{n\mathbf{k}} - i\Gamma) + I(\epsilon_{m\mathbf{k}} - i\Gamma, \epsilon_{n\mathbf{k}} + i\Gamma) \\
&\quad - I(\epsilon_{m\mathbf{k}} + i\Gamma, \epsilon_{n\mathbf{k}} - i\Gamma) - I(\epsilon_{m\mathbf{k}} + i\Gamma, \epsilon_{n\mathbf{k}} + i\Gamma). \tag{5.29}
\end{aligned}$$

In this context, for two numbers $a, b \in \mathbb{C}$ we define

$$I(a, b) = \int \frac{d\epsilon}{(\epsilon - a)(\epsilon - b)^2}, \tag{5.30}$$

$$\begin{aligned}
I(a, b) &= \left(\frac{1}{a - b} \right)^2 \left[\int \left\{ \frac{1}{\epsilon - a} - \frac{\epsilon}{(\epsilon - b)^2} + \frac{2b - a}{(\epsilon - b)^2} \right\} d\epsilon \right], \\
&= \left(\frac{1}{a - b} \right)^2 \left[\int \left\{ \frac{1}{\epsilon - a} - \frac{(\epsilon - b)}{(\epsilon - b)^2} + \frac{b - a}{(\epsilon - b)^2} \right\} d\epsilon \right], \\
&= \left(\frac{1}{a - b} \right)^2 \left[\int \left\{ \frac{1}{\epsilon - a} - \frac{1}{(\epsilon - b)} + \frac{b - a}{(\epsilon - b)^2} \right\} d\epsilon \right], \\
&= \frac{1}{(a - b)^2} \left[\ln(\epsilon - a) - \ln(\epsilon - b) + \frac{a - b}{\epsilon - b} \right]. \tag{5.31}
\end{aligned}$$

5.1.4. Numerical Results and Discussion

Let us suppose that the electric field is applied along \hat{x} and the magnetization of the ferromagnet rotates in the (x, y) plane. In this scenario, our symmetry analysis from Eqs.(5.5-5.6) yields to

$$\begin{aligned} \frac{h_{\parallel}}{E} &= [h_{DL}^{\parallel} \delta_{DL} \cos 3\phi + h_{3m}^{\parallel} \cos \phi - h_{PH}^{\parallel} \sin 2\phi] \hat{x} \\ &+ [h_{FL}^{\parallel} (1 + \delta_{FL} \sin 3\phi) - h_{3m}^{\parallel} \sin \phi + h_{PH}^{\parallel} \cos 2\phi] \hat{y}, \end{aligned} \quad (5.32)$$

$$\frac{h_{\perp}}{E} = [h_{DL}^z \cos \phi + h_{PH}^z \sin 2\phi] \hat{z}. \quad (5.33)$$

We contrast Eqs.(5.32-5.33) with the profiles obtained for the angular dependence of the effective field components by means of Eqs.(5.24-5.25). We plot these outcomes in Fig.5.4 for the instances with low (a-c) and high (b-d) band filling, fixing the cubic spin-orbit coupling at $t_{R3} = 0.05t$.

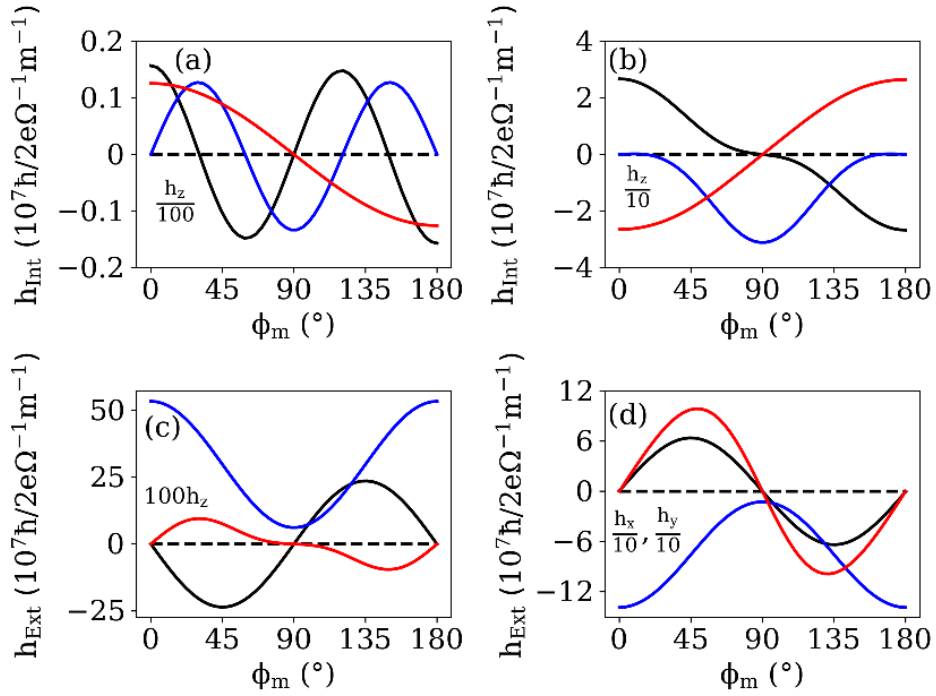


Figure 5.4. – Angular dependence of the effective field components h_x (black lines), h_y (blue lines) and h_z (red lines), when the magnetization rotates in the (x,y) plane. We indicate a scaling factor of a given component whenever is necessary. The system's parameters are given by $t = 1$, $t_R = 0.1t$, $t_{R3} = 0.05t$, $\Delta = 0.5t$ and the homogeneous disorder $\Gamma = 0.1t$. The intrinsic (a,b) and extrinsic (c,d) contributions are plotted for $\mu = -5t$ (left panels) and $\mu = 2t$ (right panels).

5. Unconventional Responses in Trigonal Crystals – 5.1. Spin-Orbit Torque for Field Free Switching in C_{3v} crystals

From Fig.5.4 (a) it is clear that a 3-fold dependence can be assigned to h_x and h_y , which can be attributed to the trigonal anisotropy terms δ_{DL} and δ_{FL} , respectively. Moreover, in the same low-band filling regime we can see that h_z is dominated by the conventional intrinsic contribution due to the damping-like term h_{DL}^z . Conversely, at high band filling [Fig.5.4(b)] the h_{3m}^{\parallel} contribution takes place as it can be checked by looking at h_y depicted in blue lines. Regarding the extrinsic contributions, it is evident that h_x and h_y are not trivial because of the planar and field like terms at low band filling [Fig.5.4(c)], while on the contrary h_{PH}^z becomes relevant at high band filling [Fig.5.4(d)]. For all these reasons, we deduce that our model calculations matches with our symmetry predictions; however, we will notice in the section of realistic simulations that indeed the higher-order expansion has certain limitations that we will discuss below.

Having checked the angular dependence of the effective fields, we fit our results with the predictions developed from the invariant theory to get a magnitude of each expression as a function of the band filling and the cubic spin-orbit coupling. We communicate our results in Fig.5.5.

5. Unconventional Responses in Trigonal Crystals – 5.1. Spin-Orbit Torque for Field Free Switching in C_{3v} crystals

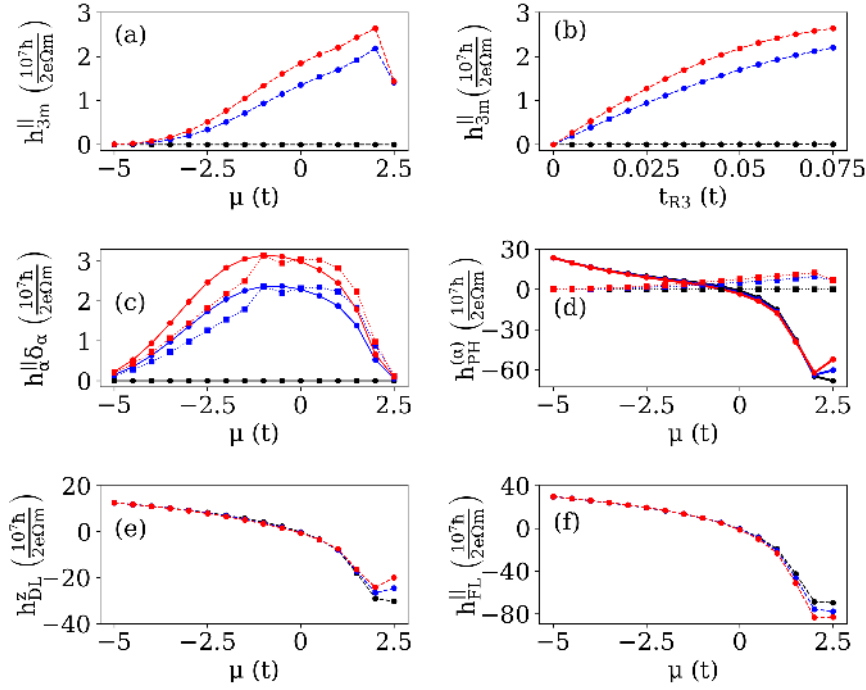


Figure 5.5. – Effective field’s components extracted from fitting the numerical results with Eqs.(5.32) and (5.33). The panels show (a) h_{3m}^{\parallel} , (c) $h_{DL}^{\parallel} \delta_{DL}$ (solid lines) and $h_{FL}^{\parallel} \delta_{FL}$ (dotted lines), (d) h_{PH}^{\parallel} (solid lines) and h_{PH}^z (dotted lines), (e) h_{DL}^z and (f) h_{FL}^z , for different values of cubic spin-orbit coupling t_{R3} (black, blue and red lines stand for $t_{R3} = 0, 0.05, 0.075$, respectively). completeness, panel (b) reports h_{3m}^{\parallel} as a function of t_{R3} for different values of μ (black, blue and red lines symbolizes the instances $\mu = -5t, t, 2t$, accordingly).

Taking note of Figs.5.5(a-b), we deduce that h_{3m}^{\parallel} requires cubic spin-orbit coupling and increase with the band filling, confirming its sensitivity to the trigonal warping of the Fermi surface. Unlike h_{3m}^{\parallel} , $h_{\alpha}^{\parallel} \delta_{\alpha}$ ($\alpha = DL, FL$) follows a parabolic behavior in the energy range and reaches a maximum close to the neutrality point $\mu = 0$ [Fig.5.5(c)]. Exceptionally, the Planar contributions characterized in Fig.5.5(d) exhibit different behaviors as a function of t_{R3} and μ : h_{PH}^{\parallel} does not require t_{R3} and follows a similar tendency to h_{DL}^z and h_{FL}^z [Figs.5.5(e-f)], while on the contrary h_{PH}^z increases with the band filling and requires $t_{R3} \neq 0$. The salient features of the different torque components for C_{3v} systems are summarized in Table 5.2.

5.1.5. First Principles Case Study: CuPt(111)/Co

For the sake of completeness, we present below the first principle calculations performed by Dr. Armando Pezo on CuPt(111)/Co bilayer. Although I did not perform the calculations myself, I actively participated to the discussion of these calculations. As explained above, this material has been recently experimentally demonstrated to

5. Unconventional Responses in Trigonal Crystals – 5.1. Spin-Orbit Torque for Field Free Switching in C_{3v} crystals

Component	Physical origin	Source
$h_{FL}^{\parallel}, h_{FL}^z, h_{PH}^{\parallel}$	Extrinsic	Linear Rashba
h_{PH}^z, h_{3m}^z	Extrinsic	Linear + cubic Rashba
$h_{DL}^{\parallel}, h_{DL}^z$	Intrinsic	Linear Rashba
δ_{FL}, δ_{DL}	Intrinsic	Linear + cubic Rashba
$h_{3m}^{\parallel}, h_{\chi}^{\parallel}, h_{\chi}^z$	Intrinsic	Linear + cubic Rashba

Table 5.2. – Summary of the minimal model analysis.

host a sizable “3m” torque [10]. Here, a CuPt/Co slab geometry containing 12 layers has been considered, such that the $L1_1$ phase is made up of stacking elemental fcc layers along the [111] direction. The band structure and spin textures were determined by employing fully relativistic density functional theory. The spin-orbit coupling was described within a fully relativistic pseudo-potential formulation and used the generalized gradient approximation (GGA) for the exchange-correlation functional. The calculations are converged for a 400 Ry plane-wave cut-off for the real-space grid with a $13 \times 13 \times 1$ k-points sampling of the Brillouin zone. The conjugate gradient algorithm was used to minimize the atomic forces below $0.01 \text{ eV}\text{\AA}^{-1}$. The momentum-resolved spin texture at the Fermi level is reported in Fig.5.6 and displays a very clear hexagonal symmetry, suggesting an effectively large cubic spin-orbit coupling interaction.

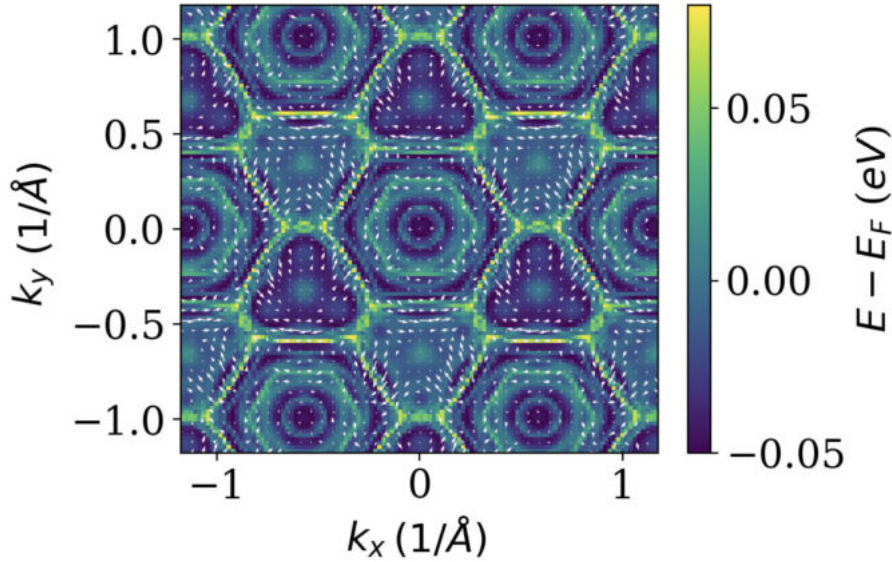


Figure 5.6. – Spin texture in momentum space close to Fermi level for a selected band of CuPt(111)/Co slab computed from first principles. A strong hexagonal symmetry is obtained, suggesting the presence of a large cubic spin-orbit coupling interaction.

Analogous to the model analysis, the components of the effective fields for this material are computed when the magnetization rotates in the (x,y) plane. The intrinsic

5. Unconventional Responses in Trigonal Crystals – 5.1. Spin-Orbit Torque for Field Free Switching in C_{3v} crystals

and extrinsic profiles are available in Fig.5.7. The calculations were developed by taking $\Gamma = 0.025$ eV in the zero-temperature limit.

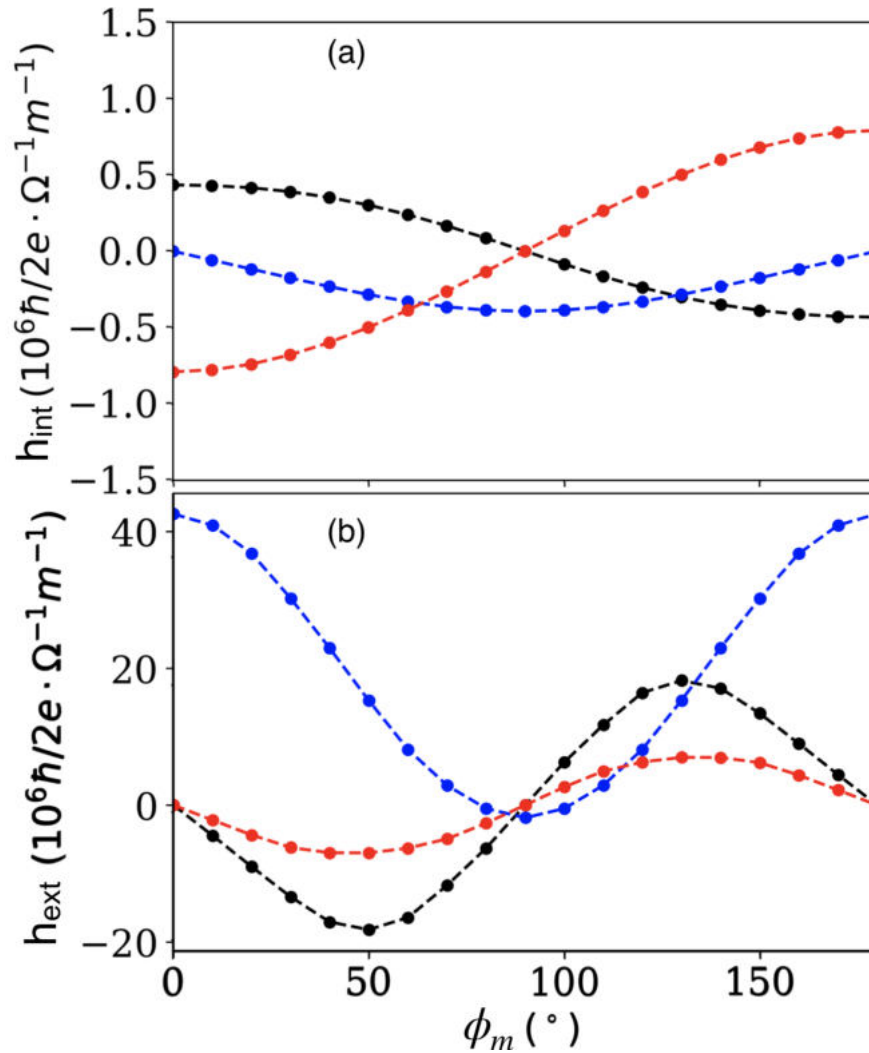


Figure 5.7. – Angular dependence of the intrinsic (top) and extrinsic (bottom) spin-orbit field components when the magnetization is rotated in the (x, y) plane. The black, blue and red curves represent the x, y and z components of the effective fields, correspondingly.

5. Unconventional Responses in Trigonal Crystals – 5.1. Spin-Orbit Torque for Field Free Switching in C_{3v} crystals

The realistic simulations illustrated in Fig.5.7 have a good agreement with our symmetry prognosis in (5.32-5.33). The intrinsic spin-orbit torque is composed of the damping-like torque (h_z) and the "3m" torque (h_x, h_y), with $h_{3m}^{\parallel}/h_{DL}^z \sim 0.67$, indicating that the "3m" torque is about the same order of magnitude as the damping-like torque. The extrinsic torque is one order of magnitude larger and is composed of the field-like torque and the planar Hall torque. The possible discrepancies between our numerical predictions and our symmetry analysis in Eqs. (5.32-5.33) can be explained by the neglect of higher-order terms in the character table expansion and the large values of cubic spin-orbit coupling. Nevertheless, we can extract $h_{PH}^{\parallel}/h_{FL}^{\parallel} \sim 1$ and $h_{PH}^z/h_{PH}^{\parallel} \sim 0.4$, meaning that the planar Hall torque is as large as the field-like torque and anisotropic, hence it must impact the magnetization switching and dynamics. We emphasize that the relative magnitude of the intrinsic to extrinsic torques is not meaningful since the extrinsic torque is inversely proportional to the disorder broadening Γ , which is taken as a (small) free parameter in our model.

The presence of these unconventional torques is particularly interesting for applications as they not only enable field-free switching but also impact the current-driven auto-oscillations. Our minimal model suggests that C_{3v} crystals could host such torques. Nonetheless, we emphasize that this is not a sufficient condition. As a matter of fact, in a previous study, the computations of the spin-orbit torque in vanadium-based Janus transition metal dichalcogenides VSeTe do not display such torque, in spite of the similar crystal symmetries [293]. This absence was attributed to the fact that in this material, the electronic transport here is mostly driven by states at Γ -point and therefore the crystal symmetries are not *imprinted* on the Bloch states. In contrast, in the $L1_1$ CuPt the Fermi surface shows a very strong warping, indicating that the Bloch states have a strong symmetry character and enabling the onset of the "3m" torque as well as other unconventional torques. Since the indicator to the presence of this torque is the trigonal warping of the Fermi surface, many other materials could display such effects: For example, Bi-based topological insulators $(\text{Bi,Sb})_2(\text{Se,Te})_3$ [301, 302, 303], and Bi_4Te_3 [304], but also possibly in the recently grown $\text{LaAlO}_3/\text{EuTiO}_3/\text{SrTiO}_3$ all-oxide heterostructure [305].

We conclude the first part of this Chapter by emphasizing that other unconventional torques are yet to be found in low-symmetry crystals that could lead to original current-driven dynamics, as already reported in WTe_2/Py [129, 275, 276] and Fe_3GeTe_2 [11, 291]. In this context, one needs to keep in mind that the general form of the spin-orbit field used in this work is obtained via a low-order expansion of the character table that is formally valid only when the spin-orbit coupling is smaller than the exchange. In materials where the spin-orbit coupling and the exchange are of the same order of magnitude, much more complex torques are expected.

5.2. Chiral Hall Effect

As we emphasize in the introduction of this manuscript, the Hall effect necessitates the presence of an effective magnetic field to occur. The usual setup for its realization is an external magnetic field or a magnetization perpendicular to the applied electric field, something that is commonly allowed by Neumann principle and Onsager reciprocity. Nevertheless, the symmetry analysis could also suggest innovative arrangements that defy the regular and anomalous Hall effect. Inspired on Juretschke's early predictions about the conductivity coefficients in Antimony, introducing an identical technique about 50 years ago [306], in this work we write the full conductivity tensor and reveal the microscopic origin of the unconventional responses in trigonal magnetic crystals. In this frame, new experiments in CuPt/CoPt heterostructures performed by Prof. Jingsheng Chen and his team, in the National University of Singapore (NUS), demonstrate that a Hall effect is guaranteed by symmetry, when the external magnetic field and the electric field are applied *collinearly*. Exceptionally, although antisymmetric in both \vec{B} and \vec{m} , this Hall effect is symmetric when both \vec{B} and \vec{m} change sign, in a similar manner to what was reported in the magnetic Weyl semimetal $\text{Co}_3\text{Sn}_2\text{S}_2$ [83]. Accordingly, we entitle this contribution as the **chiral Hall effect (CHE)**. Regarding its microscopic origin, whereas $\text{Co}_3\text{Sn}_2\text{S}_2$ is centrosymmetric and it has been claimed a connection between CHE observed here and the tilting of the Weyl nodes, in our case we can show that its origin is (again) related to the trigonal warping of the Fermi surface. Applying the same symmetry considerations through the Invariant Theory, tight binding model calculations and realistic simulations in the system, we elucidate the elementary role of cubic Rashba spin-orbit interaction and a proper band filling to observe the CHE.

This Chapter's section is organized as follows: In subsection 5.2.1 we present the expression for the conductivity tensor, identifying the CHE as one of the terms in our expansion. Then, in subsection 5.2.2 we implement model calculations to verify the microscopic origin of the CHE and its angular dependence with respect to the electric field and magnetic field angles. In subsection 5.2.3 I discuss the realistic calculations performed by Dr. Armando Pezo to corroborate our theory in a more realistic scenario. Finally, I discuss our findings about the CHE and its further implications. This work is expected to be published in Physical Review Letters.

5.2.1. Symmetry Analysis

Firstly, we apply the Invariant Theory to find the transverse current in a system subjected to an in-plane electric field $\vec{E} = E_x\hat{x} + E_y\hat{y}$ and an in-plane magnetic field $\vec{B} = B_x\hat{x} + B_y\hat{y}$ (The magnetic field \vec{B} and the magnetization \vec{m} play the same role in our expansion, because they are both axial vectors). In order to mimic the features of 2-D perpendicularly magnetized heterostructures, such as the CuPt/CoPt mentioned before, we also take into account an out-of plane magnetization m_z . Besides, we perform symmetry calculations taking into account a mirror symmetry along \hat{x} rather

5. Unconventional Responses in Trigonal Crystals – 5.2. Chiral Hall Effect

than \hat{y} to compare directly with the experiment. Then, applying the symmetry analysis up to first order in electric field and third order in magnetic components, the in-plane polar current is given by

$$\begin{aligned}
\vec{J} &= m_z \hat{z} \times \vec{E} + \{(E_x B_x - E_y B_y) \hat{x} - (E_x B_y + E_y B_x) \hat{y}\} + m_z^2 \vec{E} \\
&+ m_z^3 \hat{z} \times \vec{E} + m_z^2 [\{E_x B_x - E_y B_y\} \hat{x} - \{E_x B_y + E_y B_x\} \hat{y}] \\
&+ B_x (B_x^2 - 3B_y^2) \vec{E} + B_y (3B_x^2 - B_y^2) (\hat{z} \times \vec{E}) \\
&+ \left[\{E_x B_x (B_x^2 - 3B_y^2) + E_y B_y (3B_x^2 - B_y^2)\} \hat{x} - \{E_x B_y (3B_x^2 - B_y^2) - E_y B_x (B_x^2 - 3B_y^2)\} \hat{y} \right] \\
&+ \left[\{E_x B_x (B_x^2 - 3B_y^2) - E_y B_y (3B_x^2 - B_y^2)\} \hat{x} + \{E_x B_y (3B_x^2 - B_y^2) + E_y B_x (B_x^2 - 3B_y^2)\} \hat{y} \right] \\
&+ m_z \left[\{E_y (B_x^2 - B_y^2) - 2E_x B_x B_y\} \hat{x} + \{E_x (B_x^2 - B_y^2) + 2E_y B_x B_y\} \hat{y} \right]. \tag{5.34}
\end{aligned}$$

Then, the Hall current is obtained after projecting into the transverse direction $\hat{z} \times \hat{E}$ and imposing Onsager reciprocity. If we parametrize the electric and magnetic fields in the form $\vec{E} = E(\cos \phi_I \hat{x} + \sin \phi_I \hat{y})$ and $\vec{B} = B(\cos \phi_B \hat{x} + \sin \phi_B \hat{y})$, where ϕ_I (ϕ_B) is the angle between the electric (magnetic field) with respect to the \hat{x} axis, we deduce that the magnitude of the Hall current is

$$\begin{aligned}
J_H &= \vec{J} \cdot (\hat{z} \times \hat{E}), \\
&= \sigma_H \cos \theta + \sigma_H^\perp \cos^3 \theta + \sigma_H^\parallel \sin^3 \theta \sin 3\phi_B + \sigma_{PH} \sin^2 \theta \sin(2\phi_B - 2\phi_I) \\
&+ \sigma_\chi \sin \theta \cos \theta \cos(\phi_B + 2\phi_I), \tag{5.35}
\end{aligned}$$

being θ the angle between the magnetization or the magnetic field with respect to \hat{z} . Let us comment about the physics pertaining each term in Eq.(5.2.2). From left to right, we first observe the regular anomalous Hall effect σ_H arising on the Berry curvature. In fact, the regular Hall effect must exhibit the same symmetry. Second, σ_H^\perp is an out-of plane correction to σ_H that appears when the magnetization has an out-of plane component along \hat{z} . In contrast, the in-plane correction to σ_H , i.e. σ_H^\parallel is different from zero whenever the applied magnetic field or the magnetization display an in-plane component, and it also follows a 3-fold rotation as a function of the magnetic angle. The fourth term is the planar Hall effect that is non zero as soon as $\theta \neq 0, \pi$. Besides, this response is also non zero if $\phi_B - \phi_I \neq 0, \pi/2$. In other words, the planar Hall effect requires the electric and magnetic fields neither aligned nor perpendicular to each other. Last but not least, we obtain the so-called "chiral Hall effect" in the trigonal crystal: It needs both in-plane and out-of plane magnetic components, which in this case are represented by (B_x, B_y, m_z) . Moreover, it is non zero even though $\phi_B - \phi_I = 0, \pi/2$. We reckon this expression as the most symmetry dependent term in the trigonal crystal, allowing multiple configurations between the external fields that are forbidden for the other contributions. Setting $\phi_I = \phi_B$ for both fields parallel between each other, Eq.(5.2.2) becomes

$$J_H = \sigma_H \cos \theta + \sigma_H^\perp \cos^3 \theta + \sigma_H^\parallel \sin^3 \theta \sin 3\phi_B + \sigma_\chi \sin \theta \cos \theta \cos 3\phi_B. \quad (5.36)$$

5.2.2. Model Calculations

Regarding the transport in this system, the expression for the linear conductivity in Eq.(5.35) contains a few subtleties that we mean to clarify. When the electric field is applied in a given angle ϕ_I with respect to, say, \hat{x} , the intrinsic Berry curvature identity

$$\sigma_{xy} = \frac{e^2}{\hbar} \sum_n \int_{BZ} \frac{d^2 k}{4\pi^2} \Omega_{n\mathbf{k}}^z f_{n\mathbf{k}} \quad (5.37)$$

is only capable to give us information about the terms that are independent of ϕ_I , because the corresponding current is only proportional to $\hat{z} \times \vec{E}$. To put it in the language of the Invariant Theory, it just retains terms belonging to the A_2 representation. Then, the usual conductivity coefficient is the source of the well-known intrinsic anomalous Hall effect σ_H and its anisotropic corrections (in or out-of plane) σ_H^\perp and σ_H^\parallel , respectively. Accordingly, the only explanation for the planar Hall effect and the CHE is an extrinsic mechanism collecting the transverse current upon the injection of \vec{E} . Defining the injected (parallel) and transverse (perpendicular) projections of the velocity operator as

$$\hat{v}_\parallel = (\hat{E} \cdot \hat{v}) = \hat{v}_x \cos \phi_E + \hat{v}_y \sin \phi_E, \quad (5.38)$$

$$\hat{v}_\perp = (\hat{z} \times \hat{E}) \cdot \hat{v} = -\hat{v}_x \sin \phi_E + \hat{v}_y \cos \phi_E, \quad (5.39)$$

the extrinsic contribution to the Hall conductivity, recasting Eq.(2.42), is

$$\sigma_H^{Ext} = \frac{e^2}{4\pi\hbar} \int d\epsilon \partial_\epsilon f(\epsilon) \text{Re}[\text{Tr} \{ \hat{v}_\parallel (G^R - G^A) \hat{v}_\perp (G^R - G^A) \}], \quad (5.40)$$

where a k-dependent integration is implicit. We verify the existence of the extrinsic terms predicted by symmetry considerations using the tight binding model defined in subsection 5.1.3, with an appropriate adaptation of the mirror symmetry along \hat{x} rather than \hat{y} . Our results for the case $\phi_I = 0^\circ$ and $\phi_I = \phi_M = \phi_B$ are depicted in Figs. 5.8 and 5.9, respectively. As we notice from Fig. 5.8(a), at low band filling the conductivity is dominated by the Planar Hall effect, describing a 2-fold oscillation that is slightly deviated by σ_χ when $\phi_I = 0^\circ$ and possibly other terms that are not included in our expansion. On the other hand, at high band filling [Fig. 5.8(b)] the conductivity is dominated by σ_χ , with a clear 1-fold oscillation that matches our symmetry considerations. Besides, we identify that whereas σ_{PH} does not require cubic spin-orbit to appear, σ_χ does. On the other hand, when the electric and magnetic field rotate together, i.e, $\phi_I = \phi_B$, at low band filling [Fig. 5.9 (a)] the conductivity gives us an angular dependence that cannot be accounted for in our symmetry analysis. We attribute this fact to higher order terms in the expansion since its magnitude is

5. Unconventional Responses in Trigonal Crystals – 5.2. Chiral Hall Effect

very small and cannot be explained by the planar Hall effect. Most importantly, at high band filling [Fig. 5.9 (b)] we find a 3-fold oscillation if $t_{R3} \neq 0$, revealing that a signature for the CHE is the trigonal warping of the Fermi surface in these systems. In order to corroborate our prediction in a realistic scenario, we describe the results obtained from DFT simulations in the next subsection.

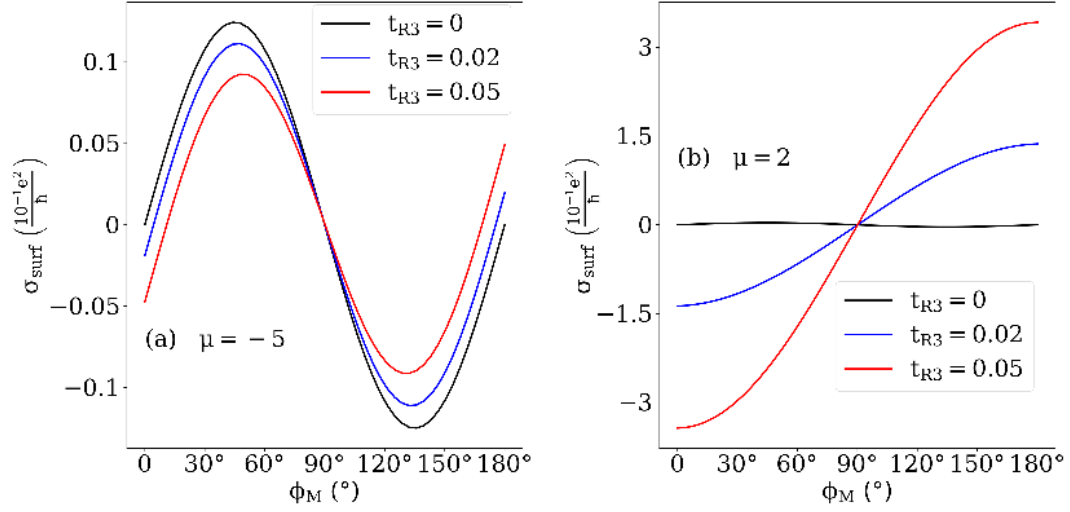


Figure 5.8. – Extrinsic contribution to the Hall conductivity as a function of the magnetization angle ϕ_M , when $\phi_I = 0^\circ$. We compute this term for the case $t = 1$, $t_R = 0.1t$ and $\Delta = 0.5t$, fixing $\theta = 10^\circ$ and $\Gamma = 0.1t$.

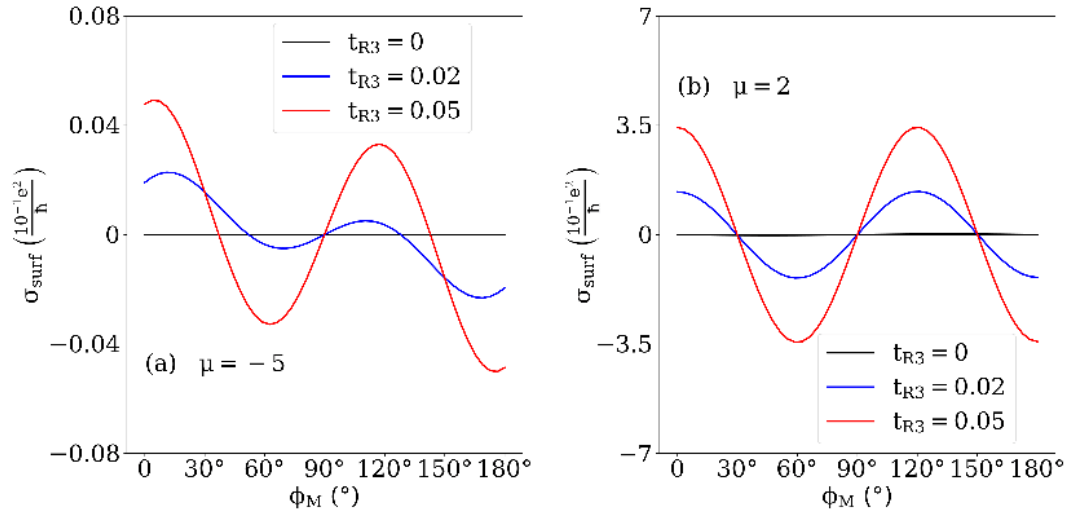


Figure 5.9. – Extrinsic contribution to the Hall conductivity as a function of the magnetization angle ϕ_M , when $\phi_I = \phi_M$. We compute this term for the case $t = 1$, $t_R = 0.1t$ and $\Delta = 0.5t$, fixing $\theta = 10^\circ$ and $\Gamma = 0.1t$.

5.2.3. Realistic Simulations

In this subsection the existence of the CHE in a realistic scenario is demonstrated. The realistic simulations were performed by Dr. Armando Pezo, and we include it here for the sake of completeness. In complete analogy to the case of the spin-orbit torque, a slab system of CuPt/Co grown along the $L1_1$ direction composed of 12 layers is considered, within the frame of a fully relativistic density functional theory. The SOC is described with a fully relativistic pseudo-potential formulation, using the generalized gradient approximation (GGA) for the exchange correlation functional. The calculations are converged for a 400 Ry plane-wave cut-off for the real-space grid with a $13 \times 13 \times 1$ k-point sampling for the Brillouin zone. In addition, the conjugate gradient algorithm was applied to minimize the atomic forces below 0.01 eV/\AA . The extrinsic contribution to the Hall conductivity is computed by taking Eq.(5.40) for same instances taken into account for the model calculations. First, when the electric field is along \hat{x} and $\theta = 10^\circ$, the results are reported as a function of the magnetization angle in Fig.5.10. Here the conductivity coefficient follows a combination between a two-fold and a one-fold oscillation, which is expected to be an interplay between the Planar Hall effect and the projection of the CHE in the direction of the electric field fixed before. This profile matches reasonably with the symmetry analysis shown by Eq.(5.35).

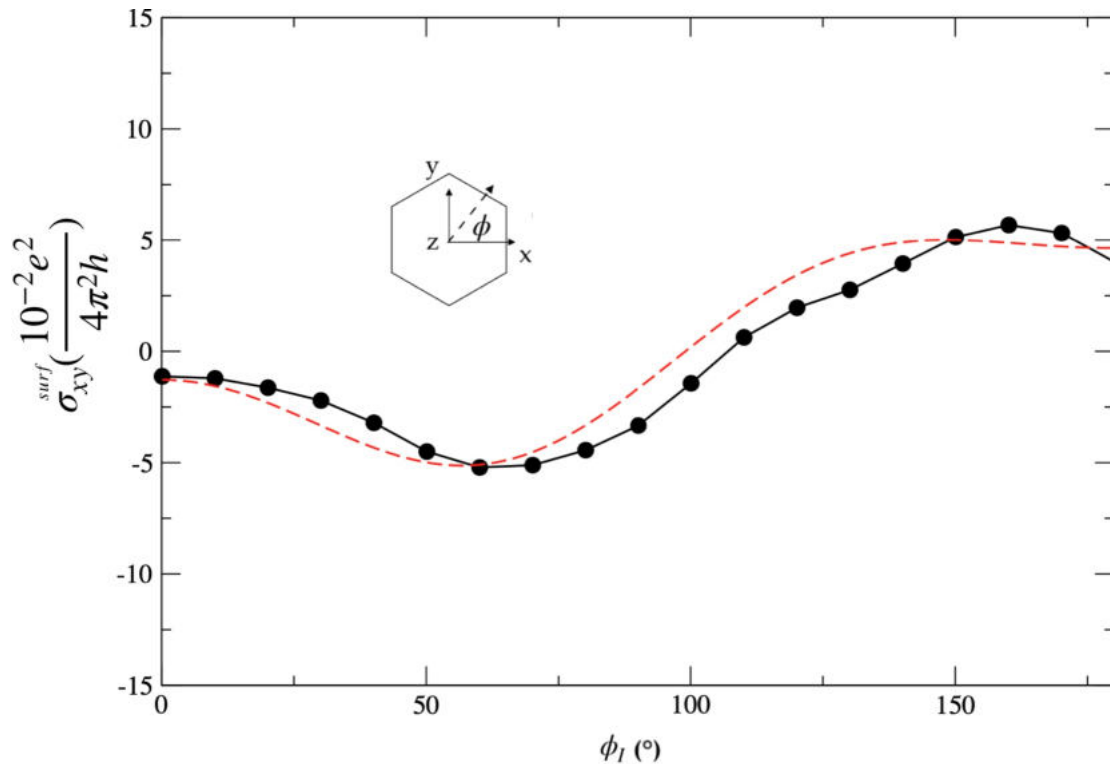


Figure 5.10. – CHE for the realistic simulation as a function of the magnetization angle, when $\phi_I = 0^\circ$ (black line). Dotted red line shows the symmetry prediction.

5. Unconventional Responses in Trigonal Crystals – 5.2. Chiral Hall Effect

Second, the extrinsic Hall conductivity is calculated by using Eq.(5.40), now with the constrain that the electric and in-plane magnetization angles rotates in the (x,y) in the same rate, when the inclination of the out-of plane magnetization is $\theta = 10^\circ$. Our findings are summarized by Fig.5.11. Here a 3-fold oscillation appears clearly, putting in evidence the manifestation of the CHE in these samples. Although a small mismatch exists between the numerical calculation and the 3-fold rotation predicted by the Invariant Theory, the difference can be explained by noticing that the expansion in electric and magnetization components is a perturbative approach, which typically relies on the fact that the cubic-spin orbit coupling is much smaller than the magnetic exchange. If the Fermi level is larger enough for this case, and thus the trigonal warping is strong, then it is natural to observe a deviation from what we introduce through symmetry considerations.

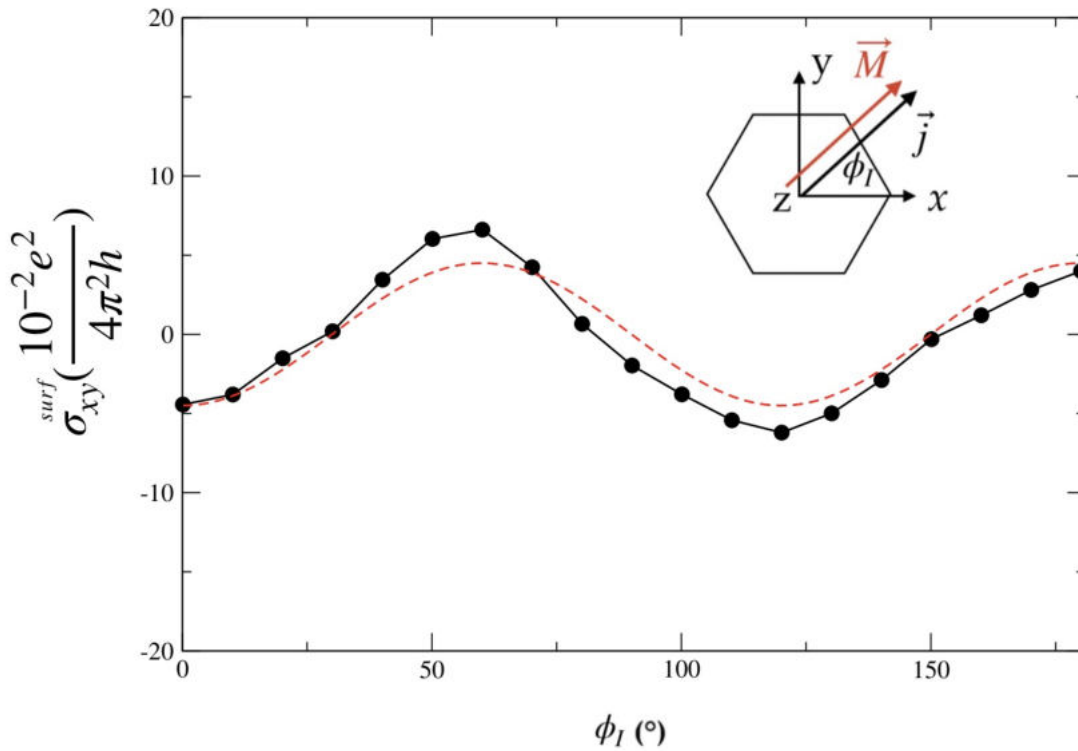


Figure 5.11. – CHE for the realistic simulation as a function of the magnetization angle, when $\phi_I = \phi_B$ (black lines). Dotted red line shows the corresponding symmetry prediction.

5.3. Conclusions and Prospects

In this chapter we deduce that the trigonal warping of the Fermi surface can be used as a fingerprint of the **CHE** and several unconventional spin-orbit torques in crystals with C_{3v} symmetry point group. For the former case, it is important to notice that the **CHE** permits a transverse current when the electric and magnetic fields injected are aligned between them in the presence of an out-of plane magnetization. The corresponding current is antisymmetric in both the applied magnetic field and the magnetization. In the latter instance, maybe the most important torque detected throughout this analysis is the h_{3m} torque component, which is able to produce deterministic field-free switching. The effective field found here is very important to improve the efficiency in realistic systems that can be designed for new memory devices.

In the case of the symmetry dependent Hall effect identified here, its extrinsic nature coincides to what is expected from the semiclassical formalism. Nevertheless, during this work we did not make any particular assumption about the scattering mechanism governing this contribution. Then, one could wonder how side-jump or skew scattering mechanisms arising from spin-orbit coupled impurities might influence the chiral Hall effect. From the semiclassical viewpoint, these additional ingredients should be accounted for in the distribution function through the Boltzmann equation and in the wave-function itself. In the Green function formalism, this should be included as an initial assumption for the self-energy, before solving the Dyson equations written in Keldysh formalism, for example. Traditionally, the anomalous transport and damping-like torques (i.e., torque that are even in magnetization) are either associated with **BC** or with skew and side-jump scattering. An interesting research direction would be to consider how impurity scattering and **BC** can cooperate to bring about new features that cannot be described from the mechanisms presented earlier.

As far as the spin-orbit fields are concerned, the impact of the unconventional torque components on the magnetization undoubtedly deserves further analysis. For instance, the chiral Hall torques obtained from symmetry analysis could bring interesting new features such as original current-frequency tuning or unexpected forms of oscillations. Of course, a better understand of the conditions under which these new fields appear in experiments, and possibly dominate over the conventional torque components, is necessary.

5. Unconventional Responses in Trigonal Crystals – 5.3. Conclusions and Prospects

A natural question that arises is whether there is a unique dependence of the responses depicted on the warping of the Fermi surface. In the light of a previous work in the magnetic WSM $\text{Co}_3\text{Sn}_2\text{S}_2$ [83], this does not seem to be the case as this material exhibits CHE and possesses inversion symmetry (it belongs to the D_{3d} symmetry point group). The challenge is to verify whether this effect can be attributed to the physics of the Weyl points in this system or to a different mechanism that can be tracked down to the Fermi surface or the electronic band structure. This system cannot accommodate the spin-orbit torques, unless we are able to design a slab, but it is still unclear if the unusual torques predicted in this work can also be only attributed to the warping of the Fermi surface. It seems that is not the case since VSeTe_2 belongs to C_{3v} and the "3m" torque is absent [293]. Despite of the relative match between our symmetry analysis, model and realistic calculations, it is straightforward to observe that it will occur if the cubic Rashba term is much smaller than the magnetic exchange. How large is the range of validity of the approximation also needs to be further explored. Assuming that this relation holds, materials with C_{nv} , $n \neq 3$ symmetry point group are fascinating platforms that could be addressed with the same reasoning, in order to investigate new sources of spin-orbit torques that arise on the crystalline symmetries of the samples. In this sense, the emerging contributions would be strongly dependent on the n -fold rotation of the crystal under consideration.

6. General Conclusion

Summary

In conclusion, in this doctoral Thesis we present a theoretical investigation of non-linear transport phenomena in quantum materials and heterostructures. Here, we must emphasize the growing importance of higher-order effects in electronic transport and spin-orbitronics for the elaboration of novel electronic devices. From the symmetry perspective, we show that nonlinear effects at higher orders in electric field can even appear in non-magnetic materials with the additional absence of certain symmetries of the system. One of the most remarkable cases in this context is the second order Hall effect, where a Hall current emerges as the leading order contribution to the transport as long as inversion symmetry is broken. At the third order in electric field, which is an ongoing topic of our research, the current could appear even in the presence of time reversal and inversion symmetries. We are developing further exploration to understand their nature at the minimal and lattice level, in order to extend it properly for realistic calculations.

The analysis of higher order responses also uncover several properties of quantum materials encoded in the quantum geometry. In non-magnetic materials this cannot be detected in linear response regime through the Berry curvature. Firstly, in the case of time reversal invariant Weyl semimetals, we demonstrate how the surface states impact the nonlinear Hall effect driven by the Berry curvature dipole [1]. We observe a strong thickness dependence of the conductivity coefficients in the type II regime, where the Weyl cones are strongly tilted, determined by the slab geometry under consideration. The enhancement of the nonlinear response in one of the slabs adopted is attributed to an increase of the relative number of states at the surface rather than the bulk, and the topological surface states exhibit a smaller impact than the trivial states on the transport. This behavior can be followed in experiments by studying the Berry curvature dipole as a function of the thickness of the slab. For all these reasons, we encourage the readers to explore the nonlinear Hall signal driven by the Berry curvature dipole in other material interfaces and heterostructures that are not necessarily topological.

Secondly, we investigate the electric-induced magneto-optical Kerr effect as a probe of the second order Hall effect in non-magnetic materials. Here, we demonstrate that the Kerr angle can reach values of the order of nanoradians, even in absence of spin-orbit coupling. The values of the [MOKE](#) efficiency obtained are comparable

with previous experiments. In addition, we analyze the relation between the non-equilibrium orbital magnetization and the BCD in selected systems, finding that the ratio between both quantities is proportional to the Fermi energy in the vicinity of Dirac cones and the gap of topological insulators. In view of this work, we thus conclude that the nonlinear MOKE response not only constitutes an evidence of the second order Hall effect, but it could serve as a hallmark of the non-equilibrium orbital accumulation in light metals.

Finally and as we commented earlier, the possible emergence of a given response is determined by the symmetries of the crystal. In this frame, and since higher order responses are not limited to electric components, we study the spin-orbit torque's family in trigonal crystals by means of the Invariant Theory [8]. Here, a wide variety of new torques induced by a linear electric field are predicted up to third order in magnetization components, going beyond the regular field-like and damping-like contributions. Particularly, one of them is able to promote the field-free switching of the perpendicular magnetization in trigonal ferromagnets, which can be used in the fabrication of more efficient magnetic memory devices. The fact that a given response is allowed by symmetry is not sufficient to be observed it, and for this instance we deduce that the new torques are a consequence of the interplay between the cubic spin-orbit coupling and a proper band filling, resulting in the trigonal warping of the Fermi surface. A similar work was performed to explain the origin of an unconventional Hall effect (tagged as the chiral Hall effect) in the same systems, where the external electric and magnetic field are aligned collinearly. Here we conclude that the chiral Hall effect is allowed by symmetry and its microscopic origin relies on the cubic spin-orbit coupling of the system. Therefore, the chiral Hall effect dominates at high band filling when the trigonal warping of the Fermi surface is sizable.

References

- [1] Diego García Ovalle, Armando Pezo, and Aurélien Manchon. “Influence of the surface states on the nonlinear Hall effect in Weyl semimetals”. In: *Phys. Rev. B* 106 (21 Dec. 2022), p. 214435. DOI: [10.1103/PhysRevB.106.214435](https://doi.org/10.1103/PhysRevB.106.214435). URL: <https://link.aps.org/doi/10.1103/PhysRevB.106.214435> (cit. on pp. 10, 67, 132).
- [2] Guilhem Manchon, Sumit Ghosh, Cyrille Barreteau, et al. “Semirealistic tight-binding model for spin-orbit torques”. In: *Phys. Rev. B* 101 (17 May 2020), p. 174423. DOI: [10.1103/PhysRevB.101.174423](https://doi.org/10.1103/PhysRevB.101.174423). URL: <https://link.aps.org/doi/10.1103/PhysRevB.101.174423> (cit. on pp. 10, 68).
- [3] Dennis Wawrzik, Jih-Shih You, Jorge I. Facio, et al. “Infinite Berry Curvature of Weyl Fermi Arcs”. In: *Phys. Rev. Lett.* 127 (5 July 2021), p. 056601. DOI: [10.1103/PhysRevLett.127.056601](https://doi.org/10.1103/PhysRevLett.127.056601). URL: <https://link.aps.org/doi/10.1103/PhysRevLett.127.056601> (cit. on pp. 11, 66).
- [4] C. Stamm, C. Murer, M. Berritta, et al. “Magneto-Optical Detection of the Spin Hall Effect in Pt and W Thin Films”. In: *Phys. Rev. Lett.* 119 (8 Aug. 2017), p. 087203. DOI: [10.1103/PhysRevLett.119.087203](https://doi.org/10.1103/PhysRevLett.119.087203). URL: <https://link.aps.org/doi/10.1103/PhysRevLett.119.087203> (cit. on pp. 13, 88, 96).
- [5] Y. K. Kato, R. C. Myers, A. C. Gossard, et al. “Observation of the spin Hall effect in semiconductors.” In: *Science (New York, N.Y.)* 306 (Dec. 2004), p. 1910. ISSN: 1095-9203. DOI: [10.1126/science.1105514](https://doi.org/10.1126/science.1105514). URL: <http://www.ncbi.nlm.nih.gov/pubmed/15539563> (cit. on pp. 13, 87, 96).
- [6] Joolee Son, Kyung-Han Kim, Y. H. Ahn, et al. “Strain Engineering of the Berry Curvature Dipole and Valley Magnetization in Monolayer MoS₂”. In: *Phys. Rev. Lett.* 123 (3 July 2019), p. 036806. DOI: [10.1103/PhysRevLett.123.036806](https://doi.org/10.1103/PhysRevLett.123.036806). URL: <https://link.aps.org/doi/10.1103/PhysRevLett.123.036806> (cit. on pp. 13, 35–37, 63, 88, 96).
- [7] Liang Fu. “Hexagonal Warming Effects in the Surface States of the Topological Insulator Bi₂Te₃”. In: *Phys. Rev. Lett.* 103 (26 Dec. 2009), p. 266801. DOI: [10.1103/PhysRevLett.103.266801](https://doi.org/10.1103/PhysRevLett.103.266801). URL: <https://link.aps.org/doi/10.1103/PhysRevLett.103.266801> (cit. on pp. 14, 33).
- [8] Diego García Ovalle, Armando Pezo, and Aurélien Manchon. “Spin-orbit torque for field-free switching in C_{3v} crystals”. In: *Phys. Rev. B* 107 (9 Mar. 2023), p. 094422. DOI: [10.1103/PhysRevB.107.094422](https://doi.org/10.1103/PhysRevB.107.094422). URL: <https://link.aps.org/doi/10.1103/PhysRevB.107.094422> (cit. on pp. 15, 116, 133).

- [9] Melvin J. Lax. *Symmetry Principles in Solid State and Molecular Physics*. Dover, UK: Dover Publications, 2012 (cit. on pp. 15, 41, 109, 110).
- [10] Liang Liu, Chenghang Zhou, Xinyu Shu, et al. “Symmetry-dependent field-free switching of perpendicular magnetization”. In: *Nature Nanotechnology* 16.3 (Mar. 2021), pp. 277–282. ISSN: 1748-3395. DOI: [10.1038/s41565-020-00826-8](https://doi.org/10.1038/s41565-020-00826-8). URL: <https://doi.org/10.1038/s41565-020-00826-8> (cit. on pp. 15, 40, 107, 108, 111, 112, 121).
- [11] Øyvind Johansen, Vettle Risinggård, Asle Sudbø, et al. “Current Control of Magnetism in Two-Dimensional Fe₃GeTe₂”. In: *Phys. Rev. Lett.* 122 (21 May 2019), p. 217203. DOI: [10.1103/PhysRevLett.122.217203](https://doi.org/10.1103/PhysRevLett.122.217203). URL: <https://link.aps.org/doi/10.1103/PhysRevLett.122.217203> (cit. on pp. 15, 40, 107, 111, 123).
- [12] Huiying Liu, Jianzhou Zhao, Yue-Xin Huang, et al. “Berry connection polarizability tensor and third-order Hall effect”. In: *Phys. Rev. B* 105 (4 Jan. 2022), p. 045118. DOI: [10.1103/PhysRevB.105.045118](https://doi.org/10.1103/PhysRevB.105.045118). URL: <https://link.aps.org/doi/10.1103/PhysRevB.105.045118> (cit. on pp. 16, 25, 38, 63).
- [13] E. H. Hall. “On a New Action of the Magnet on Electric Currents”. In: *American Journal of Mathematics* 2.3 (1879), pp. 287–292. ISSN: 00029327, 10806377. DOI: [10.2307/2369245](https://doi.org/10.2307/2369245). URL: <http://www.jstor.org/stable/2369245> (visited on 11/21/2023) (cit. on p. 24).
- [14] E.H. Hall. “XVIII. On the “Rotational Coefficient” in nickel and cobalt”. In: *The London, Edinburgh, and Dublin Philosophical Magazine and Journal of Science* 12.74 (1881), pp. 157–172. DOI: [10.1080/14786448108627086](https://doi.org/10.1080/14786448108627086). URL: <https://doi.org/10.1080/14786448108627086> (cit. on p. 24).
- [15] Naoto Nagaosa, Jairo Sinova, Shigeki Onoda, et al. “Anomalous Hall effect”. In: *Review of Modern Physics* 82 (May 2010), p. 1539. ISSN: 0034-6861. DOI: [10.1103/RevModPhys.82.1539](https://doi.org/10.1103/RevModPhys.82.1539). URL: <http://link.aps.org/doi/10.1103/RevModPhys.82.1539> (cit. on pp. 24, 25, 28, 50, 90).
- [16] E. Ramsden. *Hall-Effect Sensors: Theory and Application*. Elsevier Science, 2011. ISBN: 9780080523743. URL: <https://books.google.fr/books?id=R8VAjMitH1QC> (cit. on p. 24).
- [17] David Vanderbilt. *Berry Phases in Electronic Structure Theory: Electric Polarization, Orbital Magnetization and Topological Insulators*. Cambridge University Press, 2018. DOI: [10.1017/9781316662205](https://doi.org/10.1017/9781316662205) (cit. on p. 24).
- [18] F. D. M. Haldane. “Model for a Quantum Hall Effect without Landau Levels: Condensed-Matter Realization of the “Parity Anomaly””. In: *Phys. Rev. Lett.* 61 (18 Oct. 1988), pp. 2015–2018. DOI: [10.1103/PhysRevLett.61.2015](https://doi.org/10.1103/PhysRevLett.61.2015). URL: <https://link.aps.org/doi/10.1103/PhysRevLett.61.2015> (cit. on p. 24).

- [19] Masaru Onoda and Naoto Nagaosa. “Quantized Anomalous Hall Effect in Two-Dimensional Ferromagnets: Quantum Hall Effect in Metals”. In: *Phys. Rev. Lett.* 90 (20 May 2003), p. 206601. DOI: [10.1103/PhysRevLett.90.206601](https://doi.org/10.1103/PhysRevLett.90.206601). URL: <https://link.aps.org/doi/10.1103/PhysRevLett.90.206601> (cit. on p. 24).
- [20] Yuanbo Zhang, Yan-Wen Tan, Horst L. Stormer, et al. “Experimental observation of the quantum Hall effect and Berry’s phase in graphene”. In: *Nature* 438.7065 (Nov. 2005), pp. 201–204. ISSN: 1476-4687. DOI: [10.1038/nature04235](https://doi.org/10.1038/nature04235). URL: <https://doi.org/10.1038/nature04235> (cit. on p. 24).
- [21] C. L. Kane and E. J. Mele. “Quantum Spin Hall Effect in Graphene”. In: *Phys. Rev. Lett.* 95 (22 Nov. 2005), p. 226801. DOI: [10.1103/PhysRevLett.95.226801](https://doi.org/10.1103/PhysRevLett.95.226801). URL: <https://link.aps.org/doi/10.1103/PhysRevLett.95.226801> (cit. on p. 24).
- [22] C. L. Kane and E. J. Mele. “ Z_2 Topological Order and the Quantum Spin Hall Effect”. In: *Phys. Rev. Lett.* 95 (14 Sept. 2005), p. 146802. DOI: [10.1103/PhysRevLett.95.146802](https://doi.org/10.1103/PhysRevLett.95.146802). URL: <https://link.aps.org/doi/10.1103/PhysRevLett.95.146802> (cit. on p. 24).
- [23] B. Andrei Bernevig and Shou-Cheng Zhang. “Quantum Spin Hall Effect”. In: *Phys. Rev. Lett.* 96 (10 Mar. 2006), p. 106802. DOI: [10.1103/PhysRevLett.96.106802](https://doi.org/10.1103/PhysRevLett.96.106802). URL: <https://link.aps.org/doi/10.1103/PhysRevLett.96.106802> (cit. on p. 24).
- [24] K. S. Novoselov, Z. Jiang, Y. Zhang, et al. “Room-Temperature Quantum Hall Effect in Graphene”. In: *Science* 315.5817 (2007), pp. 1379–1379. DOI: [10.1126/science.1137201](https://doi.org/10.1126/science.1137201). URL: <https://www.science.org/doi/abs/10.1126/science.1137201> (cit. on p. 24).
- [25] Tomas Jungwirth, Jörg Wunderlich, and Kamil Olejník. “Spin Hall effect devices”. In: *Nature Materials* 11.5 (May 2012), pp. 382–390. ISSN: 1476-4660. DOI: [10.1038/nmat3279](https://doi.org/10.1038/nmat3279). URL: <https://doi.org/10.1038/nmat3279> (cit. on p. 24).
- [26] Jairo Sinova, Sergio O. Valenzuela, J. Wunderlich, et al. “Spin Hall effects”. In: *Rev. Mod. Phys.* 87 (4 Oct. 2015), pp. 1213–1260. DOI: [10.1103/RevModPhys.87.1213](https://doi.org/10.1103/RevModPhys.87.1213). URL: <https://link.aps.org/doi/10.1103/RevModPhys.87.1213> (cit. on pp. 24, 39, 40, 86).
- [27] D. J. Thouless, M. Kohmoto, M. P. Nightingale, et al. “Quantized Hall Conductance in a Two-Dimensional Periodic Potential”. In: *Phys. Rev. Lett.* 49 (6 Aug. 1982), pp. 405–408. DOI: [10.1103/PhysRevLett.49.405](https://doi.org/10.1103/PhysRevLett.49.405). URL: <https://link.aps.org/doi/10.1103/PhysRevLett.49.405> (cit. on p. 25).
- [28] M.V. Berry. “Quantal phase factors accompanying adiabatic changes”. In: *Proc. R. Soc. Lond.* (1984). DOI: <https://doi.org/10.1098/rspa.1984.0023>. URL: <https://royalsocietypublishing.org/doi/abs/10.1098/rspa.1984.0023> (cit. on pp. 25, 27, 28, 170).

- [29] M. Z. Hasan and C. L. Kane. “Colloquium: Topological insulators”. In: *Rev. Mod. Phys.* 82 (4 Nov. 2010), pp. 3045–3067. DOI: [10.1103/RevModPhys.82.3045](https://doi.org/10.1103/RevModPhys.82.3045). URL: <https://link.aps.org/doi/10.1103/RevModPhys.82.3045> (cit. on p. 25).
- [30] N. P. Armitage, E. J. Mele, and Ashvin Vishwanath. “Weyl and Dirac semimetals in three-dimensional solids”. In: *Rev. Mod. Phys.* 90 (1 Jan. 2018), p. 015001. DOI: [10.1103/RevModPhys.90.015001](https://doi.org/10.1103/RevModPhys.90.015001). URL: <https://link.aps.org/doi/10.1103/RevModPhys.90.015001> (cit. on pp. 25, 65).
- [31] Inti Sodemann and Liang Fu. “Quantum Nonlinear Hall Effect Induced by Berry Curvature Dipole in Time-Reversal Invariant Materials”. In: *Phys. Rev. Lett.* 115 (21 Nov. 2015), p. 216806. DOI: [10.1103/PhysRevLett.115.216806](https://doi.org/10.1103/PhysRevLett.115.216806). URL: <https://link.aps.org/doi/10.1103/PhysRevLett.115.216806> (cit. on pp. 25, 33, 57, 63, 88, 90).
- [32] Ryuichi Shindou and Naoto Nagaosa. “Orbital Ferromagnetism and Anomalous Hall Effect in Antiferromagnets on the Distorted fcc Lattice”. In: *Phys. Rev. Lett.* 87 (11 Aug. 2001), p. 116801. DOI: [10.1103/PhysRevLett.87.116801](https://doi.org/10.1103/PhysRevLett.87.116801). URL: <https://link.aps.org/doi/10.1103/PhysRevLett.87.116801> (cit. on pp. 25, 28).
- [33] Hua Chen, Qian Niu, and A H Macdonald. “Anomalous Hall Effect Arising from Noncollinear Antiferromagnetism”. In: *Physical Review Letters* 112 (Jan. 2014), p. 017205. ISSN: 0031-9007. DOI: [10.1103/PhysRevLett.112.017205](https://doi.org/10.1103/PhysRevLett.112.017205). URL: <http://link.aps.org/doi/10.1103/PhysRevLett.112.017205> (cit. on pp. 25, 28, 30).
- [34] Satoru Nakatsuji, Naoki Kiyohara, and Tomoya Higo. “Large anomalous Hall effect in a non-collinear antiferromagnet at room temperature”. In: *Nature* 527 (2015), p. 212. ISSN: 0028-0836. DOI: [10.1038/nature15723](https://doi.org/10.1038/nature15723). URL: <http://dx.doi.org/10.1038/nature15723> (cit. on pp. 25, 30, 88).
- [35] Ajaya K Nayak, Julia Erika Fischer, Binghai Yan Yan Sun, et al. “Large anomalous Hall effect driven by non-vanishing Berry curvature in non-collinear antiferromagnet Mn₃Ge”. In: *Science Advances* 2 (2016), e1501870. ISSN: 2375-2548. DOI: [10.1126/sciadv.1501870](https://doi.org/10.1126/sciadv.1501870). URL: <https://www.science.org/doi/10.1126/sciadv.1501870> (cit. on pp. 25, 30, 88).
- [36] Qiong Ma, Su-Yang Xu, Huitao Shen, et al. “Observation of the nonlinear Hall effect under time-reversal-symmetric conditions”. In: *Nature* 565.7739 (Jan. 2019), pp. 337–342. ISSN: 1476-4687. DOI: [10.1038/s41586-018-0807-6](https://doi.org/10.1038/s41586-018-0807-6). URL: <https://doi.org/10.1038/s41586-018-0807-6> (cit. on pp. 25, 34, 81, 88, 91).
- [37] Kaifei Kang, Tingxin Li, Egon Sohn, et al. “Nonlinear anomalous Hall effect in few-layer WTe₂”. In: *Nature Materials* 18.4 (Apr. 2019), pp. 324–328. ISSN: 1476-4660. DOI: [10.1038/s41563-019-0294-7](https://doi.org/10.1038/s41563-019-0294-7). URL: <https://doi.org/10.1038/s41563-019-0294-7> (cit. on pp. 25, 34, 88, 91).

- [38] Lars Onsager. “Reciprocal Relations in Irreversible Processes. I.” In: *Phys. Rev.* 37 (4 Feb. 1931), pp. 405–426. DOI: [10.1103/PhysRev.37.405](https://doi.org/10.1103/PhysRev.37.405). URL: <https://link.aps.org/doi/10.1103/PhysRev.37.405> (cit. on p. 26).
- [39] Lars Onsager. “Reciprocal Relations in Irreversible Processes. II.” In: *Phys. Rev.* 38 (12 Dec. 1931), pp. 2265–2279. DOI: [10.1103/PhysRev.38.2265](https://doi.org/10.1103/PhysRev.38.2265). URL: <https://link.aps.org/doi/10.1103/PhysRev.38.2265> (cit. on p. 27).
- [40] W. H. Kleiner. “Space-Time Symmetry of Transport Coefficients”. In: *Phys. Rev.* 142 (2 Feb. 1966), pp. 318–326. DOI: [10.1103/PhysRev.142.318](https://doi.org/10.1103/PhysRev.142.318). URL: <https://link.aps.org/doi/10.1103/PhysRev.142.318> (cit. on p. 27).
- [41] W. H. Kleiner. “Space-Time Symmetry Restrictions on Transport Coefficients. II. Two Theories Compared”. In: *Phys. Rev.* 153 (3 Jan. 1967), pp. 726–727. DOI: [10.1103/PhysRev.153.726](https://doi.org/10.1103/PhysRev.153.726). URL: <https://link.aps.org/doi/10.1103/PhysRev.153.726> (cit. on p. 27).
- [42] W. H. Kleiner. “Space-Time Symmetry Restrictions on Transport Coefficients. III. Thermogalvanomagnetic Coefficients”. In: *Phys. Rev.* 182 (3 June 1969), pp. 705–709. DOI: [10.1103/PhysRev.182.705](https://doi.org/10.1103/PhysRev.182.705). URL: <https://link.aps.org/doi/10.1103/PhysRev.182.705> (cit. on p. 27).
- [43] M. Seemann, D. Ködderitzsch, S. Wimmer, et al. “Symmetry-imposed shape of linear response tensors”. In: *Phys. Rev. B* 92 (15 Oct. 2015), p. 155138. DOI: [10.1103/PhysRevB.92.155138](https://doi.org/10.1103/PhysRevB.92.155138). URL: <https://link.aps.org/doi/10.1103/PhysRevB.92.155138> (cit. on p. 27).
- [44] J. Železný, H. Gao, Aurélien Manchon, et al. “Spin-orbit torques in locally and globally noncentrosymmetric crystals: Antiferromagnets and ferromagnets”. In: *Phys. Rev. B* 95 (1 Jan. 2017), p. 014403. DOI: [10.1103/PhysRevB.95.014403](https://doi.org/10.1103/PhysRevB.95.014403). URL: <https://link.aps.org/doi/10.1103/PhysRevB.95.014403> (cit. on pp. 27, 107).
- [45] Robert Karplus and J. M. Luttinger. “Hall Effect in Ferromagnetics”. In: *Phys. Rev.* 95 (5 Sept. 1954), pp. 1154–1160. DOI: [10.1103/PhysRev.95.1154](https://doi.org/10.1103/PhysRev.95.1154). URL: <https://link.aps.org/doi/10.1103/PhysRev.95.1154> (cit. on p. 27).
- [46] Ganesh Sundaram and Qian Niu. “Wave-packet dynamics in slowly perturbed crystals: Gradient corrections and Berry-phase effects”. In: *Phys. Rev. B* 59 (23 June 1999), pp. 14915–14925. DOI: [10.1103/PhysRevB.59.14915](https://doi.org/10.1103/PhysRevB.59.14915). URL: <https://link.aps.org/doi/10.1103/PhysRevB.59.14915> (cit. on pp. 27, 52).
- [47] E. J. König, M. Dzero, A. Levchenko, et al. “Gyrotropic Hall effect in Berry-curved materials”. In: *Phys. Rev. B* 99 (15 Apr. 2019), p. 155404. DOI: [10.1103/PhysRevB.99.155404](https://doi.org/10.1103/PhysRevB.99.155404). URL: <https://link.aps.org/doi/10.1103/PhysRevB.99.155404> (cit. on pp. 28, 90).
- [48] L. Berger. “Side-Jump Mechanism for the Hall Effect of Ferromagnets”. In: *Phys. Rev. B* 2 (11 Dec. 1970), pp. 4559–4566. DOI: [10.1103/PhysRevB.2.4559](https://doi.org/10.1103/PhysRevB.2.4559). URL: <https://link.aps.org/doi/10.1103/PhysRevB.2.4559> (cit. on p. 28).

- [49] L. Berger. “Influence of spin-orbit interaction on the transport processes in ferromagnetic nickel alloys, in the presence of a degeneracy of the 3d band”. In: *Physica* 30.6 (1964), pp. 1141–1159. ISSN: 0031-8914. DOI: [https://doi.org/10.1016/0031-8914\(64\)90105-3](https://doi.org/10.1016/0031-8914(64)90105-3). URL: <https://www.sciencedirect.com/science/article/pii/0031891464901053> (cit. on p. 28).
- [50] Ncholu Manyala, Yvan Sidis, John F. DiTusa, et al. “Large anomalous Hall effect in a silicon-based magnetic semiconductor”. In: *Nature Materials* 3.4 (Apr. 2004), pp. 255–262. ISSN: 1476-4660. DOI: [10.1038/nmat1103](https://doi.org/10.1038/nmat1103). URL: <https://doi.org/10.1038/nmat1103> (cit. on p. 28).
- [51] Li Ye, Yuan Tian, Xiaofeng Jin, et al. “Temperature dependence of the intrinsic anomalous Hall effect in nickel”. In: *Phys. Rev. B* 85 (22 June 2012), p. 220403. DOI: [10.1103/PhysRevB.85.220403](https://doi.org/10.1103/PhysRevB.85.220403). URL: <https://link.aps.org/doi/10.1103/PhysRevB.85.220403> (cit. on p. 29).
- [52] Enke Liu, Yan Sun, Nitesh Kumar, et al. “Giant anomalous Hall effect in a ferromagnetic kagome-lattice semimetal”. In: *Nature Physics* 14.11 (Nov. 2018), pp. 1125–1131. ISSN: 1745-2481. DOI: [10.1038/s41567-018-0234-5](https://doi.org/10.1038/s41567-018-0234-5). URL: <https://doi.org/10.1038/s41567-018-0234-5> (cit. on p. 29).
- [53] Biao Meng, Hao Wu, Yang Qiu, et al. “Large anomalous Hall effect in ferromagnetic Weyl semimetal candidate PrAlGe”. In: *APL Materials* 7.5 (2019), p. 051110. DOI: [10.1063/1.5090795](https://doi.org/10.1063/1.5090795). URL: <https://doi.org/10.1063/1.5090795> (cit. on p. 29).
- [54] Meng Huang, Shanshan Wang, Zhaohao Wang, et al. “Colossal Anomalous Hall Effect in Ferromagnetic van der Waals CrTe₂”. In: *ACS Nano* 15.6 (June 2021), pp. 9759–9763. ISSN: 1936-0851. DOI: [10.1021/acsnano.1c00488](https://doi.org/10.1021/acsnano.1c00488). URL: <https://doi.org/10.1021/acsnano.1c00488> (cit. on p. 29).
- [55] Madhav Prasad Ghimire, Jorge I. Facio, Jhih-Shih You, et al. “Creating Weyl nodes and controlling their energy by magnetization rotation”. In: *Phys. Rev. Res.* 1 (3 Dec. 2019), p. 032044. DOI: [10.1103/PhysRevResearch.1.032044](https://doi.org/10.1103/PhysRevResearch.1.032044). URL: <https://link.aps.org/doi/10.1103/PhysRevResearch.1.032044> (cit. on p. 29).
- [56] Akihiro Ozawa and Kentaro Nomura. “Two-Orbital Effective Model for Magnetic Weyl Semimetal in Kagome-Lattice Shandite”. In: *Journal of the Physical Society of Japan* 88.12 (2019), p. 123703. DOI: [10.7566/JPSJ.88.123703](https://doi.org/10.7566/JPSJ.88.123703). URL: <https://doi.org/10.7566/JPSJ.88.123703> (cit. on p. 29).
- [57] Jie Liu, Linchao Ding, Liangcai Xu, et al. *Tuning the anomalous Nernst and Hall effects with shifting the chemical potential in Fe-doped and Ni-doped Co₃Sn₂S₂*. 2023. arXiv: [2303.08715](https://arxiv.org/abs/2303.08715) [cond-mat.str-el] (cit. on p. 29).

- [58] Mizuki Ohno, Susumu Minami, Yusuke Nakazawa, et al. “Maximizing intrinsic anomalous Hall effect by controlling the Fermi level in simple Weyl semimetal films”. In: *Phys. Rev. B* 105 (20 May 2022), p. L201101. DOI: [10.1103/PhysRevB.105.L201101](https://doi.org/10.1103/PhysRevB.105.L201101). URL: <https://link.aps.org/doi/10.1103/PhysRevB.105.L201101> (cit. on p. 30).
- [59] Shuo-Ying Yang, Yaojia Wang, Brenden R. Ortiz, et al. “Giant, unconventional anomalous Hall effect in the metallic frustrated magnet candidate, KV3Sb5”. In: *Science Advances* 6.31 (2020), eabb6003. DOI: [10.1126/sciadv.abb6003](https://doi.org/10.1126/sciadv.abb6003). URL: <https://www.science.org/doi/abs/10.1126/sciadv.abb6003> (cit. on p. 30).
- [60] Gang Xu, Biao Lian, and Shou-Cheng Zhang. “Intrinsic Quantum Anomalous Hall Effect in the Kagome Lattice Cs₂LiMn₃F₁₂”. In: *Phys. Rev. Lett.* 115 (18 Oct. 2015), p. 186802. DOI: [10.1103/PhysRevLett.115.186802](https://doi.org/10.1103/PhysRevLett.115.186802). URL: <https://link.aps.org/doi/10.1103/PhysRevLett.115.186802> (cit. on p. 30).
- [61] Chun-Chih Tseng, Xuetao Ma, Zhaoyu Liu, et al. “Anomalous Hall effect at half filling in twisted bilayer graphene”. In: *Nature Physics* 18.9 (Sept. 2022), pp. 1038–1042. ISSN: 1745-2481. DOI: [10.1038/s41567-022-01697-7](https://doi.org/10.1038/s41567-022-01697-7). URL: <https://doi.org/10.1038/s41567-022-01697-7> (cit. on p. 30).
- [62] J Kubler and C. Felser. “Non-collinear antiferromagnets and the anomalous Hall effect”. In: *Europhysics Letters (EPL)* 108 (2014), p. 67001. DOI: [10.1209/0295-5075/108/67001](https://doi.org/10.1209/0295-5075/108/67001). URL: <https://iopscience.iop.org/article/10.1209/0295-5075/108/67001> (cit. on p. 30).
- [63] V. Bonbien, Fengjun Zhuo, Akshaykumar Salimath, et al. “Topological Aspects of Antiferromagnets”. In: *Journal of Physics D: Applied Physics* 55 (2022), p. 103002. ISSN: 0022-3727. DOI: [10.1088/1361-6463/ac28fa](https://doi.org/10.1088/1361-6463/ac28fa). URL: <https://iopscience.iop.org/article/10.1088/1361-6463/ac28fa> (cit. on p. 30).
- [64] Christoph Sürgers, Wolfram Kittler, Thomas Wolf, et al. “Anomalous Hall effect in the noncollinear antiferromagnet Mn₅Si₃”. In: *AIP Advances* 6.5 (Mar. 2016), p. 055604. ISSN: 2158-3226. DOI: [10.1063/1.4943759](https://doi.org/10.1063/1.4943759). URL: <https://doi.org/10.1063/1.4943759> (cit. on p. 30).
- [65] Yang Zhang, Yan Sun, Hao Yang, et al. “Strong anisotropic anomalous Hall effect and spin Hall effect in the chiral antiferromagnetic compounds Mn₃X (X = Ge, Sn, Ga, Ir, Rh, and Pt)”. In: *Phys. Rev. B* 95 (7 Feb. 2017), p. 075128. DOI: [10.1103/PhysRevB.95.075128](https://doi.org/10.1103/PhysRevB.95.075128). URL: <https://link.aps.org/doi/10.1103/PhysRevB.95.075128> (cit. on p. 30).
- [66] Tomoya Higo, Huiyuan Man, Daniel B. Gopman, et al. “Large magneto-optical Kerr effect and imaging of magnetic octupole domains in an antiferromagnetic metal”. In: *Nature Photonics* 12.2 (Feb. 2018), pp. 73–78. ISSN: 1749-4893. DOI: [10.1038/s41566-017-0086-z](https://doi.org/10.1038/s41566-017-0086-z). URL: <https://doi.org/10.1038/s41566-017-0086-z> (cit. on pp. 30, 87, 88).

- [67] Libor Smejkal, Rafael González-Hernández, T. Jungwirth, et al. “Crystal time-reversal symmetry breaking and spontaneous Hall effect in collinear antiferromagnets”. In: *Science Advances* 6.23 (2020), eaaz8809. DOI: [10.1126/sciadv.aaz8809](https://doi.org/10.1126/sciadv.aaz8809). URL: <https://www.science.org/doi/abs/10.1126/sciadv.aaz8809> (cit. on pp. 30, 31).
- [68] Zexin Feng, Xiaorong Zhou, Libor Šmejkal, et al. “An anomalous Hall effect in altermagnetic ruthenium dioxide”. In: *Nature Electronics* 5.11 (Nov. 2022), pp. 735–743. ISSN: 2520-1131. DOI: [10.1038/s41928-022-00866-z](https://doi.org/10.1038/s41928-022-00866-z). URL: <https://doi.org/10.1038/s41928-022-00866-z> (cit. on pp. 30, 31).
- [69] Nirmal J. Ghimire, A. S. Botana, J. S. Jiang, et al. “Large anomalous Hall effect in the chiral-lattice antiferromagnet CoNb3S6”. In: *Nature Communications* 9.1 (Aug. 2018), p. 3280. ISSN: 2041-1723. DOI: [10.1038/s41467-018-05756-7](https://doi.org/10.1038/s41467-018-05756-7). URL: <https://doi.org/10.1038/s41467-018-05756-7> (cit. on p. 31).
- [70] T. Suzuki, R. Chisnell, A. Devarakonda, et al. “Large anomalous Hall effect in a half-Heusler antiferromagnet”. In: *Nature Physics* 12.12 (Dec. 2016), pp. 1119–1123. ISSN: 1745-2481. DOI: [10.1038/nphys3831](https://doi.org/10.1038/nphys3831). URL: <https://doi.org/10.1038/nphys3831> (cit. on p. 31).
- [71] T. Shang, Y. Xu, D. J. Gawryluk, et al. “Anomalous Hall resistivity and possible topological Hall effect in the EuAl₄ antiferromagnet”. In: *Phys. Rev. B* 103 (2 Jan. 2021), p. L020405. DOI: [10.1103/PhysRevB.103.L020405](https://link.aps.org/doi/10.1103/PhysRevB.103.L020405). URL: <https://link.aps.org/doi/10.1103/PhysRevB.103.L020405> (cit. on p. 31).
- [72] Yihao Wang, Cong Xian, Jian Wang, et al. “Anisotropic anomalous Hall effect in triangular itinerant ferromagnet Fe₃GeTe₂”. In: *Phys. Rev. B* 96 (13 Oct. 2017), p. 134428. DOI: [10.1103/PhysRevB.96.134428](https://link.aps.org/doi/10.1103/PhysRevB.96.134428). URL: <https://link.aps.org/doi/10.1103/PhysRevB.96.134428> (cit. on p. 31).
- [73] Mario Novak, Satoshi Sasaki, Kouji Segawa, et al. “Large linear magnetoresistance in the Dirac semimetal TlBiSSe”. In: *Phys. Rev. B* 91 (4 Jan. 2015), p. 041203. DOI: [10.1103/PhysRevB.91.041203](https://link.aps.org/doi/10.1103/PhysRevB.91.041203). URL: <https://link.aps.org/doi/10.1103/PhysRevB.91.041203> (cit. on p. 31).
- [74] Jiaji Zhao, Bingyan Jiang, Jinying Yang, et al. “Magnetotransport induced by anomalous Hall effect”. In: *Phys. Rev. B* 107 (6 Feb. 2023), p. L060408. DOI: [10.1103/PhysRevB.107.L060408](https://link.aps.org/doi/10.1103/PhysRevB.107.L060408). URL: <https://link.aps.org/doi/10.1103/PhysRevB.107.L060408> (cit. on p. 31).
- [75] Xiangyu Cao, Jie-Xiang Yu, Pengliang Leng, et al. “Giant nonlinear anomalous Hall effect induced by spin-dependent band structure evolution”. In: *Phys. Rev. Res.* 4 (2 May 2022), p. 023100. DOI: [10.1103/PhysRevResearch.4.023100](https://link.aps.org/doi/10.1103/PhysRevResearch.4.023100). URL: <https://link.aps.org/doi/10.1103/PhysRevResearch.4.023100> (cit. on p. 31).

- [76] M. K. Hooda, O. Pavlosiuk, Z. Hossain, et al. “Magnetotransport properties of the topological semimetal SrAgBi”. In: *Phys. Rev. B* 106 (4 July 2022), p. 045107. DOI: [10.1103/PhysRevB.106.045107](https://doi.org/10.1103/PhysRevB.106.045107). URL: <https://link.aps.org/doi/10.1103/PhysRevB.106.045107> (cit. on p. 31).
- [77] Tian Liang, Jingjing Lin, Quinn Gibson, et al. “Anomalous Hall effect in ZrTe5”. In: *Nature Physics* 14.5 (May 2018), pp. 451–455. ISSN: 1745-2481. DOI: [10.1038/s41567-018-0078-z](https://doi.org/10.1038/s41567-018-0078-z). URL: <https://doi.org/10.1038/s41567-018-0078-z> (cit. on p. 32).
- [78] Antu Laha, Sudip Malick, Ratnadwip Singha, et al. “Magnetotransport properties of the correlated topological nodal-line semimetal YbCdGe”. In: *Phys. Rev. B* 99 (24 June 2019), p. 241102. DOI: [10.1103/PhysRevB.99.241102](https://doi.org/10.1103/PhysRevB.99.241102). URL: <https://link.aps.org/doi/10.1103/PhysRevB.99.241102> (cit. on p. 32).
- [79] Antu Laha, Sougata Mardanya, Bahadur Singh, et al. “Magnetotransport properties of the topological nodal-line semimetal CaCdSn”. In: *Phys. Rev. B* 102 (3 July 2020), p. 035164. DOI: [10.1103/PhysRevB.102.035164](https://doi.org/10.1103/PhysRevB.102.035164). URL: <https://link.aps.org/doi/10.1103/PhysRevB.102.035164> (cit. on p. 32).
- [80] T. McGuire and R. Potter. “Anisotropic magnetoresistance in ferromagnetic 3d alloys”. In: *IEEE Transactions on Magnetism* 11.4 (1975), pp. 1018–1038. DOI: [10.1109/TMAG.1975.1058782](https://doi.org/10.1109/TMAG.1975.1058782) (cit. on p. 32).
- [81] S. Nandy, Girish Sharma, A. Taraphder, et al. “Chiral Anomaly as the Origin of the Planar Hall Effect in Weyl Semimetals”. In: *Phys. Rev. Lett.* 119 (17 Oct. 2017), p. 176804. DOI: [10.1103/PhysRevLett.119.176804](https://doi.org/10.1103/PhysRevLett.119.176804). URL: <https://link.aps.org/doi/10.1103/PhysRevLett.119.176804> (cit. on p. 32).
- [82] Nitesh Kumar, Satya N. Guin, Claudia Felser, et al. “Planar Hall effect in the Weyl semimetal GdPtBi”. In: *Phys. Rev. B* 98 (4 July 2018), p. 041103. DOI: [10.1103/PhysRevB.98.041103](https://doi.org/10.1103/PhysRevB.98.041103). URL: <https://link.aps.org/doi/10.1103/PhysRevB.98.041103> (cit. on p. 32).
- [83] Bingyan Jiang, Lujunyu Wang, Ran Bi, et al. “Chirality-Dependent Hall Effect and Antisymmetric Magnetoresistance in a Magnetic Weyl Semimetal”. In: *Phys. Rev. Lett.* 126 (23 June 2021), p. 236601. DOI: [10.1103/PhysRevLett.126.236601](https://doi.org/10.1103/PhysRevLett.126.236601). URL: <https://link.aps.org/doi/10.1103/PhysRevLett.126.236601> (cit. on pp. 33, 124, 131).
- [84] S. Nandy and Inti Sodemann. “Symmetry and quantum kinetics of the nonlinear Hall effect”. In: *Phys. Rev. B* 100 (19 Nov. 2019), p. 195117. DOI: [10.1103/PhysRevB.100.195117](https://doi.org/10.1103/PhysRevB.100.195117). URL: <https://link.aps.org/doi/10.1103/PhysRevB.100.195117> (cit. on pp. 33, 58).
- [85] Takahiro Morimoto, Shudan Zhong, Joseph Orenstein, et al. “Semiclassical theory of nonlinear magneto-optical responses with applications to topological Dirac/Weyl semimetals”. In: *Phys. Rev. B* 94 (24 Dec. 2016), p. 245121. DOI: [10.1103/PhysRevB.94.245121](https://doi.org/10.1103/PhysRevB.94.245121). URL: <https://link.aps.org/doi/10.1103/PhysRevB.94.245121> (cit. on pp. 33, 90).

- [86] Z. Z. Du, C. M. Wang, Hai Peng Sun, et al. “Quantum theory of the nonlinear Hall effect”. In: *Nature Communications* 12 (2021), p. 5038. ISSN: 20411723. DOI: [10.1038/s41467-021-25273-4](https://doi.org/10.1038/s41467-021-25273-4). URL: <https://www.nature.com/articles/s41467-021-25273-4> (cit. on pp. 33, 58, 65).
- [87] Rikuto Oiwa and Hiroaki Kusunose. “Systematic Analysis Method for Nonlinear Response Tensors”. In: *Journal of the Physical Society of Japan* 91.1 (2022), p. 014701. DOI: [10.7566/JPSJ.91.014701](https://doi.org/10.7566/JPSJ.91.014701). eprint: <https://doi.org/10.7566/JPSJ.91.014701>. URL: <https://doi.org/10.7566/JPSJ.91.014701> (cit. on pp. 33, 62).
- [88] Akimitsu Kirikoshi and Satoru Hayami. “Microscopic mechanism for intrinsic nonlinear anomalous Hall conductivity in noncollinear antiferromagnetic metals”. In: *Phys. Rev. B* 107 (15 Apr. 2023), p. 155109. DOI: [10.1103/PhysRevB.107.155109](https://doi.org/10.1103/PhysRevB.107.155109). URL: <https://link.aps.org/doi/10.1103/PhysRevB.107.155109> (cit. on pp. 33, 58).
- [89] Xing-Guo Ye, Huiying Liu, Peng-Fei Zhu, et al. “Control over Berry Curvature Dipole with Electric Field in WTe_2 ”. In: *Phys. Rev. Lett.* 130 (1 Jan. 2023), p. 016301. DOI: [10.1103/PhysRevLett.130.016301](https://doi.org/10.1103/PhysRevLett.130.016301). URL: <https://link.aps.org/doi/10.1103/PhysRevLett.130.016301> (cit. on p. 35).
- [90] Z. Z. Du, C. M. Wang, Hai-Zhou Lu, et al. “Band Signatures for Strong Nonlinear Hall Effect in Bilayer WTe_2 ”. In: *Phys. Rev. Lett.* 121 (26 Dec. 2018), p. 266601. DOI: [10.1103/PhysRevLett.121.266601](https://doi.org/10.1103/PhysRevLett.121.266601). URL: <https://link.aps.org/doi/10.1103/PhysRevLett.121.266601> (cit. on pp. 35, 89, 91–93, 97).
- [91] Jhih-Shih You, Shiang Fang, Su-Yang Xu, et al. “Berry curvature dipole current in the transition metal dichalcogenides family”. In: *Phys. Rev. B* 98 (12 Sept. 2018), p. 121109. DOI: [10.1103/PhysRevB.98.121109](https://doi.org/10.1103/PhysRevB.98.121109). URL: <https://link.aps.org/doi/10.1103/PhysRevB.98.121109> (cit. on p. 35).
- [92] Zhihai He and Hongming Weng. “Giant nonlinear Hall effect in twisted bilayer WTe_2 ”. In: *npj Quantum Materials* 6.1 (Dec. 2021), p. 101. ISSN: 2397-4648. DOI: [10.1038/s41535-021-00403-9](https://doi.org/10.1038/s41535-021-00403-9). URL: <https://doi.org/10.1038/s41535-021-00403-9> (cit. on p. 35).
- [93] Sobhit Singh, Jinwoong Kim, Karin M. Rabe, et al. “Engineering Weyl Phases and Nonlinear Hall Effects in T_d - MoTe_2 ”. In: *Phys. Rev. Lett.* 125 (4 July 2020), p. 046402. DOI: [10.1103/PhysRevLett.125.046402](https://doi.org/10.1103/PhysRevLett.125.046402). URL: <https://link.aps.org/doi/10.1103/PhysRevLett.125.046402> (cit. on p. 35).
- [94] Yang Zhang, Jeroen van den Brink, Claudia Felser, et al. “Electrically tuneable nonlinear anomalous Hall effect in two-dimensional transition-metal dichalcogenides WTe_2 and MoTe_2 ”. In: *2D Materials* 5.4 (July 2018), p. 044001. DOI: [10.1088/2053-1583/aad1ae](https://doi.org/10.1088/2053-1583/aad1ae). URL: <https://doi.org/10.1088/2053-1583/aad1ae> (cit. on p. 35).

- [95] Benjamin T. Zhou, Cheng-Ping Zhang, and K.T. Law. “Highly Tunable Nonlinear Hall Effects Induced by Spin-Orbit Couplings in Strained Polar Transition-Metal Dichalcogenides”. In: *Phys. Rev. Applied* 13 (2 Feb. 2020), p. 024053. DOI: [10.1103/PhysRevApplied.13.024053](https://doi.org/10.1103/PhysRevApplied.13.024053). URL: <https://link.aps.org/doi/10.1103/PhysRevApplied.13.024053> (cit. on pp. 35, 36).
- [96] Raffaele Battilomo, Niccoló Scopigno, and Carmine Ortix. “Berry Curvature Dipole in Strained Graphene: A Fermi Surface Warping Effect”. In: *Phys. Rev. Lett.* 123 (19 Nov. 2019), p. 196403. DOI: [10.1103/PhysRevLett.123.196403](https://doi.org/10.1103/PhysRevLett.123.196403). URL: <https://link.aps.org/doi/10.1103/PhysRevLett.123.196403> (cit. on pp. 35, 36).
- [97] Pierre A. Pantaleón, Tony Low, and Francisco Guinea. “Tunable large Berry dipole in strained twisted bilayer graphene”. In: *Phys. Rev. B* 103 (20 May 2021), p. 205403. DOI: [10.1103/PhysRevB.103.205403](https://doi.org/10.1103/PhysRevB.103.205403). URL: <https://link.aps.org/doi/10.1103/PhysRevB.103.205403> (cit. on p. 35).
- [98] Cheng-Ping Zhang, Jiewen Xiao, Benjamin T. Zhou, et al. “Giant nonlinear Hall effect in strained twisted bilayer graphene”. In: *Phys. Rev. B* 106 (4 July 2022), p. L041111. DOI: [10.1103/PhysRevB.106.L041111](https://doi.org/10.1103/PhysRevB.106.L041111). URL: <https://link.aps.org/doi/10.1103/PhysRevB.106.L041111> (cit. on p. 35).
- [99] Sai Satyam Samal, S. Nandy, and Kush Saha. “Nonlinear transport without spin-orbit coupling or warping in two-dimensional Dirac semimetals”. In: *Phys. Rev. B* 103 (20 May 2021), p. L201202. DOI: [10.1103/PhysRevB.103.L201202](https://doi.org/10.1103/PhysRevB.103.L201202). URL: <https://link.aps.org/doi/10.1103/PhysRevB.103.L201202> (cit. on p. 35).
- [100] Chuanchang Zeng, Snehasish Nandy, and Sumanta Tewari. “Nonlinear transport in Weyl semimetals induced by Berry curvature dipole”. In: *Phys. Rev. B* 103 (24 June 2021), p. 245119. DOI: [10.1103/PhysRevB.103.245119](https://doi.org/10.1103/PhysRevB.103.245119). URL: <https://link.aps.org/doi/10.1103/PhysRevB.103.245119> (cit. on pp. 35, 66, 75).
- [101] Jorge I. Facio, Dmitri Efremov, Klaus Koepernik, et al. “Strongly Enhanced Berry Dipole at Topological Phase Transitions in BiTeI”. In: *Phys. Rev. Lett.* 121 (24 Dec. 2018), p. 246403. DOI: [10.1103/PhysRevLett.121.246403](https://doi.org/10.1103/PhysRevLett.121.246403). URL: <https://link.aps.org/doi/10.1103/PhysRevLett.121.246403> (cit. on p. 35).
- [102] Yuki M. Itahashi, Toshiya Ideue, Shintaro Hoshino, et al. “Giant second harmonic transport under time-reversal symmetry in a trigonal superconductor”. In: *Nature Communications* 13.1 (Mar. 2022), p. 1659. ISSN: 2041-1723. DOI: [10.1038/s41467-022-29314-4](https://doi.org/10.1038/s41467-022-29314-4). URL: <https://doi.org/10.1038/s41467-022-29314-4> (cit. on p. 35).

- [103] Ding-Fu Shao, Shu-Hui Zhang, Gautam Gurung, et al. “Nonlinear Anomalous Hall Effect for Néel Vector Detection”. In: *Phys. Rev. Lett.* 124 (6 Feb. 2020), p. 067203. DOI: [10.1103/PhysRevLett.124.067203](https://doi.org/10.1103/PhysRevLett.124.067203). URL: <https://link.aps.org/doi/10.1103/PhysRevLett.124.067203> (cit. on pp. 35, 58, 85).
- [104] Rui-Chun Xiao, Ding-Fu Shao, Wenjuan Huang, et al. “Electrical detection of ferroelectriclike metals through the nonlinear Hall effect”. In: *Phys. Rev. B* 102 (2 July 2020), p. 024109. DOI: [10.1103/PhysRevB.102.024109](https://doi.org/10.1103/PhysRevB.102.024109). URL: <https://link.aps.org/doi/10.1103/PhysRevB.102.024109> (cit. on p. 35).
- [105] Kyung-Hwan Jin, Eunseok Oh, Roland Stania, et al. “Enhanced Berry Curvature Dipole and Persistent Spin Texture in the Bi(110) Monolayer”. In: *Nano Letters* 21.22 (2021). PMID: 34747625, pp. 9468–9475. DOI: [10.1021/acs.nanolett.1c02811](https://doi.org/10.1021/acs.nanolett.1c02811). URL: <https://doi.org/10.1021/acs.nanolett.1c02811> (cit. on p. 35).
- [106] Atasi Chakraborty, Kamal Das, Subhajit Sinha, et al. “Nonlinear anomalous Hall effects probe topological phase-transitions in twisted double bilayer graphene”. In: *2D Materials* 9.4 (Sept. 2022), p. 045020. DOI: [10.1088/2053-1583/ac8b93](https://doi.org/10.1088/2053-1583/ac8b93). URL: <https://doi.org/10.1088/2053-1583/ac8b93> (cit. on p. 36).
- [107] Subhajit Sinha, Pratap Chandra Adak, Atasi Chakraborty, et al. “Berry curvature dipole senses topological transition in a moiré superlattice”. In: *Nature Physics* 18.7 (July 2022), pp. 765–770. ISSN: 1745-2481. DOI: [10.1038/s41567-022-01606-y](https://doi.org/10.1038/s41567-022-01606-y). URL: <https://doi.org/10.1038/s41567-022-01606-y> (cit. on p. 36).
- [108] Shen Lai, Huiying Liu, Zhaowei Zhang, et al. “Third-order nonlinear Hall effect induced by the Berry-connection polarizability tensor”. In: *Nature Nanotechnology* 16.8 (Aug. 2021), pp. 869–873. ISSN: 1748-3395. DOI: [10.1038/s41565-021-00917-0](https://doi.org/10.1038/s41565-021-00917-0). URL: <https://doi.org/10.1038/s41565-021-00917-0> (cit. on p. 38).
- [109] Cong Wang, Rui-Chun Xiao, Huiying Liu, et al. “Room-temperature third-order nonlinear Hall effect in Weyl semimetal TaIrTe₄”. In: *National Science Review* 9.12 (Feb. 2022). nwac020. ISSN: 2095-5138. DOI: [10.1093/nsr/nwac020](https://doi.org/10.1093/nsr/nwac020). URL: <https://doi.org/10.1093/nsr/nwac020> (cit. on p. 38).
- [110] Xing-Guo Ye, Peng-Fei Zhu, Wen-Zheng Xu, et al. “Orbital polarization and third-order anomalous Hall effect in WTe₂”. In: *Phys. Rev. B* 106 (4 July 2022), p. 045414. DOI: [10.1103/PhysRevB.106.045414](https://doi.org/10.1103/PhysRevB.106.045414). URL: <https://link.aps.org/doi/10.1103/PhysRevB.106.045414> (cit. on pp. 38, 105).
- [111] Miaomiao Wei, Longjun Xiang, Luyang Wang, et al. “Quantum third-order nonlinear Hall effect of a four-terminal device with time-reversal symmetry”. In: *Phys. Rev. B* 106 (3 July 2022), p. 035307. DOI: [10.1103/PhysRevB.106.035307](https://doi.org/10.1103/PhysRevB.106.035307). URL: <https://link.aps.org/doi/10.1103/PhysRevB.106.035307> (cit. on p. 38).

- [112] T. Tanaka, H. Kontani, M. Naito, et al. “Intrinsic spin Hall effect and orbital Hall effect in $4d$ and $5d$ transition metals”. In: *Phys. Rev. B* 77 (16 Apr. 2008), p. 165117. DOI: [10.1103/PhysRevB.77.165117](https://doi.org/10.1103/PhysRevB.77.165117). URL: <https://link.aps.org/doi/10.1103/PhysRevB.77.165117> (cit. on pp. 39, 86, 88).
- [113] H. Kontani, T. Tanaka, D. S. Hirashima, et al. “Giant Orbital Hall Effect in Transition Metals: Origin of Large Spin and Anomalous Hall Effects”. In: *Phys. Rev. Lett.* 102 (1 Jan. 2009), p. 016601. DOI: [10.1103/PhysRevLett.102.016601](https://doi.org/10.1103/PhysRevLett.102.016601). URL: <https://link.aps.org/doi/10.1103/PhysRevLett.102.016601> (cit. on p. 39).
- [114] Dongwook Go, Daegeun Jo, Changyoung Kim, et al. “Intrinsic Spin and Orbital Hall Effects from Orbital Texture”. In: *Phys. Rev. Lett.* 121 (8 Aug. 2018), p. 086602. DOI: [10.1103/PhysRevLett.121.086602](https://doi.org/10.1103/PhysRevLett.121.086602). URL: <https://link.aps.org/doi/10.1103/PhysRevLett.121.086602> (cit. on p. 39).
- [115] Sayantika Bhowal and S. Satpathy. “Intrinsic orbital moment and prediction of a large orbital Hall effect in two-dimensional transition metal dichalcogenides”. In: *Phys. Rev. B* 101 (12 Mar. 2020), p. 121112. DOI: [10.1103/PhysRevB.101.121112](https://doi.org/10.1103/PhysRevB.101.121112). URL: <https://link.aps.org/doi/10.1103/PhysRevB.101.121112> (cit. on p. 39).
- [116] Guoqiang Yu, Pramey Upadhyaya, Yabin Fan, et al. “Switching of perpendicular magnetization by spin-orbit torques in the absence of external magnetic fields.” In: *Nature Nanotechnology* 9 (2014), p. 548. ISSN: 1748-3395. DOI: [10.1038/nnano.2014.94](https://doi.org/10.1038/nnano.2014.94). URL: <http://www.ncbi.nlm.nih.gov/pubmed/24813694> (cit. on pp. 39, 107).
- [117] Yasufumi Araki. “Strain-induced nonlinear spin Hall effect in topological Dirac semimetal”. In: *Scientific Reports* 8.1 (Oct. 2018), p. 15236. ISSN: 2045-2322. DOI: [10.1038/s41598-018-33655-w](https://doi.org/10.1038/s41598-018-33655-w). URL: <https://doi.org/10.1038/s41598-018-33655-w> (cit. on p. 39).
- [118] Satoru Hayami, Megumi Yatsushiro, and Hiroaki Kusunose. “Nonlinear spin Hall effect in \mathcal{PT} -symmetric collinear magnets”. In: *Phys. Rev. B* 106 (2 July 2022), p. 024405. DOI: [10.1103/PhysRevB.106.024405](https://doi.org/10.1103/PhysRevB.106.024405). URL: <https://link.aps.org/doi/10.1103/PhysRevB.106.024405> (cit. on p. 39).
- [119] Margarita Davydova, Maksym Serbyn, and Hiroaki Ishizuka. “Symmetry-allowed nonlinear orbital response across the topological phase transition in centrosymmetric materials”. In: *Phys. Rev. B* 105 (12 Mar. 2022), p. L121407. DOI: [10.1103/PhysRevB.105.L121407](https://doi.org/10.1103/PhysRevB.105.L121407). URL: <https://link.aps.org/doi/10.1103/PhysRevB.105.L121407> (cit. on pp. 39, 58).
- [120] Keita Hamamoto, Motohiko Ezawa, Kun Woo Kim, et al. “Nonlinear spin current generation in noncentrosymmetric spin-orbit coupled systems”. In: *Phys. Rev. B* 95 (22 June 2017), p. 224430. DOI: [10.1103/PhysRevB.95.224430](https://doi.org/10.1103/PhysRevB.95.224430). URL: <https://link.aps.org/doi/10.1103/PhysRevB.95.224430> (cit. on p. 39).

- [121] Priyadarshini Kapri, Bashab Dey, and Tarun Kanti Ghosh. “Role of Berry curvature in the generation of spin currents in Rashba systems”. In: *Phys. Rev. B* 103 (16 Apr. 2021), p. 165401. DOI: [10.1103/PhysRevB.103.165401](https://doi.org/10.1103/PhysRevB.103.165401). URL: <https://link.aps.org/doi/10.1103/PhysRevB.103.165401> (cit. on p. 40).
- [122] Aniruddha Pan and D. C. Marinescu. “Nonlinear spin-current generation in quantum wells with arbitrary Rashba-Dresselhaus spin-orbit interactions”. In: *Phys. Rev. B* 99 (24 June 2019), p. 245204. DOI: [10.1103/PhysRevB.99.245204](https://doi.org/10.1103/PhysRevB.99.245204). URL: <https://link.aps.org/doi/10.1103/PhysRevB.99.245204> (cit. on p. 40).
- [123] A Manchon, J. Zelezný, M. Miron, et al. “Current-induced spin-orbit torques in ferromagnetic and antiferromagnetic systems”. In: *Review of Modern Physics* 91 (2019), p. 035004. DOI: [10.1103/RevModPhys.91.035004](https://doi.org/10.1103/RevModPhys.91.035004). URL: <https://journals.aps.org/rmp/abstract/10.1103/RevModPhys.91.035004> (cit. on pp. 40, 86, 106).
- [124] A. Manchon and S. Zhang. “Theory of nonequilibrium intrinsic spin torque in a single nanomagnet”. In: *Phys. Rev. B* 78 (21 Dec. 2008), p. 212405. DOI: [10.1103/PhysRevB.78.212405](https://doi.org/10.1103/PhysRevB.78.212405). URL: <https://link.aps.org/doi/10.1103/PhysRevB.78.212405> (cit. on p. 40).
- [125] Shuai Hu, Ding-Fu Shao, Huanglin Yang, et al. “Efficient perpendicular magnetization switching by a magnetic spin Hall effect in a noncollinear antiferromagnet”. In: *Nature Communications* 13.1 (Aug. 2022), p. 4447. ISSN: 2041-1723. DOI: [10.1038/s41467-022-32179-2](https://doi.org/10.1038/s41467-022-32179-2). URL: <https://doi.org/10.1038/s41467-022-32179-2> (cit. on p. 41).
- [126] V. P. Amin, Junwen Li, M. D. Stiles, et al. “Intrinsic spin currents in ferromagnets”. In: *Phys. Rev. B* 99 (22 June 2019), p. 220405. DOI: [10.1103/PhysRevB.99.220405](https://doi.org/10.1103/PhysRevB.99.220405). URL: <https://link.aps.org/doi/10.1103/PhysRevB.99.220405> (cit. on p. 40).
- [127] Takeshi Seki, Satoshi Iihama, Tomohiro Taniguchi, et al. “Large spin anomalous Hall effect in $L1_0$ -FePt: Symmetry and magnetization switching”. In: *Phys. Rev. B* 100 (14 Oct. 2019), p. 144427. DOI: [10.1103/PhysRevB.100.144427](https://doi.org/10.1103/PhysRevB.100.144427). URL: <https://link.aps.org/doi/10.1103/PhysRevB.100.144427> (cit. on p. 40).
- [128] T.C. Chuang, C.F. Pai, and S.Y. Huang. “Cr-induced Perpendicular Magnetic Anisotropy and Field-Free Spin-Orbit-Torque Switching”. In: *Phys. Rev. Appl.* 11 (6 June 2019), p. 061005. DOI: [10.1103/PhysRevApplied.11.061005](https://doi.org/10.1103/PhysRevApplied.11.061005). URL: <https://link.aps.org/doi/10.1103/PhysRevApplied.11.061005> (cit. on p. 40).

- [129] D. MacNeill, G. M. Stiehl, M. H. D. Guimaraes, et al. “Control of spin-orbit torques through crystal symmetry in WTe₂/ferromagnet bilayers”. In: *Nature Physics* 13 (2017), p. 300. ISSN: 1745-2473. DOI: [10.1038/nphys3933](https://doi.org/10.1038/nphys3933). URL: <https://www.nature.com/articles/nphys3933> (cit. on pp. 40, 107, 123).
- [130] Alisha M. Humphries, Tao Wang, Eric R. J. Edwards, et al. “Observation of spin-orbit effects with spin rotation symmetry”. In: *Nature Communications* 8.1 (Oct. 2017), p. 911. ISSN: 2041-1723. DOI: [10.1038/s41467-017-00967-w](https://doi.org/10.1038/s41467-017-00967-w). URL: <https://doi.org/10.1038/s41467-017-00967-w> (cit. on p. 40).
- [131] Hyung Keun Gweon, Kyung-Jin Lee, and Sang Ho Lim. “Influence of MgO Sputtering Power and Post annealing on Strength and Angular Dependence of Spin-Orbit Torques in Pt/Co/MgO Trilayers”. In: *Phys. Rev. Appl.* 11 (1 Jan. 2019), p. 014034. DOI: [10.1103/PhysRevApplied.11.014034](https://doi.org/10.1103/PhysRevApplied.11.014034). URL: <https://link.aps.org/doi/10.1103/PhysRevApplied.11.014034> (cit. on p. 40).
- [132] Kevin Garello, Ioan Mihai Miron, Can Onur Avci, et al. “Symmetry and magnitude of spin-orbit torques in ferromagnetic heterostructures”. In: *Nature Nanotechnology* 8.8 (Aug. 2013), pp. 587–593. ISSN: 1748-3395. DOI: [10.1038/nnano.2013.145](https://doi.org/10.1038/nnano.2013.145). URL: <https://doi.org/10.1038/nnano.2013.145> (cit. on p. 40).
- [133] Christopher Safranski, Eric A. Montoya, and Ilya N. Krivorotov. “Spin-orbit torque driven by a planar Hall current”. In: *Nature Nanotechnology* 14.1 (Jan. 2019), pp. 27–30. ISSN: 1748-3395. DOI: [10.1038/s41565-018-0282-0](https://doi.org/10.1038/s41565-018-0282-0). URL: <https://doi.org/10.1038/s41565-018-0282-0> (cit. on p. 41).
- [134] Eun-Sang Park, Dong-Kyu Lee, Fei Xue, et al. “Strong higher-order angular dependence of spin-orbit torque in W/CoFeB bilayer”. In: *Phys. Rev. B* 107 (6 Feb. 2023), p. 064411. DOI: [10.1103/PhysRevB.107.064411](https://doi.org/10.1103/PhysRevB.107.064411). URL: <https://link.aps.org/doi/10.1103/PhysRevB.107.064411> (cit. on p. 41).
- [135] E.I. Blount. “Formalisms of Band Theory”. In: ed. by Frederick Seitz and David Turnbull. Vol. 13. *Solid State Physics*. Academic Press, 1962, pp. 305–373. DOI: [https://doi.org/10.1016/S0081-1947\(08\)60459-2](https://doi.org/10.1016/S0081-1947(08)60459-2). URL: <https://www.sciencedirect.com/science/article/pii/S0081194708604592> (cit. on pp. 48, 49).
- [136] Claudio Aversa and J. E. Sipe. “Nonlinear optical susceptibilities of semiconductors: Results with a length-gauge analysis”. In: *Phys. Rev. B* 52 (20 Nov. 1995), pp. 14636–14645. DOI: [10.1103/PhysRevB.52.14636](https://doi.org/10.1103/PhysRevB.52.14636). URL: <https://link.aps.org/doi/10.1103/PhysRevB.52.14636> (cit. on pp. 48, 49).
- [137] Alain Bérard and Hervé Mohrbach. “Monopole and Berry phase in momentum space in noncommutative quantum mechanics”. In: *Phys. Rev. D* 69 (12 June 2004), p. 127701. DOI: [10.1103/PhysRevD.69.127701](https://doi.org/10.1103/PhysRevD.69.127701). URL: <https://link.aps.org/doi/10.1103/PhysRevD.69.127701> (cit. on p. 51).

- [138] Di Xiao, Junren Shi, and Qian Niu. “Berry Phase Correction to Electron Density of States in Solids”. In: *Phys. Rev. Lett.* 95 (13 Sept. 2005), p. 137204. DOI: [10.1103/PhysRevLett.95.137204](https://doi.org/10.1103/PhysRevLett.95.137204). URL: <https://link.aps.org/doi/10.1103/PhysRevLett.95.137204> (cit. on pp. 51–53).
- [139] T. Thonhauser. “Theory of Orbital Magnetization in Solids”. In: *International Journal of Modern Physics B* 25.11 (2011), pp. 1429–1458. DOI: [10.1142/S0217979211058912](https://doi.org/10.1142/S0217979211058912). URL: <https://doi.org/10.1142/S0217979211058912> (cit. on pp. 51, 53).
- [140] Di Xiao, Wang Yao, and Qian Niu. “Valley-Contrasting Physics in Graphene: Magnetic Moment and Topological Transport”. In: *Phys. Rev. Lett.* 99 (23 Dec. 2007), p. 236809. DOI: [10.1103/PhysRevLett.99.236809](https://doi.org/10.1103/PhysRevLett.99.236809). URL: <https://link.aps.org/doi/10.1103/PhysRevLett.99.236809> (cit. on pp. 52, 91).
- [141] A. Crépieux and P. Bruno. “Theory of the anomalous Hall effect from the Kubo formula and the Dirac equation”. In: *Phys. Rev. B* 64 (1 June 2001), p. 014416. DOI: [10.1103/PhysRevB.64.014416](https://doi.org/10.1103/PhysRevB.64.014416). URL: <https://link.aps.org/doi/10.1103/PhysRevB.64.014416> (cit. on p. 53).
- [142] Shigeki Onoda, Naoyuki Sugimoto, and Naoto Nagaosa. “Quantum transport theory of anomalous electric, thermoelectric, and thermal Hall effects in ferromagnets”. In: *Phys. Rev. B* 77 (16 Apr. 2008), p. 165103. DOI: [10.1103/PhysRevB.77.165103](https://doi.org/10.1103/PhysRevB.77.165103). URL: <https://link.aps.org/doi/10.1103/PhysRevB.77.165103> (cit. on p. 53).
- [143] Shigeki Onoda, Naoyuki Sugimoto, and Naoto Nagaosa. “Theory of Non-Equilibrium States Driven by Constant Electromagnetic Fields: — Non-Commutative Quantum Mechanics in the Keldysh Formalism —”. In: *Progress of Theoretical Physics* 116.1 (July 2006), pp. 61–86. ISSN: 0033-068X. DOI: [10.1143/PTP.116.61](https://doi.org/10.1143/PTP.116.61). URL: <https://doi.org/10.1143/PTP.116.61> (cit. on pp. 53, 54).
- [144] Varga Bonbien and Aurélien Manchon. “Symmetrized decomposition of the Kubo-Bastin formula”. In: *Phys. Rev. B* 102 (8 Aug. 2020), p. 085113. DOI: [10.1103/PhysRevB.102.085113](https://doi.org/10.1103/PhysRevB.102.085113). URL: <https://link.aps.org/doi/10.1103/PhysRevB.102.085113> (cit. on pp. 55, 56, 90, 116).
- [145] Guobao Zhu, Shengyuan A. Yang, Cheng Fang, et al. “Theory of orbital magnetization in disordered systems”. In: *Phys. Rev. B* 86 (21 Dec. 2012), p. 214415. DOI: [10.1103/PhysRevB.86.214415](https://doi.org/10.1103/PhysRevB.86.214415). URL: <https://link.aps.org/doi/10.1103/PhysRevB.86.214415> (cit. on p. 56).
- [146] Cheng-Ping Zhang, Xue-Jian Gao, Ying-Ming Xie, et al. “Higher-order nonlinear anomalous Hall effects induced by Berry curvature multipoles”. In: *Phys. Rev. B* 107 (11 Mar. 2023), p. 115142. DOI: [10.1103/PhysRevB.107.115142](https://doi.org/10.1103/PhysRevB.107.115142). URL: <https://link.aps.org/doi/10.1103/PhysRevB.107.115142> (cit. on p. 57).

- [147] Zhi-Fan Zhang, Zhen-Gang Zhu, and Gang Su. “Theory of nonlinear response for charge and spin currents”. In: *Phys. Rev. B* 104 (11 Sept. 2021), p. 115140. DOI: [10.1103/PhysRevB.104.115140](https://doi.org/10.1103/PhysRevB.104.115140). URL: <https://link.aps.org/doi/10.1103/PhysRevB.104.115140> (cit. on p. 57).
- [148] Mahmut Sait Okyay, Shunsuke A. Sato, Kun Woo Kim, et al. “Second harmonic Hall responses of insulators as a probe of Berry curvature dipole”. In: *Communications Physics* 5.1 (Nov. 2022), p. 303. ISSN: 2399-3650. DOI: [10.1038/s42005-022-01086-9](https://doi.org/10.1038/s42005-022-01086-9). URL: <https://doi.org/10.1038/s42005-022-01086-9> (cit. on p. 58).
- [149] Habib Rostami and Marco Polini. “Nonlinear anomalous photocurrents in Weyl semimetals”. In: *Phys. Rev. B* 97 (19 May 2018), p. 195151. DOI: [10.1103/PhysRevB.97.195151](https://doi.org/10.1103/PhysRevB.97.195151). URL: <https://link.aps.org/doi/10.1103/PhysRevB.97.195151> (cit. on p. 58).
- [150] Yang Gao, Furu Zhang, and Wei Zhang. “Second-order nonlinear Hall effect in Weyl semimetals”. In: *Phys. Rev. B* 102 (24 Dec. 2020), p. 245116. DOI: [10.1103/PhysRevB.102.245116](https://doi.org/10.1103/PhysRevB.102.245116). URL: <https://link.aps.org/doi/10.1103/PhysRevB.102.245116> (cit. on p. 58).
- [151] Pankaj Bhalla, Kamal Das, Dimitrie Culcer, et al. “Resonant Second-Harmonic Generation as a Probe of Quantum Geometry”. In: *Phys. Rev. Lett.* 129 (22 Nov. 2022), p. 227401. DOI: [10.1103/PhysRevLett.129.227401](https://doi.org/10.1103/PhysRevLett.129.227401). URL: <https://link.aps.org/doi/10.1103/PhysRevLett.129.227401> (cit. on p. 58).
- [152] Da Ma, Arpit Arora, Giovanni Vignale, et al. “Anomalous Skew-Scattering Nonlinear Hall Effect and Chiral Photocurrents in \mathcal{PT} -Symmetric Antiferromagnets”. In: *Phys. Rev. Lett.* 131 (7 Aug. 2023), p. 076601. DOI: [10.1103/PhysRevLett.131.076601](https://doi.org/10.1103/PhysRevLett.131.076601). URL: <https://link.aps.org/doi/10.1103/PhysRevLett.131.076601> (cit. on p. 58).
- [153] Pan He, Hiroki Isobe, Dapeng Zhu, et al. “Quantum frequency doubling in the topological insulator Bi₂Se₃”. In: *Nature Communications* 12.1 (Jan. 2021), p. 698. ISSN: 2041-1723. DOI: [10.1038/s41467-021-20983-1](https://doi.org/10.1038/s41467-021-20983-1). URL: <https://doi.org/10.1038/s41467-021-20983-1> (cit. on pp. 62, 85).
- [154] Pan He, Gavin Kok Wai Koon, Hiroki Isobe, et al. “Graphene moiré superlattices with giant quantum nonlinearity of chiral Bloch electrons”. In: *Nature Nanotechnology* 17.4 (Apr. 2022), pp. 378–383. ISSN: 1748-3395. DOI: [10.1038/s41565-021-01060-6](https://doi.org/10.1038/s41565-021-01060-6). URL: <https://doi.org/10.1038/s41565-021-01060-6> (cit. on p. 62).
- [155] Hiroki Isobe, Su-Yang Xu, and Liang Fu. “High-frequency rectification via chiral Bloch electrons”. In: *Science Advances* 6.13 (2020), eaay2497. DOI: [10.1126/sciadv.aay2497](https://doi.org/10.1126/sciadv.aay2497). URL: <https://www.science.org/doi/abs/10.1126/sciadv.aay2497> (cit. on p. 62).

- [156] Archana Tiwari, Fangchu Chen, Shazhou Zhong, et al. “Giant c-axis nonlinear anomalous Hall effect in Td-MoTe₂ and WTe₂”. In: *Nature Communications* 12.1 (Apr. 2021), p. 2049. ISSN: 2041-1723. DOI: [10.1038/s41467-021-22343-5](https://doi.org/10.1038/s41467-021-22343-5). URL: <https://doi.org/10.1038/s41467-021-22343-5> (cit. on p. 62).
- [157] E. L. Ivchenko and G. E. Pikus. “New photogalvanic effect in gyrotropic crystals”. In: *Soviet Journal of Experimental and Theoretical Physics Letters* 27 (June 1978). Provided by the SAO/NASA Astrophysics Data System, p. 604. URL: <https://ui.adsabs.harvard.edu/abs/1978JETPL..27..604I> (cit. on p. 62).
- [158] V.M. Edelstein. “Spin polarization of conduction electrons induced by electric current in two-dimensional asymmetric electron systems”. In: *Solid State Communications* 73.3 (1990), pp. 233–235. ISSN: 0038-1098. DOI: [https://doi.org/10.1016/0038-1098\(90\)90963-C](https://doi.org/10.1016/0038-1098(90)90963-C). URL: <https://www.sciencedirect.com/science/article/pii/003810989090963C> (cit. on p. 62).
- [159] A. Manchon, H. C. Koo, J. Nitta, et al. “New perspectives for Rashba spin–orbit coupling”. In: *Nature Materials* 14.9 (Sept. 2015), pp. 871–882. ISSN: 1476-4660. DOI: [10.1038/nmat4360](https://doi.org/10.1038/nmat4360). URL: <https://doi.org/10.1038/nmat4360> (cit. on pp. 62, 86).
- [160] Annika Johansson, Jürgen Henk, and Ingrid Mertig. “Edelstein effect in Weyl semimetals”. In: *Physical Review B* 97 (2018), p. 085417. ISSN: 24699969. DOI: [10.1103/PhysRevB.97.085417](https://doi.org/10.1103/PhysRevB.97.085417). URL: <https://journals.aps.org/prb/abstract/10.1103/PhysRevB.97.085417> (cit. on pp. 62, 66).
- [161] Annika Johansson, Börge Göbel, Jürgen Henk, et al. “Spin and orbital Edelstein effects in a two-dimensional electron gas: Theory and application to SrTiO₃ interfaces”. In: *Phys. Rev. Res.* 3 (1 Mar. 2021), p. 013275. DOI: [10.1103/PhysRevResearch.3.013275](https://doi.org/10.1103/PhysRevResearch.3.013275). URL: <https://link.aps.org/doi/10.1103/PhysRevResearch.3.013275> (cit. on p. 62).
- [162] Luca Chirolli, Maria Teresa Mercaldo, Claudio Guarcello, et al. “Colossal Orbital Edelstein Effect in Noncentrosymmetric Superconductors”. In: *Phys. Rev. Lett.* 128 (21 May 2022), p. 217703. DOI: [10.1103/PhysRevLett.128.217703](https://doi.org/10.1103/PhysRevLett.128.217703). URL: <https://link.aps.org/doi/10.1103/PhysRevLett.128.217703> (cit. on p. 62).
- [163] Daisuke Hara, M. S. Bahramy, and Shuichi Murakami. “Current-induced orbital magnetization in systems without inversion symmetry”. In: *Phys. Rev. B* 102 (18 Nov. 2020), p. 184404. DOI: [10.1103/PhysRevB.102.184404](https://doi.org/10.1103/PhysRevB.102.184404). URL: <https://link.aps.org/doi/10.1103/PhysRevB.102.184404> (cit. on pp. 62, 69).
- [164] Taiki Yoda, Takehito Yokoyama, and Shuichi Murakami. “Orbital Edelstein Effect as a Condensed-Matter Analog of Solenoids”. In: *Nano Letters* 18.2 (Feb. 2018), pp. 916–920. ISSN: 1530-6984. DOI: [10.1021/acs.nanolett.7b04300](https://doi.org/10.1021/acs.nanolett.7b04300). URL: <https://doi.org/10.1021/acs.nanolett.7b04300> (cit. on pp. 62, 88, 90).

- [165] Yang Zhang, Yan Sun, and Binghai Yan. “Berry curvature dipole in Weyl semimetal materials: An ab initio study”. In: *Phys. Rev. B* 97 (4 Jan. 2018), p. 041101. DOI: [10.1103/PhysRevB.97.041101](https://doi.org/10.1103/PhysRevB.97.041101). URL: <https://link.aps.org/doi/10.1103/PhysRevB.97.041101> (cit. on p. 65).
- [166] Xiangang Wan, Ari M. Turner, Ashvin Vishwanath, et al. “Topological semimetal and Fermi-arc surface states in the electronic structure of pyrochlore iridates”. In: *Phys. Rev. B* 83 (May 2011), p. 205101. ISSN: 1098-0121. DOI: [10.1103/PhysRevB.83.205101](https://doi.org/10.1103/PhysRevB.83.205101). URL: <http://link.aps.org/doi/10.1103/PhysRevB.83.205101> (cit. on p. 65).
- [167] H.B. Nielsen and Masao Ninomiya. “The Adler-Bell-Jackiw anomaly and Weyl fermions in a crystal”. In: *Physics Letters B* 130.6 (1983), pp. 389–396. ISSN: 0370-2693. DOI: [https://doi.org/10.1016/0370-2693\(83\)91529-0](https://doi.org/10.1016/0370-2693(83)91529-0). URL: <https://www.sciencedirect.com/science/article/pii/0370269383915290> (cit. on p. 65).
- [168] Lijun Meng, Jiafang Wu, Jianxin Zhong, et al. “A type of robust superlattice type-I Weyl semimetal with four Weyl nodes”. In: *Nanoscale* 11 (39 2019), pp. 18358–18366. DOI: [10.1039/C9NR04551A](https://doi.org/10.1039/C9NR04551A). URL: <http://dx.doi.org/10.1039/C9NR04551A> (cit. on p. 65).
- [169] B. Q. Lv, H. M. Weng, B. B. Fu, et al. “Experimental Discovery of Weyl Semimetal TaAs”. In: *Phys. Rev. X* 5 (3 July 2015), p. 031013. DOI: [10.1103/PhysRevX.5.031013](https://doi.org/10.1103/PhysRevX.5.031013). URL: <https://link.aps.org/doi/10.1103/PhysRevX.5.031013> (cit. on p. 65).
- [170] Su-Yang Xu, Ilya Belopolski, Nasser Alidoust, et al. “Discovery of a Weyl fermion semimetal and topological Fermi arcs”. In: *Science* 349.6248 (2015), pp. 613–617. DOI: [10.1126/science.aaa9297](https://doi.org/10.1126/science.aaa9297). URL: <https://www.science.org/doi/abs/10.1126/science.aaa9297> (cit. on p. 65).
- [171] Yan Sun, Shu-Chun Wu, and Binghai Yan. “Topological surface states and Fermi arcs of the noncentrosymmetric Weyl semimetals TaAs, TaP, NbAs, and NbP”. In: *Phys. Rev. B* 92 (11 Sept. 2015), p. 115428. DOI: [10.1103/PhysRevB.92.115428](https://doi.org/10.1103/PhysRevB.92.115428). URL: <https://link.aps.org/doi/10.1103/PhysRevB.92.115428> (cit. on p. 65).
- [172] Ke Deng, Guoliang Wan, Peng Deng, et al. “Experimental observation of topological Fermi arcs in type-II Weyl semimetal MoTe₂”. In: *Nature Physics* 12.12 (Dec. 2016), pp. 1105–1110. ISSN: 1745-2481. DOI: [10.1038/nphys3871](https://doi.org/10.1038/nphys3871). URL: <https://doi.org/10.1038/nphys3871> (cit. on p. 65).
- [173] A. Tamai, Q. S. Wu, I. Cucchi, et al. “Fermi Arcs and Their Topological Character in the Candidate Type-II Weyl Semimetal MoTe₂”. In: *Phys. Rev. X* 6 (3 Aug. 2016), p. 031021. DOI: [10.1103/PhysRevX.6.031021](https://doi.org/10.1103/PhysRevX.6.031021). URL: <https://link.aps.org/doi/10.1103/PhysRevX.6.031021> (cit. on p. 65).

- [174] E. Y. Bruno, A. Tamai, Q. S. Wu, et al. “Observation of large topologically trivial Fermi arcs in the candidate type-II Weyl semimetal WTe_2 ”. In: *Phys. Rev. B* 94 (12 Sept. 2016), p. 121112. DOI: [10.1103/PhysRevB.94.121112](https://doi.org/10.1103/PhysRevB.94.121112). URL: <https://link.aps.org/doi/10.1103/PhysRevB.94.121112> (cit. on p. 65).
- [175] Yun Wu, Daixiang Mou, Na Hyun Jo, et al. “Observation of Fermi arcs in the type-II Weyl semimetal candidate WTe_2 ”. In: *Phys. Rev. B* 94 (12 Sept. 2016), p. 121113. DOI: [10.1103/PhysRevB.94.121113](https://doi.org/10.1103/PhysRevB.94.121113). URL: <https://link.aps.org/doi/10.1103/PhysRevB.94.121113> (cit. on p. 65).
- [176] Satya N. Guin, Praveen Vir, Yang Zhang, et al. “Zero-Field Nernst Effect in a Ferromagnetic Kagome-Lattice Weyl-Semimetal $\text{Co}_3\text{Sn}_2\text{S}_2$ ”. In: *Advanced Materials* 31.25 (2019), p. 1806622. DOI: <https://doi.org/10.1002/adma.201806622>. URL: <https://onlinelibrary.wiley.com/doi/abs/10.1002/adma.201806622> (cit. on p. 65).
- [177] Noam Morali, Rajib Batabyal, Pranab Kumar Nag, et al. “Fermi-arc diversity on surface terminations of the magnetic Weyl semimetal $\text{Co}_3\text{Sn}_2\text{S}_2$ ”. In: *Science* 365.6459 (2019), pp. 1286–1291. DOI: [10.1126/science.aav2334](https://doi.org/10.1126/science.aav2334). URL: <https://www.science.org/doi/abs/10.1126/science.aav2334> (cit. on p. 65).
- [178] Guowei Li, Qiunan Xu, Wujun Shi, et al. “Surface states in bulk single crystal of topological semimetal $\text{Co}_3\text{Sn}_2\text{S}_2$ toward water oxidation”. In: *Science Advances* 5.8 (2019), eaaw9867. DOI: [10.1126/sciadv.aaw9867](https://doi.org/10.1126/sciadv.aaw9867). URL: <https://www.science.org/doi/abs/10.1126/sciadv.aaw9867> (cit. on p. 65).
- [179] Qi Wang, Yuanfeng Xu, Rui Lou, et al. “Large intrinsic anomalous Hall effect in half-metallic ferromagnet $\text{Co}_3\text{Sn}_2\text{S}_2$ with magnetic Weyl fermions”. In: *Nature Communications* 9.1 (Sept. 2018), p. 3681. ISSN: 2041-1723. DOI: [10.1038/s41467-018-06088-2](https://doi.org/10.1038/s41467-018-06088-2). URL: <https://doi.org/10.1038/s41467-018-06088-2> (cit. on p. 65).
- [180] Y. Okamura, S. Minami, Y. Kato, et al. “Giant magneto-optical responses in magnetic Weyl semimetal $\text{Co}_3\text{Sn}_2\text{S}_2$ ”. In: *Nature Communications* 11.1 (Sept. 2020), p. 4619. ISSN: 2041-1723. DOI: [10.1038/s41467-020-18470-0](https://doi.org/10.1038/s41467-020-18470-0). URL: <https://doi.org/10.1038/s41467-020-18470-0> (cit. on p. 65).
- [181] Junya Ikeda, Kohei Fujiwara, Junichi Shiogai, et al. “Critical thickness for the emergence of Weyl features in $\text{Co}_3\text{Sn}_2\text{S}_2$ thin films”. In: *Communications Materials* 2.1 (Feb. 2021), p. 18. ISSN: 2662-4443. DOI: [10.1038/s43246-021-00122-5](https://doi.org/10.1038/s43246-021-00122-5). URL: <https://doi.org/10.1038/s43246-021-00122-5> (cit. on p. 65).
- [182] Weizhen Meng, Xiaoming Zhang, Tingli He, et al. “Ternary compound HfCuP : An excellent Weyl semimetal with the coexistence of type-I and type-II Weyl nodes”. In: *Journal of Advanced Research* 24 (2020), pp. 523–528. ISSN: 2090-1232. DOI: <https://doi.org/10.1016/j.jare.2020.05.026>. URL: <https://www.sciencedirect.com/science/article/pii/S2090123220301090> (cit. on p. 66).

- [183] Minping Zhang, Zongxian Yang, and Guangtao Wang. “Coexistence of Type-I and Type-II Weyl Points in the Weyl-Semimetal OsC_2 ”. In: *The Journal of Physical Chemistry C* 122.6 (Feb. 2018), pp. 3533–3538. ISSN: 1932-7447. DOI: [10.1021/acs.jpcc.8b00920](https://pubs.acs.org/doi/10.1021/acs.jpcc.8b00920). URL: <https://pubs.acs.org/doi/10.1021/acs.jpcc.8b00920> (cit. on p. 66).
- [184] Timothy M. McCormick, Itamar Kimchi, and Nandini Trivedi. “Minimal models for topological Weyl semimetals”. In: *Phys. Rev. B* 95 (7 Feb. 2017), p. 075133. DOI: [10.1103/PhysRevB.95.075133](https://link.aps.org/doi/10.1103/PhysRevB.95.075133). URL: <https://link.aps.org/doi/10.1103/PhysRevB.95.075133> (cit. on pp. 66–68, 71).
- [185] Ac Potter, Itamar Kimchi, and Ashvin Vishwanath. “Quantum Oscillations from Surface Fermi-Arcs in Weyl and Dirac Semi-Metals”. In: *Nature communications* 5 (2014), p. 5161. ISSN: 2041-1723. DOI: [10.1038/ncomms6161](https://www.nature.com/articles/ncomms6161). URL: <https://www.nature.com/articles/ncomms6161> (cit. on p. 66).
- [186] Daniel Bulmash and Xiao Liang Qi. “Quantum oscillations in Weyl and Dirac semimetal ultrathin films”. In: *Physical Review B - Condensed Matter and Materials Physics* 93.8 (2016), p. 081103. ISSN: 1550235X. DOI: [10.1103/PhysRevB.93.081103](https://journals.aps.org/prb/abstract/10.1103/PhysRevB.93.081103). URL: <https://journals.aps.org/prb/abstract/10.1103/PhysRevB.93.081103> (cit. on p. 66).
- [187] C. M. Wang, Hai Zhou Lu, and Shun Qing Shen. “Anomalous Phase Shift of Quantum Oscillations in 3D Topological Semimetals”. In: *Physical Review Letters* 117 (2016), p. 077201. ISSN: 10797114. DOI: [10.1103/PhysRevLett.117.077201](https://journals.aps.org/prl/abstract/10.1103/PhysRevLett.117.077201). URL: <https://journals.aps.org/prl/abstract/10.1103/PhysRevLett.117.077201> (cit. on p. 66).
- [188] Philip J W Moll, Nityan L Nair, Toni Helm, et al. “Transport evidence for Fermi-arc-mediated chirality transfer in the Dirac semimetal Cd_3As_2 ”. In: *Nature* 535 (2016), p. 266. ISSN: 0028-0836. DOI: [10.1038/nature18276](https://www.nature.com/articles/nature18276). URL: <https://www.nature.com/articles/nature18276> (cit. on p. 66).
- [189] M. Breitzkreuz and P. W. Brouwer. “Large Contribution of Fermi Arcs to the Conductivity of Topological Metals”. In: *Phys. Rev. Lett.* 123 (6 Aug. 2019), p. 066804. DOI: [10.1103/PhysRevLett.123.066804](https://link.aps.org/doi/10.1103/PhysRevLett.123.066804). URL: <https://link.aps.org/doi/10.1103/PhysRevLett.123.066804> (cit. on p. 66).
- [190] J. Chesta Lopez, L. E. F. Foa Torres, and A. S. Nunez. “Multiterminal conductance at the surface of a Weyl semimetal”. In: *Phys. Rev. B* 97 (12 Mar. 2018), p. 125419. DOI: [10.1103/PhysRevB.97.125419](https://link.aps.org/doi/10.1103/PhysRevB.97.125419). URL: <https://link.aps.org/doi/10.1103/PhysRevB.97.125419> (cit. on p. 66).
- [191] E. V. Gorbar, V. A. Miransky, I. A. Shovkovy, et al. “Chiral separation and chiral magnetic effects in a slab: The role of boundaries”. In: *Phys. Rev. B* 92 (24 Dec. 2015), p. 245440. DOI: [10.1103/PhysRevB.92.245440](https://link.aps.org/doi/10.1103/PhysRevB.92.245440). URL: <https://link.aps.org/doi/10.1103/PhysRevB.92.245440> (cit. on p. 66).

- [192] P. S. Alekseev, A. P. Dmitriev, I. V. Gornyi, et al. “Magnetoresistance of compensated semimetals in confined geometries”. In: *Phys. Rev. B* 95 (16 Apr. 2017), p. 165410. DOI: [10.1103/PhysRevB.95.165410](https://doi.org/10.1103/PhysRevB.95.165410). URL: <https://link.aps.org/doi/10.1103/PhysRevB.95.165410> (cit. on p. 66).
- [193] Timo Schumann, Luca Galletti, David A. Kealhofer, et al. “Observation of the Quantum Hall Effect in Confined Films of the Three-Dimensional Dirac Semimetal Cd_3As_2 ”. In: *Phys. Rev. Lett.* 120 (1 Jan. 2018), p. 016801. DOI: [10.1103/PhysRevLett.120.016801](https://doi.org/10.1103/PhysRevLett.120.016801). URL: <https://link.aps.org/doi/10.1103/PhysRevLett.120.016801> (cit. on p. 66).
- [194] Giacomo Resta, Shu-Ting Pi, Xiangang Wan, et al. “High surface conductivity of Fermi-arc electrons in Weyl semimetals”. In: *Phys. Rev. B* 97 (8 Feb. 2018), p. 085142. DOI: [10.1103/PhysRevB.97.085142](https://doi.org/10.1103/PhysRevB.97.085142). URL: <https://link.aps.org/doi/10.1103/PhysRevB.97.085142> (cit. on p. 66).
- [195] Saswata Roy and Awadhesh Narayan. “Non-linear Hall effect in multi-Weyl semimetals”. In: *Journal of Physics: Condensed Matter* 34.38 (July 2022), p. 385301. DOI: [10.1088/1361-648X/ac8091](https://doi.org/10.1088/1361-648X/ac8091). URL: <https://dx.doi.org/10.1088/1361-648X/ac8091> (cit. on p. 68).
- [196] Kyoung-Whan Kim, Hogyun Jeong, Jeongwoo Kim, et al. “Vertical transverse transport induced by hidden in-plane Berry curvature in two dimensions”. In: *Phys. Rev. B* 104 (8 Aug. 2021), p. L081114. DOI: [10.1103/PhysRevB.104.L081114](https://doi.org/10.1103/PhysRevB.104.L081114). URL: <https://link.aps.org/doi/10.1103/PhysRevB.104.L081114> (cit. on p. 69).
- [197] Dennis Wawrzik, Jhih-Shih You, Jorge I. Facio, et al. “Infinite Berry Curvature of Weyl Fermi Arcs”. In: *Phys. Rev. Lett.* 127 (5 July 2021), p. 056601. DOI: [10.1103/PhysRevLett.127.056601](https://doi.org/10.1103/PhysRevLett.127.056601). URL: <https://link.aps.org/doi/10.1103/PhysRevLett.127.056601> (cit. on pp. 75, 84).
- [198] F. Y. Bruno, A. Tamai, Q. S. Wu, et al. “Observation of large topologically trivial Fermi arcs in the candidate type-II Weyl semimetal WTe_2 ”. In: *Phys. Rev. B* 94 (12 Sept. 2016), p. 121112. DOI: [10.1103/PhysRevB.94.121112](https://doi.org/10.1103/PhysRevB.94.121112). URL: <https://link.aps.org/doi/10.1103/PhysRevB.94.121112> (cit. on p. 81).
- [199] Yun Wu, Daixiang Mou, Na Hyun Jo, et al. “Observation of Fermi arcs in the type-II Weyl semimetal candidate WTe_2 ”. In: *Phys. Rev. B* 94 (12 Sept. 2016), p. 121113. DOI: [10.1103/PhysRevB.94.121113](https://doi.org/10.1103/PhysRevB.94.121113). URL: <https://link.aps.org/doi/10.1103/PhysRevB.94.121113> (cit. on p. 81).
- [200] Kaifei Kang, Tingxin Li, Egon Sohn, et al. “Nonlinear anomalous Hall effect in few-layer WTe_2 ”. In: *Nature Materials* 18.4 (Apr. 2019), pp. 324–328. ISSN: 1476-4660. DOI: [10.1038/s41563-019-0294-7](https://doi.org/10.1038/s41563-019-0294-7). URL: <https://doi.org/10.1038/s41563-019-0294-7> (cit. on pp. 81, 96).
- [201] P. Hohenberg and W. Kohn. “Inhomogeneous Electron Gas”. In: *Phys. Rev.* 136 (3B Nov. 1964), B864–B871. DOI: [10.1103/PhysRev.136.B864](https://doi.org/10.1103/PhysRev.136.B864). URL: <https://link.aps.org/doi/10.1103/PhysRev.136.B864> (cit. on p. 81).

- [202] W. Kohn and L. J. Sham. “Self-Consistent Equations Including Exchange and Correlation Effects”. In: *Phys. Rev.* 140 (4A Nov. 1965), A1133–A1138. DOI: [10.1103/PhysRev.140.A1133](https://doi.org/10.1103/PhysRev.140.A1133). URL: <https://link.aps.org/doi/10.1103/PhysRev.140.A1133> (cit. on p. 81).
- [203] John P. Perdew, J. A. Chevary, S. H. Vosko, et al. “Atoms, molecules, solids, and surfaces: Applications of the generalized gradient approximation for exchange and correlation”. In: *Phys. Rev. B* 46 (11 Sept. 1992), pp. 6671–6687. DOI: [10.1103/PhysRevB.46.6671](https://doi.org/10.1103/PhysRevB.46.6671). URL: <https://link.aps.org/doi/10.1103/PhysRevB.46.6671> (cit. on p. 81).
- [204] G. Kresse and J. Furthmüller. “Efficiency of ab-initio total energy calculations for metals and semiconductors using a plane-wave basis set”. In: *Computational Materials Science* 6.1 (1996), pp. 15–50. ISSN: 0927-0256. DOI: [https://doi.org/10.1016/0927-0256\(96\)00008-0](https://doi.org/10.1016/0927-0256(96)00008-0). URL: <https://www.sciencedirect.com/science/article/pii/0927025696000080> (cit. on p. 81).
- [205] G. Kresse and J. Furthmüller. “Efficient iterative schemes for ab initio total-energy calculations using a plane-wave basis set”. In: *Phys. Rev. B* 54 (16 Oct. 1996), pp. 11169–11186. DOI: [10.1103/PhysRevB.54.11169](https://doi.org/10.1103/PhysRevB.54.11169). URL: <https://link.aps.org/doi/10.1103/PhysRevB.54.11169> (cit. on p. 81).
- [206] G. Kresse and D. Joubert. “From ultrasoft pseudopotentials to the projector augmented-wave method”. In: *Phys. Rev. B* 59 (3 Jan. 1999), pp. 1758–1775. DOI: [10.1103/PhysRevB.59.1758](https://doi.org/10.1103/PhysRevB.59.1758). URL: <https://link.aps.org/doi/10.1103/PhysRevB.59.1758> (cit. on p. 81).
- [207] QuanSheng Wu, ShengNan Zhang, Hai-Feng Song, et al. “WannierTools: An open-source software package for novel topological materials”. In: *Computer Physics Communications* 224 (2018), pp. 405–416. ISSN: 0010-4655. DOI: <https://doi.org/10.1016/j.cpc.2017.09.033>. URL: <https://www.sciencedirect.com/science/article/pii/S0010465517303442> (cit. on p. 81).
- [208] Lujin Min, Hengxin Tan, Zhijian Xie, et al. “Strong room-temperature bulk nonlinear Hall effect in a spin-valley locked Dirac material”. In: *Nature Communications* 14.1 (Jan. 2023), p. 364. ISSN: 2041-1723. DOI: [10.1038/s41467-023-35989-0](https://doi.org/10.1038/s41467-023-35989-0). URL: <https://doi.org/10.1038/s41467-023-35989-0> (cit. on p. 85).
- [209] Teng Ma, Hao Chen, Kunihiro Yananose, et al. “Growth of bilayer MoTe2 single crystals with strong non-linear Hall effect”. In: *Nature Communications* 13.1 (Sept. 2022), p. 5465. ISSN: 2041-1723. DOI: [10.1038/s41467-022-33201-3](https://doi.org/10.1038/s41467-022-33201-3). URL: <https://doi.org/10.1038/s41467-022-33201-3> (cit. on p. 85).
- [210] Igor Zutic, Jaroslav Fabian, and S Das Sarma. “Spintronics: Fundamentals and applications”. In: *Review of Modern Physics* 76 (2004), p. 323. DOI: [10.1103/RevModPhys.76.323](https://doi.org/10.1103/RevModPhys.76.323). URL: <https://journals.aps.org/rmp/abstract/10.1103/RevModPhys.76.323> (cit. on p. 86).

- [211] B Andrei Bernevig, Taylor L Hughes, and Shou-cheng Zhang. “Orbitronics : The Intrinsic Orbital Current in p -Doped Silicon”. In: *Physical Review Letters* 95 (2005), p. 066601. DOI: [10.1103/PhysRevLett.95.066601](https://doi.org/10.1103/PhysRevLett.95.066601). URL: <https://link.aps.org/doi/10.1103/PhysRevLett.95.066601> (cit. on pp. 86, 88).
- [212] Dongwook Go, Jan-philipp Hanke, Patrick M Buhl, et al. “Toward surface orbitronics : giant orbital magnetism from the orbital Rashba effect at the surface of sp-metals”. In: *Scientific Reports* 7 (2017), p. 46742. DOI: [10.1038/srep46742](https://doi.org/10.1038/srep46742). URL: <http://dx.doi.org/10.1038/srep46742> (cit. on pp. 86, 88).
- [213] Daegeun Jo, Dongwook Go, and Hyun-woo Lee. “Gigantic intrinsic orbital Hall effects in weakly spin-orbit coupled metals”. In: *Physical Review B* 98 (2018), p. 214405. DOI: [10.1103/PhysRevB.98.214405](https://doi.org/10.1103/PhysRevB.98.214405). URL: <https://journals.aps.org/prb/abstract/10.1103/PhysRevB.98.214405> (cit. on pp. 86, 87).
- [214] Leandro Salemi, Marco Berritta, and Peter M. Oppeneer. “Quantitative comparison of electrically induced spin and orbital polarizations in heavy-metal/ 3d-metal bilayers”. In: *Physical Review Materials* 5 (7 July 2021). ISSN: 24759953. DOI: [10.1103/PhysRevMaterials.5.074407](https://doi.org/10.1103/PhysRevMaterials.5.074407). URL: <https://link.aps.org/doi/10.1103/PhysRevMaterials.5.074407> (cit. on p. 87).
- [215] Armando Pezo, Diego Garcia Ovalle, and Aurelien Manchon. “Orbital Hall effect in crystals: inter-atomic versus intra-atomic contributions”. In: *Physical Review B* 106 (2022), p. 104414. ISSN: 24699969. DOI: [10.1103/PhysRevB.106.104414](https://doi.org/10.1103/PhysRevB.106.104414). URL: <https://link.aps.org/doi/10.1103/PhysRevB.106.104414> (cit. on p. 87).
- [216] Leandro Salemi and Peter M. Oppeneer. “First-principles theory of intrinsic spin and orbital Hall and Nernst effects in metallic monoatomic crystals”. In: *Physical Review Materials* 6 (2022), p. 095001. DOI: [10.1103/physrevmaterials.6.095001](https://doi.org/10.1103/physrevmaterials.6.095001). URL: <https://link.aps.org/doi/10.1103/PhysRevMaterials.6.095001> (cit. on p. 87).
- [217] Dongwook Go and Hyun-woo Lee. “Orbital torque : Torque generation by orbital current injection”. In: *Physical Review Research* 2 (2020), p. 13177. ISSN: 0031-899X. DOI: [10.1103/PhysRevResearch.2.013177](https://doi.org/10.1103/PhysRevResearch.2.013177). URL: <https://doi.org/10.1103/PhysRevResearch.2.013177> (cit. on p. 87).
- [218] Shilei Ding, Andrew Ross, Dongwook Go, et al. “Harnessing Orbital-to-Spin Conversion of Interfacial Orbital Currents for Efficient Spin-Orbit Torques”. In: *Physical Review Letters* 125 (2020), p. 177201. ISSN: 10797114. DOI: [10.1103/PhysRevLett.125.177201](https://doi.org/10.1103/PhysRevLett.125.177201). URL: <https://doi.org/10.1103/PhysRevLett.125.177201> (cit. on p. 87).
- [219] H. Nakayama, Matthias Althammer, Y.-T. Chen, et al. “Spin Hall Magnetoresistance Induced by a Nonequilibrium Proximity Effect”. In: *Physical Review Letters* 110 (May 2013), p. 206601. ISSN: 0031-9007. DOI: [10.1103/PhysRevLett.110.206601](https://doi.org/10.1103/PhysRevLett.110.206601).

- 110.206601. URL: <http://link.aps.org/doi/10.1103/PhysRevLett.110.206601> (cit. on p. 87).
- [220] S O Valenzuela and M Tinkham. “Direct electronic measurement of the spin Hall effect.” In: *Nature* 442 (July 2006), p. 176. ISSN: 1476-4687. DOI: [10.1038/nature04937](https://doi.org/10.1038/nature04937). URL: <http://www.ncbi.nlm.nih.gov/pubmed/16838016> (cit. on p. 87).
- [221] Stefan Blügel and Gustav Bihlmayer. *Magnetism of Low-dimensional Systems : Theory*. Ed. by H. Kronmüller and S. Parkin. 2007. DOI: [10.1002/9780470022184](https://doi.org/10.1002/9780470022184). URL: <http://doi.wiley.com/10.1002/9780470022184> (cit. on p. 87).
- [222] J Hanke, F Freimuth, A K Nandy, et al. “Role of Berry phase theory for describing orbital magnetism : From magnetic heterostructures to topological orbital ferromagnets”. In: *Physical Review B* 94 (2016), 121114(R). DOI: [10.1103/PhysRevB.94.121114](https://doi.org/10.1103/PhysRevB.94.121114). URL: <https://link.aps.org/doi/10.1103/PhysRevMaterials.6.095001> (cit. on p. 87).
- [223] Shilei Ding, Zhongyu Liang, Dongwook Go, et al. “Observation of the Orbital Rashba-Edelstein Magnetoresistance”. In: *Physical Review Letters* 128 (2022), p. 067201. ISSN: 0031-9007. DOI: [10.1103/physrevlett.128.067201](https://doi.org/10.1103/physrevlett.128.067201). URL: <https://doi.org/10.1103/PhysRevLett.128.067201> (cit. on p. 87).
- [224] S. Yamaguchi, Y. Okimoto, K. Ishibashi, et al. “Magneto-optical Kerr effects in perovskite-type transition-metal oxides: $\text{La}_{1-x}\text{Sr}_x\text{MnO}_3$ and $\text{La}_{1-x}\text{Sr}_x\text{CoO}_3$ ”. In: *Phys. Rev. B* 58 (11 Sept. 1998), pp. 6862–6870. DOI: [10.1103/PhysRevB.58.6862](https://doi.org/10.1103/PhysRevB.58.6862). URL: <https://link.aps.org/doi/10.1103/PhysRevB.58.6862> (cit. on p. 87).
- [225] R. Carey, D. M. Newman, and M. L. Wears. “Giant low-temperature enhancement of magneto-optic Kerr effects in PtMnSb”. In: *Phys. Rev. B* 62 (3 July 2000), pp. 1520–1523. DOI: [10.1103/PhysRevB.62.1520](https://doi.org/10.1103/PhysRevB.62.1520). URL: <https://link.aps.org/doi/10.1103/PhysRevB.62.1520> (cit. on p. 87).
- [226] V. N. Antonov, B. N. Harmon, and A. N. Yaresko. “Electronic structure and magneto-optical Kerr effect of Tm monochalcogenides”. In: *Phys. Rev. B* 63 (20 May 2001), p. 205112. DOI: [10.1103/PhysRevB.63.205112](https://doi.org/10.1103/PhysRevB.63.205112). URL: <https://link.aps.org/doi/10.1103/PhysRevB.63.205112> (cit. on p. 87).
- [227] Kartik Samanta, Marjana Ležaić, Maximilian Merte, et al. “Crystal Hall and crystal magneto-optical effect in thin films of SrRuO₃”. In: *Journal of Applied Physics* 127.21 (2020), p. 213904. DOI: [10.1063/5.0005017](https://doi.org/10.1063/5.0005017). URL: <https://doi.org/10.1063/5.0005017> (cit. on p. 87).
- [228] Ming-Chun Jiang and Guang-Yu Guo. “Large magneto-optical effect and magnetic anisotropy energy in two-dimensional metallic ferromagnet Fe_3GeTe_2 ”. In: *Phys. Rev. B* 105 (1 Jan. 2022), p. 014437. DOI: [10.1103/PhysRevB.105.014437](https://doi.org/10.1103/PhysRevB.105.014437). URL: <https://link.aps.org/doi/10.1103/PhysRevB.105.014437> (cit. on p. 87).

- [229] Jeffrey McCord. “Progress in magnetic domain observation by advanced magneto-optical microscopy”. In: *Journal of Physics D: Applied Physics* 48.33 (July 2015), p. 333001. DOI: [10.1088/0022-3727/48/33/333001](https://doi.org/10.1088/0022-3727/48/33/333001). URL: <https://dx.doi.org/10.1088/0022-3727/48/33/333001> (cit. on pp. 87, 89).
- [230] A. Cebollada, D. Weller, J. Sticht, et al. “Enhanced magneto-optical Kerr effect in spontaneously ordered FePt alloys: Quantitative agreement between theory and experiment”. In: *Phys. Rev. B* 50 (5 Aug. 1994), pp. 3419–3422. DOI: [10.1103/PhysRevB.50.3419](https://link.aps.org/doi/10.1103/PhysRevB.50.3419). URL: <https://link.aps.org/doi/10.1103/PhysRevB.50.3419> (cit. on p. 87).
- [231] Pieter M Oppeneer. “Theory of the magneto-optical Kerr effect in ferromagnetic compounds”. PhD thesis. 1999 (cit. on pp. 87, 89, 90).
- [232] P. M. Oppeneer, V. N. Antonov, T. Kraft, et al. “First-principles study of the giant magneto-optical Kerr effect in MnBi and related compounds”. In: *Journal of Applied Physics* 80.2 (July 1996), pp. 1099–1105. ISSN: 0021-8979. DOI: [10.1063/1.362847](https://doi.org/10.1063/1.362847). URL: <https://doi.org/10.1063/1.362847> (cit. on p. 87).
- [233] Olivier Trépanier, Rémi N. Duchesne, Jérémie J. Boudreault, et al. “Magneto-optical Kerr effect in Weyl semimetals with broken inversion and time-reversal symmetries”. In: *Phys. Rev. B* 106 (12 Sept. 2022), p. 125104. DOI: [10.1103/PhysRevB.106.125104](https://link.aps.org/doi/10.1103/PhysRevB.106.125104). URL: <https://link.aps.org/doi/10.1103/PhysRevB.106.125104> (cit. on p. 87).
- [234] Jean-Michel Parent, René Côté, and Ion Garate. “Magneto-optical Kerr effect and signature of the chiral anomaly in a Weyl semimetal in magnetic field”. In: *Phys. Rev. B* 102 (24 Dec. 2020), p. 245126. DOI: [10.1103/PhysRevB.102.245126](https://link.aps.org/doi/10.1103/PhysRevB.102.245126). URL: <https://link.aps.org/doi/10.1103/PhysRevB.102.245126> (cit. on p. 87).
- [235] Wanxiang Feng, Guang-Yu Guo, Jian Zhou, et al. “Large magneto-optical Kerr effect in noncollinear antiferromagnets Mn_3X ($X = Rh, Ir, Pt$)”. In: *Phys. Rev. B* 92 (14 Oct. 2015), p. 144426. DOI: [10.1103/PhysRevB.92.144426](https://link.aps.org/doi/10.1103/PhysRevB.92.144426). URL: <https://link.aps.org/doi/10.1103/PhysRevB.92.144426> (cit. on p. 87).
- [236] Mingxing Wu, Hironari Isshiki, Taishi Chen, et al. “Magneto-optical Kerr effect in a non-collinear antiferromagnet Mn_3Ge ”. In: *Applied Physics Letters* 116.13 (2020), p. 132408. DOI: [10.1063/1.5143959](https://doi.org/10.1063/1.5143959). URL: <https://doi.org/10.1063/1.5143959> (cit. on p. 87).
- [237] Na Wang, Jun Chen, Ning Ding, et al. “Magneto-optical Kerr effect and magnetoelasticity in a weakly ferromagnetic RuF_4 monolayer”. In: *Phys. Rev. B* 106 (6 Aug. 2022), p. 064435. DOI: [10.1103/PhysRevB.106.064435](https://link.aps.org/doi/10.1103/PhysRevB.106.064435). URL: <https://link.aps.org/doi/10.1103/PhysRevB.106.064435> (cit. on p. 87).

- [238] Nikhil Sivadas, Satoshi Okamoto, and Di Xiao. “Gate-Controllable Magneto-optic Kerr Effect in Layered Collinear Antiferromagnets”. In: *Phys. Rev. Lett.* 117 (26 Dec. 2016), p. 267203. DOI: [10.1103/PhysRevLett.117.267203](https://doi.org/10.1103/PhysRevLett.117.267203). URL: <https://link.aps.org/doi/10.1103/PhysRevLett.117.267203> (cit. on p. 87).
- [239] Gyung-Min Choi and David G. Cahill. “Kerr rotation in Cu, Ag, and Au driven by spin accumulation and spin-orbit coupling”. In: *Phys. Rev. B* 90 (21 Dec. 2014), p. 214432. DOI: [10.1103/PhysRevB.90.214432](https://doi.org/10.1103/PhysRevB.90.214432). URL: <https://link.aps.org/doi/10.1103/PhysRevB.90.214432> (cit. on p. 88).
- [240] Víctor H. Ortiz, Sinisa Coh, and Richard B. Wilson. “Magneto-optical Kerr spectra of gold induced by spin accumulation”. In: *Phys. Rev. B* 106 (1 July 2022), p. 014410. DOI: [10.1103/PhysRevB.106.014410](https://doi.org/10.1103/PhysRevB.106.014410). URL: <https://link.aps.org/doi/10.1103/PhysRevB.106.014410> (cit. on p. 88).
- [241] Jorge Puebla, Florent Auvray, Mingran Xu, et al. “Direct optical observation of spin accumulation at nonmagnetic metal/oxide interface”. In: *Applied Physics Letters* 111 (9 Aug. 2017). ISSN: 00036951. DOI: [10.1063/1.4990113](https://doi.org/10.1063/1.4990113). URL: <https://doi.org/10.1063/1.4990113> (cit. on p. 88).
- [242] Yiwei Zhao, Jin Cao, Zeying Zhang, et al. “Berry curvature dipole and nonlinear Hall effect in two-dimensional $\text{Nb}_{2n+1}\text{Si}_n\text{Te}_{4n+2}$ ”. In: *Phys. Rev. B* 107 (20 May 2023), p. 205124. DOI: [10.1103/PhysRevB.107.205124](https://doi.org/10.1103/PhysRevB.107.205124). URL: <https://link.aps.org/doi/10.1103/PhysRevB.107.205124> (cit. on pp. 89, 99, 100).
- [243] Yugui Yao, Leonard Kleinman, A. H. MacDonald, et al. “First Principles Calculation of Anomalous Hall Conductivity in Ferromagnetic bcc Fe”. In: *Phys. Rev. Lett.* 92 (3 Jan. 2004), p. 037204. DOI: [10.1103/PhysRevLett.92.037204](https://doi.org/10.1103/PhysRevLett.92.037204). URL: <https://link.aps.org/doi/10.1103/PhysRevLett.92.037204> (cit. on p. 90).
- [244] Kazuaki Takasan, Takahiro Morimoto, Joseph Orenstein, et al. “Current-induced second harmonic generation in inversion-symmetric Dirac and Weyl semimetals”. In: *Phys. Rev. B* 104 (16 Oct. 2021), p. L161202. DOI: [10.1103/PhysRevB.104.L161202](https://doi.org/10.1103/PhysRevB.104.L161202). URL: <https://link.aps.org/doi/10.1103/PhysRevB.104.L161202> (cit. on p. 90).
- [245] Young-Gwan Choi, Daegeun Jo, Kyung-Hun Ko, et al. “Observation of the orbital Hall effect in a light metal Ti”. In: *Nature* 619.7968 (July 2023), pp. 52–56. ISSN: 1476-4687. DOI: [10.1038/s41586-023-06101-9](https://doi.org/10.1038/s41586-023-06101-9). URL: <https://doi.org/10.1038/s41586-023-06101-9> (cit. on p. 96).
- [246] J. Hu, X. Liu, C. L. Yue, et al. “Enhanced electron coherence in atomically thin Nb_3SiTe_6 ”. In: *Nature Physics* 11.6 (June 2015), pp. 471–476. ISSN: 1745-2481. DOI: [10.1038/nphys3321](https://doi.org/10.1038/nphys3321). URL: <https://doi.org/10.1038/nphys3321> (cit. on p. 102).

- [247] J. Ebad-Allah, A. A. Tsirlin, Y. L. Zhu, et al. “Signatures of van Hove singularities in the anisotropic in-plane optical conductivity of the topological semimetal Nb_3SiTe_6 ”. In: *Phys. Rev. B* 107 (11 Mar. 2023), p. 115115. DOI: [10.1103/PhysRevB.107.115115](https://doi.org/10.1103/PhysRevB.107.115115). URL: <https://link.aps.org/doi/10.1103/PhysRevB.107.115115> (cit. on p. 102).
- [248] Ioan Mihai Miron, Gilles Gaudin, S. Auffret, et al. “Current-driven spin torque induced by the Rashba effect in a ferromagnetic metal layer.” In: *Nature Materials* 9 (Mar. 2010), p. 230. ISSN: 1476-1122. DOI: [10.1038/nmat2613](https://doi.org/10.1038/nmat2613). URL: <http://www.ncbi.nlm.nih.gov/pubmed/20062047> (cit. on p. 106).
- [249] Luqiao Liu, Takahiro Moriyama, D. C. Ralph, et al. “Spin-Torque Ferromagnetic Resonance Induced by the Spin Hall Effect”. In: *Physical Review Letters* 106 (Jan. 2011), p. 036601. ISSN: 0031-9007. DOI: [10.1103/PhysRevLett.106.036601](https://doi.org/10.1103/PhysRevLett.106.036601). URL: <http://link.aps.org/doi/10.1103/PhysRevLett.106.036601> (cit. on p. 106).
- [250] Young-Wan Oh, Seung-Heon Chris Baek, Y M Kim, et al. “Field-free switching of perpendicular magnetization through spin-orbit torque in antiferromagnet/ferromagnet/oxide structures.” In: *Nature Nanotechnology* 11 (2016), p. 878. ISSN: 1748-3395. DOI: [10.1038/nnano.2016.109](https://doi.org/10.1038/nnano.2016.109). URL: <http://www.ncbi.nlm.nih.gov/pubmed/27428279> (cit. on p. 106).
- [251] Shunsuke Fukami, Chaoliang Zhang, Samik DuttaGupta, et al. “Magnetization switching by spin-orbit torque in an antiferromagnet/ferromagnet bilayer system”. In: *Nature Materials* 15 (2016), p. 535. ISSN: 1476-1122. DOI: [10.1038/nmat4566](https://doi.org/10.1038/nmat4566). URL: <https://www.nature.com/articles/nmat4566> (cit. on p. 106).
- [252] Yong-Chang Lau, Davide Betto, Karsten Rode, et al. “Spin-orbit torque switching without an external field using interlayer exchange coupling”. In: *Nature Nanotechnology* 11 (2016), p. 758. ISSN: 1748-3387. DOI: [10.1038/nnano.2016.84](https://doi.org/10.1038/nnano.2016.84). URL: <http://www.nature.com/doi/10.1038/nnano.2016.84> (cit. on p. 106).
- [253] Jinwu Wei, Xiao Wang, Baoshan Cui, et al. “Field-Free Spin–Orbit Torque Switching in Perpendicularly Magnetized Synthetic Antiferromagnets”. In: *Advanced Functional Materials* 32 (2022), p. 2109455. ISSN: 16163028. DOI: [10.1002/adfm.202109455](https://doi.org/10.1002/adfm.202109455). URL: <https://onlinelibrary.wiley.com/doi/10.1002/adfm.202109455> (cit. on p. 106).
- [254] Seung Heon C. Baek, Vivek P. Amin, Young Wan Oh, et al. “Spin currents and spin-orbit torques in ferromagnetic trilayers”. In: *Nature Materials* 17 (2018), p. 509. ISSN: 14764660. DOI: [10.1038/s41563-018-0041-5](https://doi.org/10.1038/s41563-018-0041-5). URL: <https://www.nature.com/articles/s41563-018-0041-5> (cit. on p. 106).

- [255] Jeongchun Ryu, Ryan Thompson, Jae Yeol Park, et al. “Efficient spin–orbit torque in magnetic trilayers using all three polarizations of a spin current”. In: *Nature Electronics* 5 (2022), p. 217. ISSN: 25201131. DOI: [10.1038/s41928-022-00735-9](https://doi.org/10.1038/s41928-022-00735-9). URL: <https://www.nature.com/articles/s41928-022-00735-9> (cit. on p. 106).
- [256] V. P. Amin, J. Zemen, and M. D. Stiles. “Interface-Generated Spin Currents”. In: *Physical Review Letters* 121 (2018), p. 136805. ISSN: 0031-9007. DOI: [10.1103/PhysRevLett.121.136805](https://doi.org/10.1103/PhysRevLett.121.136805). URL: <https://link.aps.org/doi/10.1103/PhysRevLett.121.136805> (cit. on p. 106).
- [257] Maria B. Lifshits and Michel I. Dyakonov. “Swapping Spin Currents: Interchanging Spin and Flow Directions”. In: *Physical Review Letters* 103 (Oct. 2009), p. 186601. ISSN: 0031-9007. DOI: [10.1103/PhysRevLett.103.186601](https://doi.org/10.1103/PhysRevLett.103.186601). URL: <http://link.aps.org/doi/10.1103/PhysRevLett.103.186601> (cit. on p. 106).
- [258] Hamed Ben Mohamed Saidaoui and Aurélien Manchon. “Spin-Swapping Transport and Torques in Ultrathin Magnetic Bilayers”. In: *Physical Review Letters* 117 (2016), p. 036601. ISSN: 0031-9007. DOI: [10.1103/PhysRevLett.117.036601](https://doi.org/10.1103/PhysRevLett.117.036601). URL: <https://link.aps.org/doi/10.1103/PhysRevLett.117.036601> (cit. on p. 106).
- [259] Ziyang Luo, Qi Zhang, Yanjun Xu, et al. “Spin-Orbit Torque in a Single Ferromagnetic Layer Induced by Surface Spin Rotation”. In: *Physical Review Applied* 11 (2019), p. 064021. ISSN: 2331-7019. DOI: [10.1103/PhysRevApplied.11.064021](https://doi.org/10.1103/PhysRevApplied.11.064021). URL: <https://doi.org/10.1103/PhysRevApplied.11.064021> (cit. on p. 106).
- [260] Christian Ortiz Pauyac, Mairbek Chshiev, Aurelien Manchon, et al. “Spin Hall and Spin Swapping Torques in Diffusive Ferromagnets”. In: *Physical Review Letters* 120 (2018), p. 176802. ISSN: 10797114. DOI: [10.1103/PhysRevLett.120.176802](https://doi.org/10.1103/PhysRevLett.120.176802). URL: <https://doi.org/10.1103/PhysRevLett.120.176802> (cit. on p. 106).
- [261] Arnab Bose, D D Lam, S Bhuktare, et al. “Observation of Anomalous Spin Torque Generated by a Ferromagnet”. In: *Physical Review Applied* 9.6 (2018), p. 64026. ISSN: 2331-7019. DOI: [10.1103/PhysRevApplied.9.064026](https://doi.org/10.1103/PhysRevApplied.9.064026). URL: <https://doi.org/10.1103/PhysRevApplied.9.064026> (cit. on p. 107).
- [262] Baoshan Cui, Hao Wu, Dong Li, et al. “Field-Free Spin-Orbit Torque Switching of Perpendicular Magnetization by the Rashba Interface”. In: *ACS Applied Materials and Interfaces* 11.42 (2019), pp. 39369–39375. ISSN: 19448252. DOI: [10.1021/acsami.9b13622](https://doi.org/10.1021/acsami.9b13622). URL: <https://pubs.acs.org/doi/10.1021/acsami.9b13622> (cit. on p. 107).

- [263] Armin Razavi, Hao Wu, Qiming Shao, et al. “Deterministic spin-orbit torque switching by a light-metal insertion”. In: *Nano Letters* 20 (2020), p. 3703. ISSN: 15306992. DOI: [10.1021/acs.nanolett.0c00647](https://doi.org/10.1021/acs.nanolett.0c00647). URL: <https://pubs.acs.org/doi/10.1021/acs.nanolett.0c00647> (cit. on p. 107).
- [264] Min Gu Kang, Jong Guk Choi, Jimin Jeong, et al. “Electric-field control of field-free spin-orbit torque switching via laterally modulated Rashba effect in Pt/Co/AlO_x structures”. In: *Nature Communications* 12 (2021), p. 7111. ISSN: 20411723. DOI: [10.1038/s41467-021-27459-2](https://doi.org/10.1038/s41467-021-27459-2). URL: <https://www.nature.com/articles/s41467-021-27459-2> (cit. on p. 107).
- [265] C K Safeer, Emilie Jué, Alexandre Lopez, et al. “Spin-orbit torque magnetization switching controlled by geometry.” In: *Nature Nanotechnology* 11 (2016), p. 143. ISSN: 1748-3395. DOI: [10.1038/nnano.2015.252](https://doi.org/10.1038/nnano.2015.252). URL: <http://www.nature.com/nnano/journal/vaop/ncurrent/full/nnano.2015.252.html#close> (cit. on p. 107).
- [266] Long You, OukJae Lee, Debanjan Bhowmik, et al. “Switching of perpendicularly polarized nanomagnets with spin orbit torque without an external magnetic field by engineering a tilted anisotropy”. In: *Proceedings of the National Academy of Sciences* 112 (2015), p. 10310. ISSN: 0027-8424. DOI: [10.1073/pnas.1507474112](https://doi.org/10.1073/pnas.1507474112). URL: <http://www.pnas.org/lookup/doi/10.1073/pnas.1507474112> (cit. on p. 107).
- [267] Liang Liu, Qing Qin, Weinan Lin, et al. “Current-induced magnetization switching in all-oxide heterostructures”. In: *Nature Nanotechnology* 14 (2019), p. 939. ISSN: 17483395. DOI: [10.1038/s41565-019-0534-7](https://doi.org/10.1038/s41565-019-0534-7). URL: <http://dx.doi.org/10.1038/s41565-019-0534-7> (cit. on p. 107).
- [268] Hongwei Li, Gaili Wang, Dan Li, et al. “Field-Free Deterministic Magnetization Switching with Ultralow Current Density in Epitaxial Au/Fe 4 N Bilayer Films”. In: *ACS Applied Materials and Interfaces* 11 (2019), p. 16965. ISSN: 19448252. DOI: [10.1021/acsami.9b00129](https://doi.org/10.1021/acsami.9b00129). URL: <https://pubs.acs.org/doi/10.1021/acsami.9b00129> (cit. on p. 107).
- [269] Xinyu Shu, Liang Liu, Jing Zhou, et al. “Field-Free Switching of Perpendicular Magnetization Induced by Longitudinal Spin-Orbit-Torque Gradient”. In: *Physical Review Applied* 17 (2022), p. 024031. ISSN: 23317019. DOI: [10.1103/PhysRevApplied.17.024031](https://doi.org/10.1103/PhysRevApplied.17.024031). URL: <https://doi.org/10.1103/PhysRevApplied.17.024031> (cit. on p. 107).
- [270] Shaohai Chen, Jihang Yu, Qidong Xie, et al. “Free Field Electric Switching of Perpendicularly Magnetized Thin Film by Spin Current Gradient”. In: *ACS Applied Materials and Interfaces* 11.33 (2019), pp. 30446–30452. ISSN: 19448252. DOI: [10.1021/acsami.9b09146](https://doi.org/10.1021/acsami.9b09146). URL: <https://pubs.acs.org/doi/10.1021/acsami.9b09146> (cit. on p. 107).

- [271] Alexandr Chernyshov, Mason Overby, Xinyu Liu, et al. “Evidence for reversible control of magnetization in a ferromagnetic material by means of spin–orbit magnetic field”. In: *Nature Physics* 5 (Aug. 2009), p. 656. ISSN: 1745-2473. DOI: [10.1038/nphys1362](https://doi.org/10.1038/nphys1362). URL: <http://www.nature.com/doi/10.1038/nphys1362> (cit. on p. 107).
- [272] M. Endo, F. Matsukura, and H. Ohno. “Current induced effective magnetic field and magnetization reversal in uniaxial anisotropy (Ga,Mn)As”. In: *Applied Physics Letters* 97 (2010), p. 222501. ISSN: 00036951. DOI: [10.1063/1.3520514](https://doi.org/10.1063/1.3520514). URL: <http://scitation.aip.org/content/aip/journal/apl/97/22/10.1063/1.3520514> (cit. on p. 107).
- [273] C. Ciccarelli, L. Anderson, V. Tshitoyan, et al. “Room-temperature spin-orbit torque in NiMnSb”. In: *Nature Physics* 12 (2016), p. 855. ISSN: 1745-2473. DOI: [10.1038/nphys3772](https://doi.org/10.1038/nphys3772). URL: <http://arxiv.org/abs/1510.03356> (cit. on p. 107).
- [274] David Macneill, Gregory M. Stiehl, Marcos H.D. Guimarães, et al. “Thickness dependence of spin-orbit torques generated by WTe₂”. In: *Physical Review B* 96 (2017), p. 054450. ISSN: 24699969. DOI: [10.1103/PhysRevB.96.054450](https://doi.org/10.1103/PhysRevB.96.054450). eprint: [1707.03757](https://arxiv.org/abs/1707.03757). URL: <https://link.aps.org/doi/10.1103/PhysRevB.96.054450> (cit. on p. 107).
- [275] Shuyuan Shi, Shiheng Liang, Zhifeng Zhu, et al. “All-electric magnetization switching and Dzyaloshinskii–Moriya interaction in WTe₂/ferromagnet heterostructures”. In: *Nature Nanotechnology* 14 (2019), p. 945. ISSN: 17483395. DOI: [10.1038/s41565-019-0525-8](https://doi.org/10.1038/s41565-019-0525-8). URL: <http://dx.doi.org/10.1038/s41565-019-0525-8> (cit. on pp. 107, 123).
- [276] Qidong Xie, Weinan Lin, Soumya Sarkar, et al. “Field-free magnetization switching induced by the unconventional spin-orbit torque from WTe₂”. In: *APL Materials* 9 (2021), p. 051114. ISSN: 2166532X. DOI: [10.1063/5.0048926](https://doi.org/10.1063/5.0048926). URL: <https://doi.org/10.1063/5.0048926> (cit. on pp. 107, 123).
- [277] I-hsuan Kao, Ryan Muzzio, Hantao Zhang, et al. “Deterministic switching of a perpendicularly polarized magnet using unconventional spin – orbit torques in WTe₂”. In: *Nature Materials* (2022). DOI: [10.1038/s41563-022-01275-5](https://doi.org/10.1038/s41563-022-01275-5). URL: <https://www.nature.com/articles/s41563-022-01275-5> (cit. on p. 107).
- [278] Fei Xue, Christoph Rohmann, Junwen Li, et al. “Unconventional spin-orbit torque in transition metal dichalcogenide-ferromagnet bilayers from first-principles calculations”. In: *Physical Review B* 102 (2020), p. 014401. ISSN: 24699969. DOI: [10.1103/PhysRevB.102.014401](https://doi.org/10.1103/PhysRevB.102.014401). URL: <https://link.aps.org/doi/10.1103/PhysRevB.102.014401> (cit. on p. 107).

- [279] Marcos H.D. Guimarães, Gregory M. Stiehl, David MacNeill, et al. “Spin-Orbit Torques in NbSe₂/Permalloy Bilayers”. In: *Nano Letters* 18 (2018), p. 1311. ISSN: 15306992. DOI: [10.1021/acs.nanolett.7b04993](https://doi.org/10.1021/acs.nanolett.7b04993). URL: <https://pubs.acs.org/doi/10.1021/acs.nanolett.7b04993> (cit. on p. 107).
- [280] J. Zelezný, Y. Zhang, C. Felser, et al. “Spin-Polarized Current in Noncollinear Antiferromagnets”. In: *Physical Review Letters* 119 (2017), p. 187204. DOI: [10.1103/PhysRevLett.119.187204](https://doi.org/10.1103/PhysRevLett.119.187204). URL: <https://link.aps.org/doi/10.1103/PhysRevLett.119.187204> (cit. on p. 107).
- [281] Yang Zhang, J. Zelezny, Yan Sun, et al. “Spin Hall effect emerging from a non-collinear magnetic lattice without spin-orbit coupling”. In: *New Journal of Physics* 20 (2018), p. 073028. DOI: [10.1088/1367-2630/aad1eb](https://doi.org/10.1088/1367-2630/aad1eb). URL: <https://dx.doi.org/10.1088/1367-2630/aad1eb> (cit. on p. 107).
- [282] Motoi Kimata, Hua Chen, Kouta Kondou, et al. “Magnetic and magnetic inverse spin Hall effects in a non-collinear antiferromagnet”. In: *Nature* 565 (2019), p. 627. ISSN: 1476-4687. DOI: [10.1038/s41586-018-0853-0](https://doi.org/10.1038/s41586-018-0853-0). URL: <http://dx.doi.org/10.1038/s41586-018-0853-0> (cit. on p. 107).
- [283] Srikrishna Ghosh, Aurelien Manchon, and Jakub Železný. “Unconventional Robust Spin-Transfer Torque in Noncollinear Antiferromagnetic Junctions”. In: *Physical Review Letters* 128 (2022), p. 097702. ISSN: 0031-9007. DOI: [10.1103/physrevlett.128.097702](https://doi.org/10.1103/physrevlett.128.097702). URL: <https://link.aps.org/doi/10.1103/PhysRevLett.128.097702> (cit. on p. 107).
- [284] Xianzhe Chen, Shuyuan Shi, Guoyi Shi, et al. “Observation of the antiferromagnetic spin Hall effect”. In: *Nature Materials* 20.6 (2021), p. 800. ISSN: 14764660. DOI: [10.1038/s41563-021-00946-z](https://doi.org/10.1038/s41563-021-00946-z). URL: <http://dx.doi.org/10.1038/s41563-021-00946-z> (cit. on p. 107).
- [285] Arnab Bose, Nathaniel J. Schreiber, Rakshit Jain, et al. “Tilted spin current generated by the collinear antiferromagnet ruthenium dioxide”. In: *Nature Electronics* 5 (2022), p. 267. ISSN: 25201131. DOI: [10.1038/s41928-022-00744-8](https://doi.org/10.1038/s41928-022-00744-8). URL: <https://www.nature.com/articles/s41928-022-00744-8> (cit. on p. 107).
- [286] H. Bai, L. Han, X. Y. Feng, et al. “Observation of Spin Splitting Torque in a Collinear Antiferromagnet RuO₂”. In: *Physical Review Letters* 128 (2022), p. 197202. ISSN: 0031-9007. DOI: [10.1103/physrevlett.128.197202](https://doi.org/10.1103/physrevlett.128.197202). eprint: [2109.05933](https://arxiv.org/abs/2109.05933). URL: <https://link.aps.org/doi/10.1103/PhysRevLett.128.197202> (cit. on p. 107).
- [287] T. Nan, C. X. Quintela, J. Irwin, et al. “Controlling spin current polarization through non-collinear antiferromagnetism”. In: *Nature Communications* 11 (2020), p. 4671. ISSN: 20411723. DOI: [10.1038/s41467-020-17999-4](https://doi.org/10.1038/s41467-020-17999-4). eprint: [1912.12586](https://arxiv.org/abs/1912.12586). URL: <http://dx.doi.org/10.1038/s41467-020-17999-4> (cit. on p. 107).

- [288] H. Bai, X. F. Zhou, H. W. Zhang, et al. “Control of spin-orbit torques through magnetic symmetry in differently oriented noncollinear antiferromagnetic Mn₃Pt”. In: *Physical Review B* 104 (2021), p. 104401. ISSN: 24699969. DOI: [10.1103/PhysRevB.104.104401](https://doi.org/10.1103/PhysRevB.104.104401). URL: <https://link.aps.org/doi/10.1103/PhysRevB.104.104401> (cit. on p. 107).
- [289] Kouta Kondou, Hua Chen, Takahiro Tomita, et al. “Giant field-like torque by the out-of-plane magnetic spin Hall effect in a topological antiferromagnet”. In: *Nature Communications* 12.1 (2021), pp. 1–8. ISSN: 20411723. DOI: [10.1038/s41467-021-26453-y](https://doi.org/10.1038/s41467-021-26453-y). URL: <https://www.nature.com/articles/s41467-021-26453-y> (cit. on p. 107).
- [290] Cheng Gong and Xiang Zhang. “Two-dimensional magnetic crystals and emergent heterostructure devices”. In: *Science* 363 (2019), p. 706. DOI: [10.1126/science.aav4450](https://doi.org/10.1126/science.aav4450). URL: <https://www.science.org/doi/10.1126/science.aav4450> (cit. on p. 107).
- [291] Kaixuan Zhang, Seungyun Han, Youjin Lee, et al. “Gigantic Current Control of Coercive Field and Magnetic Memory Based on Nanometer-Thin Ferromagnetic van der Waals Fe₃GeTe₂”. In: *Advanced Materials* 33 (2021), p. 2004110. ISSN: 15214095. DOI: [10.1002/adma.202004110](https://doi.org/10.1002/adma.202004110). URL: <https://onlinelibrary.wiley.com/doi/10.1002/adma.202004110> (cit. on pp. 107, 123).
- [292] Slimane Laref, Kyoung-whan Kim, and Aurélien Manchon. “Elusive Dzyaloshinskii-Moriya interaction in monolayer Fe₃GeTe₂”. In: *Physical Review B* 102 (2020), 060402(R). ISSN: 0031-899X. DOI: [10.1103/PhysRevB.102.060402](https://doi.org/10.1103/PhysRevB.102.060402). URL: <https://doi.org/10.1103/PhysRevB.102.060402> (cit. on p. 107).
- [293] Idris Smaili, Slimane Laref, Jose H. Garcia, et al. “Janus monolayers of magnetic transition metal dichalcogenides as an all-in-one platform for spin-orbit torque”. In: *Physical Review B* 104 (2021), p. 104415. ISSN: 24699969. DOI: [10.1103/PhysRevB.104.104415](https://doi.org/10.1103/PhysRevB.104.104415). URL: <https://doi.org/10.1103/PhysRevB.104.104415> (cit. on pp. 108, 123, 131).
- [294] Mildred S Dresselhaus. *Group Theory: Application to the Physics of Condensed Matter*. Springer, 2008. ISBN: 9783540328971. DOI: <https://doi.org/10.1007/978-3-540-32899-5> (cit. on pp. 109, 110).
- [295] Luqiao Liu, Chi-Feng Pai, D. C. Ralph, et al. “Magnetic Oscillations Driven by the Spin Hall Effect in 3-Terminal Magnetic Tunnel Junction Devices”. In: *Physical Review Letters* 109 (Oct. 2012), p. 186602. ISSN: 0031-9007. DOI: [10.1103/PhysRevLett.109.186602](https://doi.org/10.1103/PhysRevLett.109.186602). URL: <http://link.aps.org/doi/10.1103/PhysRevLett.109.186602> (cit. on p. 112).
- [296] V. E. Demidov, Sergei Urazhdin, Henning Ulrichs, et al. “Magnetic nano-oscillator driven by pure spin current.” In: *Nature Materials* 11 (Dec. 2012), p. 1028. ISSN: 1476-1122. DOI: [10.1038/nmat3459](https://doi.org/10.1038/nmat3459). URL: <http://www.ncbi.nlm.nih.gov/pubmed/23064497> (cit. on p. 112).

- [297] Daichi Kurebayashi and Naoto Nagaosa. “Theory of current-driven dynamics of spin textures on the surface of a topological insulator”. In: *Physical Review B* 100 (2019), p. 134407. ISSN: 24699969. DOI: [10.1103/PhysRevB.100.134407](https://doi.org/10.1103/PhysRevB.100.134407). URL: <https://link.aps.org/doi/10.1103/PhysRevB.100.134407> (cit. on p. 113).
- [298] Yusuke Imai, Terufumi Yamaguchi, Ai Yamakage, et al. “Spintronic properties of topological surface Dirac electrons with hexagonal warping”. In: *Physical Review B* 103 (2021), p. 54402. ISSN: 24699969. DOI: [10.1103/PhysRevB.103.054402](https://doi.org/10.1103/PhysRevB.103.054402). URL: <https://doi.org/10.1103/PhysRevB.103.054402> (cit. on p. 113).
- [299] Yong Long Zhou, Hou Jian Duan, Yong Jia Wu, et al. “Nonlinear antidamping spin-orbit torque originating from intraband transport on the warped surface of a topological insulator”. In: *Physical Review B* 105.7 (2022), pp. 1–10. ISSN: 24699969. DOI: [10.1103/PhysRevB.105.075415](https://doi.org/10.1103/PhysRevB.105.075415). URL: <https://link.aps.org/doi/10.1103/PhysRevB.105.075415> (cit. on p. 113).
- [300] Jia Yu Li, Rui Qiang Wang, Ming Xun Deng, et al. “In-plane magnetization effect on current-induced spin-orbit torque in a ferromagnet/topological insulator bilayer with hexagonal warping”. In: *Physical Review B* 99 (2019), p. 155139. ISSN: 24699969. DOI: [10.1103/PhysRevB.99.155139](https://doi.org/10.1103/PhysRevB.99.155139). URL: <https://link.aps.org/doi/10.1103/PhysRevB.99.155139> (cit. on p. 113).
- [301] Y L Chen, J G Analytis, J-H Chu, et al. “Experimental realization of a three-dimensional topological insulator, Bi₂Te₃.” In: *Science (New York, N.Y.)* 325.5937 (July 2009), pp. 178–81. ISSN: 1095-9203. DOI: [10.1126/science.1173034](https://doi.org/10.1126/science.1173034). URL: <http://www.ncbi.nlm.nih.gov/pubmed/19520912> (cit. on p. 123).
- [302] D Hsieh, Y Xia, D Qian, et al. “A tunable topological insulator in the spin helical Dirac transport regime”. In: *Nature* 460 (Aug. 2009), p. 1101. ISSN: 0028-0836. URL: <http://dx.doi.org/10.1038/nature08234>http://www.nature.com/nature/journal/v460/n7259/supinfo/nature08234_S1.html (cit. on p. 123).
- [303] Zhanybek Alpichshev, J. G. Analytis, J. H. Chu, et al. “STM imaging of electronic waves on the surface of Bi₂Te₃: Topologically protected surface states and hexagonal warping effects”. In: *Physical Review Letters* 104 (2010), p. 016401. ISSN: 00319007. DOI: [10.1103/PhysRevLett.104.016401](https://doi.org/10.1103/PhysRevLett.104.016401). URL: <https://link.aps.org/doi/10.1103/PhysRevLett.104.016401> (cit. on p. 123).
- [304] Thais Chagas, Omar A. Ashour, Guilherme A. S. Ribeiro, et al. “Multiple strong topological gaps and hexagonal warping in Bi₄Te₃”. In: *Phys. Rev. B* 105 (8 Feb. 2022), p. L081409. DOI: [10.1103/PhysRevB.105.L081409](https://doi.org/10.1103/PhysRevB.105.L081409). URL: <https://link.aps.org/doi/10.1103/PhysRevB.105.L081409> (cit. on p. 123).

- [305] Yu Chen, Maria D'Antuono, Nicholas B. Brookes, et al. "Ferromagnetic Quasi-Two-Dimensional Electron Gas with Trigonal Crystal Field Splitting". In: *ACS Applied Electronic Materials* 4 (2022), pp. 3226–3231. ISSN: 26376113. DOI: [10.1021/acsaelm.2c00447](https://doi.org/10.1021/acsaelm.2c00447). URL: <https://pubs.acs.org/doi/10.1021/acsaelm.2c00447> (cit. on p. 123).
- [306] H. J. Juretschke. "Symmetry of galvanomagnetic effects in antimony". In: *Acta Crystallographica* 8.11 (Nov. 1955), pp. 716–722. DOI: [10.1107/S0365110X55002181](https://doi.org/10.1107/S0365110X55002181). URL: <https://doi.org/10.1107/S0365110X55002181> (cit. on p. 124).
- [307] Vladimir Litvinov. *Magnetism in Topological Insulators*. 1st ed. Springer International Publishing, 2020. ISBN: 978-3-030-12052-8;978-3-030-12053-5. DOI: <https://doi.org/10.1007/978-3-030-12053-5> (cit. on p. 171).
- [308] B. Andrei Bernevig with Taylor L. Hughes. *Topological insulators and topological superconductors*. Princeton University Press, 2013. ISBN: 9780691151755,069115175X. DOI: <https://doi.org/10.1515/9781400846733> (cit. on p. 171).

Appendices

A. Berry Phase Theory in Quantum Mechanics

As it was stated by M.Berry [28], in this appendix we explain the emergence of a non-trivial phase in the wave function. If we take a parameter dependent hamiltonian $\mathcal{H}(\lambda(t))$ and its eigenstates $|\Psi(\lambda(t))\rangle$, an additional geometrical phase factor is acquired as a consequence of the adiabatic evolution of the system between $t = 0$ and $t = T$. If the Hamiltonian is time independent, then its eigenstates satisfy the time independent Schrodinger equation:

$$\hat{H}|\psi_n\rangle = E_n|\psi_n\rangle. \quad (\text{A1})$$

On the other hand, if the Hamiltonian is time dependent, but varies slowly in time, it remains in the same state up to two phase factors that depend on the energy and the geometry:

$$|\psi\rangle = |\psi\rangle e^{i\theta_n(t)} e^{i\gamma_n(t)}, \quad (\text{A2})$$

where $\theta_n(t)$ is a dynamical phase given by

$$\theta_n(t) = -\frac{1}{\hbar} \int_0^T E_n(t') dt'. \quad (\text{A3})$$

For the additional geometrical phase $\gamma_n(t)$, if we replace Eq.(A2) into the time dependent Schrodinger equation

$$\hat{H}|\psi_n\rangle = i\hbar \frac{d|\psi_n\rangle}{dt}, \quad (\text{A4})$$

we have

$$\begin{aligned} \hat{H}|\psi_n\rangle e^{i\theta_n(t)} e^{i\gamma_n(t)} &= E_n|\psi_n\rangle e^{i\theta_n(t)} e^{i\gamma_n(t)} \\ &= i\hbar \frac{\partial}{\partial t} \left(|\psi_n\rangle e^{i\theta_n(t)} e^{i\gamma_n(t)} \right) \\ &= i\hbar \left(\frac{\partial |\psi_n\rangle}{\partial t} - \frac{i}{\hbar} E_n |\psi_n\rangle + i |\psi_n\rangle \frac{d\gamma_n}{dt} \right) e^{i\theta_n} e^{i\gamma_n} \end{aligned}$$

whence

$$\frac{\partial |\psi_n\rangle}{\partial t} + i |\psi_n\rangle \frac{d\gamma_n}{dt} = 0. \quad (\text{A5})$$

Taking the inner product of Eq.(A5) with $\langle \psi_n |$ and the orthogonality relation $\langle \psi_n | \psi_m \rangle = \delta_{nm}$,

$$\left\langle \psi_n \left| \frac{\partial \psi_n}{\partial t} \right. \right\rangle + i \frac{d\gamma_n}{dt} = 0. \quad (\text{A6})$$

Using the parameter dependence of the Hamiltonian, we find that

$$\frac{d\gamma_n}{dt} = -\frac{1}{i} \left\langle \psi_n \left| \frac{\partial \psi_n}{\partial t} \right. \right\rangle = i \langle \psi_n | \vec{\nabla}_\lambda \psi_n \rangle \frac{\partial \lambda}{\partial t} \quad (\text{A7})$$

and finally

$$\gamma_n(t) = \int_{\lambda(0)}^{\lambda(T)} i \langle \psi_n | \vec{\nabla}_\lambda \psi_n \rangle d\lambda. \quad (\text{A8})$$

We can also express the Berry phase in terms of the Berry connection:

$$\gamma_n = \oint \vec{\mathcal{A}}_n(\lambda) \cdot d\lambda. \quad (\text{A9})$$

The Berry connection is related to the overlapping of eigenstates between two near points in the parameter space λ , $\delta\lambda$ [307]:

$$\langle \psi_n(\lambda) | \psi_n(\lambda + \delta\lambda) \rangle \simeq 1 + \left\langle \psi_n \left| \frac{\partial \psi_n}{\partial \lambda} \right. \right\rangle \delta\lambda + \dots = e^{-i\vec{\mathcal{A}}_n \cdot \lambda}. \quad (\text{A10})$$

Notice that the Berry phase defined in Eq.(A10) is Gauge dependent. Then, if we perform a Gauge transformation of the form

$$\vec{\mathcal{A}}_n \rightarrow \vec{\mathcal{A}}_n - \vec{\nabla}_\lambda f,$$

where $f(\lambda)$ is an scalar function, the Berry phase must be unchanged. Thus, for a cyclic adiabatic evolution of $f(\lambda)$, [308]

$$f(\lambda(T)) - f(\lambda(0)) = 2\pi m, \quad m \in \mathbb{Z} \quad (\text{A11})$$

holds. By using Stokes' theorem, Eq.(A9) becomes a flux integral of the Berry curvature $\vec{\Omega} = \vec{\nabla} \times \vec{\mathcal{A}}$:

$$\gamma_n = \oint_{S(\lambda)} \vec{\Omega} \cdot \vec{d}S. \quad (\text{A12})$$